Permittivities retrieval of a dihedral structure using radar polarimetry

Orian Couderc

université PARIS-SACLAY

NNT : 2019SACLC009

Thèse de doctorat

CentraleSupélec

Permittivities retrieval of a dihedral structure using radar polarimetry

Thèse de doctorat de l'Université Paris-Saclay
préparée à Centrale-Supélec

Ecole doctorale n°575 : Electrical, optical, bio : physics and engineering (EOBE)

Spécialité de doctorat : Electronique et Optoélectronique, Nano et Microtechnologies

Thèse présentée et soutenue à Gif-sur-Yvette le 08 février 2019 par

Orian COUDERC

Composition du jury :

Raphaël Gillard Professeur, INSA Rennes (IETR)	Président
Philippe Paillou Professeur, Université de Bordeaux (Laboratoire d'Astrophysique de Bordeaux)	Rapporteur
Daniele Riccio Professeur, Université de Naples (Department of Electrical Engineering and Information Technology)	Rapporteur
Albane Saintenoy Maître de conférences, Géosciences Paris Sud (INSU)	Examinateur
Pierre Sabouroux Maître de conférences, Université de Provence (Institut Fresnel)	Examinateur
Laetitia Thirion-Lefevre Professeure adjointe, CentraleSupélec (SONDRA)	Examinateur
Régis Guinvarc'h Professeur, CentraleSupélec (SONDRA)	Directeur de thèse

Remerciements

Une première pensée part pour l'équipe Vision de Fugro Intersite de mon année 2013/2014 de césure, ainsi qu'à Jean-Christophe Cexus, encadrant de mon stage de master recherche et de Projet de Fin d'Etudes à l'ENSTA Bretagne sans qui, je pense, je n'aurais effectué de thèse.
Je remercie aussi la Fondation Supélec d'avoir financé ce doctorat et aussi au laboratoire SONDRA et à travers celui-ci, ses différents directeurs, M. Lesturgie, S. Azzarian et S. Saillant, de m'avoir accueilli. Ma gratitude va aussi aux membres du jury pour s'être intéressé à ma thèse.

Bien sûr, un énorme et grand merci à Laetitia Thirion-Lefevre et Régis Guinvarc'h. Je suis parti de Master Recherche et de troisième année d'école d'ingénieur avec la seule bonne parole d'Alexandre Baussard à votre sujet... et ma confiance en cette parole a été très bien placée. De très bons conseils et mais aussi tout à l'écoute du thésard trimant, le duo, sympathique et compétant, fait en sorte que le doctorant s'en sorte grandi et content. Pour ces trois années de conseils et d'efforts pour que ma thèse se déroule au mieux, tant au plan professionnel que personnel, merci du fond du cœur.

Dans la même veine et aussi pour son aide avec les mesures effectuées en chambre anéchoique et les mesures au bâtiment Eiffel, je remercie Israel Hinostroza. De bonne humeur, de bonne volonté et toujours curieux et intéressé, cela a été un vrai plaisir de travailler avec toi. Concernant les mesures, je souhaites aussi exprimer ma gratitude auprès du laboratoire Geeps. Notamment, envers Mohammed Serhir, qui toujours prêt à faire un aparté philosophique ou artistique prêtant à réflection entre deux mesures, apporte par la même occasion une bouffée d'air au doctorant enfermé dans sa dernière année de thèse. Je remercie aussi Vincent Polledri pour son expertise de la sonde coaxiale du Geeps concernant la mesure de permittivité au contact, et Joel Legrand pour ce qui concerne la mise en oeuvre des mesures dans les chambres anéchoiques.
Je remercie aussi Thierry Letertre pour ses conseils avisés lorsqu'il s'agit d'expérimentations ou de leur mise en oeuvre. J'en profites aussi pour saluer François Doyelle qui au cours de son stage pour son magistère m'aura aider à explorer les pistes théoriques possibles concernant la méthode du chapitre 3. I also take the occasion to thank Professor Kamal Sarabandi from the University of Michigan for suggesting us to use the polarimetric ratio in order to by-pass calibration issues.

En ce qui concerne la vie au laboratoire SONDRA, Virginie Bouvier est incontournable. Partageant plusieurs rôles, confidente des thésards et souvent leur porte-parole, elle est aussi leur premier rempart face à l'administration. Merci pour tout le taff abbatu pour nous et ta bienveillance !
Concernant le quotidien, je pense aussi au groupe de thésards, avec qui l'on s'est suivi et encouragé durant cette période : Eugénie Terreaux, Pedro Mendes Ruiz, Uy Hour Tan, Ammar Mian et Bruno Mériaux. Une grande partie de mes meilleurs souvenirs de SONDRA partiront sans aucun doute avec les pauses café et déjeuners passées avec vous à déblatérer sur nos thèses respectives mais aussi, et surtout, sur n'importe quoi d'autre, souvent en compagnie d'Israel, de Thierry et Chengfang. Je trouve d'ailleurs assez merveilleux que ce groupe du midi ait pu s'entendre à ce point-là, alors que nous sommes issu de profils étudiants/professionnels mais aussi de cultures et modes de vie et de religions assez différents. Mais peut être que cela est du aux madeleines et aux cigarettes choconoisettes. On pourrait, sur ce point, remercier Bijou pour les quelques centaines d'euros dépensées à leurs bénéfices et les quelques kilos pris par leurs consommateurs. La crêpière, rêvée, me parait toujours bien loin... Merci à mon acolyte d'IGARSS, Giovanni Manfredi pour sa bonne humeur mais aussi son sérieux et sa persévérance quand il s'agissait de travailler ensemble malgré les difficultés du sujet. J'ai aussi une pensée pour les nouveaux venus et les anciens thésards/post-doc : Alice, Samir, Vlad, Marie-José, Thibault et Dihia. Bon courage à vous !

Tels Raoul Duke et Maître Gonzo ou le Duc et Walter, nous parcourûmes une partie de l'Ouest Américain : le Circus Circus à Las Vegas, l'I15 et Baker, le lotissement de Jeffrey Lebowski et le bowling à L.A., la maison de Hunter S. Thompson à San Francisco,... On reviendra pour le Matrix Club une autre fois. Des souvenirs impérissables ont été formé à travers l'Autriche (le Mozart

dépressif de Vienne, la voiture égarée à Innsbruck) mais aussi les Etats-Unis (le loueur de chaines pour pneu à Mariposa, le poulet du Général) et la Russie (les Lénines, Sainte Clara, le Fear and Loathing en partant, et le terminal de Prague). Dominique, j'ai bon espoir à ce qu'on voyage encore pour découvrir d'autres personnes, cultures, cuisines et bibines locales, et que d'autres souvenirs aussi inattendus se forment.
Un grand merci à Romuald Petit, Thomas Faucon, Judith Riou et Mathilde Huguet dont les amitiés sont et furent précieuses durant ces années.
Enfin, je remercie ma famille pour leur soutien tout au long de mes études.

Résumé étendu

Le domaine des contrôles non destructifs traite généralement de la caractérisation et de la surveillance des matériaux composant des structures telles que des bâtiments ou de grands ouvrages de type barrages ou digues. Dans cette optique, plusieurs techniques ont été mises en place afin de s'assurer de la pérennité de ces structures et de leurs fonctions via leurs caractéristiques mécaniques et leur intégrité physique. Dans le domaine électromagnétique, différentes méthodes de mesure ont été établies afin de maintenir cette surveillance : de la détection de changement brut sur les signaux rétrodiffusés à l'estimation des paramètres caractérisant électromagnétiquement un matériau, sa permittivité diélectrique et sa perméabilité magnétique. Dès lors, myriade de méthodes ont été développées afin de déterminer ses quantités. Tout d'abord, on a les méthodes usant d'échantillons du matériel nécessitant donc l'extraction d'un morceau de la structure afin de l'analyser (modèle de ligne de transmission ou cavité). De même que dans les méthodes utilisables uniquement en laboratoire, on trouve des techniques d'espace libre, ou par la mesure de la réflexion et/ou transmission d'ondes via une configuration bistatique d'antennes, l'estimation de permittivité et de perméabilité est possible. Si ces techniques ont certifié leurs fiabilités et leurs précisions, elles se cantonnent à un usage de caractérisation de matériaux en laboratoire et non sur le terrain.
Les mesures au contact ou même en champ proche se rapprochent plus d'un côté applicatif : la mesure de permittivité au contact à l'aide d'un guide d'onde ou d'une sonde coaxiale via la mesure de son coefficient de réflexion préalablement calibrée à l'air ou à l'eau pure. Plus connu, le géoradar utilise, lui, en champ proche la différence de vitesse due à la permittivité matériau au sein de chaque couche composant le sous-sol et les réflexions à chaque interface afin d'imager ces interfaces permettant la détection d'anomalies. Parmi ses applications courantes, on trouve notamment la détection de mines, la détection de structures enterrées dans le domaine de l'archéologie, et le contrôle non-destructif de structures telles que les routes ou les ponts.
En champ lointain, la mesure de permittivité est plus difficile surtout dans le domaine des micro-ondes. Des exemples d'études en optique sont, elles, plus fréquentes. En configuration bistatique, l'estimation peut s'effectuer en spéculaire par inversion directe de la mesure des coefficients de Fresnel, ou par la mesure de certaines de ses caractéristiques liées intrinsèquement au matériau à analyser. Dans le domaine de la polarimétrie radar, plus précisément dans l'imagerie radar en configuration monostatique, quelques études peuvent se trouver sur l'inversion de permittivité d'un sol rugueux. Nonobstant, la configuration monostatique rend l'estimation de caractéristiques d'une telle scène compliquée de par la propagation de la puissance émise dans la direction spéculaire, c'est-à-dire au loin du récepteur. De fait, cette estimation s'effectue donc sur un signal faible soumis au bruit. La structure dièdrique, représentative de scènes type rue-bâtiment ou arbre-sol, elle, est plus à même à renvoyer la puissance émise notamment grâce à l'effet double rebond.
Ainsi notre étude portera dans un premier temps sur l'analyse de ce type de structure dans le cas métallique parfait, puis dans le cas d'un dièdre composé de matériaux diélectriques. Ensuite, nous mettrons en place trois méthodes d'inversion de permittivités pour ce type de structure dont nous ferons une analyse paramétrique. Pour finir, ces méthodes seront soumises à l'expérience en environnement contrôlé puis à des mesures en situation.

De l'estimation de permittivité à distance

De prime abord, en regardant ce qui a été effectué dans le domaine de l'optique, on trouve déjà des solutions d'estimation de permittivité en champ lointain. En configuration bistatique et plus spécifiquement grâce à la diffusion spéculaire, les auteurs de [1] purent déterminer la permittivité complexe d'un matériau via la modélisation par les coefficients de Fresnel du champ rétrodiffusé. En mesurant l'angle de Pseudo-Brewster, et la réflectivité du matériau (module du coefficient de Fresnel mesuré avec le matériau en face), ils parviennent à retrouver l'indice de réfraction du milieu, c'est-à-dire la racine carrée de la permittivité. Dans une configuration identique, l'inversion analytique des coefficients de Fresnel pour la détermination de la permittivité a été effectuée dans [2]. Par la connaissance du coefficient en polarisation horizontale et de l'angle d'incidence, ou des coefficients co-polarisés, l'auteur est capable de remonter jusqu'à la connaissance de la permittivité ϵ. De même dans [3], cette quantité est obtenue par la mesure du ratio entre les coefficients co-polarisés. Ainsi plusieurs autres méthodes dérivent des solutions de ce domaine, on trouve notamment [4, 5] qui estiment la permittivité du sol grâce depuis les images radar et l'hypothèse de sol rugueux.
Dans le cadre de dièdre, on note tout d'abord, la présence de solutions analytiques pour le cas métal parfait dans [6] et dans [7]. Ces deux articles traitent de configurations différentes : l'un [6] travaille en monostatique pour un angle dièdre quelconque alors que le second [7] conserve un angle dièdre droit mais calcule sa solution dans une configuration bistatique. Ces solutions reposent toutes les deux sur l'approximation de l'Optique Physique mêlée à l'Optique Géométrique. Pour ce qui est du cas d'un dièdre diélectrique, on retrouve dans une kyrielle d'articles une modélisation du mécanisme de double rebond par la succession de coefficients de Fresnel, chacun correspondant à la réflexion sur une plaque homogène définie par une permittivité relative. Ce modèle se formalise par l'équation suivante :

$$R_p^{\mathrm{DB}} = R_p(\phi, \epsilon_1) R_p(\frac{\pi}{2} - \phi, \epsilon_2), \tag{1}$$

, où p indique la polarisation à l'emission ainsi qu'à la réception, ϕ l'angle d'incidence défini comme dans la Figure 1, ϵ_1 (resp. ϵ_2) est la permittivité relative de la plaque horizontale (resp. verticale) et R désigne le coefficient de Fresnel (à la polarisation p). Le système de polarisation à l'émission est illustré, ainsi que les dimensions du dièdre en Figure 1. Cette approche de modélisation est commune aux études de décompositions polarimétriques, tout comme aux premières tentatives d'estimation de permittivités via la mesure d'angles de Brewster du double rebond.

Notre approche consiste alors à utiliser l'équation (1) afin d'en extraire les permittivités mises en jeu.

Méthodes d'extraction des permittivités du double rebond

Une première méthode que l'on pourrait qualifier d'idéale résulte de l'inversion directe des permittivités des coefficients R_H^{DB} et R_V^{DB} à un angle d'incidence donné. Mathématiquement, elle se formalise de la façon suivante :

$$\begin{aligned} \epsilon_1 &= \left(\frac{\cos\phi \sin\phi}{X_2^-} \right)^2 + \sin^2\phi \\ \epsilon_2 &= (X_2^+)^2 + \cos\phi^2 \end{aligned} \tag{2}$$

où X_2^- et X_2^+ sont définis par :

$$X_2^{\pm} = \frac{1}{2\sin\phi} \left(Q \pm \sqrt{Q^2 + R} \right) \tag{3}$$

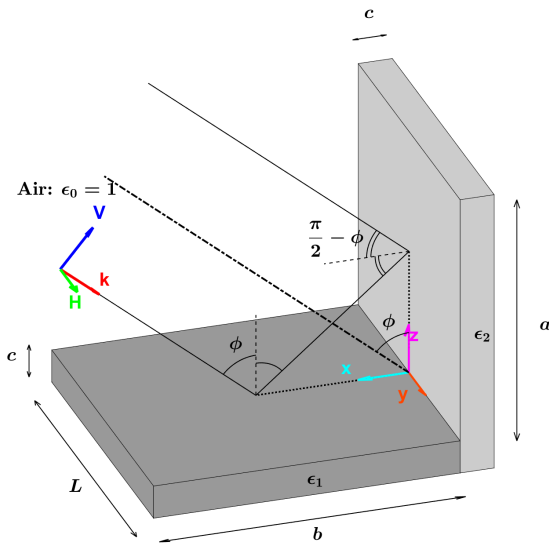

FIGURE 1 – Configuration du dièdre

avec :

$$
\begin{aligned}
Q &= \frac{K\Lambda(\cos^2\phi - \sin^2\phi)}{\Lambda - \Gamma\cos^2\phi} \\
R &= 4\sin^2\phi\cos^2\phi\left(1 + \frac{\cos^2\phi - \sin^2\phi}{\Lambda - \Gamma\cos^2\phi}\Gamma\right)
\end{aligned}
\tag{4}
$$

K, Λ et Γ sont des variables dépendantes de R_H^{DB} et R_V^{DB}, telles que :

$$
\begin{aligned}
K &= \frac{R_H^{\mathrm{DB}} + 1}{R_H^{\mathrm{DB}} - 1} \\
\Lambda &= (R_V^{\mathrm{DB}} - 1) - K(R_V^{\mathrm{DB}} + 1) \\
\Gamma &= (R_V^{\mathrm{DB}} - 1)\left(1 - K^2\right).
\end{aligned}
\tag{5}
$$

Des simulations utilisant le logiciel commercial FEKO [8] et sa méthode d'Optique Géométrique RL-GO, ont été effectuées sur un dièdre de 18 mètres en longueur, hauteur et largeur et d'un mètre d'épaisseur afin d'en collecter les champs rétrodiffusés dans les deux polarisations dans la bande [0.3, 1] GHz. Afin d'extraire R_H^{DB} et R_V^{DB} des champs, l'hypothèse du mécanisme de double rebond dominant est effectuée afin que l'on puisse approximer par la suite, le champ comme la multiplication des coefficients de double rebonds par celui de la composante double rebond rétrodiffusée par un dièdre métallique parfaitement conducteur (Conducteur Electriquement Parfait, CEP) de même dimension. La composante double rebond du champ rétrodiffusé par un dièdre CEP est calculée à partir des dimensions du dièdre et des articles [6, 7].
Deux autres méthodes ont été mises en place : l'une utilisant la polarisation HH seule, l'autre le ratio entre R_H^{DB} et R_V^{DB}. Les avantages de ces méthodes, l'utilisation d'une seule polarisation, ou la manipulation d'une quantité relative via le ratio entre HH et VV, sont balancés par la nécessité de deux angles d'incidences afin de déterminer les deux permittivités en jeu. Les schémas résumant ses méthodes sont disponibles à la fin des Chapitres 3 et 4 dans les Figures 3.15 et 4.16. La méthode usant de la mesure à une polarisation nécessite comme la méthode idéale de calibrer la mesure en usant la composante double rebond d'un dièdre CEP de même dimension. Au contraire, par le calcul du ratio entre les champs rétrodiffusés HH et VV et aux vues des approximations effectuées précédemment, cette étape de calibration est évitée dans la méthode d'inversion par ratio des coefficients.

Toutes ces méthodes mises en place, en théorie, sont testées sur des simulations FEKO où l'on s'écarte de la configuration requise afin d'en déterminer les variations sur le résultat de l'inversion. Notamment, l'influence des paramètres suivants est étudié : la dimension électrique du dièdre (dimension d'une plaque par la longueur d'onde), l'angle du dièdre (angle formé par les deux plaques), le comportement à la composition de permittivités d'une des deux plaques. D'autres paramètres plus liés à l'acquisition de la mesure sont aussi creusés : l'erreur sur l'angle d'incidence, l'angle d'azimuth et la déviation de polarisation. Un tableau résumant les études effectuées et qualifiant la sensibilité des méthodes à ces paramètres est donné dans la Table 1.

	Méthode idéale	Polarization unique	Ratio
Polarisations requises	HH et VV	**HH**	HH et VV
Nombre de mesures	**une**	deux	deux
Normalisation avec un dièdre CEP	oui	oui	**non**
Sensibilité à l'angle dièdre	très forte	forte	forte
Composition de permittivité	loi de mélange	dépendente des angles d'incidence	loi de mélange
Sensibilité à l'angle d'incidence	forte	forte	forte
Angle d'azimuth	avec normalisation d'un dièdre CED : oui	avec normalisation d'un dièdre CED **oui**	**ok**
Angle de rotation	partiellement, selon les domaines d'incidence	**ok**	forte

TABLE 1 – Résumé des trois méthodes et de leurs études paramétriques.

Ce tableau présente sur les trois premières lignes le paramétrage de chacune des méthodes développées et leurs caractéristiques. Les dernières lignes présentent qualitativement les diverses sensibilités des méthodes à certains paramètres liés soit à l'objet soit à l'outil de mesure.

Validation expérimentale des méthodes

Des mesures sont effectuées dans l'environnement contrôlé de la chambre anéchoïque du laboratoire Geeps à CentraleSupélec afin de valider ces méthodes. Dans cette optique, un dièdre est construit à l'aide de deux plaques de dimension 0.25 m de côté, l'une en nylon, l'autre en PVC. Le dièdre résultant est de dimension $(a, b, c, L) = (0.22, 0.25, 0.06, 0.25)$ mètres. Un système quasi-monostatique est formé de deux antennes identiques fonctionnant sur la plage fréquentielle [2,19] GHz. Les dièdre et les antennes sont représentés en Figure 2. Néanmoins, vu les dimensions du dièdre et du fait que la distance entre l'objet-cible et l'appareil de mesure est limitée à 4.3 mètres, on travaille dans la bande [5,18] GHz. De plus, ces treize GHz de bande sont utiles afin de pouvoir finement distinguer les différents phénomènes présents après le passage dans le domaine temporel des mesures. Cela est appuyé par le fait que les permittivités du PVC et du nylon sont quasiment réelles. En effet, ces dernières ont été mesurées à l'aide d'une sonde coaxiale fonctionnant entre 0.5 et 6 GHz en trois points de chacune des plaques. Le nylon est mesuré en partie réelle entre 2.5 et 3 (2.7 entre 5 et 6 GHz) et sa partie imaginaire oscille autour de zéro dans l'intervalle $[-0.1, 0.1]$. Ce dernier comportement se retrouve aussi dans le cas du PVC. Cependant la partie réelle du PVC est, elle, estimée au-dessus de 3 en variant légèrement autour de 3.2. On supposera que ces valeurs de permittivités seront toujours valables sur la plage fréquentielle $[6, 18]$ GHz.

FIGURE 2 – Les antennes et le dièdre utilisés

Grâce à la ligne d'acquisition automatique des mesures de la chambre anéchoïque, on est en mesure d'acquérir des données tous les degrés de rotation de l'objet (ici le dièdre). Ainsi on obtient les mesures co-polarisées pour l'intervalle $[0, 90]$ degrés d'incidence. De prime abord, ces mesures présentent des motifs d'interférences dont on se débarrasse en les filtrant après passage dans le domaine temporel. En effet le double rebond étant localisé à la même distance que l'arrête centrale de l'objet [9], le filtrage temporel (et donc en distance) permet d'isoler cette contribution.

Ainsi la méthode usant du ratio polarimétrique a pu être validée. Pour les deux autres méthodes qui requièrent les coefficients complexes R_H^{DB} et R_V^{DB}, il s'agit alors de remonter à ces coefficients et on sépare dès lors le problème en deux : l'amplitude et la phase. Pour l'amplitude, on utilise la calibration de la chambre anéchoïque par un objet canonique dont on connait la réponse théorique parfaite, dans notre cas une sphère métallique (Surface radar équivalente, [10]) de diamètre 0.25 mètre afin de compenser les divers phénomènes pouvant dégrader la mesure. En calculant l'erreur commise entre la mesure et la théorie dans le cas de la sphère, on compense l'erreur qui a aussi été commise dans la mesure du dièdre (sous l'hypothèse d'une mesure qui aurait été fait dans les exactes mêmes conditions). Pour ce qui est de la phase, on doit compenser le mouvement de rotation du plateau sur lequel repose le dièdre même si celui-ci a soigneusement été placé au centre de rotation estimé. Pour résoudre ce problème, on utilise un dièdre métallique avec les mêmes paramétrages fréquentiels et de positionnement. Avec cette mesure, on peut utiliser la phase des champs rétrodiffusés par cet objet pour obtenir la correction en phase à appliquer sur la mesure filtrée du dièdre diélectrique. Grâce à ces opérations sur l'amplitude et la phase de la mesure, on peut approcher les coefficients de double rebonds tels qu'ils sont formulés dans l'équation (1).

En conséquence, on peut appliquer, par exemple, la méthode idéale formulée par l'équation (2). La figure 3 présente les résultats de l'inversion pour cette méthode à 10 GHz en partie réelle et imaginaire sur la plage d'incidence $[10, 80]$ degrés pour les deux permittivités. De ces courbes, on observe que ϵ_1 est calculé à une valeur avoisinante à $2 - i$ sur l'intervalle $[15, 42]$ degrés. Dans le cas de ϵ_2, dans le même domaine angulaire, l'estimation oscille autour d'une valeur de $3 - 0i$ puis $2.5 - 0.8i$ dès qu'on se rapproche de 45 degrés. A 45 degrés, on observe un changement radical des courbes dû à un problème mathématique connu [11] intrinsèque aux coefficients de double rebonds. Dans le second domaine angulaire $[50, 75]$ degrés, ϵ_1 évolue de $2 - 1i$ à $2.5 - 0i$ et ϵ_2 lui se stabilise vers une valeur de $2.5 - 1i$.

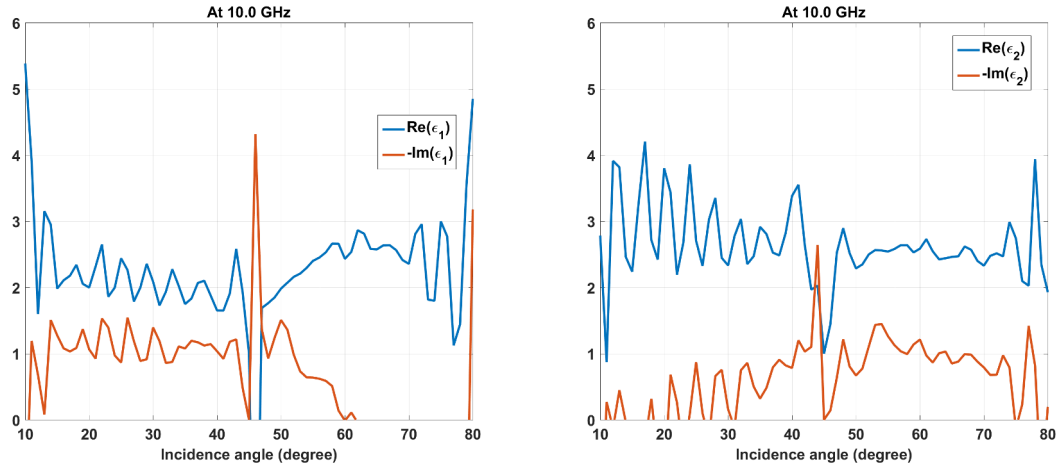

FIGURE 3 – Parties réelles et imaginaires de ϵ_1 et ϵ_2 à 10 GHz.

Conclusion.

Lors de ces travaux de thèse, trois méthodes d'inversion de permittivités diélectriques d'une structure dièdrique ont été établies. Le modèle sur lequel elles reposent est celui du double rebond, qui est la composition successive des coefficients de Fresnel à chacune des interfaces du dièdre. Ce modèle, valide en champ lointain et pour des dimensions électriques de dièdre grandes, porte dans sa formulation l'information diélectrique de la structure illuminée. Cette dernière est représentée par deux plaques, homogènes et isotropes, de permittivités relatives différentes. En utilisant les coefficients de double rebond en HH et VV, une première méthode a été mise place et est l'inversion directe de ces coefficients. Les deux autres méthodes utilisent soit la connaissance seule du coefficient en HH, soit le quotient entre VV et HH, pour déterminer les deux permittivités à l'aide de deux mesures. Les deux premières méthodes nécessitent la normalisation des champs rétrodiffusés par celui d'un dièdre CEP de même dimension que celui mesuré. La méthode usant du ratio polarimétrique est plus souple sur ce point-là étant donné que cette étape n'a pas lieu et que l'on peut se passer de la connaissance des dimensions du dièdre.

Ces méthodes furent validées par des mesures effectuées dans la chambre anéchoïque du Geeps. De la mesure du champ rétrodiffusé d'un dièdre formé d'une plaque de PVC et d'une de nylon, on est parvenu à appliquer la méthode usant du ratio polarimétrique après application d'un filtrage temporel pour sélectionner la contribution du double rebond. Les deux autres méthodes nécessitant les coefficients double rebonds bruts, elles nécessitent la calibration de la chambre anéchoïque par un objet canonique afin d'obtenir l'amplitude de coefficients recherchés. Pour la phase, on mesure un dièdre métallique dans des conditions proches de la mesure du dièdre diélectrique. Après obtention de coefficients double rebond approchés, on a pu appliquer les deux premières méthodes. La méthode idéale présente des résultats proches de ceux attendus (vis-à-vis de la mesure effectuée par une sonde coaxiale), quant à la méthode usant d'une seule polarisation, les résultats sont cohérents sur certaines parties angulaires.
Fort de ces résultats, des mesures ont été effectuées sur un dièdre formé par l'angle d'un mur en béton dans un parking de CentraleSupélec avec le même paramétrage que les mesures en chambre anéchoïque. La méthode du ratio polarimétrique y a été testée avec succès.

Contents

List of Figures

List of Tables

Introduction

Radar remote sensing is a technique used for various applications, ranging for vegetation mapping and/or monitoring to probing the surface of comets. In all these applications, the electromagnetic properties of materials are key parameters. Lots of techniques have been developed to infer typically the permittivity of the materials, whereas other techniques could actually make use of this permittivity, for instance to assess the integrity and resilience of buildings or natural structures to age, environment hazards or mechanical constraints.
Among those techniques we have to distinguish the ones whose utility is entirely dedicated to the estimation of permittivity and the ones that can also be used for integrity assessment. This need for *in-situ* application discards most of the destructive and near-field techniques. This is mainly due to the accessibility of the structure to monitor and the need to maintain its integrity. Ground Penetration Radar is widely used for monitoring accessible roads and lands and their subsurfaces. Nevertheless, it requires to be extremely close to the object under study.
From a far distance, applications relying on permittivity estimation are focused on the determination of the moisture content for agriculture concerns and forest monitoring. However this range of applications can be extended to structures analysis, land or pollution monitoring and remote sensing for spatial missions.

In monostatic radar, a double bounce on a dihedral structure is particularly interesting as it can give a strong backscattered signal. This kind of structure is actually quite common. Of course in urban areas, most buildings present a dihedral configuration, typically between the building and the ground. More generally, manmade structures have vertically oriented walls, so over the ground it gives a double bounce. This is true for bridges, dams etc. For natural scenes, this can also be the case. The trees in a forest, provided they are roughly orthogonal to the ground, can give a double bounce. Mountains can have extremely steepy faces, so they could exhibit a double bounce. Rocks on a ground or a beach are another example of natural double bounces. In this strong signature, useful information about the material might be embedded.

The first chapter deals with the dihedral configuration as it could be found in the literature. The PEC case in bistatic and monostatic configurations are presented along with their solutions provided by the Physical Optics approximation. It also gives the opportunity to introduce the double bounce scattering mechanism. As the goal is to extract permittivity, an insight is given on the permittivity estimation, first in the case of a planar surface in bistatic configuration where the optical domain provides some interesting solutions, and then in the microwave domain where adaptation of these methods is applied for rough surfaces. In the case of a dielectric dihedral, an existing method relying on the estimation of Brewster angles is presented in this chapter along with the double bounce equation.

The next three chapters are quite similar in terms of organisation: during a first movement, a theoretical inversion process is developed in order to invert the two permittivities composing the dihedral using the double bounce equation at one or two polarisations. Then the method is illustrated using numerical data from the Geometrical Optics method of FEKO on a modelled dihedral made of two homogeneous plates with different permittivities. Then follows a parametric study to have an insight on what can be done or expected from each method when the configuration steps

away from the reference case. Two groups of parameters are studied for each method: one bound to the object geometry or characterisation, and the other to the positioning of the measurement system. Three parameters are analysed for each group: the electrical dimension, the dihedral angle and the permittivity composition for the first group, and the incidence angle error, the change in azimuth angle and the roll angle of the device for the second.
The first method presented is the direct mathematical inversion of the double bounce coefficient written for both polarisations. This method provides an explicit expression of the permittivities of the two components of the dihedral structure: the vertical and the horizontal faces. However to do so, an accurate calibration of the complex data is absolutely required, and we have to deal with an indetermination at 45°. The second method is using the horizontal polarization of the double bounce coefficient as it is the most handy to measure in terms of backscattered power given the double bounce effect. However this requirement imposes a constraint which is the need to use two incidence angles to be able to determine permittivities. In addition, we still need to accurately calibrate the data. The last method we developed is using the ratio between the vertical and the horizontal double bounce coefficients in order to get rid off this calibration step. As the previous method, this condition implies to use two incidence angles.

The three methods are then assessed using measured data from the controlled environment of the Geeps anechoic chamber. A dihedral of PVC and nylon was made and its permittivities were measured using a near-field probe. We collected data for the full incidence angle range $[0, 90]$ degrees and for the 5-18 GHz frequency range. After a time gating operation to select the double bounce contribution of these measurements, we applied the three different methods. As the ratio is the more handy to assess, this was the first method we tested. Then a calibration of the anechoic chamber and the data collected was performed to be able to apply the two first methods. Finally an *in-situ* measurement of the permittivity of a concrete wall corner from a parking lot at CentraleSupélec was performed. After time gating the signal to isolate the double bounce component, the ratio method was successfully used to invert the permittivity involved.

Chapter 1

Context and state of the art

In this chapter the reasons and aim of the study are presented: as the vertical structure strongly signs in monostatic configuration, one may be able to invert the field or SAR measurement to obtain information about the considered structure. In our case, we will focus on the permittivities retrieval from the double bounce scattering of a dihedral structure. First solutions from the literature for PEC (Perfect Electric Conductor) dihedral are exposed. Then an insight on the existing solutions in the optical domain follows and the double bounce model for the dielectric case used all along the manuscript is exposed.

1.1 Interests of the dihedral structure and PEC solutions

In monostatic configuration, a dihedral arrangement in front of the measuring device got a strong backscattering. This can easily be seen for instance in SAR images. In Fig. 1.2 taken from [12], a Pauli decomposition [1] [13] is computed from a PolSAR image of Bretigny airbase such that red colour corresponds to the double bounce scattering, blue with the single scattering and green the asymmetric scattering. An optical image from Google is displayed in Fig. 1.1. From Fig. 1.2, we clearly see that most of the buildings are strongly signing as a double bounce. Lands, the forest canopy and rotated building are signing with cross polarization signatures.

The strong backscattered fields from the double bounce mechanism can be detected in forest areas with tree-ground structures, in cities with building-streets configurations. Within these types of structures, variations could be found in terms of shape, materials, inclination. In urban areas many materials could be found usually: concrete, glass and for buildings before the fifties, masonry and wood (as illustrated in Fig. 1.5). Due to shape and orientation, some buildings are not looking like a parallellipede on a ground soil and others are not built with a sharp 90 $^\circ$ between the building front and the ground as depicted in Fig. 1.3. In the case of forest areas (Fig. 1.4), with shape of tree-ground, we coud infer through the estimation of the permittivity of the soil to retrieve its water content.

As a result, inverting the permittivity in a monostatic configuration takes sense by considering buildings or structures that can be modelled by a dihedral as they naturally reflect more power and therefore are more easily exploitable.

When looking at the literature, approximated solutions of the scattered fields using Physical Optics and Geometrical Optics are given for PEC (Perfect Electric Conductor) dihedral in [6,7]. [6] considers the case of a dihedral with any angle between the plates whereas [7] considers a right angle

1. It decomposes Sinclair matrice over the Pauli basis. In the monostatic case, the basis is reduced to three components. This decomposition can be interpreted through the backscattering of canonical elements: the sphere (or plate), the dihedral and a 45 degree oriented dihedral. These elements respectively represent the scattering mechanism of single bounce, double bounce and volume.

Figure 1.1 – Image of Bretigny airbase from Google in 2018.

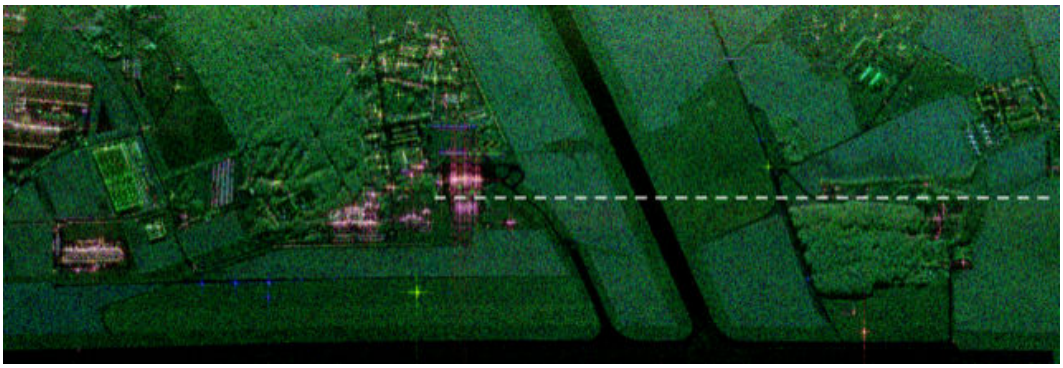

Figure 1.2 – From [12]: the Pauli decomposition of the Bretigny airbase area from the SAR image taken by the ONERA in X band.

Figure 1.3 – An example of building in Amsterdam.

dihedral but calculates the fields in bistatic configuration. As they are the main articles used in our work, the appendix A presents the main results of these papers in their own notations (shortly reminded at the beginning). In both papers P.O. serves the calculations of the single reflection and the combination P.O. with G.O. the double bounce reflection.

Figure 1.4 – Forest nearby Dzerjinsk.

Credit: Wikimedia Common,
<https://commons.wikimedia.org>

Figure 1.5 – Front buildings in Amsterdam.

Credit: Wikimedia Common,
<https://commons.wikimedia.org>

An example of the Physical Optics solution provided in [7] and abbreviated A.P.O. for Analytical Physical Optics (in the article and when used in this manuscript) is given in amplitude and phase in Fig. 1.6 for a PEC (Perfect Electric Conductor) dihedral of dimension $(a, b, L) = (0.25, 0.25, 0.5)$ m. a, b, L are the dimensions of the dihedral as displayed in [7] or in Fig. 1.10. The example is computed at 10 GHz (as in the article) in the monostatic configuration as in Fig. (1.10). The electric field amplitude shows the backscattering of each plate with their main lobes at 0 and 90 degrees and their decreasing side lobes from 3 to 20 degrees and from 87 to 70 degrees. Between 20 and 70 degrees the double bounce is the main contribution. In phase, as the double bounce is a succession of bounce on each PEC plate, we get a total phase difference of 180 degrees between HH and VV quite steady between 20 and 70 degrees.
In Fig. 1.7, we displayed the magnitude of the copolarised backscattered fields in the general monostatic configuration of the same dihedral at the same frequency (10 GHz). The solution have been calculated for an incidence angle in the 0- 90 degrees interval and a azimuth angle going from 0 to 180 degrees (for the angles definition see [7] or the appendix A). We observe that when the emitter and receiver are not perfectly in front of the dihedral (*i.e.*, at azimuth 90 degrees) as the case we illustrated just before, the fields magnitude in both polarization are quickly decreasing. This phenomenon can be seen for any incidence angle. For instance at $\phi = 45$ degrees, we lost for

both polarisation at least 25 dB when we move the measurement device from 90 degrees azimuth to 80 or 100 degrees in azimuth. Hence, one might conclude that the majority of the backscattered power from the double bounce contribution in the SAR image after an azimuth compression is coming from the contribution near the azimuth angle of 90 degrees. It also gives us an insight on the boundaries of the study as we might have not enough backscattered power to be measured outside the region near the azimuth angle of 90 degrees.

In [14] the authors use in addition of P.O. and G.O. methods, the physical theory of diffraction to take into account edge diffraction. In [15] a P.O. solution is put in place for a dihedral made with a loaded impedance.

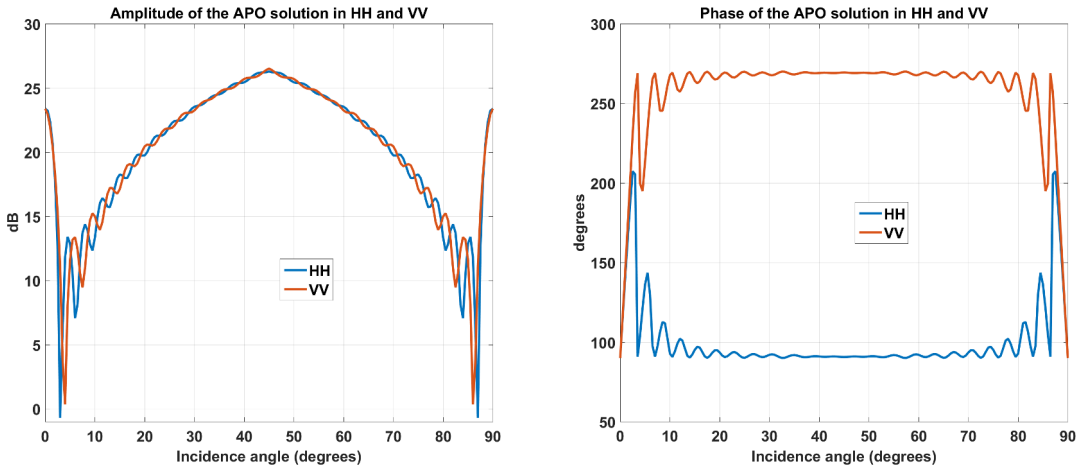

Figure 1.6 – Illustration in amplitude and phase of the APO (analytical physical optics) solution in HH and VV polarization from [7] for a dihedral of 0.25m ×0.25 m ×0.5m dimension (as in [7]) in monostatic configuration.

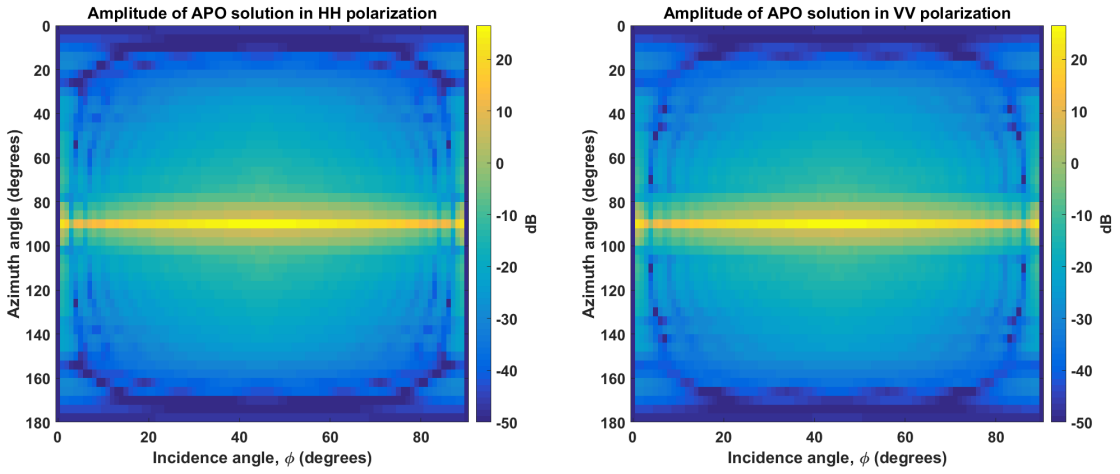

Figure 1.7 – Illustration in amplitude of the APO (analytical physical optics) solution in HH and VV polarization from [7] for a dihedral of 0.25m ×0.25 m ×0.5m dimension (as in [7]) in a general monostatic configuration.

In the same kind of approach, [16] combines of G.O. and P.O. to provide solutions for single, double and triple reflections of parallelepiped lying on the ground. So here, the scene is more

complex as it deals with dielectrics from a rectangular building and a rough surface for a general monostatic configuration (unlike in [6, 14]).

As it deals with dielectric relative permittivities, we first have a look on what has been done in the optical field where the estimation of permittivity of a plate in bistatic configuration has already been developed and validated.

1.2 Permittivity measurement

Permittivity and permeability are two parameters that are classically used to characterise a material from an electric or a magnetic field. Hence numerous ways to measure them have been developed [17]. Concerning the permittivity retrieval, the first methods rely on the transmission line model where a sample is extracted from the material and submitted to an electric field. Among techniques that can only be used in a laboratory, we also have the free space techniques: two separated antennas pointing toward each other with the material sample in between. Then by measuring the reflection or the transmission parameter, one could infer the permittivity. However even if these methods have shown their accuracy and their reliability [18, 19], they are not designed for *in-situ* measurements.

Literature provides some methods to characterise the material at contact or at near-field distance. From the transmission line model, the determination of the permittivity could be done using the open-ended waveguide or coaxial line. By measuring the reflection coefficient of such device for air and the material, one could determine the permittivity of the material. At near-field distance, a common technique for non-destructive testing is the Ground Penetration Radar [20], which takes advantages of the penetration capability of low frequencies and the reflection of the different layers or permittivities of the ground, to image the underground. With the help of such technique, one can detect the different layers composing a surface or the anomalies within the subsurface. Many applications are using this method: landmine detection [21], archaeological studies, or non-destructive testing (bridge and road monitoring [22, 23]). This technique relies on the permittivity contrast between layers.

Now from a far distance, works in the specular direction were carried out in [1, 24, 25] where the authors bind the permittivity of a plate to different quantities from the Fresnel coefficients. For recall, the Fresnel coefficients are the coefficients binding the incident to the scattered plane wave in the specular direction after reflection on an infinite interface between the media and air (displayed in Fig. 1.8). They are expressed differently with the polarization H or V as function of the incidence angle ϕ and the relative (to air) permittivity ϵ. Under the $e^{i\omega t}$ convention (as the rest of the manuscript), physical relative permittivity has its real part greater than 1 and its imaginary part is negative or null. The expressions of the Fresnel coefficients are given in Eqs. (1.1).

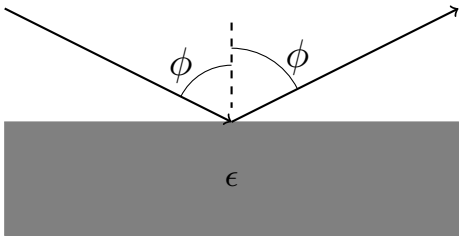

Figure 1.8 – Specular configuration.

$$
\begin{aligned}
R_V(\phi,\epsilon) &= \frac{\epsilon\cos\phi - \sqrt{\epsilon - \sin\phi^2}}{\epsilon\cos\phi + \sqrt{\epsilon - \sin\phi^2}} \\
R_H(\phi,\epsilon) &= \frac{\cos\phi - \sqrt{\epsilon - \sin\phi^2}}{\cos\phi + \sqrt{\epsilon - \sin\phi^2}}
\end{aligned}
\tag{1.1}
$$

A more general expression could be found in [26] that is not considering equal magnetic permeabilities between the two media and the first media as air. An example of the Fresnel coefficients computed with Eqs. (1.1) is given in Fig.1.9 for a permittivity set to $10-3i$. The plot of amplitudes shows a drop in VV polarisation at 72 degrees. The incidence angle ϕ_{PB} where this minimum occurs is called the Pseudo-Brewster angle ([1]) for a complex permittivity. For a real permittivity, VV magnitude is equal to zero at the Brewster angle ϕ_B. It means by conservation that nothing is reflected, the incident wave is fully transmitted in the media at this angle. We can also notice that for 0 and 90 degrees of incidence, amplitude of coefficients are equal. In term of phase, we observe that the sign of the VV coefficient is changing at the Pseudo-Brewster angle, which is not the case for HH which slowly evolves in the incidence angle range.

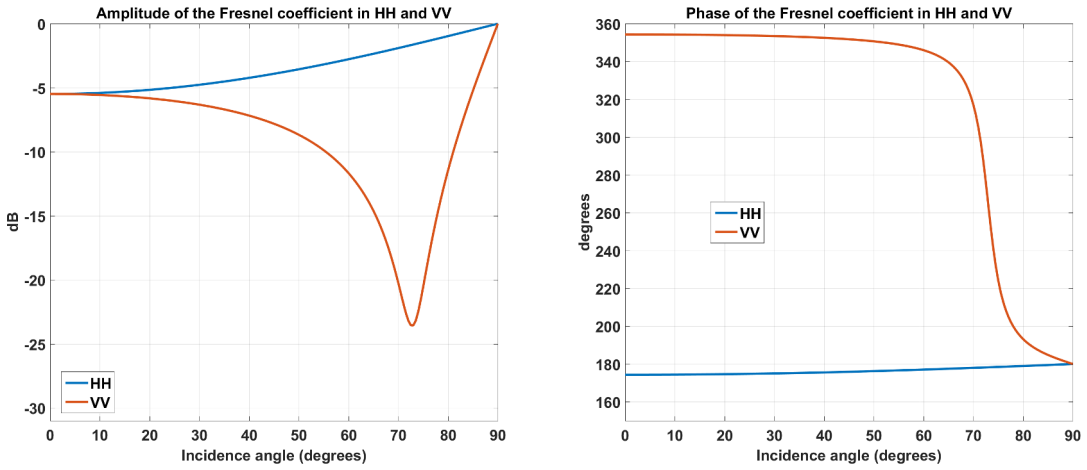

Figure 1.9 – Amplitude and phase of the Fresnel coefficients in horizontal and vertical polarization for $\epsilon = 10 - 3i$.

Those angles, the Brewster and the Pseudo-Brewster angles, are intrinsically bound to the relative permittivity of the media. For the Brewster angle, solving $\forall\epsilon, R_V(\phi,\epsilon) = 0$ leads to:

$$\phi_B = \arctan(\sqrt{\epsilon}). \tag{1.2}$$

For the Pseudo-Brewster angle, we can approximate (from Eqs. (14, 17, 18) in [1]) :

$$\phi_{PB} \approx \arctan(\sqrt{|\epsilon|}). \tag{1.3}$$

In [1], through the measurements of ϕ_{PB} and the magnitude of the reflectance (squared absolute value of a Fresnel coefficient at 0 degree), the authors are able to determine graphically the complex refractive index (square root of the permittivity).
In [2], the concept is further pushed as the author is able to fully retrieve the permittivity from the knowledge of either both Fresnel coefficients taken at the same incidence, or the HH Fresnel coefficient and the incidence angle. Both ways are explicitly written in the Eqs. (1.4).

$$\begin{aligned}\epsilon &= \frac{(1+R_V(\phi))(1-R_H(\phi))}{(1-R_V(\phi))(1+R_H(\phi))} \\ \epsilon &= \frac{1+R_H^2(\phi)-2\cos(2\phi)R_H(\phi)}{1+R_H(\phi)}\end{aligned} \tag{1.4}$$

One last interesting approach from the optic domain is from [3] where a solution (Eq. (1.5)) to retrieve the permittivity in specular configuration is provided using the ratio between polarization of the Fresnel coefficients: $\rho(\phi) = \frac{R_V(\phi)}{R_H(\phi)}$.

$$\epsilon = (1 + \frac{(1-\rho(\phi))^2}{(1+\rho(\phi))^2}\tan^2(\phi))\sin^2(\phi) \tag{1.5}$$

In same scope we can also find ellipsometry approaches as in [27–29] using the measurement of the received power to infer the permittivity of the plate.

In monostatic configuration, most of the studies are focused to the retrieval of ground permittivity [4, 30]. In fact, the use of the permittivity is more used in the spatial exploration domain to retrieve the materials (water in general) at the surface or embedded in planet or celestial bodies [31–33] through the modelling the backscattered signature. Retrieval of the permittivity of the ground can be done through the use of either the copolarised ratio or from the far-field signature of an object. In the first category, we find the articles [4] and [5] that are using the co-polorised ratio from the backscattering fields to retrieve the permittivity of a rough surface.
In [34] and in [35], the permittivity of a plate is retrieve by the reflection measurement in far-field at normal incidence.
One main drawback, as stated at the beginning, of these studies in monostatic configuration is the fact that by considering a plate, the backscattered fields are weak outside the measurement at normal incidence as the power is mainly diffused in the specular direction. The previous authors bypassed this issue by considering either a rough surface or by placing their study at normal incidence.

1.3 Double bounce scattering

As exposed previously, in airborne radar monostatic case, double bounce from buildings are backscattering more than bare surfaces or vegetated areas. Hence, to retrieve permittivity we might want to use this component as they contain a significant and meaningful characterization of the structure. The first approach to model the building and the double bounce is to design a right angle dihedral.

In [16] a dielectric scene is handled and one could notice in the formulation of the double scattering contributions the presence of products of Fresnel coefficients in all the scattering components, one bound to the wall and another bound to the ground. A version of this product can be found in several other papers as a double bounce equation used to model the wave interaction with two orthogonal surfaces made of different homogeneous materials for a monostatic radar in front of it. It is given by the following equation written in Forward Scattering Convention (see [36] for the FSA definition):

$$R_p^{\mathrm{DB}} = R_p(\phi, \epsilon_1)R_p(\frac{\pi}{2} - \phi, \epsilon_2), \tag{1.6}$$

where $R_p(\phi, \epsilon)$ denotes the Fresnel coefficient at $p = \{V, H\}$ polarisation as defined in Eqs. (1.1), ϕ is the incidence angle. ϵ_1 and ϵ_2 are respectively the relative permittivities of the horizontal and vertical surfaces. The last three variables are illustrated in Fig. (1.6) with a dihedral and the incident reference frame (defining the H and V polarization relatively to the global frame). The double bounce equation can be seen as a cascade of reflections from each surface added coherently

from direct and inverse paths.

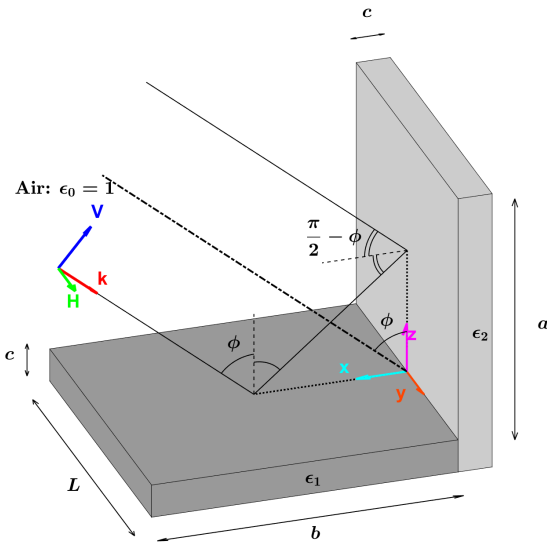

Figure 1.10 – Dielectric dihedral, its dimensions, a double bounce and its central ray.

In [37] this equation is used to model the double bounce between trees and the ground in the polarimetric decomposition of PolSAR images. As [38] proposes a decomposition derived from [37] we implicitly retrieve it, but also in [39] in α quantity as ratio between polarization.

We illustrate this equation in HH and VV polarizations in Fig. 1.11 for an incidence angle range from 0 to 90 degrees and $\epsilon_1 = 10 - 3i$ and $\epsilon_2 = 2.4 - 4.5i$ (permittivities of bitumen and concrete at 600 MHz [40]). From the amplitude plot, we observe two drops in VV polarizations indicating the two Pseudo-Brewster angles at 25 and 72 degrees from respectively ϵ_2 and ϵ_1. As underlined in [40, 41], the combination of these two drops spreads over a large incidence angle domain making VV component inferior to HH of at least 10 dB in the $[20, 70]$ degree range. In addition of this double bounce effect, we can use the phase shift between VV and HH to detect the double bounce. For PEC (Perfect Electric Conductor) we had a 180 degrees phase shift between the two polarizations where the double bounce was the dominant contribution. In the dielectric case, the phase shift still exists but it is not any more a constant 180 degrees. It depends on the two complex permittivities. The only exception of this statement is for real permittivities where the phase shift is 0 degrees inside the domain defined by the two Brewster angles and 180 degrees outside. Each vertical coefficient has a change of sign at its Brewster angle and as one coefficient evolves in $\frac{\pi}{2} - \phi$, we get 0 degrees shift between the two Brewster angles.

The question raising is linked to the possibility to retrieve both permittivity from the double bounce component. As the double bounce contribution is quite strong in the $[20, 70]$ incidence angle, we could retrieve permittivities from Eq.(1.6) in this range. A first attempt in this goal was performed in [42, 43] where the authors use Eq.(1.6) to identify the Brewster angles relative to ground and trunk and therefore determine the assumed real permittivities. This approach reaches its limits as soon as we consider complex permittivities. As underlined in the section before in Eq .(1.3) through [1], with Pseudo Brewster angles, only the modulus of the permittivity can be approximately retrieved. If we take for instance Fig. 1.11 where the Pseudo-Brewster angles are 25 and 72 degrees, we could estimate a modulus of 4.6 and 9.5 for respectively $|\epsilon_2| = 5.1$ and $|\epsilon_1| = 10.4$. By doing so, we still miss a part of information on the permittivity involved. More-

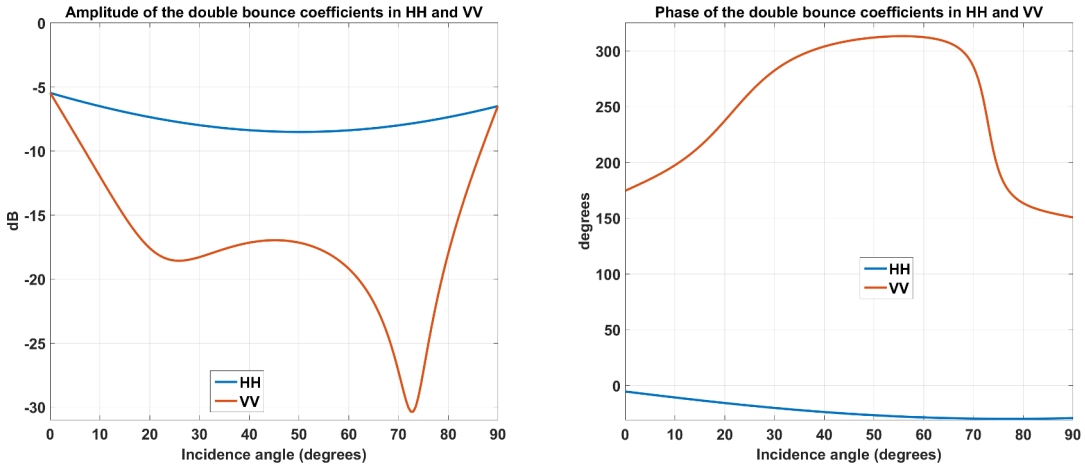

Figure 1.11 – Amplitude and phase of the theoretical double bounce coefficients in HH and VV polarization for $\epsilon_1 = 10 - 3i$ and $\epsilon_2 = 2.4 - 4.5i$.

over, it requires to estimate properly the Pseudo-Brewster angles, therefore needing several angular measurements.

We could wonder given the last two sections if by using the different strategies developed for instance in [2] or in [3,4] we can retrieve the permittivities from the vertical and horizontal surfaces through Eq. (1.6). Establishing such methods is the goal of the next three chapters. For the rest of the manuscript, FSA convention is always used (exception made of A.2.1) as the $e^{i\omega t}$ convention (implying to have a negative or null imaginary part of the permittivity for the physical condition).

Chapter 2

Ideal method

In the previous chapter, we simplify the urban structure by a dihedral arrangement. In monostatic configuration, it is from this structure that we obtain the more power back. It is possible to model the signature of such building using the double bounce reflection of the signal for either a PEC material or a dielectric one.
In this chapter, we will use the double bounce reflection coefficients to retrieve the two permittivities of the dihedral arrangement. The first part will focus on the analytical process to obtain solutions and it will be then illustrated using a simulation made using the commercial electromagnetic code FEKO [8]. We explore what can or can not be done with this method regarding the parameters of the object and of the measuring device. Finally an example of application is provided: the moisture retrieval of a soil from a ground-building structure at 500 MHz.
Compared to the two other methods, this method is qualified as "ideal" as the solutions are provided as an explicit expression of the inputs.

2.1 Theory

In this section, we present the analytical development of the method. It first focuses on how we invert the permittivities from the double bounce equation and how we identify the solutions.

2.1.1 Finding the solutions

Given Eq. (1.6) exposed in 1.3, we will directly invert the two permittivities from the HH and VV components of this equation. To do so, we define the following variables:

$$\begin{aligned} X_1 &= \sqrt{\epsilon_1 - \sin^2\phi} \\ X_2 &= \sqrt{\epsilon_2 - \cos^2\phi} \end{aligned} \tag{2.1}$$

and also the intermediate quantities:

$$\begin{aligned} K &= \frac{R_H^{\mathrm{DB}} + 1}{R_H^{\mathrm{DB}} - 1} \\ \Lambda &= (R_V^{\mathrm{DB}} - 1) - K(R_V^{\mathrm{DB}} + 1) \\ \Gamma &= (R_V^{\mathrm{DB}} - 1)\big(1 - K^2\big). \end{aligned} \tag{2.2}$$

Then the HH component of the double bounce equation can be written as :

$$R_H^{\mathrm{DB}} = \frac{\cos\phi - X_1}{\cos\phi + X_1}\frac{\sin\phi - X_2}{\sin\phi + X_2}. \tag{2.3}$$

or also after introducing K:

$$X_1 = \frac{\cos\phi\sin\phi + KX_2\cos\phi}{-(K\sin\phi + X_2)}. \tag{2.4}$$

By doing the similar operation on VV component, we obtain:

$$R_V^{\mathrm{DB}} = \frac{\Big((X_1^2+\sin^2\phi)\cos\phi - X_1\Big)}{\Big((X_1^2+\sin^2\phi)\cos\phi + X_1\Big)}\frac{\Big((X_2^2+\cos^2\phi)\sin\phi - X_2\Big)}{\Big((X_2^2+\cos^2\phi)\sin\phi + X_2\Big)}. \tag{2.5}$$

By substituting inside the last equation X_1 from Eq. (2.4) we get the following four degree equation in X_2:

$$AX_2^4 + BX_2^3 + CX_2^2 + DX_2 + E = 0 \tag{2.6}$$

where

$$\begin{aligned}
A &= (\Lambda-\Gamma)\sin\phi\cos\phi + \Gamma\sin^3\phi\cos\phi\\
B &= K\Lambda\cos\phi(\sin^2\phi - \cos^2\phi)\\
C &= \big(2\Gamma(1-\sin^2\phi)\sin^2\phi - \Lambda\big)\cos\phi\sin\phi\\
D &= K\Lambda\cos\phi\sin^2\phi(\cos^2\phi - \sin^2\phi)\\
E &= \Lambda\cos^3\phi\sin^3\phi - \Gamma\sin^5\phi\cos^3\phi
\end{aligned}$$

This four degree equation can be factored by $(X_2^2 - \sin^2\phi)$ such that we obtain:

$$AX_2^2 + BX_2 + C' = 0 \tag{2.7}$$

with $C' = -\Lambda\cos\phi\sin\phi + (\Gamma+\Lambda)\cos\phi\sin^3\phi - \Gamma\cos\phi\sin^5\phi$.

The solutions X_2^+ and X_2^- of this equation are given by:

$$X_2^{\pm} = \frac{1}{2\sin\phi}\left(Q \pm \sqrt{Q^2+R}\right) \tag{2.8}$$

with:

$$\begin{aligned}
Q &= \frac{K\Lambda(\cos^2\phi - \sin^2\phi)}{\Lambda - \Gamma\cos^2\phi}\\
R &= 4\sin^2\phi\cos^2\phi\left(1 + \frac{\cos^2\phi - \sin^2\phi}{\Lambda - \Gamma\cos^2\phi}\Gamma\right)
\end{aligned} \tag{2.9}$$

2.1.2 Identification of the solutions

The full proof of the identification of the solutions can be found in the appendix B.1. Here only the methodology and the results are exposed.

In short, by replacing the intermediate quantities K, Λ and Γ by their expressions using R_H^{DB} and R_V^{DB}, we can express them as functions of X_1 and X_2 using Eq. (2.3) and Eq. (2.5). Then by replacing these quantities in Eq. (2.8) we obtain: $X_2^+ = X_2$ and $X_2^- = \dfrac{\cos\phi\sin\phi}{X_1}$. It means that from $(R_H^{\mathrm{DB}}, R_V^{\mathrm{DB}})$ measured we can calculate $X_2^{\pm}$ (Eq. (2.8)) and then determine ϵ_1 and ϵ_2 as: $\tilde{\epsilon}_2 = (X_2^+)^2 + \cos\phi^2$ and $\tilde{\epsilon}_1 = \left(\dfrac{\cos\phi\sin\phi}{X_2^-}\right)^2 + \sin^2\phi$.

2.1.3 The 45 degree issue

In [2] it has been proven that $R_H^2(\phi,\epsilon) = R_V(\phi,\epsilon)$ at $\phi = 45$ degrees. If we take into account the expression of Eq. (1.6) we immediately get $\left(R_H^{\mathrm{DB}}\right)^2 = R_V^{\mathrm{DB}}$. This equality leads to an issue as the related quantity $\Lambda - \Gamma\cos\phi^2$ tends to zero. Thus at $\phi = 45$ degrees, $\frac{\cos^2\phi - \sin^2\phi}{\Lambda - \Gamma\cos\phi^2}$ became undetermined. Therefore as this expression can be found in Q and R in Eq. (2.9), no solutions exists. The full development of this matter is exposed in the appendix section B.2.

In this part, we have built an analytical solution to retrieve the two permittivities of a dihedral arrangement with the help of the double bounce model. It uses the co-polarized Fresnel coefficients at one incidence angle to find them back. The next part illustrates this solution by inverting permittivities from simulated data.

2.2 Retrieving approximated R_H^{DB} and R_V^{DB}

In this part we use the Geometrical Optics (GO) method implemented in FEKO [8] to validate our theoretical method. In order to have reflections that can be modelled by Fresnel coefficients, each plate composing the dihedral needs to be sufficiently large regarding to the wavelength. By using RL-GO (Ray Launching Geometric Optics) method from FEKO, we are able to simulate the backscattered electric field of structure for different electrical dimension (dimension over the wavelength). In this section, we focus on retrieving the approximated R_H^{DB} and R_V^{DB} needed for the method.

2.2.1 Simulation set-up

We model a dihedral structure in FEKO made of identical square plates of $D = 18$ m side length ($a = b = L = D = 18$ m). The electrical dimension is here calculated by the side of each plates: $\frac{D}{\lambda}$. We set fifteen linearly spaced frequency points starting from 0.083 GHz to 1.016 GHz that corresponds to an electrical dimension ranging from 5 to 61 by a step of 4.
Backscattered fields are calculated for several incidence angles between $[0, 90]$ degrees with a one degree step. Permittivities are assumed to be frequency independent and they are set to $10 - 3i$ for ϵ_1 and $2.4 - 4.5i$ for ϵ_2. It respectively corresponds to a type of bitumen and a type of concrete materials at 0.6 GHz [12]. In Fig. 2.1 we illustrate using formulas from [44] the depth skin over the $[0.1, 1]$ GHz bandwidth. Hence the dihedral depth c is set to 3 m such that we can simulate it down to 0.15 GHz ($\frac{D}{\lambda} = 9$) or even down to 0.083 GHz maximum ($\frac{D}{\lambda} = 5$) but the latter case is more questionable regarding to the skin depth of ϵ_2.

2.2.2 Normalization step

By simulating this structure illuminated by a plane wave, we get the backscattered co-polarised fields HH and VV and not the required $(R_H^{\mathrm{DB}}, R_V^{\mathrm{DB}})$. To obtain them, we first assume the double bounce scattering component is preponderant (formulated in Eq. (2.10)). Then we normalize the simulated signal by the double bounce component of the signal received at the same incidence angle by an identical PEC dihedral structure as it is suggested in [44] for a dielectric plate case. By doing so, we remove the scattering part dependant on the object geometry. The latter assumption is expressed in Eq. (2.11).

$$\begin{aligned} E_{HH}(\phi) &\simeq E_{HH}^{\mathrm{DB}}(\phi) \\ E_{VV}(\phi) &\simeq E_{VV}^{\mathrm{DB}}(\phi). \end{aligned} \tag{2.10}$$

$$\begin{aligned} E_{HH}^{\mathrm{DB}}(\phi) &\simeq R_H^{\mathrm{DB}}(\phi) E_{HH,PEC}^{\mathrm{DB}}(\phi) \\ E_{VV}^{\mathrm{DB}}(\phi) &\simeq R_V^{\mathrm{DB}}(\phi) E_{VV,PEC}^{\mathrm{DB}}(\phi). \end{aligned} \tag{2.11}$$

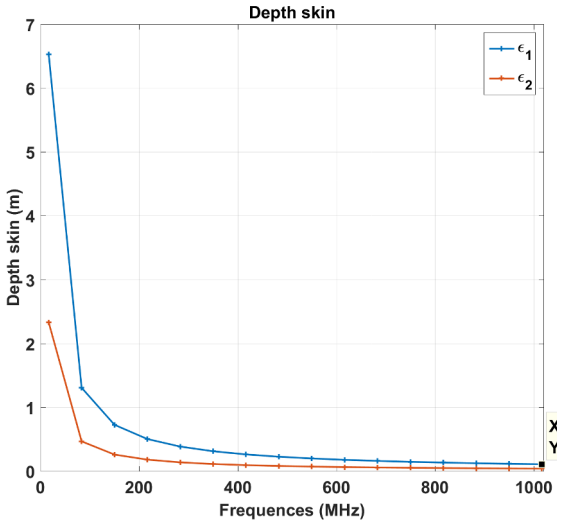

Figure 2.1 – Depth skin over the 0.1 - 1 GHz bandwidth for the two permittivities ϵ_1 and ϵ_2.

The double bounce component of a PEC dihedral can be extracted from the formulation in [6] or in [7]. In the terms of [7], it is expressed as:

$$\pm \frac{jk}{\sqrt{\pi}}(I_{xz}\sin\phi + I_{yz}\cos\phi)E^i = \left\{ \begin{array}{ll} \pm\frac{jk}{\sqrt{\pi}}(2La\sin\phi), & \text{for } \cot\phi \geq \frac{a}{b} \\ \pm\frac{jk}{\sqrt{\pi}}(2Lb\cos\phi), & \text{otherwise} \end{array} \right\} \tag{2.12}$$

where $\pm$ depends on the polarisation; E^i is the incident electric field, and I_{xz} and I_{yz} are the limiting integrals defined in equations (48) and (49) in [7] (the complete expressions of the fields can also be found in the Appendix A).

2.2.3 Application on the simulated data

By using Eq. (2.10) and Eq. (2.11), we can approximate the R_H^{DB} and R_V^{DB} coefficients for all the different electrical dimensions. In Fig. 2.2 (resp. Fig. 2.3), we compare in amplitude and in phase the theoretical R_H^{DB} (resp. R_V^{DB}) from Eq. (1.6) with the approximated coefficients. As we can see for HH polarisation, this approximation is correct for angles between $[30, 60]$ degrees and for $\frac{D}{\lambda} \geq 9$ and gets wider in domain angle with an electrical dimension increasing. From $\frac{D}{\lambda} = 20$ we get a relatively good incidence angle range, $[10, 80]$ degrees, on which the approximation is reasonable. For VV polarisation, the discussion is more difficult but the trend is similar: we have an increasing angle range from an electrical dimension from 9 to 30.

In Fig. 2.4, we plot the approximate R_H^{DB} and R_V^{DB} in amplitude and phase from a simulated data [1] at 0.3 GHz (corresponding to $\frac{D}{\lambda} = 18$) and 1 GHz (corresponding to $\frac{D}{\lambda} = 60$) and compared them with the theoretical ones computed from Eq. (1.6). As we can see, approximations and the model are in good agreement especially at 1 GHz for both polarisation in the range $[10, 80]$ degrees as the curves are very close in amplitude or in phase (less one dB off in amplitude). At 0.3 GHz, curves are less compliant outside the $[30, 65]$ degrees interval of incidence, especially at VV polarization.

1. This simulated data differs from the previous one in the c dimension that is now set to one meter as we only consider two frequencies, 0.3 GHz and 1 GHz.

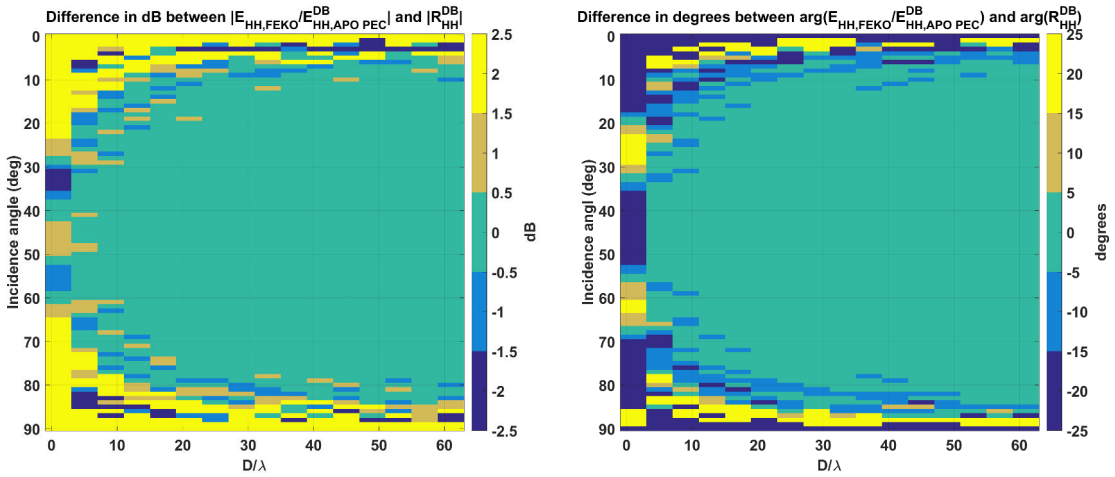

Figure 2.2 – Difference between the approximation used to get R_H^{DB} and the theoretical R_H^{DB} in amplitude (left, in dB) and phase (right, in degrees).

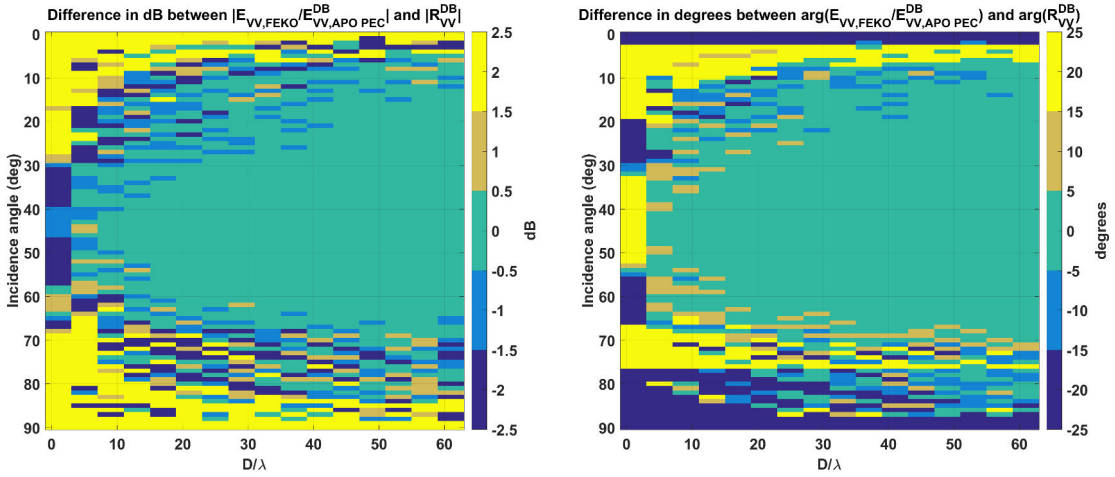

Figure 2.3 – Difference between the approximation used to get R_V^{DB} and the theoretical R_V^{DB} in amplitude (left, in dB) and phase (right, in degrees).

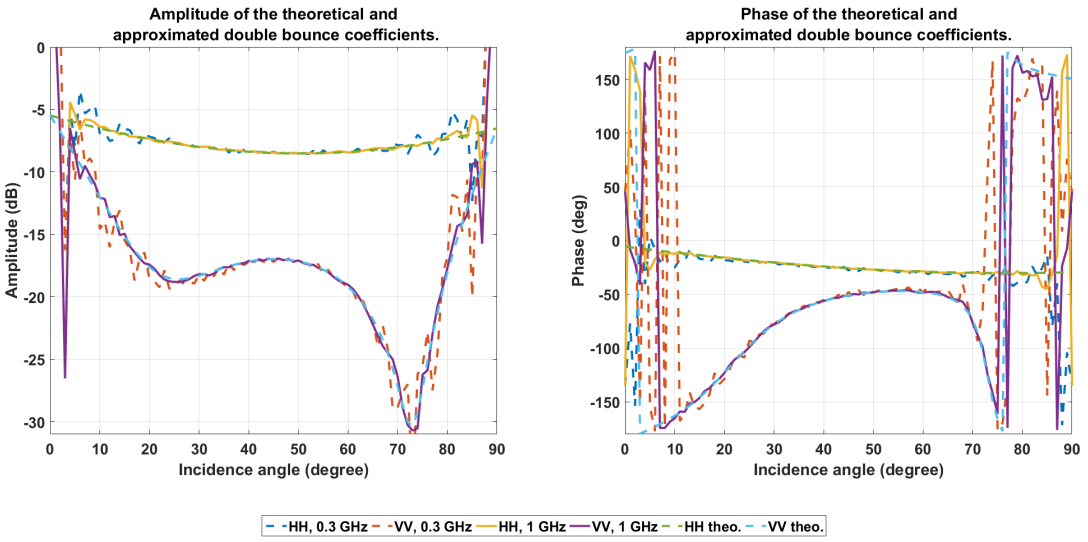

Figure 2.4 – Approximated (dashed lines) and theoretical (continuous lines) double bounce coefficients in amplitude and phase at 0.3 GHz and 1 GHz.

2.3 Domain of validity: limits and range of possibilities

In this section, limits and possibilities of the method are explored using FEKO simulations. A first part is dedicated to the sensitivity of the method to some parameters of the object: dimension, dihedral angle and permittivity. Then the influence of the measuring device such as its pose (*i.e.* position and orientation) is studied.

2.3.1 Object parameters

As we look at the object parameters that might impact the method, we think first at the geometry of the object. So the two first points will be to look at the dimensions of the object and the dihedral angle. The last point deals with the permittivity of the dihedral.

Electrical dimension

As the electrical dimension dictates the presence of the double component (as seen in section 2.2), we have a look at the inversion results along this parameter by taking back the simulation exposed in subsection 2.2.1 and used in subsection 2.2.3. Those observed trends in Fig. 2.2 and Fig. 2.3 are logically present in the inversion results. In Fig. 2.5 (resp. Fig. 2.6) we illustrate the inversion of ϵ_1 (resp. ϵ_2) with the electrical dimension. For both permittivities, for an electrical dimension between 9 and 21 we have an inversion that successfully operates locally within the $[10, 40] \cup [50, 80]$ degrees range. After $\frac{D}{\lambda} = 21$, the range of correct results increases and gets more and more homogeneous.

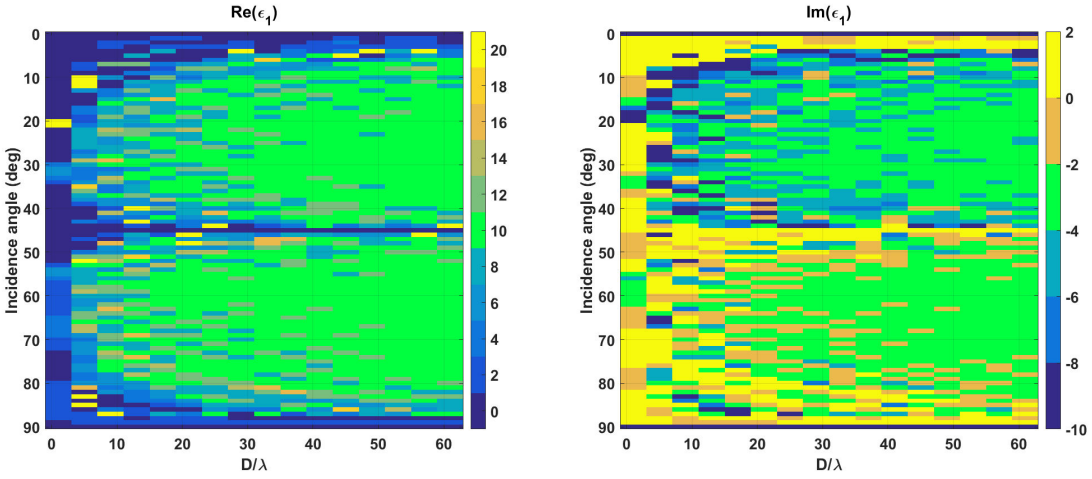

Figure 2.5 – Influence of the electrical dimension on the inversion of ϵ_1 (theoretical value: $\epsilon_1 = 10 - 3i$).

We draw for instance in Fig. 2.7 the results for ϵ_1 from the simulated example used to plot the approximated R_H^{DB} and R_V^{DB} in Fig. 2.4. We overlay the theoretical permittivity in terms of real (Re) and imaginary (Im) parts for ϵ_1. The representation is made along the incidence angle range and for the two frequencies 0.3 GHz and 1 GHz. Fig. 2.8 illustrates the same results, but for ϵ_2. The best results are obtained at 1 GHz, real part of $\tilde{\epsilon}_1$ is contained in $[9, 11]$ and its imaginary part in $[-4.5, -1.5]$ in $[10, 40] \cup [50, 80]$ degrees interval (for recall, $\epsilon_1 = 10 - 3i$). For $\epsilon_2 = 2.41 - 4.5i$, $\mathrm{Re}(\tilde{\epsilon}_2) \in [2, 3]$ and $\mathrm{Im}(\tilde{\epsilon}_2) \in [-5, -4]$ in the same interval. Accuracy degrades when frequencies go down, but it remains largely acceptable: real part of $\tilde{\epsilon}_1$ belongs to $[7, 14]$ and its imaginary part is in $[-7, 0]$. For ϵ_2, the real part ranges is $[1.7, 4]$, while its imaginary part is in $[-6, -3.5]$. In the [40,50] degrees range a discontinuity is seen that might be due to the issue at 45 degrees (see 2.1.3) spreading in this interval.

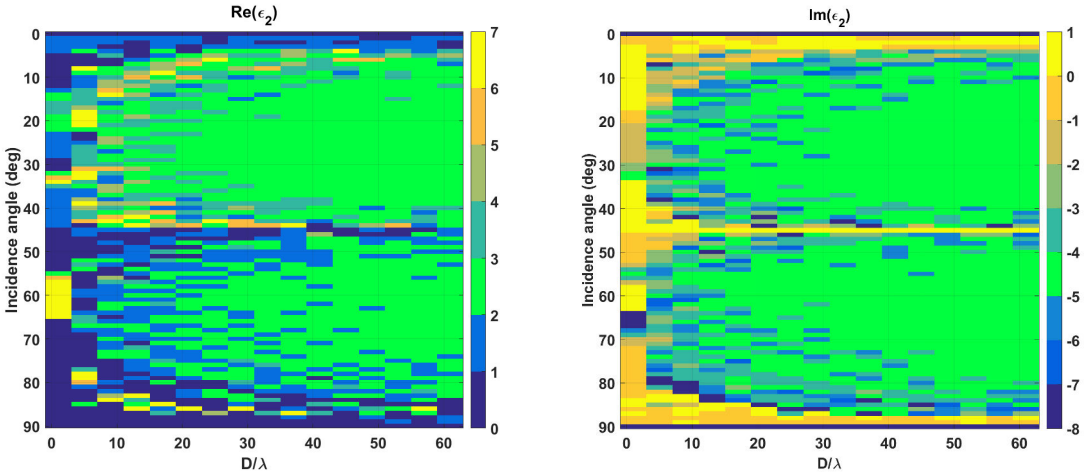

Figure 2.6 – Influence of the electrical dimension on the inversion of ϵ_2 (theoretical value: $\epsilon_2 = 2.4 - 4.5i$).

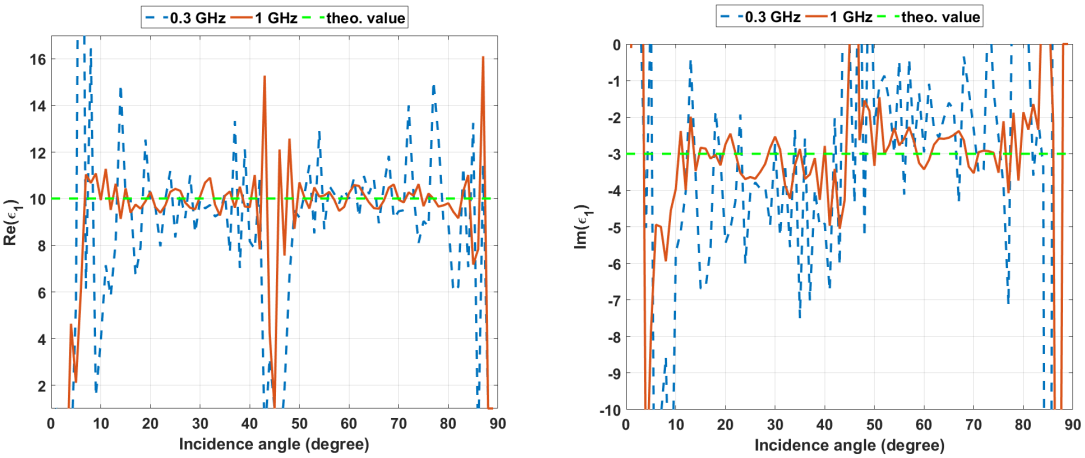

Figure 2.7 – Results and theoretical $\epsilon_1 = 10 - 3i$ in real (Re) and imaginary (Im) parts at 0.3 and 1 GHz using the ideal method.

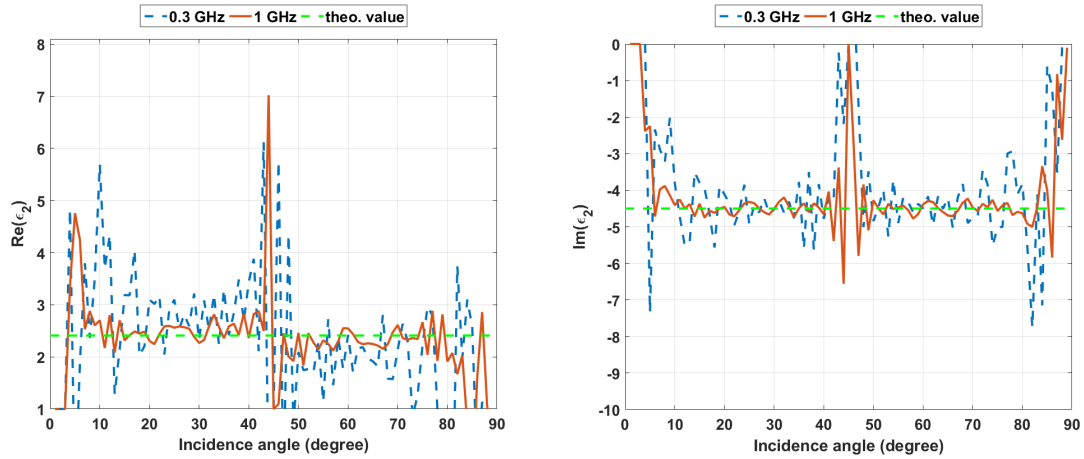

Figure 2.8 – Results and theoretical $\epsilon_2 = 2.4 - 4.5i$ in real (Re) and imaginary (Im) parts at 0.3 and 1 GHz using the ideal method.

Dihedral angle

In this subsection, we analyse the influence of the dihedral angle on the method. As depicted in Fig. 1.3 some buildings may not present a right angle with the ground. The theoretical method was developed assuming a right angle. We define ϕ_d the difference between the 90 degrees of the ideal dihedral structure and the one we consider. If $\phi_d \geq 0$ then the dihedral angle is obtuse and it is acute if ϕ_d is negative. The dimensions of the dihedral are still set to $(a, b, L, c) = (18, 18, 18, 1)$ m. As we normalize the received signal by its PEC equivalent (described in 2.2.2), we perform an identical step using now the formulation from [6] where the dihedral angle can be set. Difference is we now use the total backscattered electric fields from the PEC structure to normalize the signal and not only its double bounce component.

We used a non-linear set of $\phi_d = \{-3, -2, -1.5, -1, -0.6, -0.45, -0.3, 0, 0.3, 0.45, 0.6, 1, 1.5, 2, 3\}$ [2] degrees. A first step is then to assess the validation of the approximation made in Eq. (2.11) but considering the previous point about the normalization. We work in the following at 1 GHz.
In Fig. 2.9 and in Fig. 2.10 we look at the difference in amplitude and phase of the theoretical double bounce coefficients and the approximation used. Noticeable differences exist between the polarization HH and VV. HH approximation still holds when the dihedral angle move to ± 1 degree whereas for the vertical component even if it looks correct in amplitude, it is completely off in phase. Given the definition of HH and VV relatively to the geometry of the object, it is quite reasonable to find the kind of behaviour. However it raises questions about the results of the inversion as it requires an absolute R_H^{DB} and R_V^{DB} as inputs.

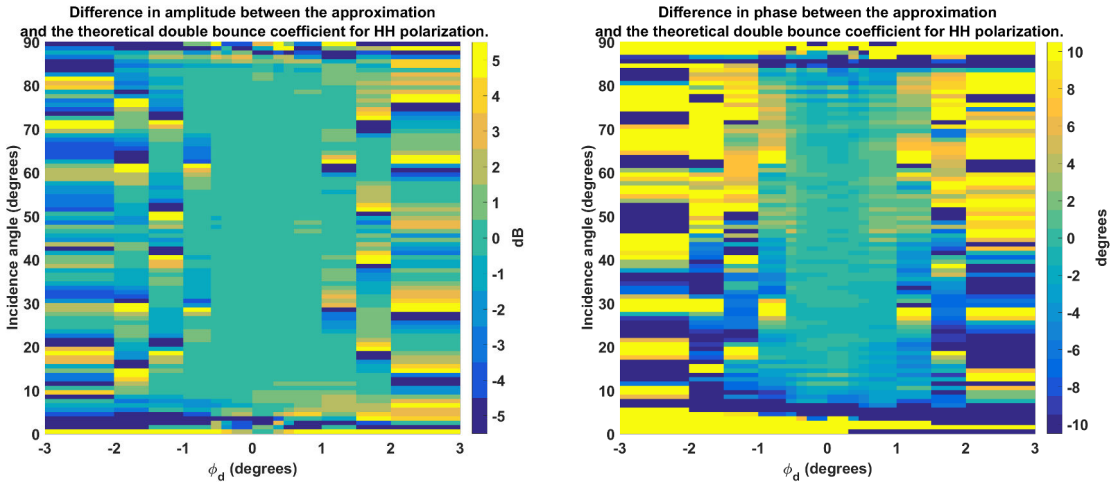

Figure 2.9 – Difference in amplitude (left) and phase (right) between the theoretical R_H^{DB} and the approximation at 1 GHz.

Fig. 2.11 and Fig. 2.12 shows the results of the inversion. We can see that except for $\phi_d = 0$ degree there is nearly no good results in both real and imaginary part. The only exception to this statement is for ϵ_2 for $\phi_d \in [-1, 1] \cap \phi \in [70, 82]$ where sometimes we get good estimate of the permittivity. However for the remaining cases, most of them are not even in the physical domain of permittivity as their imaginary part is positive.

Mix of permittivities

In cities, buildings are made of different materials as glass, concrete, bricks and wood as picitured in Fig. 1.5. Hence one last parameter to analyse is the influence of the localization of the permittivity

2. This set was defined in order to see if there were a relation between the results of the inversion and the $\frac{D}{\lambda}\sin(\phi_d)$ quantity. The latter quantity characterizes the gap in distance at the edge between a regular dihedral and the one we consider relatively to the wavelength used.

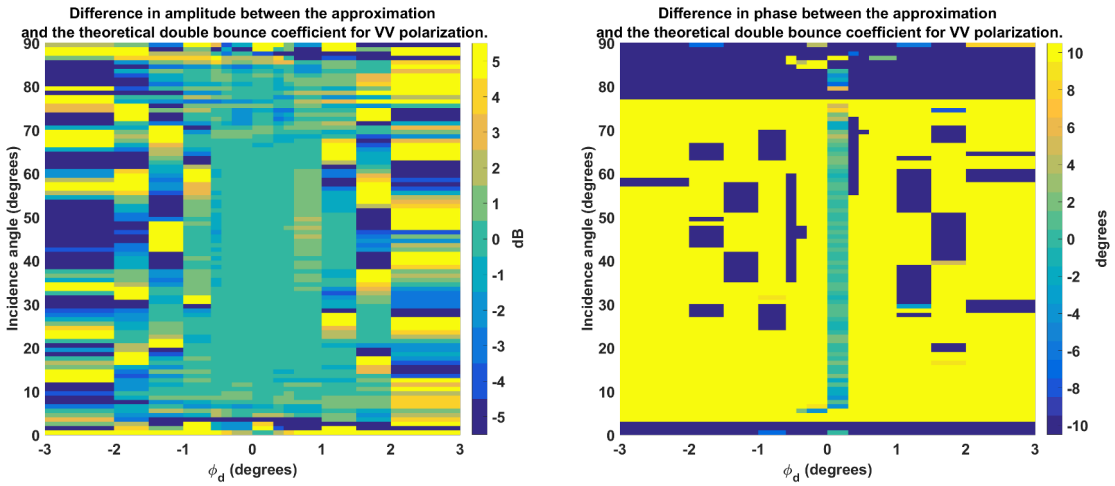

Figure 2.10 – Difference in amplitude (left) and phase (right) between the theoretical R_V^{DB} and the approximation at 1 GHz.

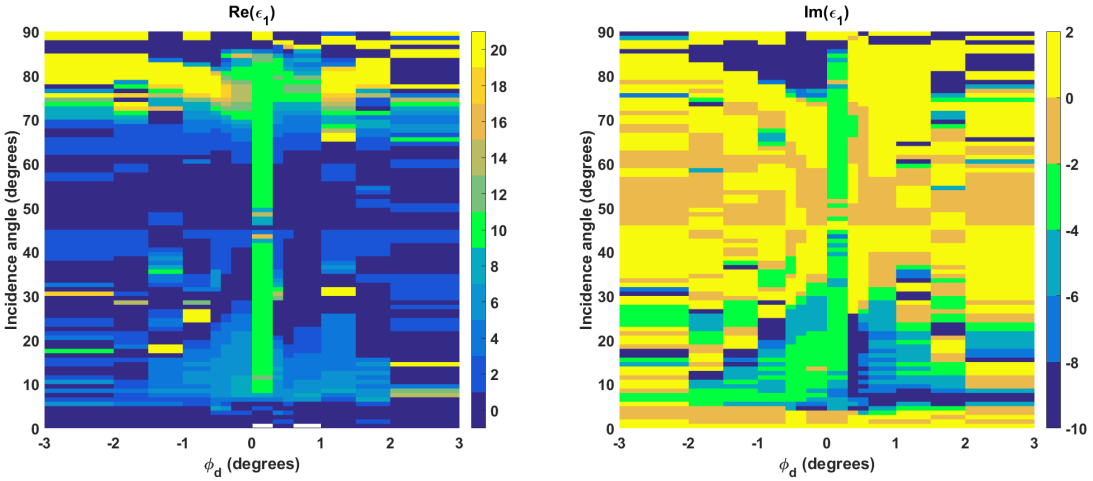

Figure 2.11 – Influence of the dihedral angle on the inversion of ϵ_1 at 1 GHz (theoretical value: $\epsilon_1 = 10 - 3i$).

within the dihedral. In this objective, we keep the plate with the $\epsilon_1 = 10 - 3i$ permittivity. We change the surface made of $\epsilon_2 = 2.4 - 4.5i$ permittivity to a composite plate made of artificial permittivities: $\epsilon_2 = 5 - 2i$ and $\epsilon_3 = 15 - 10i$. These two permittivities are chosen such that $\frac{Re(\epsilon_3)}{Re(\epsilon_2)} = 3$ and $\frac{Im(\epsilon_3)}{Im(\epsilon_2)} = 5$. This surface is equally divided between these two permittivities.

First set of simulation: We define three different simulations where the permittivities ϵ_2 and ϵ_3 are not localized at the same place. Fig. 2.13 presents the dihedral models used. The blue colour (resp. purple) defines the region where the permittivity is set to ϵ_2 (resp. ϵ_3). Respectively to their order of appearance in the figure (left to right), they are abbreviated regarding the axis of change so we have: 'vert','horiz' and 'quad'.

Results from these different models at 1 GHz are given in Fig. 2.14 for ϵ_1 and in Fig. 2.15 for the second permittivity. It is quite comforting to see that the estimation of ϵ_1 does not depend on the composition of the second plate. Little differences can be seen between the different dihedrals. In the case of the second permittivity, results can be divided in two: the estimation in the [10, 43]

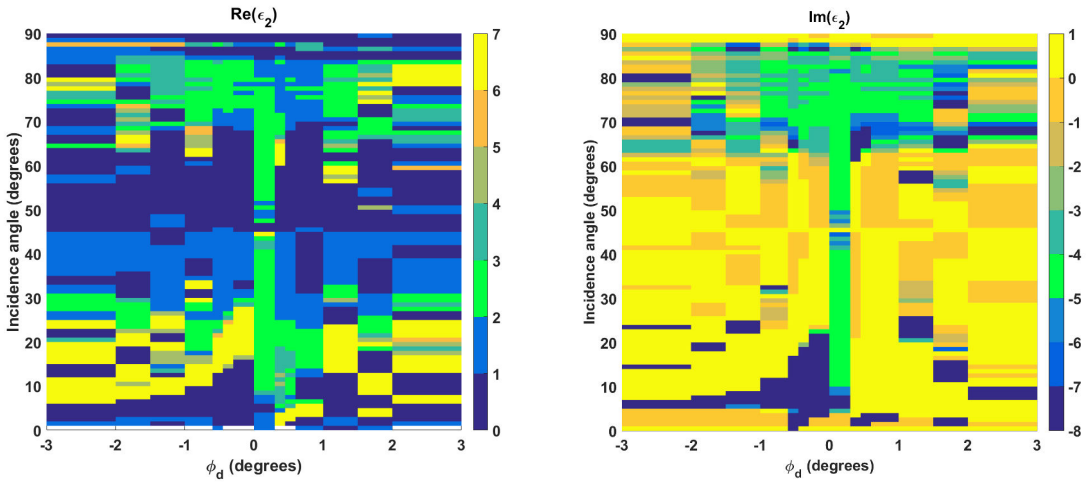

Figure 2.12 – Influence of the dihedral angle on the inversion of ϵ_2 at 1 GHz (theoretical value: $\epsilon_2 = 2.4 - 4.5i$).

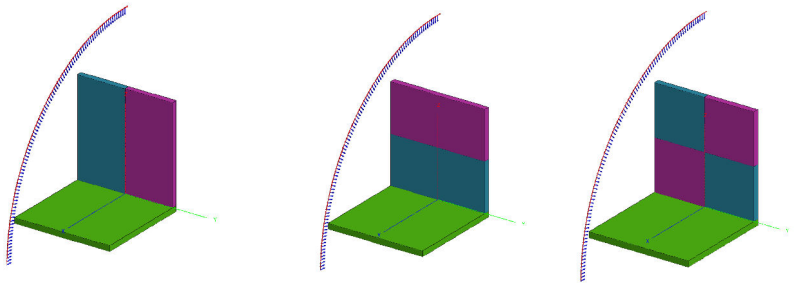

Figure 2.13 – Composite dihedrals for the first set.

degrees range, and the estimation in $[47, 80]$ degrees range.
In the first angle range, we calculate a permittivity close to $9 - 4.5i$ for every dihedrals. This estimation could be related to a mixing law. If we take the Maxwell-Garnett mixing model as formulated in [18], we can express it to get the effective permittivity ϵ_{eff}. In the notation of [18], we can obtain:

$$\epsilon_{eff} = \frac{\epsilon_m(1 + f\frac{\epsilon_i - \epsilon_m}{\epsilon_i + \epsilon_m})}{1 - f\frac{\epsilon_i - \epsilon_m}{\epsilon_i + \epsilon_m}}, \tag{2.13}$$

where ϵ_i is the permittivity of the inclusive parts in the material of ϵ_m permittivity. In the following f_v (f in [18] and in Eq. 2.13) denotes the volumetric fraction of the inclusive parts in the material. If we set $\epsilon_i = \epsilon_2$ and $\epsilon_m = \epsilon_3$ with $f_v = 0.5$ we obtain an effective permittivity of $9.0 - 5.0i$. If we swap the permittivity of the inclusive material and the surrounding material we get $\epsilon_{eff} = 8.4 - 4.2i$. The first result $9.0 - 5.0i$ is quite close to the permittivity estimated in the $[10, 43]$ degrees range. Furthermore it seems that this estimated permittivity is independent from the permittivity structure (horizontal, vertical or squared build) of the second plate.
This is quite different for the angle range $[47, 80]$ degree range where we can distinguish the 'horiz' dihedral that tends toward ϵ_2 value as the incidence angle increases. At 60 degrees it is this dihedral is seen as made of exclusively ϵ_2 permittivity. For the two other dihedrals ('vert' and 'quad'), their calculated permittivity behaves identically as before, except that it is now closer to the second permittivity calculated $8.4 - 4.2i$ by considering $\epsilon_i = \epsilon_3$ and $\epsilon_m = \epsilon_2$.

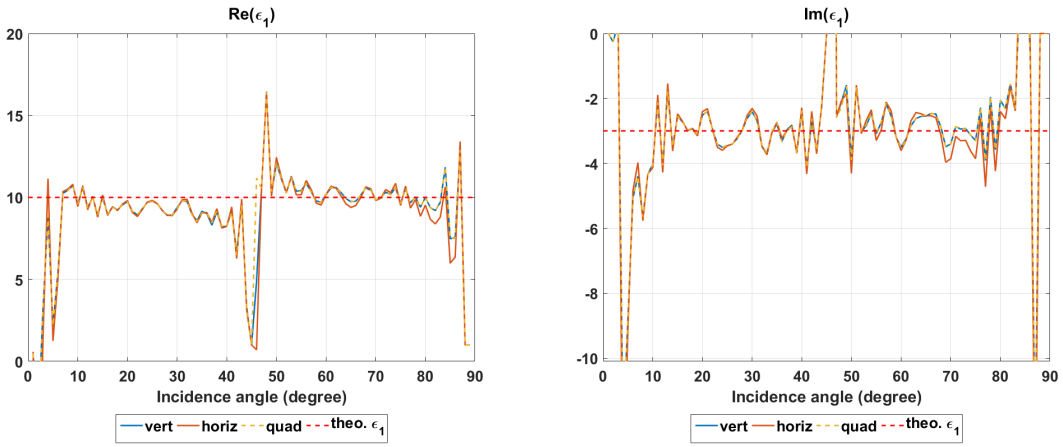

Figure 2.14 – Estimation of ϵ_1 at 1 GHz for the different dihedrals.

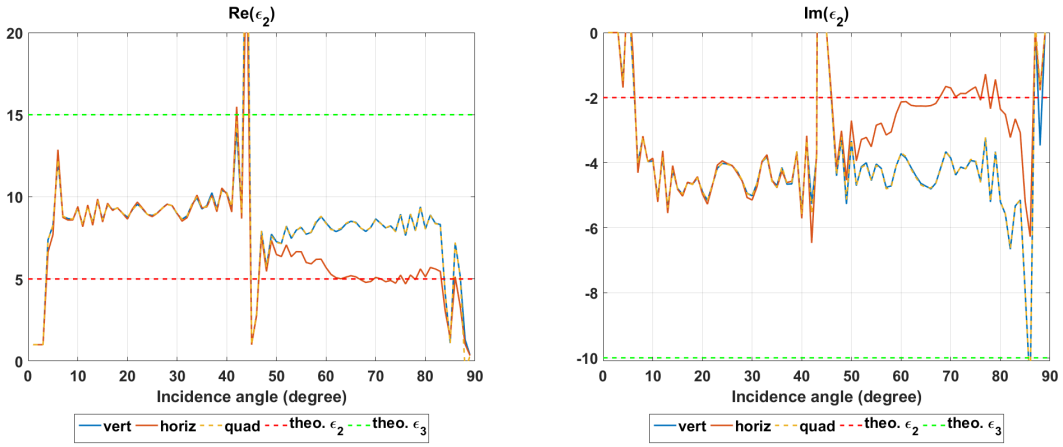

Figure 2.15 – Estimation of second permittivity at 1 GHz for the different dihedrals.

Second set of simulation: To improve the understanding of the 'horiz ' dihedral, we simulate the same kind of structure but we will now change the surface taken by ϵ_2 in the plate. An example is given in Fig. 2.16 where ϵ_2 takes 20% of the surface (or height) of the second plate. Fig. 2.17 and Fig. 2.18 we plot the results for ϵ_1 and the second permittivity at 1 GHz for surface fraction taken by ϵ_2 (specified in the legend).

Again in Fig. 2.17, the estimation of ϵ_1 does not vary with the different simulations made.
As before for ϵ_2 we will divide the study in two parts: one related to the estimation in $[10, 43]$ degrees and the other in $[50, 80]$ degrees. With the evolution of the volumetric fraction f_v we build the table 2.1 using Eq. (2.13). From this table, we can see that the curves in Fig. 2.18 roughly follows the trend described in the table suggesting a mixing model.
For the estimation in $[47, 80]$ degrees, we see the phenomenon described with the first set: the more the incidence angle increases, the more the estimated permittivity get closer to ϵ_2. Logically, the more ϵ_2 is present in the structure, the more "quickly" regarding to the incidence angle the estimation will get to ϵ_2 value. For instance at $f_v = 0.8$ or even 0.75 or 0.66 at 55 degrees, we are already close to ϵ_2.

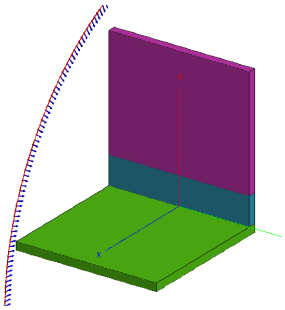

Figure 2.16 – Example of a composite dihedral from the second set.

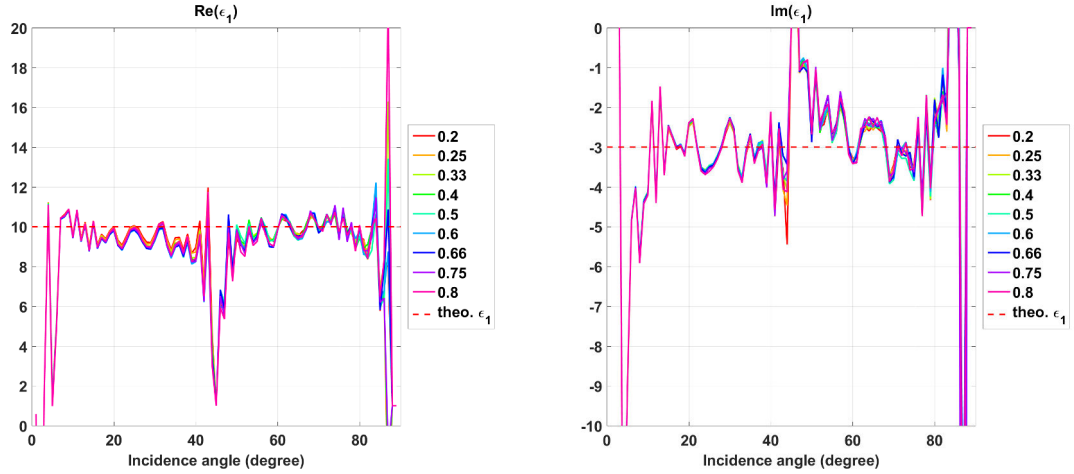

Figure 2.17 – Estimation of ϵ_1 at 1 GHz for different 'horiz' dihedrals.

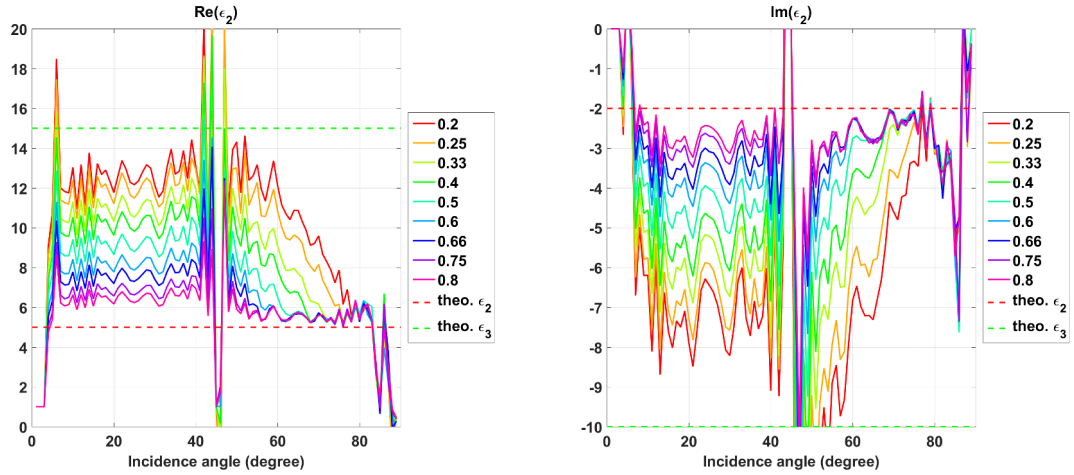

Figure 2.18 – Estimation of second permittivity at 1 GHz for different 'horiz' dihedrals.

2.3.2 Parameters of the measurement device

Here are presented the studies done to assess the influence of the parameters of the device on the method. We will focus the study on the position and orientation of the device. First the sensitivity regarding the incidence angle is addressed. Then a glimpse at parameters such as a

f_v	0.2	0.25	0.33	0.4	0.5	0.6	0.66	0.75	0.8
Real part	12.3	11.7	10.8	10.0	9.0	8.1	7.6	6.8	6.4
Imaginary part	-7.7	- 7.2	-6.4	-5.8	-5.0	-4.3	-3.9	-3.3	-3

Table 2.1 – Effective permittivities given ϵ_2 and ϵ_3 and the volumetric fraction using Eq. (2.13)

non-null azimuth angle or a roll rotation of the device is given.

Incidence angle influence

We first study the main parameter used in our method, the incidence angle ϕ. To do so, we define two different incidence angles: ϕ_c the angle at which the measurements R_H^{DB} and R_V^{DB} have been performed and ϕ_e the incidence angle we used to normalize the signal and to calculate the permittivities. In an ideal measurement, we have $\phi_e = \phi_c$. We use the simulated data from the subsection 2.3.1 at 1 GHz.
Fig. 2.19 shows the relative error made on both ϵ_1 and ϵ_2 with the evolution of ϕ_e and ϕ_c. Images are thresholded to 1 as a relative error of 1 implies that we might also estimate 0 instead of the permittivity. Obviously the line $\phi_e = \phi_c$ is the location a minimal error (less than 10%) as it is the regular functioning of the method. So we retrieve the issue at 45 degree and the degradation of the results below 10 degrees and higher than 85. However we can notice that the area of error below 10% is wider in the range $[50, 80]$ degrees. In general for both permittivities the $[50, 80]$ is a bit more comfortable than the $[10, 40]$ range. Indeed in the $[10, 40]$ incidence angle range the error increases quickly as soon as an error on the angle is made. It is not as restrictive in $[50, 80]$ degrees, especially for ϵ_2.

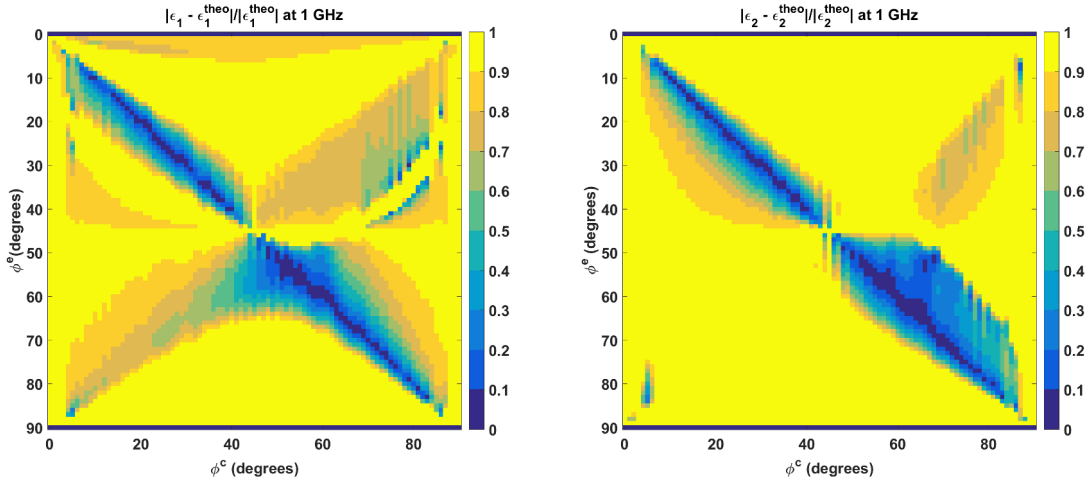

Figure 2.19 – Relative errors on ϵ_1 and ϵ_2 at 1 GHz with incorrect incidence angles ϕ_e.

To have a clearer idea, we take the data at $\phi_c = 60$ degrees and look at the results in Fig. 2.20 when ϕ_e varies between 50 and 70 degrees. In those plots the red dots display the theoretical values. $\phi_c = 60$ degrees is one of the best case according to Fig. 2.19. In the current figure, underestimating the incidence angle down of 6 degrees does not imply a large error for ϵ_1 and ϵ_2. Errors are larger when it is overestimated: at $\phi_e = 66$ degrees, we get 15 and around 6 instead of 10 and 3 for ϵ_1 and 2 and around 6 instead of 2.4 and 4.5 for ϵ_2 in real and imaginary parts.

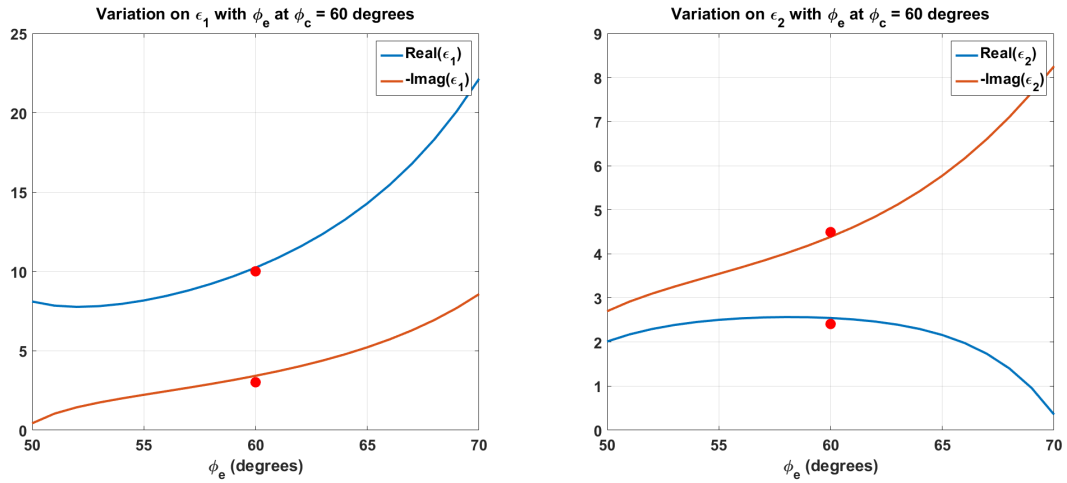

Figure 2.20 – ϵ_1 and ϵ_2 at 1 GHz with incorrect incidence angles ϕ_e and $\phi_c = 60$ degrees.

Non-null azimuth angle

Since the beginning we have considered a structure perfectly in front of the measurement device. One can wonder if the double bounce equation still holds if we rotate the structure of an angle θ in the xy plane depicted in Fig. 1.10. From the structure view point, this rotation is equivalent to a rotation in azimuth of the device. To assess this change, we simulate the same structure as the one used in 2.3.1 with one meter depth at 1 GHz. However now the co-localized emitter and receiver will not only move with the incidence angle but also with the azimuth angle. In Fig. 2.21 we display the FEKO view of all the combinations between the incidence angle $\phi \in [0, 90]$ degrees and the azimuth angle $\theta \in [-10, 10]$ degrees with a one degree step for both angle.

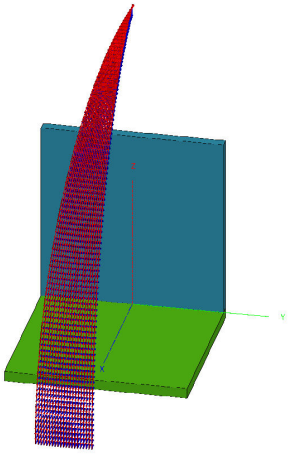

Figure 2.21 – Joint variations of the incidence angle (from top to bottom) and the azimuth angle (from left to right).

A first approach of the problem would be to apply the regular method. However we have seen in 1.3 the backscattered electric field from a PEC dihedral at a non-null azimuth angle is quite low compared to one at null azimuth angle at HH or VV. We here proceed by normalizing the electric fields by either resulting fields from an equivalent simulation made with a PEC dihedral or the fields from the PEC formulation in [7]. For sake of simplicity (and in order to stay within FEKO conventions) we simulated an equivalent PEC structure. The results of the normalization

process compared to the theoretical double bounce coefficients are shown in amplitude and phase at 1 GHz in Fig. 2.22 and Fig. 2.23 evolving with both incidence and azimuth angles. Aside from very low ($<10^\circ$) or very high ($75^\circ>$) incidence angles, we retrieve the amplitude and phase of the double bounce coefficients as in Fig. 2.4 meaning that this extension of the normalization step approximates quite well the double bounce equation for the azimuth range $[-10, 10]$ degrees.

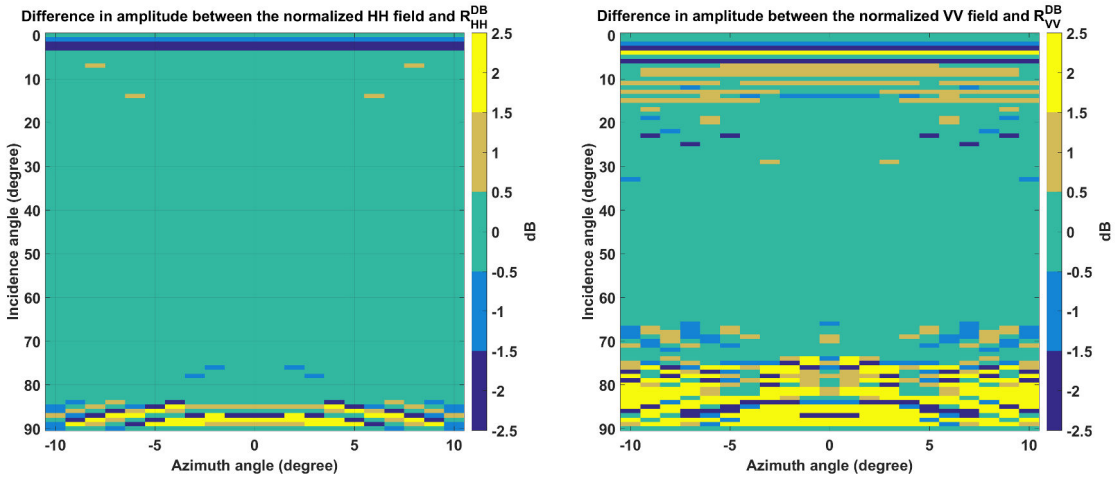

Figure 2.22 – Difference in amplitudes (dB) between the normalized backscattered electric fields and the theoretical double bounce coefficients at HH (left) and VV (right) at 1GHz.

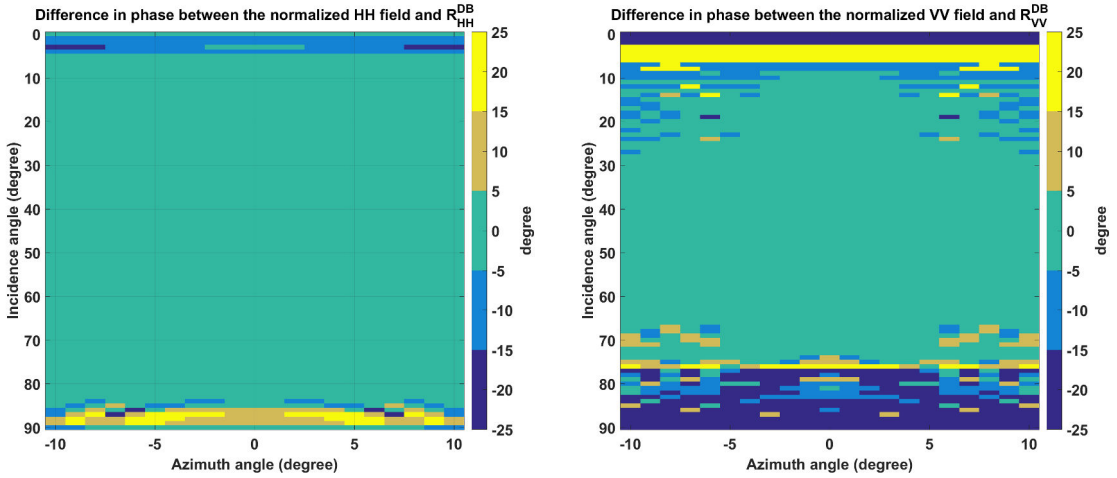

Figure 2.23 – Difference in phase (degrees) between the normalized backscattered electric fields and the theoretical double bounce coefficients at HH (left) and VV (right) at 1GHz.

Given this starting point we can directly try to invert and as a result we obtain Fig. 2.24 and Fig. 2.25. As it can be seen, the inversion handles rather well the azimuth change in the $[-10, 10]$ degrees range. We can notice in $Re(\epsilon_1)$ and $Im(\epsilon_2)$ that the results start to be degraded near and beyond ± 8 degrees. This might come from the lack of power of received signals inducing instability in the results: in the case of a PEC dihedral we have a drop of at least 30 dB between zero and ten degrees of azimuth in the field amplitude as it is illustrated on a different example in section 1.1. From these results and the invariance to azimuth angle of the approximated R_H^{DB} and R_V^{DB}, one could also retrieve the permittivities using different combination of azimuth and incidence angles.

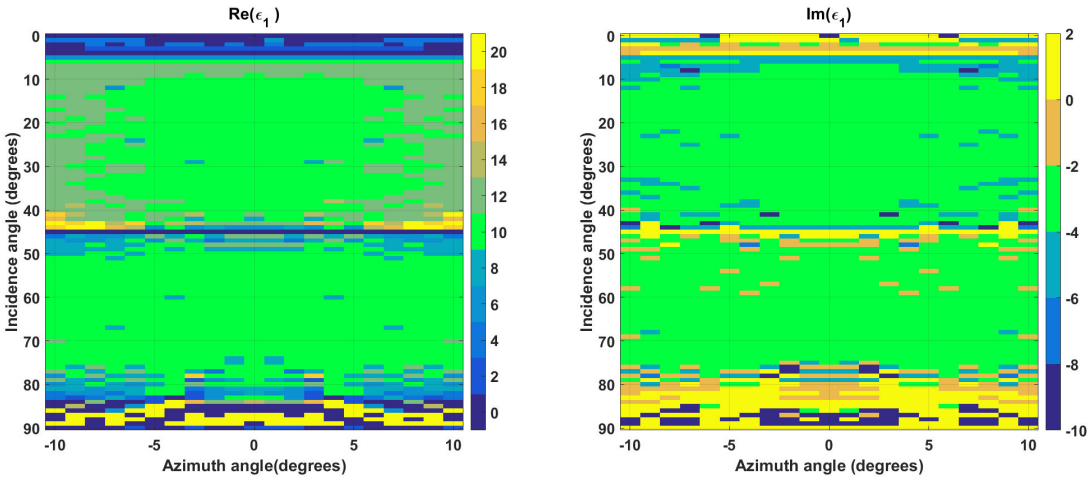

Figure 2.24 – Inversion done by normalizing the signal with an equivalent PEC structure for several azimuth angles (theoretical value: $\epsilon_1 = 10 - 3i$).

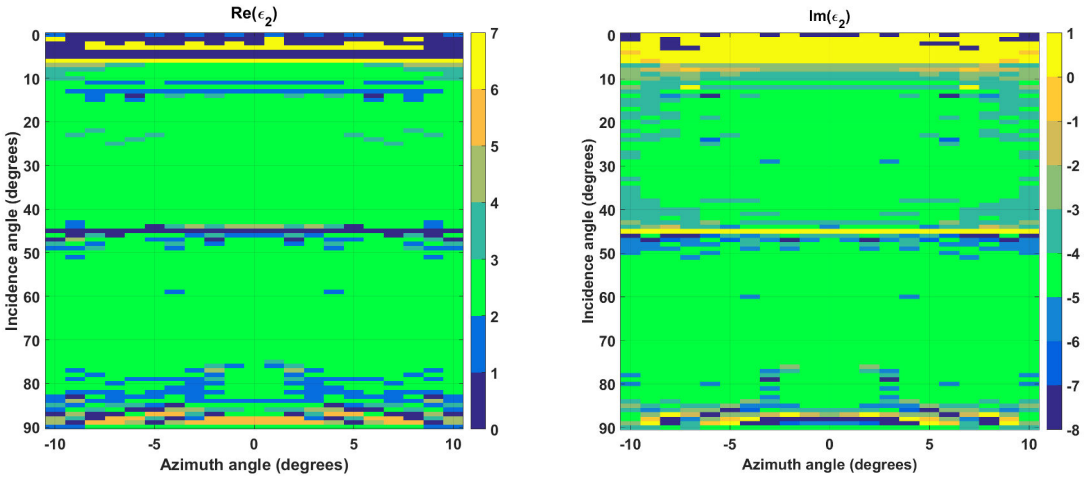

Figure 2.25 – Inversion done by normalizing the signal with an equivalent PEC structure for several azimuth angles (theoretical value: $\epsilon_2 = 2.4 - 4.5i$).

Roll angle

In the study made before, strong assumptions have been made regarding the polarization. H and V polarizations are bound to the structure orientation. In this subsection, we will look at the effect of rotating the incident and scattered H and V vectors using the propagation vector as rotation axis. This rotation is defined by the rotation angle α as defined in [36]. The configuration under simulation can be seen as a synchronized rotation of the emitter and receiver devices of α around the Line-of-Sight like a rotation in roll as displayed in Fig. 2.26. In this Figure, the vertical (resp. horizontal) incident polarization in blue (resp. green) is transformed in the purple (resp. yellow) vector due to the (positive) rotation α. As before, we simulate this case with the same structure and permittivities as in 2.3.1 with one meter depth at 1 GHz, and we define α in the $[-10, 10]$ degrees range with a degree step. Once again the results presented in Fig. 2.27 only show the inversion at 1GHz in terms of relative errors. If we only consider the area where the error is below 10% then a symmetry around the $\phi = 45$ degrees line can be observed between the two permittivities. For ϵ_1, the inversion is more flexible with α for incidence angle in $[10, 25]$ degrees. After 35 degrees a

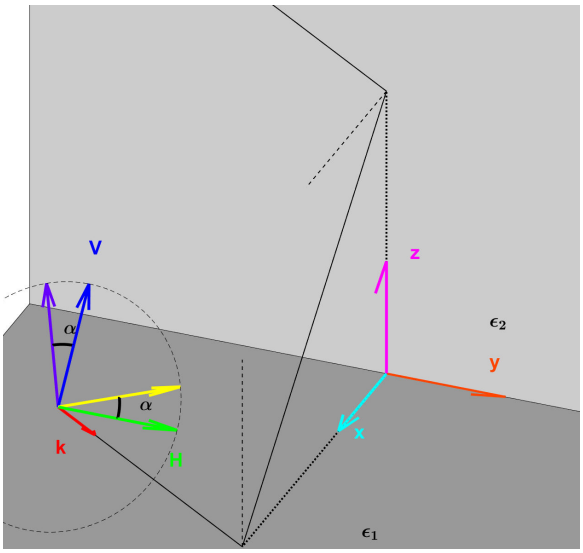

Figure 2.26 – Roll configuration.

perfect polarization as defined for the analytical solution is required. For ϵ_2, the same phenomenon can be observed but at $90 - \phi$ degrees. With α varying an asymmetry is seen between the domains of incidence angle $[10, 45]$ and $[45, 80]$ degrees. One domain generates less errors for a positive α, for instance $[10, 45]$ degrees for ϵ_1 or $[45, 80]$ for ϵ_2. However its complementary domain also gives less errors but for the negative α.

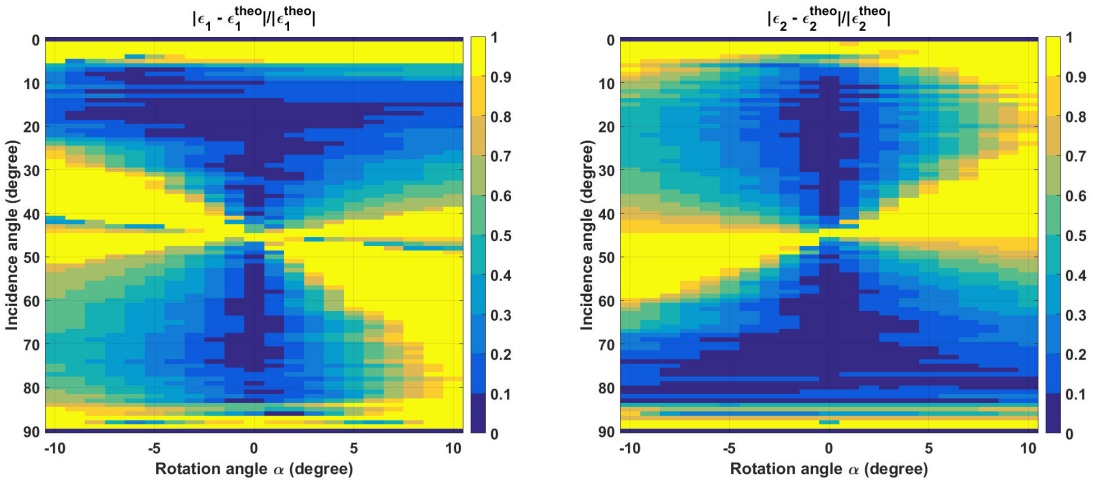

Figure 2.27 – Relative error on ϵ_1 (left) and ϵ_2 (right) for several roll angles.

2.4 Application: moisture retrieval

In the case of soil, concrete and vegetation, the permittivity of the material involved are often bind to the amount of water contained in it. As it is crucial component of the forest (Fig. 1.4) and crops monitoring, studies have been carried to retrieve the moisture content of soil [30,45,46], some others have been focused on the link between the moisture content and the permittivity ([47–50]). Here we use the model proposed in [50] where the soil permittivity is mainly characterised through

the part of sand and clay and its moisture content.

We use this model to compute the permittivities for the soil permittivity for three different moisture content (10%, 20% and 30 % volumetric moisture content). We consider a soil composed at 65 % of sand and 26% of clay at ambient temperature (20°C). It gives at 440 MHz the following permittivities: $12.87 - 2.5i$, $25 - 3.5i$ and $38.78 - 4.3i$ for the respective 10%, 20% and 30 % volumetric moisture content. In the case of a dihedral structure, these permittivities are set to ϵ_1. For ϵ_2 we consider a concrete material of permittivity $2.4 - 4.5i$ as in the previous simulation.

We simulate a dihedral structure at 440 MHz of dimensions $(a, b, L) = (20, 18, 20)$ m the permittivities previously exposed for an incidence angle varying in [10,80] degree with a one degree step. In Fig. 2.28 and in Fig. 2.29 are plotted the results for respectively ϵ_1 and ϵ_2 in terms of real and imaginary parts for the three different moisture content. The different colours are linked to the moisture content: red corresponds to the 10% volumetric moisture content, green to the 20% and blue to the 30 %. The dashed lines correspond to the theoretical value of permittivity calculated and exposed in the previous paragraph. At first sight, the real part of ϵ_1 allows to easily differentiate the three permittivities based on the three different water content. Indeed as ϵ_2 is not influence by the water content of the material characterised by ϵ_1 and that imaginary part of ϵ_1 is oscillating too much to be able to correctly make an estimate, the real part seems to be the component to look in order to see a water content change of the soil. In the $[20, 35] \cup [55, 70]$ degrees, we get curves allowing to see this difference as they don't mix each other (the blue stays above 30, the green between 20 and 30 and the red one around 12). In imaginary part, it is more difficult to see this, only the red curve seems to present such behaviour except in $[20, 35]$ degrees where it looks biased as we estimate a value close to -3.5, the theoretical green curve. Again, it is a behaviour that is retrieved for the estimation of ϵ_2 at a smaller scale. Outside this angular domain we get either the backscattering of each plate in $[10, 15]$ or in $[75, 80]$ degrees or the 45 degrees issue that appears and spreads in the $[35, 55]$ degrees domain.

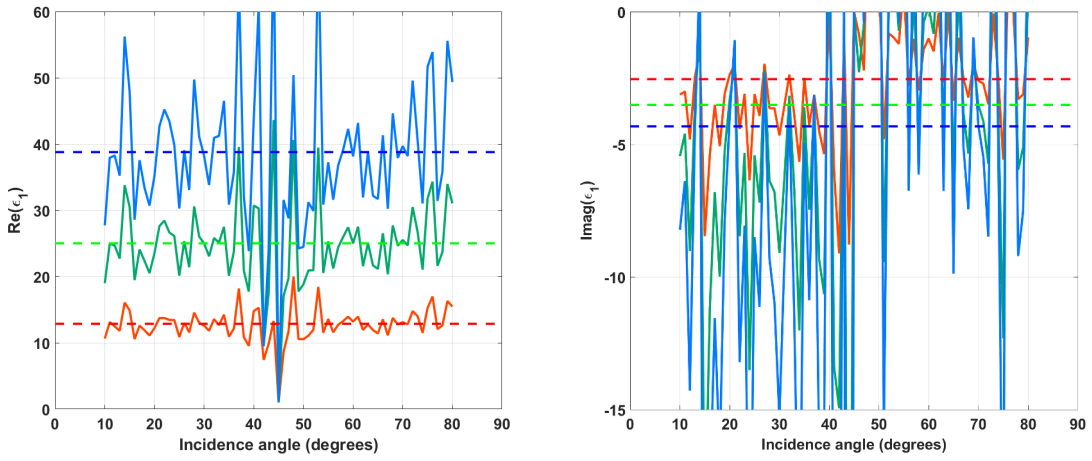

Figure 2.28 – Real and imaginary parts of ϵ_1 for different moisture content at 440 MHz (red: 10 % of volumetric moisture content, green: 20 % and blue: 30 %).

2.5 Summary of the method

Over this chapter, we have put in place a method based on the double bounce equation Eq. (1.6) to retrieve the two permittivities of a two-plate dihedral. Its coarse version uses the knowledge of the incidence angle and the measurement of R_H^{DB} and R_V^{DB}. As it has been seen, the 45 degree

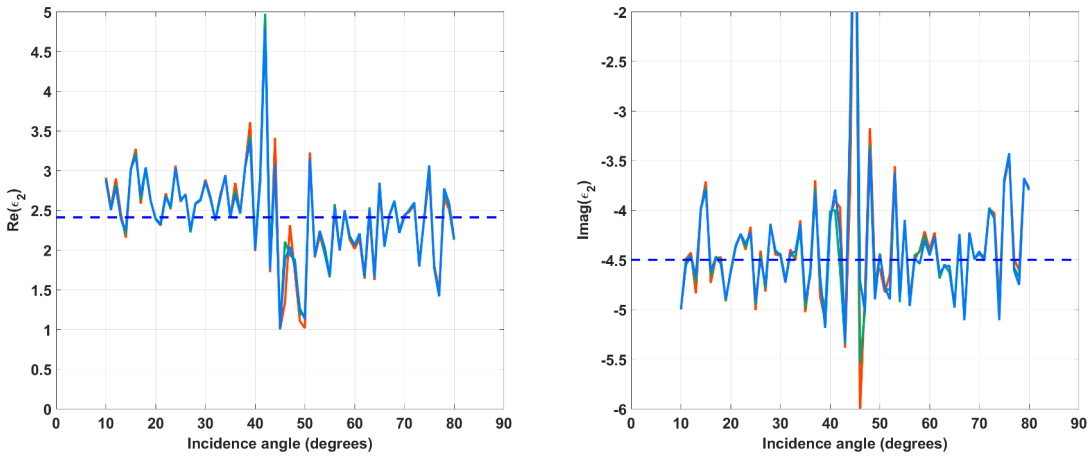

Figure 2.29 – Real and imaginary parts of ϵ_2 for different moisture content at 440 MHz (red: 10 % of volumetric moisture content, green: 20 % and blue: 30 %).

incidence angle is a mathematical limitation and to correctly retrieve R_H^{DB} and R_V^{DB} using a normalization step of the signals is mandatory. The following diagram in Fig. 2.30 summarises this process.

To sum up, this method uses the co-polarised fields HH and VV taken at one incidence angle ϕ and at one frequency. We retrieve R_H^{DB} and R_V^{DB} by normalising the fields by its equivalent for a PEC case, making the approximated R_H^{DB} and R_V^{DB} dimensionless (as expected) from the frequency and also from the dimensions of the dihedral. This latter statement can be discussed as we have seen that a minimum of 20 for the electrical dimension of each plate is required to have a reasonable interval in incidence angle on which we can perform the method.
By studying the influence of the structure on the signal we notice that the process is not robust at all to a change of the dihedral angle. However we got interesting results when one plate is made of a composition of permittivity. The method is able to detect the change of permittivity with the incidence angle when the change is horizontal (*i.e.* along the dihedral axis). As a result, a mixing law of permittivities could be observed.
About the positioning of the measurement device, movements with the azimuth angle is no problem as long as an adequate normalization step is performed. Finally, we study the influence of the incidence angle and the roll angle on the results to conclude that these two parameters appears quite critical to obtain a correct result.

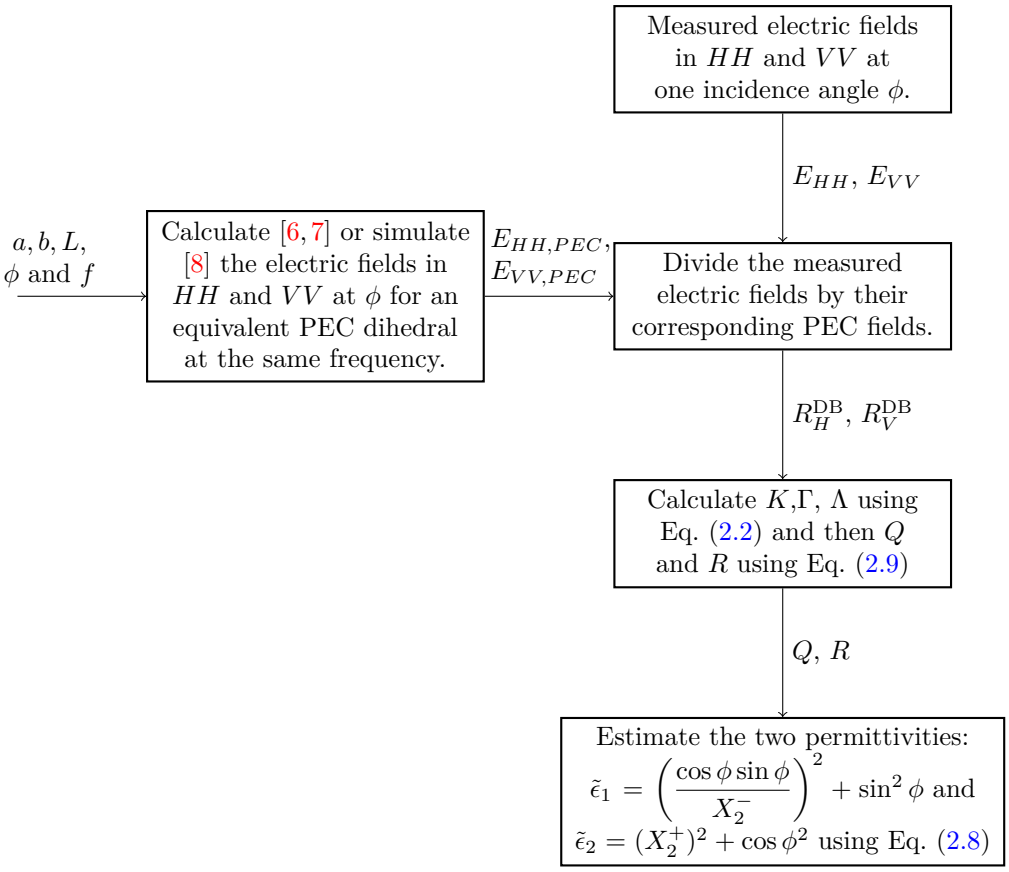

Figure 2.30 – Process of the method.

Chapter 3

One polarization method

With the previous method we have the ability to analytically determine the two permittivities of a dihedral structure given the two co-polarised backscattered fields collected at one incidence angle. The dependence on VV polarization may lead to trouble during measurements as the presence of the double Brewster effect might affect the power budget of the radar or of the measurement device. This is especially the case at or near Brewster or Pseudo-Brewster angles where the amplitude of VV field is minimal. By building a solution relying only on HH field we would avoid this issue. From a mathematical point of view, HH polarisation is also easier to handle and solve when we compare the analytical expressions from Eq. (2.3) and Eq. (2.5). In addition, one polarization system at HH would permit to retrieve the permittivities.
In this chapter we will first built the analytical background for such method and then analyse it regarding the simulations made in 2.3.

3.1 Theory

Considering now only the HH polarization, we first try to invert the permittivities from Eq. (1.6) at HH using again the variables defined in Eq. (2.1). From Eq. (2.3), we get:

$$(\cos\phi\sin\phi + X_1\sin\phi + X_2\cos\phi + X_1X_2)R_H^{\mathrm{DB}} = \cos\phi\sin\phi - (X_1\sin\phi + X_2\cos\phi) + X_1X_2 \quad (3.1)$$

that leads to:

$$X_1X_2 + (X_1\sin\phi + X_2\cos\phi)K + \cos\phi\sin\phi = 0, \quad (3.2)$$

where K is the quantity from Eq. (2.2).

From Eq. (3.2) alone we can obtain an infinite number of couples (ϵ_1, ϵ_2) that comply with it. To reduce the number of possibilities, we will now assume that we have two measurements made at (ϕ_1, ϕ_2): $R_H^{\mathrm{DB}}(\phi_1)$ and $R_H^{\mathrm{DB}}(\phi_2)$.
First, by isolating X_1 we can obtain:

$$\epsilon_1 = X_1^2 + \sin^2\phi = \frac{(\cos\phi K X_2 + \cos\phi\sin\phi)^2}{(X_2 + K\sin\phi)^2} + \sin^2\phi. \quad (3.3)$$

We define the new variables:

$$\begin{aligned} \xi_1 &= \sqrt{\epsilon_2 - \cos^2\phi_1} \\ \xi_2 &= \sqrt{\epsilon_2 - \cos^2\phi_2} \end{aligned} \quad (3.4)$$

As the permittivity should not change with the incidence angle, we can write this invariance property as:

$$\frac{(\cos\phi_1 K_1\xi_1 + \cos\phi_1\sin\phi_1)^2}{(\xi_1 + K_1\sin\phi_1)^2} + \sin^2\phi 1 = \frac{(\cos\phi_2 K_2\xi_2 + \cos\phi_2\sin\phi_2)^2}{(\xi_2 + K_2\sin\phi_2)^2} + \sin^2\phi_2 \quad (3.5)$$

If we multiply this last equation by $(\xi_1 + K_1 \sin\phi_1)^2(\xi_2 + K_2 \sin\phi_2)^2$ and after developping and regrouping terms, we can obtain the following equation:

$$a\xi_1^2\xi_2^2 + b\xi_1^2\xi_2 + c\xi_1\xi_2^2 + d\xi_1\xi_2 + e\xi_1 + f\xi_2 + g\xi_1^2 + h\xi_2^2 + k = 0. \tag{3.6}$$

Coefficients $(a, b, c, d, e, f, g, h, k)$ are defined in Eqs. (3.7).

$$\begin{aligned}
a &= \cos^2\phi_1 K_1^2 - \cos^2\phi_2 K_2^2 + (\sin^2\phi_1 - \sin^2\phi_2)\\
b &= 2K_2 \sin\phi_2 \cos^2\phi_1 (K_1^2 - 1)\\
c &= 2K_1 \sin\phi_1 \cos^2\phi_2 (K_2^2 - 1)\\
d &= 0\\
e &= 2K_1 \sin\phi_1 \sin^2\phi_2 \cos^2\phi_2 (K_2^2 - 1)\\
f &= -2K_2 \sin\phi_2 \sin^2\phi_1 \cos^2\phi_1 (K_1^2 - 1)\\
g &= \sin^2\phi_2(\cos^2\phi_1 K_1^2 K_2^2 + K_2^2(\sin^2\phi_1 - \sin^2\phi_2) - \cos^2\phi_2)\\
h &= \sin^2\phi_1(-\cos^2\phi_2 K_1^2 K_2^2 + K_1^2(\sin^2\phi_1 - \sin^2\phi_2) + \cos^2\phi_1)\\
k &= \sin^2\phi_1 \sin^2\phi_2(\cos^2\phi_1 K_2^2 - \cos^2\phi_2 K_1^2 + K_1^2 K_2^2(\sin^2\phi_1 - \sin^2\phi_2))
\end{aligned} \tag{3.7}$$

Using Eq. (3.4), we can write:

$$\xi_1^2 + \cos^2\phi_1 = \xi_2^2 + \cos^2\phi_2. \tag{3.8}$$

We substitute in Eq. (3.6) ξ_1 by $\pm\sqrt{\xi_2^2 + \cos^2\phi_2 - \cos^2\phi_1}$. It gives the following equation:

$$a\xi_2^4 + b\xi_2^3 + l\xi_2^2 + m\xi_2 + n \mp \sqrt{\xi_2^2 + \cos^2\phi_2 - \cos^2\phi_1}(c\xi_2^2 + d\xi_2 + e) = 0 \tag{3.9}$$

where

$$\begin{aligned}
l &= g + h + a(\cos^2\phi_2 - \cos^2\phi_1),\\
m &= f + b(\cos^2\phi_2 - \cos^2\phi_1)\\
n &= k + g(\cos^2\phi_2 - \cos^2\phi_1)
\end{aligned} \tag{3.10}$$

Finally we multiply Eq. (3.9) by $a\xi_2^4 + b\xi_2^3 + l\xi_2^2 + m\xi_2 + n \pm \sqrt{\xi_2^2 + \cos^2\phi_2 - \cos^2\phi_1}(c\xi_2^2 + d\xi_2 + e)$ leading to a polynomial form in ξ_2:

$$A\xi_2^8 + B\xi_2^7 + C\xi_2^6 + D\xi_2^5 + E\xi_2^4 + F\xi_2^3 + G\xi_2^2 + H\xi_2 + I = 0 \tag{3.11}$$

with

$$\begin{aligned}
A &= a^2\\
B &= 2ab\\
C &= b^2 + 2al - c^2\\
D &= 2am + 2bl - 2dc\\
E &= l^2 + 2bm + 2an - d^2 - 2ec - c^2(\cos^2\phi_2 - \cos^2\phi_1)\\
F &= 2bn + 2ml - 2de - 2dc(\cos^2\phi_2 - \cos^2\phi_1)\\
G &= m^2 + 2nl - e^2 - (d^2 + 2ec)(\cos^2\phi_2 - \cos^2\phi_1)\\
H &= 2mn - 2de(\cos^2\phi_2 - \cos^2\phi_1)\\
I &= n^2 - e^2(\cos^2\phi_2 - \cos^2\phi_1).
\end{aligned} \tag{3.12}$$

This eight degree equation can be factored by $(\xi_2 - \sin\phi_2)^2(\xi_2 + \sin\phi_2)^2$ leading to a more convenient four degree equation defined by:

$$\alpha_4\xi_2^4 + \alpha_3\xi_2^3 + \alpha_2\xi_2^2 + \alpha_1\xi_2 + \alpha_0 = 0 \tag{3.13}$$

where:

$$\begin{aligned}\alpha_4 &= A\\ \alpha_3 &= B\\ \alpha_2 &= C + 2A\sin^2\phi_2\\ \alpha_1 &= \frac{H}{\sin^2\phi_2}\\ \alpha_0 &= \frac{I}{\sin^2\phi_2}\end{aligned} \tag{3.14}$$

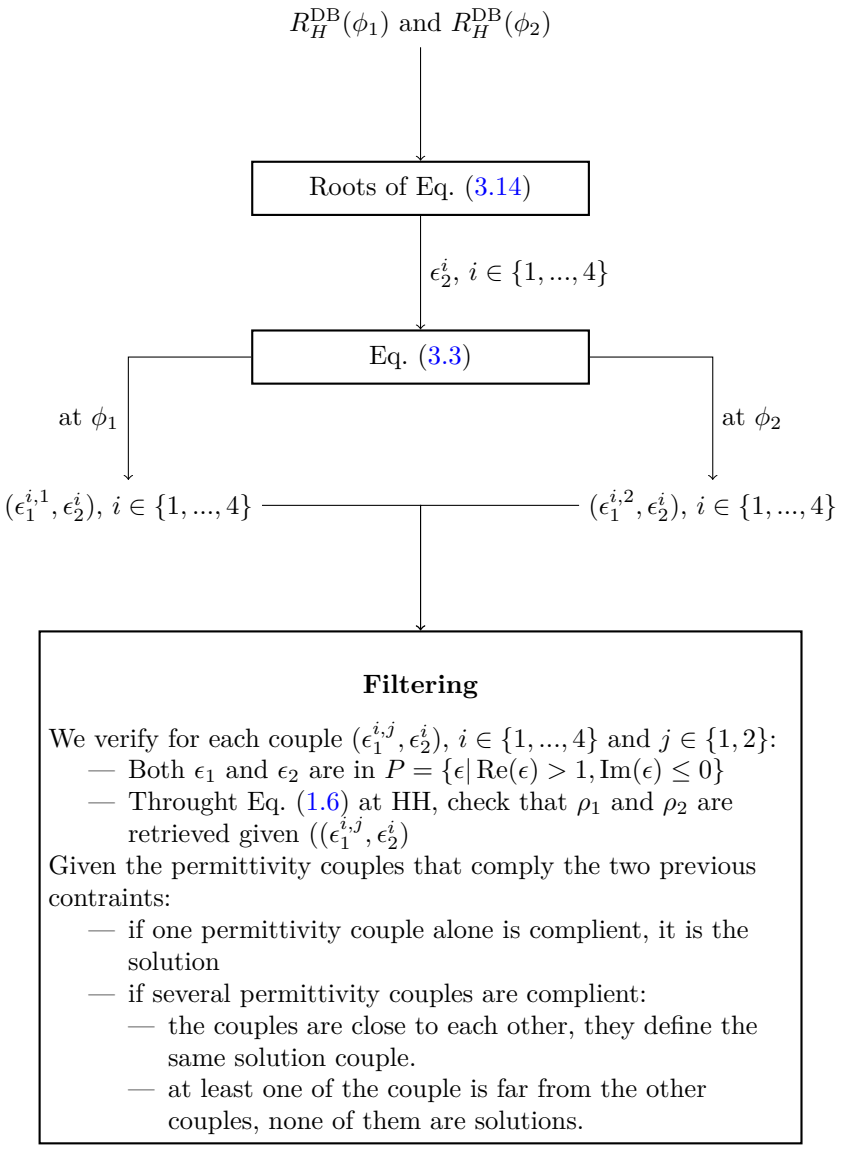

Figure 3.1 – Filtering process of the method.

From this equation, at least one of the four roots should lead to ϵ_2. To do so, we numerically computed the four candidates for ϵ_2. We can use Eq. (3.2) at ϕ_1 and also at ϕ_2 to get the associated candidates in ϵ_1. By doing so, we collect eight candidates of (ϵ_1, ϵ_2). We filter out the couples that are not in the physical domain. We also keep couples that verify at HH polarization Eq. (1.6) at ϕ_1 and ϕ_2. This process summarized in the scheme in Fig. 3.1 allows us to have for most of the

cases a unique couple solution.

3.2 Domain of validity: limits and range of possibilities

In this section, we basically take the simulation data from 2.3 and apply the new method to them. Thus, identical parameters are studied: geometry of the object, its permittivity composition, and the pose of the device. But first, a remark on the representation of the results is made.

Remark on the result representation

As the new method needs two incidence angles, it makes the representation of the results difficult when assessing them over a parameter evolution (frequency, dihedral angle, *etc.*). To partially bypass this, we count the occurrence of correct, close and the absence of results (Not a Number results (NaN)) as defined with the following binary equations:

$$\begin{aligned} \text{Correct permittivity } \epsilon &: F(\epsilon, 1) = 1 \\ \text{Close permittivity } \epsilon &: F(\epsilon, 2) = 1 \end{aligned} \tag{3.15}$$

with

$$\begin{aligned} F(\epsilon, \tau) =& (Re(\epsilon) > Re(\epsilon_{theo}) - \tau) \wedge (Re(\epsilon) < Re(\epsilon_{theo}) + \tau) \\ & \wedge (Im(\epsilon) > Im(\epsilon_{theo}) - \tau) \wedge (Im(\epsilon) < Im(\epsilon_{theo}) + \tau) \end{aligned}$$

, where $\wedge$ denotes the AND logical operator and τ is the tolerance parameter.

We calculate these percentages for combination angles $(\phi_1, \phi_2) \in [10, 80] \times [10, 80]$ for every step parameter considered. One can notice that $F(\epsilon, 1) = 1$ corresponds to the green color code in real and imaginary parts of Figures such as Figs. 2.5 – 2.11 – 2.24.
Note that the close percentage takes also into account the correct percentage as a ϵ validating $F(\epsilon, 1)$ also validates $F(\epsilon, 2)$. Hence when we look at the percentage between the correct and the close results, we look at results that are close to the theoretical results without being correct. Moreover when we look at the difference between the close and the NaN results we see the percentage of results that are not even close to the theoretical results.
Also note that as we need to have $\phi_1 \neq \phi_2$ there is a permanent percentage of NaN bound to $\phi_1 = \phi_2$ of 1.4 %.

3.2.1 Object parameters

First the object parameters will be dealt with. Studies on the geometry and the permittivity of the dihedral are carried out in this subsection.

Electrical dimension

We take the same simulation data from 2.3.1 and apply the new method of solving. To get R_H^{DB}, we use the normalisation step described in the subsection 2.2.2. We plot the correct, close and NaN curves with the electrical dimension $\frac{D}{\lambda}$ in Fig. 3.2(a) for ϵ_1 and in Fig. 3.2(b) for ϵ_2. We see that ϵ_2 is more often better estimated than ϵ_1 in the $[10, 80] \times [10, 80]$ domain. The percentage of absence of results goes from 65% to a stabilized value around 9 % between the electrical dimension of 5 to 61. The part of correct value for ϵ_1 varies from few percent to 57% on the same range, and for ϵ_2 it evolves from 6% to a value around 82%. We can notice that the trend of the correct or close results are peculiar: for ϵ_1 it has a hard time increasing, but for ϵ_2,after a quick increase, it stabilises at a high value.

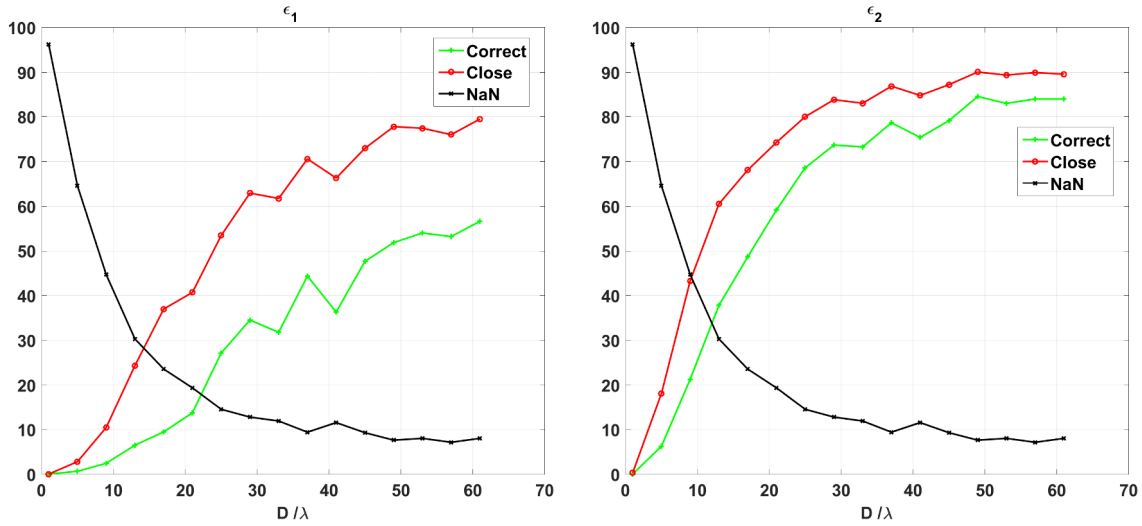

(a) For $\epsilon_1 = 10 - 3i$.

(b) For $\epsilon_2 = 2.4 - 4.5i$.

Figure 3.2 – Pencentages for both permittivities over the electrical dimension of correct, close and absence of results.

In Fig 3.3 we show the results of the inversion on the simulated data for the real and the imaginary parts of ϵ_1 and ϵ_2 at 0.3 and 1 GHz. These figures are made along the incidence angles (ϕ_1, ϕ_2). Colorbars in these figures are thresholded. The green colour is used to denote the correct interval.
One can notice the symmetry to the axis $\phi_1 = \phi_2$. Noticeable differences can be seen between 0.3 (corresponding to $\frac{D}{\lambda} = 18$) and 1 GHz (corresponding to $\frac{D}{\lambda} = 60$) results. At 1 GHz more results are determined and they are more homogeneous over the $[10, 80] \times [10, 80]$ domain. At 0.3 GHz, results are more scattered around the theoretical value. Combinations using angles below 20 degrees yield results that are more likely to be incorrect. At 1 GHz, this angle boundary is decreased to a value around 10 degrees. At $(\phi_1, \phi_2) = 80 \times [30, 80]$ degrees we notice the absence of results. This strip of 'no results' get thinner as the frequency increases. Mainly large areas of correct results can be found at 1 GHz whereas at 0.3 GHz correct results are more scattered.

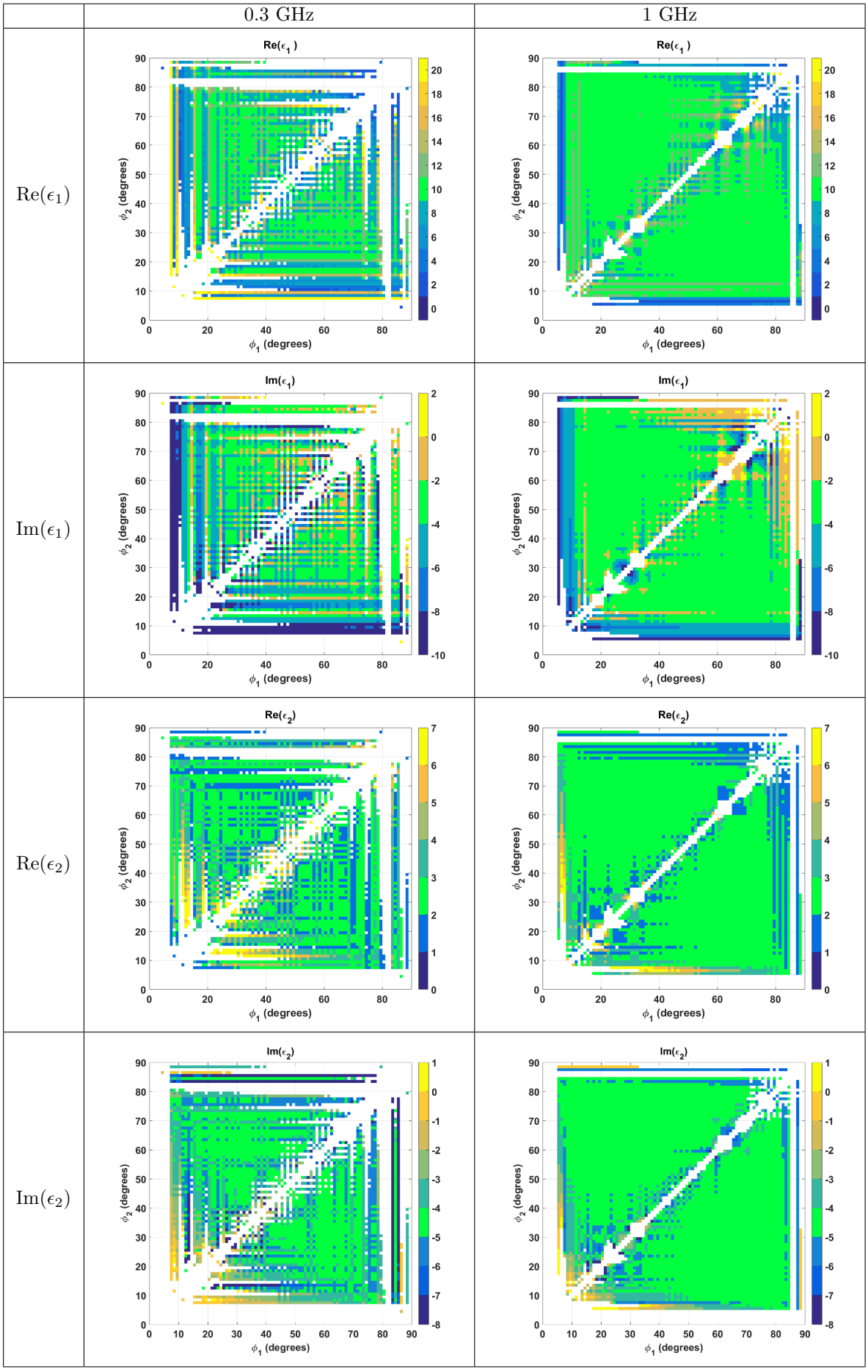

Figure 3.3 – Real and imaginary parts for ϵ_1 and ϵ_2 at 0.3 and 1 GHz.

Dihedral angle

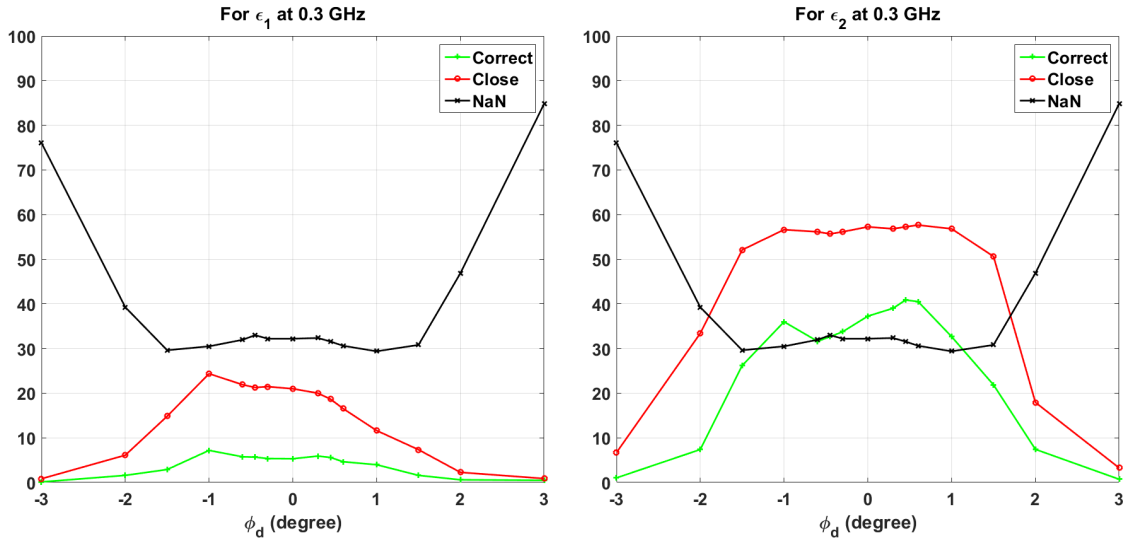

Figure 3.4 – Percentages for ϵ_1 and ϵ_2 of correct, close and absence of results at 0.3 GHz.

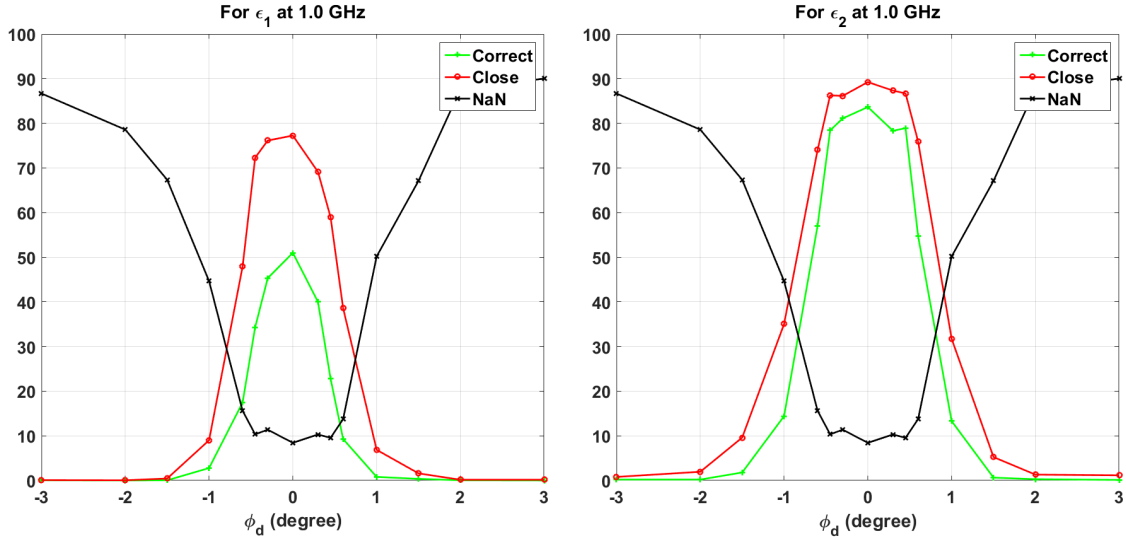

Figure 3.5 – Percentages for ϵ_1 and ϵ_2 of correct, close and absence of results at 1 GHz.

Again by taking the simulation data from 2.3.1, we compute the inversion process and as in 3.2.1 we determine the percentage of correct, close and NaN results. We plot the corresponding curves for 0.3 GHz in Fig. 3.4 and for 1 GHz in Fig.3.5. From the curves at 0.3 GHz, we see that there is less than 10% of correct results for ϵ_1 whatever ϕ_d and that the close results barely reach the 25% at best. Results from ϵ_2 are better as we can obtain more that 30% of correct results and more than 50% of close results over the $[-1.5, 1]$ degrees of ϕ_d. It is also quite surprising to see the asymmetry of the curves especially to not have their maximum at the ideal case $\phi_d = 0$. At 1 GHz, curves are getting more narrowly centred on $\phi_d = 0$ degrees. This time, correct results for ϵ_1 meets 50% and more than 80% for ϵ_2 at best. However high percentages of correct or close results are contained in the $[-1, 1]$ degree interval. Outside this interval we quickly get either no result or an erroneous one.
Nevertheless we can see with these results that we obtain a significant improvement compared to

results in 2.3.1. This is mainly due to the fact that by relying only on HH polarization is more flexible with the dihedral angle and it avoids the VV drift in phase seen in Fig. 2.9 and Fig. 2.10.

Mix of permittivities

In this part, we consider the two sets of simulations used in 2.3.1. As for the numerical illustration section, we highlight the correct results for ϵ_1 in green. For the second permittivity, as we have two permittivities on the second surface, we put in green correct results for $\epsilon_3 = 15 - 10i$ and in red the ones for $\epsilon_2 = 5 - 2i$. We remind that the abbreviated names for the different structures are defined in 2.3.1 and illustrated in Fig. 2.13.

First set of simulation: In Fig. 3.6 (resp. Fig. 3.7) we look at the results at 1GHz for ϵ_1 (resp. ϵ_2) from the first set. By looking at these figures we notice that now ϵ_1 is more difficult to retrieve. This is especially the case for the "horiz" structure where for incidence angles above 60 degrees ϵ_1 is no longer well retrieved. At $(\phi_1, \phi_2) = (65, 65)$ degrees and nearby, no results are found. Only when we look at the inferior corner of the domain, $[10, 50] \times [10, 50]$ we are able retrieve ϵ_1 but it is more disrupted than it was when we simulated the two homogeneous plates in 3.2.1. This remark also applies to the results from the "quad" and "vert" structures. In these very similar cases, we are able to find back ϵ_1 over the $[10, 80] \times [10, 80]$ degree domain but at some places it gets underestimated like in $[45, 80] \times [15, 45]$. Around the $(45, 45)$ degree point we have an area with a more pronounced error.
This is also seen in the estimation of the second permittivity. In the upper domain, $[45, 80] \times [45, 80]$, it is estimated around $8 - 4i$ as with the previous method. In the lower domain $[10, 45] \times [10, 45]$ degrees, we estimate a permittivity around $7 - 3i$, *i.e.* closer to $\epsilon_2 = 5 - 2i$. The domain $[45, 80] \times [10, 45]$ degrees and its symmetrical one seems to show a decreasing estimated permittivity as we start from $(45, 45)$ degrees with a very high real part and a very low imaginary part to arrive at $(80, 10)$ degrees with a permittivity similar to the one determined in the upper domain.
For the "horiz" case, we retrieve a similar estimation of the second permittivity on the lower domain, but in the other domains we are more likely able to find back the value of ϵ_2: especially in $[65, 80] \times [10, 45]$ degrees and its symmetric.
As with the previous method when the change of permittivity is horizontal we are able to fully retrieve the permittivity close to the central edge of the dihedral for high incidence angles. Again it seems that the estimation of the permittivity outside this domain is ruled by a mixing law.

Second set of simulation: From the second set of simulations, the inverted permittivities are presented in Fig. 3.8 and in Fig. 3.9. The figures are evolving with the percentage of the surface taken by ϵ_2 within one plate. We can see for ϵ_1 that the domain $[10, 60] \times [10, 45]$ degrees and its symmetric allow to generally retrieve a correct value. As the incidence angles increase, we get either erroneous or no solutions for the cases of 20% and 50% of ϵ_2. This is especially true in the $[45, 80] \times [45, 80]$ degrees where ϵ_1 value is overestimated. At 80%, this phenomenon is less important as we begin to see the correct value near of 65 degrees. However there is still a strip of overestimated ϵ_1 at $[45, 50]$ degrees.
For ϵ_2, we observe an increasing estimation of ϵ_2 as it takes more and more surface on the plate. At first, it is localised at high incidence angles near 80 degrees. Then, for the 50% case, the estimation of ϵ_2 can be done over $[60, 80] \times [10, 45]$ degrees and the symmettrical region. At 80% this area extends to $[50, 80] \times [10, 80]$ and its symmetric. Outside these domains, we get at 20% few combinations where ϵ_3 is correctly estimated (mainly near 50 degrees), then with 50% and 80% we get closer and closer to ϵ_2 value.

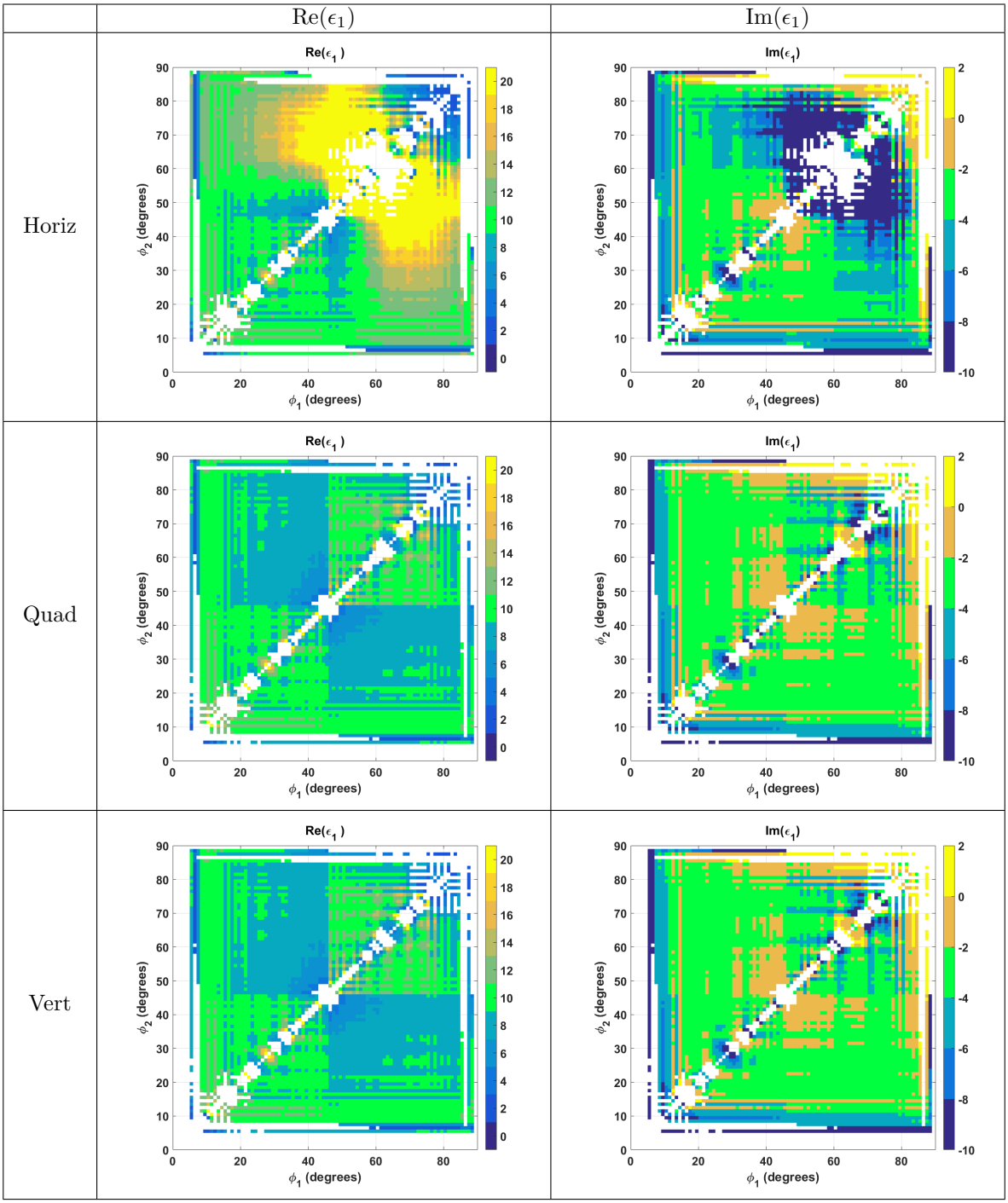

Figure 3.6 – Real and imaginary parts for ϵ_1 at 1 GHz for the different structures from the first set of simulations.

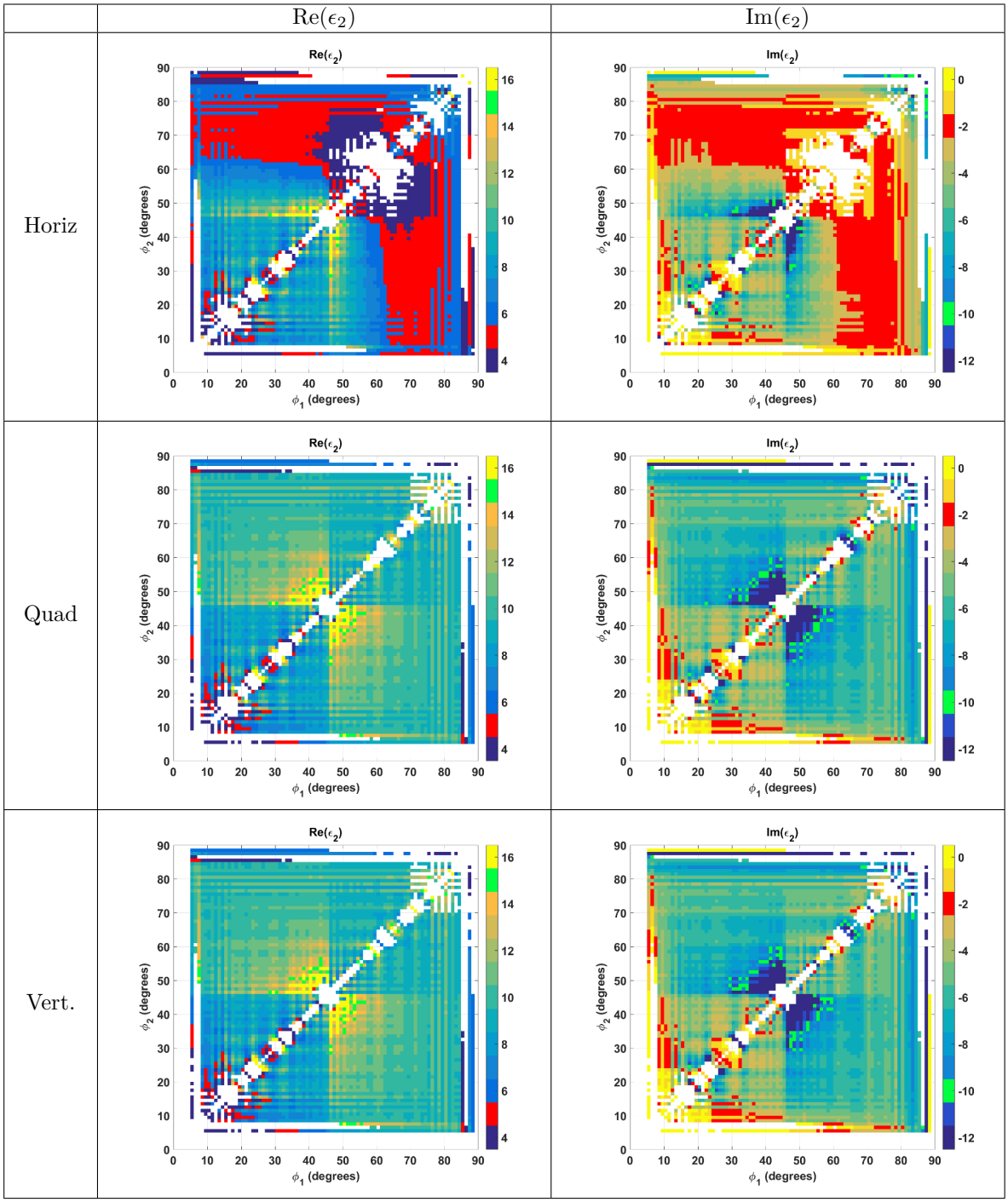

Figure 3.7 – Real and imaginary parts for the second permittivity at 1 GHz for the different structures from the first set of simulations.

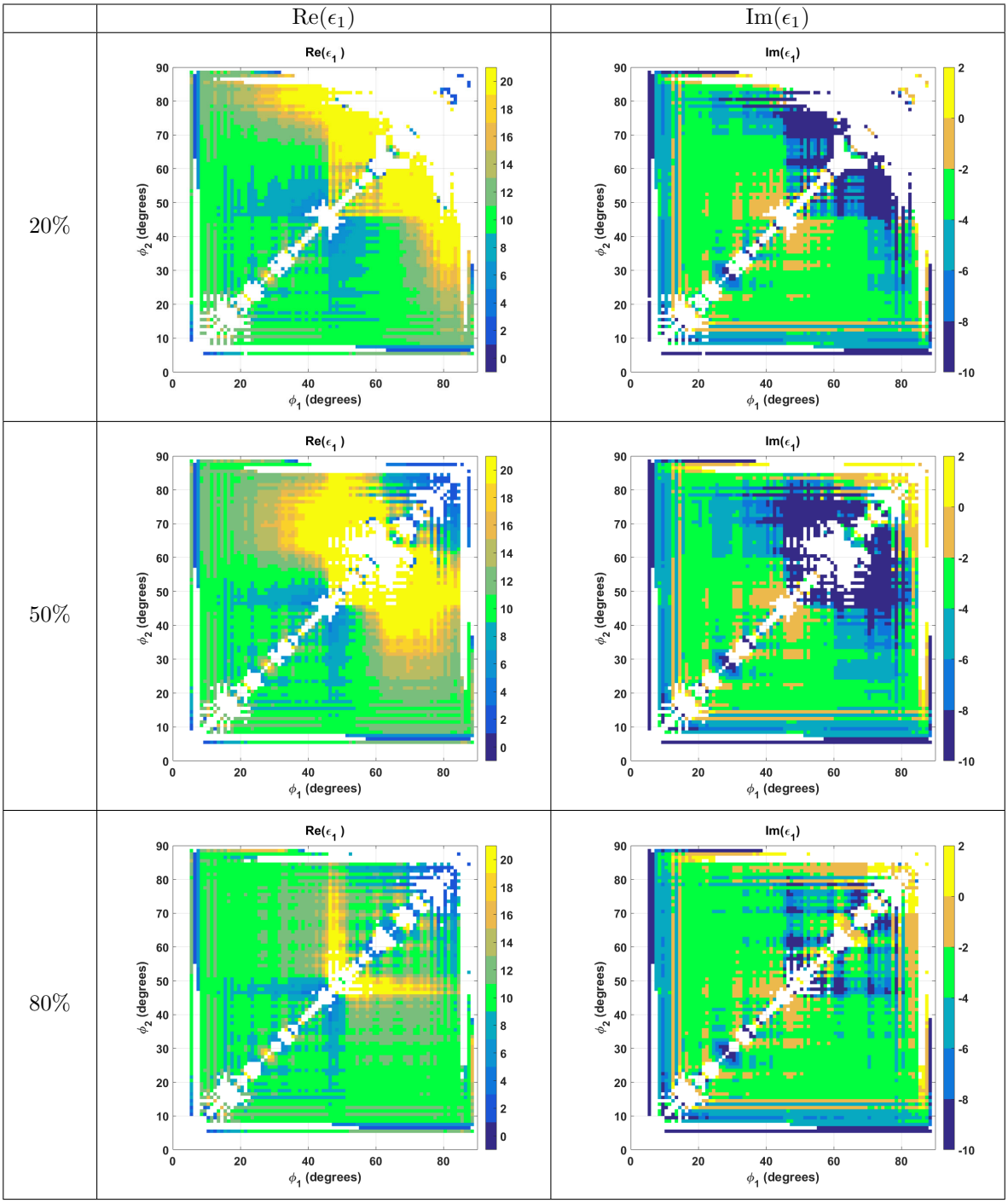

Figure 3.8 – Real and imaginary parts for ϵ_1 at 1 GHz for the different structures from the second set of simulations.

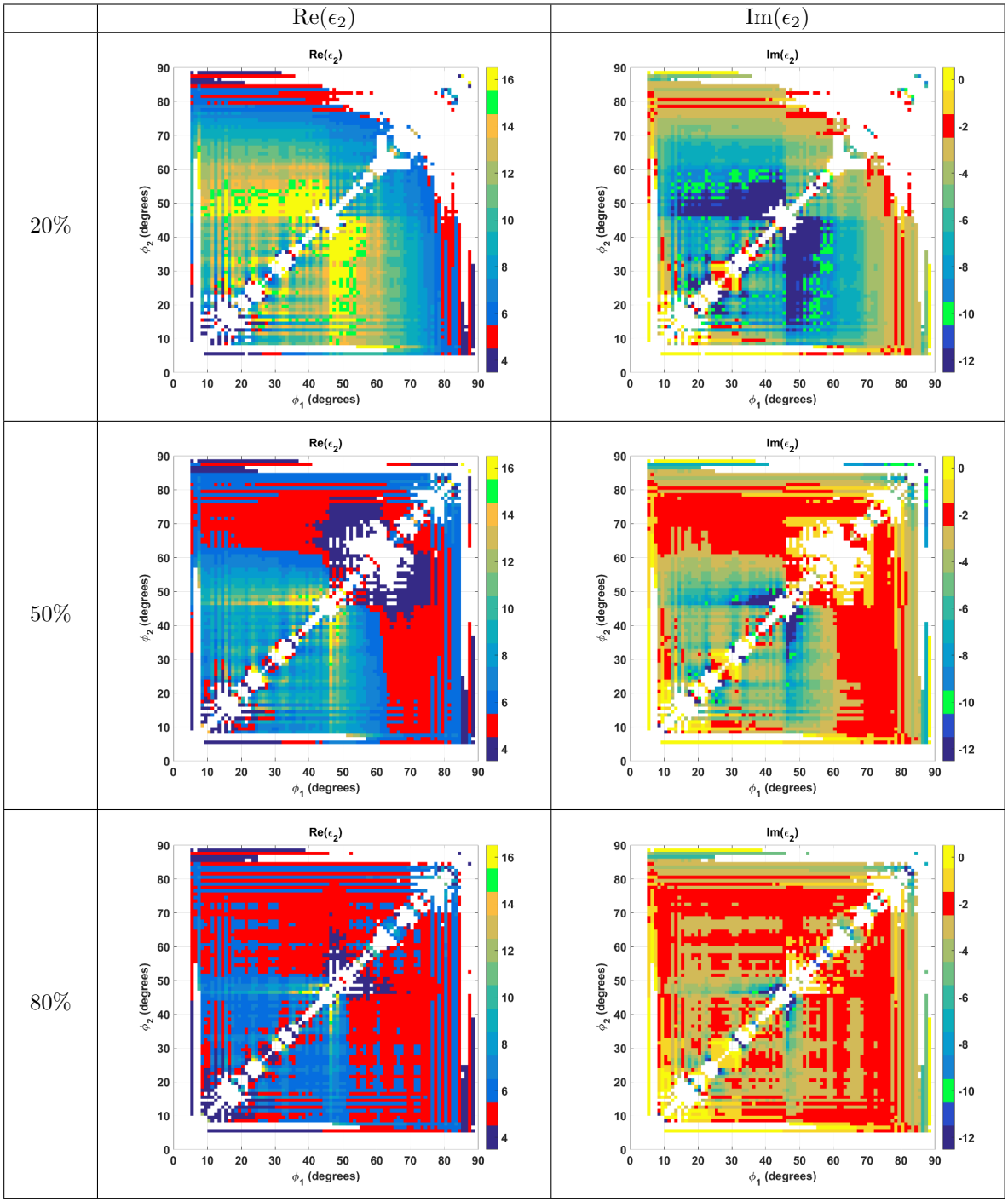

Figure 3.9 – Real and imaginary parts for the second permittivity at 1 GHz for the different structures from the second set of simulations.

3.2.2 Parameters of measurement device

Here, we look at the impact of the position and orientation of the measuring device.

Incidence angle influence

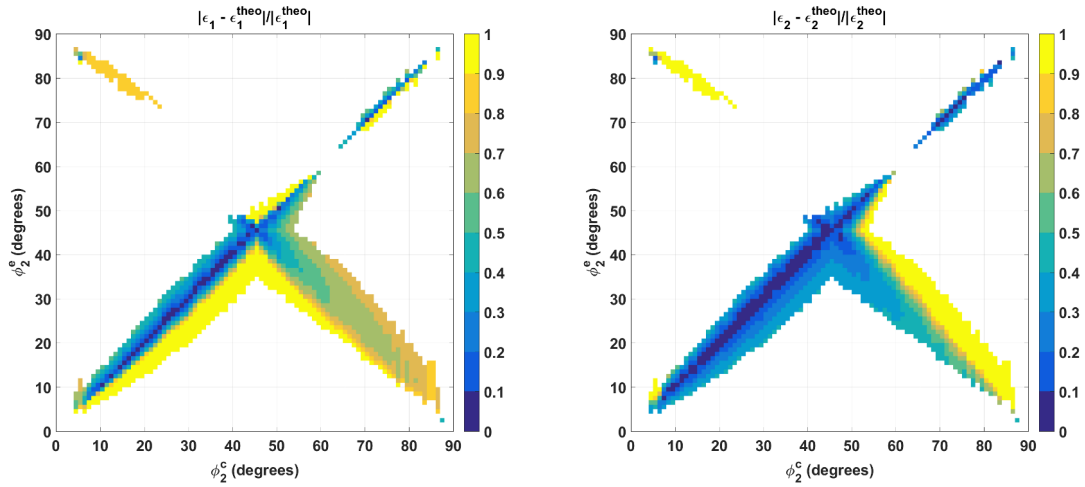

Figure 3.10 – Relative error for ϵ_1 and ϵ_2 given ϕ_2 error at 1 GHz and $\phi_1 = 60$ degrees.

As in subsection 2.3.2 we look here at the influence of the incidence angle on the results. However, we now have two incidence angles to analyse. Thus we will first set ϕ_1 and make the analysis like in 2.3.2 assuming there is no error made on ϕ_1. Then we will set also ϕ_2 and look at the error on the results given errors on both angles. We rely on the symmetry between angles observed in 3.2.1 to get identical results for ϕ_2 relatively to ϕ_1.

We set ϕ_1 to 60 degrees. This choice was made regarding subsection 2.3.2 and also regarding Fig. 3.3 where $\phi_1 = 60$ degrees implies to have correct results at 1 GHz. Then we analyse the relative error made on each permittivity for different ϕ_2 and given an error on ϕ_2 (notations are identical to the one in 2.3.2). In Fig. 3.10, the line $\phi_2^e = \phi_2^c$ is the location of the minimum of relative error as it corresponds to the ideal use of the method. If we step outside this line, the relative error quickly increases especially for angles above 55 degrees. Below this value, the method is more flexible in the $[20, 45]$ degrees interval. For ϵ_1, it is quite interesting to see that in this range, it is better to overestimate the incidence angle than to underestimate it as the variation of the error is slower in the first case. For ϵ_2, it seems to be the opposite case.
It is also interesting to see that for $\phi_2^c \in [45, 85]$ degrees we can get another permittivity couple if we compute the solution using $\phi_2^e \approx 90 - \phi_2^c$.

In Fig. 3.11 and Fig. 3.12, we set $\phi_1^c = 60$ and $\phi_2^c = 50$ degrees and we look at the variation of the estimated permittivities with an error on incidence angles $\Delta\phi_1 = \phi_1^e - \phi_1^c$ and $\Delta\phi_2 = \phi_2^e - \phi_2^c$ of ± 10 degrees.
From these figures, we see that the method allows a narrow strip of errors: from $(\Delta\phi_1, \Delta\phi_2) = (-5, -4)^\circ$ to $(\Delta\phi_1, \Delta\phi_2) = (6, 6)^\circ$, a line of correct permittivities could be observed. It means that if the incidence angle is estimated wrongly due to a small constant offset, results are still ok. Outside this strip, we see anothet strip that might be interesting: from $(\Delta\phi_1, \Delta\phi_2) = (-10, 4)^\circ$ to $(\Delta\phi_1, \Delta\phi_2) = (-4, -5)^\circ$. In this strip, we might find results quite close to the wanted permittivities. The imaginary part of ϵ_1 and the real part of ϵ_2 are correctly retrieved. On the other side we underestimate the real part of ϵ_1 (around 8) and the imaginary part of ϵ_2. In the strip defined by $(\Delta\phi_1, \Delta\phi_2) = (-10, -4)^\circ$ to $(\Delta\phi_1, \Delta\phi_2) = (-4, -5)^\circ$, the inverse phenomenon is observed.

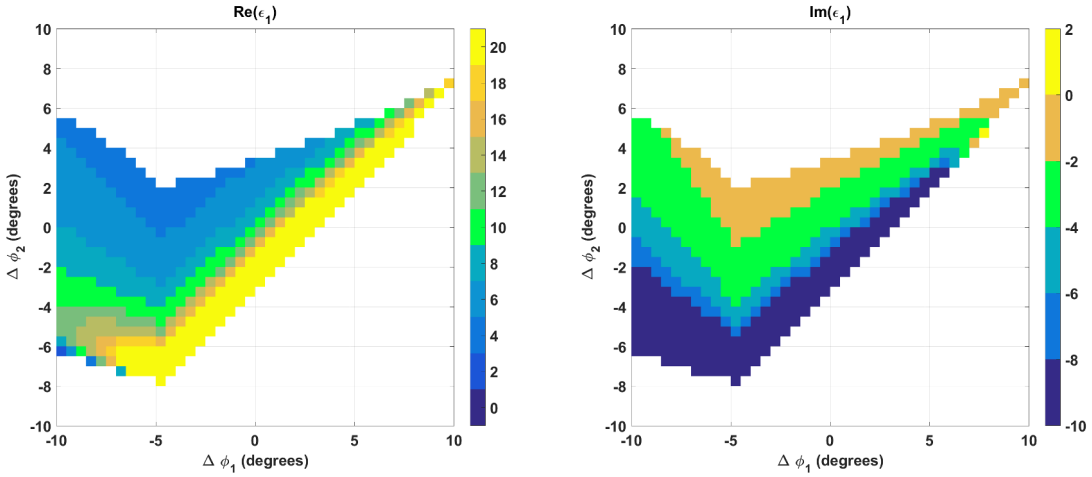

Figure 3.11 – ϵ_1 given ϕ_1 and ϕ_2 errors at 1 GHz and $\phi_1 = 60$ and $\phi_2 = 50$ degrees.

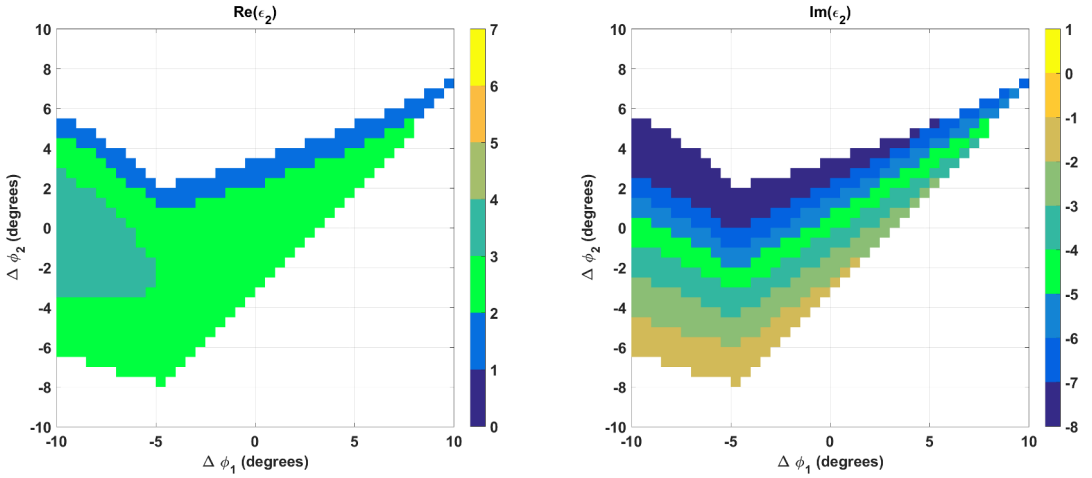

Figure 3.12 – ϵ_2 given ϕ_1 and ϕ_2 errors at 1 GHz and $\phi_1 = 60$ and $\phi_2 = 50$ degrees.

Outisde these strips of results, no physical results are found: having a positive $\Delta\phi_1$ makes the method more sensitive to $\Delta\phi_2$ error as the domain of physical results is reduced.
Anyways, the incidence angle looks to be again a critical parameter as few degrees off may lead to a large error.

Non-null azimuth angle

In 2.3.2 we have seen that by normalizing the backscattered electric field by its corresponding PEC equivalent, we can still invert even with a change in azimuth. This was due to the fact that we can retrieve through this normalization step the double bounce equation in HH and VV. Thus by taking the same simulation and normalization step at 1 GHz, we are again able to invert with the new method. Fig. 3.13 shows the proportion of correct, close and absence of results at 1 GHz versus the azimuth angle. For the close curve, no change with the variation of azimuth can be observed for either ϵ_1 or ϵ_2. However if for ϵ_2 the amount of correct results remains identical over the azimuth range considered, it is not the case for ϵ_1. For this permittivity at an azimuth angle of ± 6 degrees, changes start to be really noticeable without being dramatic as we get around 75% of correct results. The percentage of "no result" is around 6 - 7 % whatever the azimuth angle.
These results show a robustness to a change in azimuth like with the first method provided that

we apply an adapted normalization step. Likewise, the same remark can be done: we could also have cross different azimuth normalized data to perform the inversion.

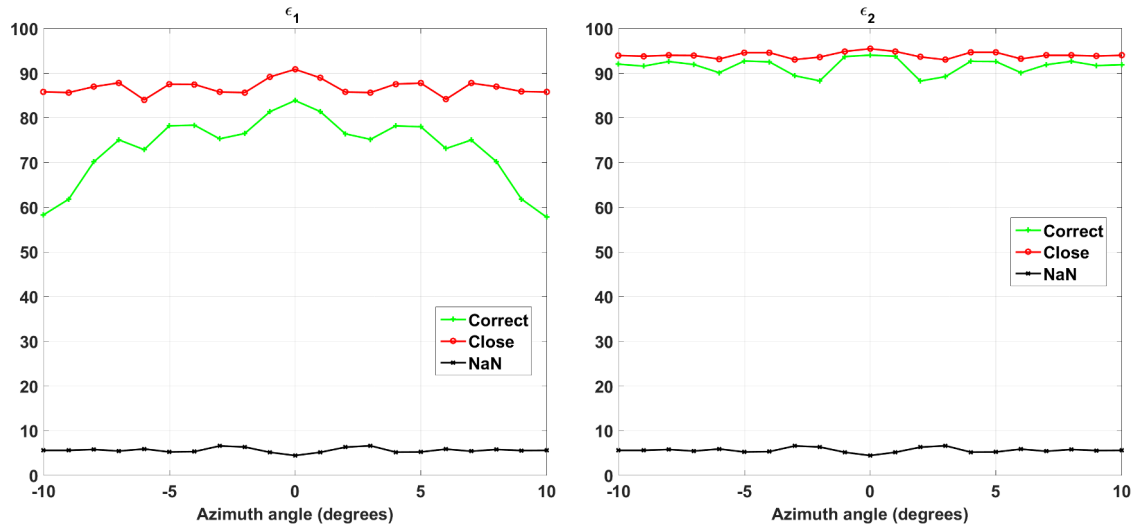

Figure 3.13 – Proportion of correct, close and no results for ϵ_1 and ϵ_2 at 1 GHz for several azimuth angles.

Roll angle

In this subsection we analyse the influence of the method to a roll rotation (*i.e.* a rotation around the line-of-sight) of the emitter-receiver device as in 2.3.2. Results in terms of percentage of correct, close and absence of results are provided in Fig. 3.14.

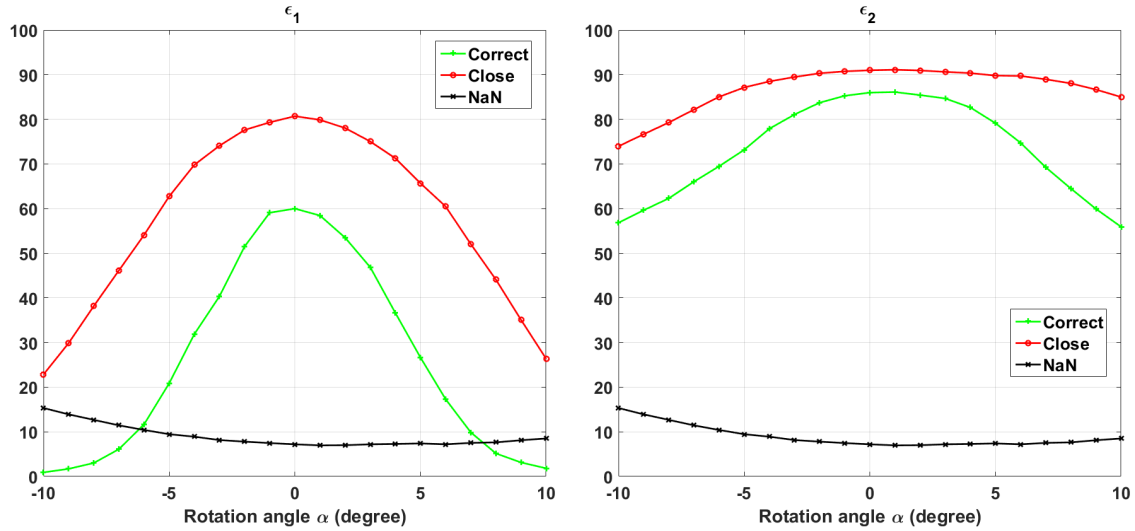

Figure 3.14 – Proportion of correct, close and no results for ϵ_1 and ϵ_2 at 1 GHz for several auxilary angles.

From those figures, we can notice that this new method is as robust to a roll rotation of the device as the method exposed in the previous chapter. For ϵ_1, we get more than 20 % of correct

results within ± 5 degrees and more than 60 % of close results in the same range. In the case of ϵ_2 we have for all the rotation angle simulated more than 55 % of correct results and more than 70% of close results. Those results are in agreement with the meaning of the rotation angle: as we rotate the device, we collect more and more from the other polarisation degrading more and more the results. The importance of the degradation of the results seems to be bound to the value of permittivity. As the illuminated dimensions of the plates are equals, one might assume that as ϵ_2 is in modulus lower than ϵ_1 its calculation is more robust to this change.

3.3 Summary of the method

Fig. 3.15 represents the process to find back the permittivities using the method developed in this chapter.
Two measurements of HH electric field at two different incidence angles are needed to make this method work. As seen, inversion is still dependent on the electrical dimension. If as the previous method, the incidence angle and the dihedral angle are still very critical parameters, the method is flexible with changes in azimuth and auxiliary angles. A noticeable difference with the previous method is the behaviour to a composite permittivity structure. Here, we do not have an evolution from one permittivity to another along the incidence angle. We rather find a mixing law on one sub-domain angle and the rest is dealing with errors. Given the results from the study made on the influence of parameters, incidence angles (ϕ_1, ϕ_2) taken in crossed domains like $(\phi_1, \phi_2) \in [50, 75] \times [15, 40]$ degrees can provide the best results for this method.
Still one main drawback of this method is its necessity to normalise the backscattered electric field with the one from an equivalent PEC structure. To bypass this step, one could use the same approach as in [3, 4] and consider the ratio of co-polarised fields. We propose to develop this third method in the next chapter.

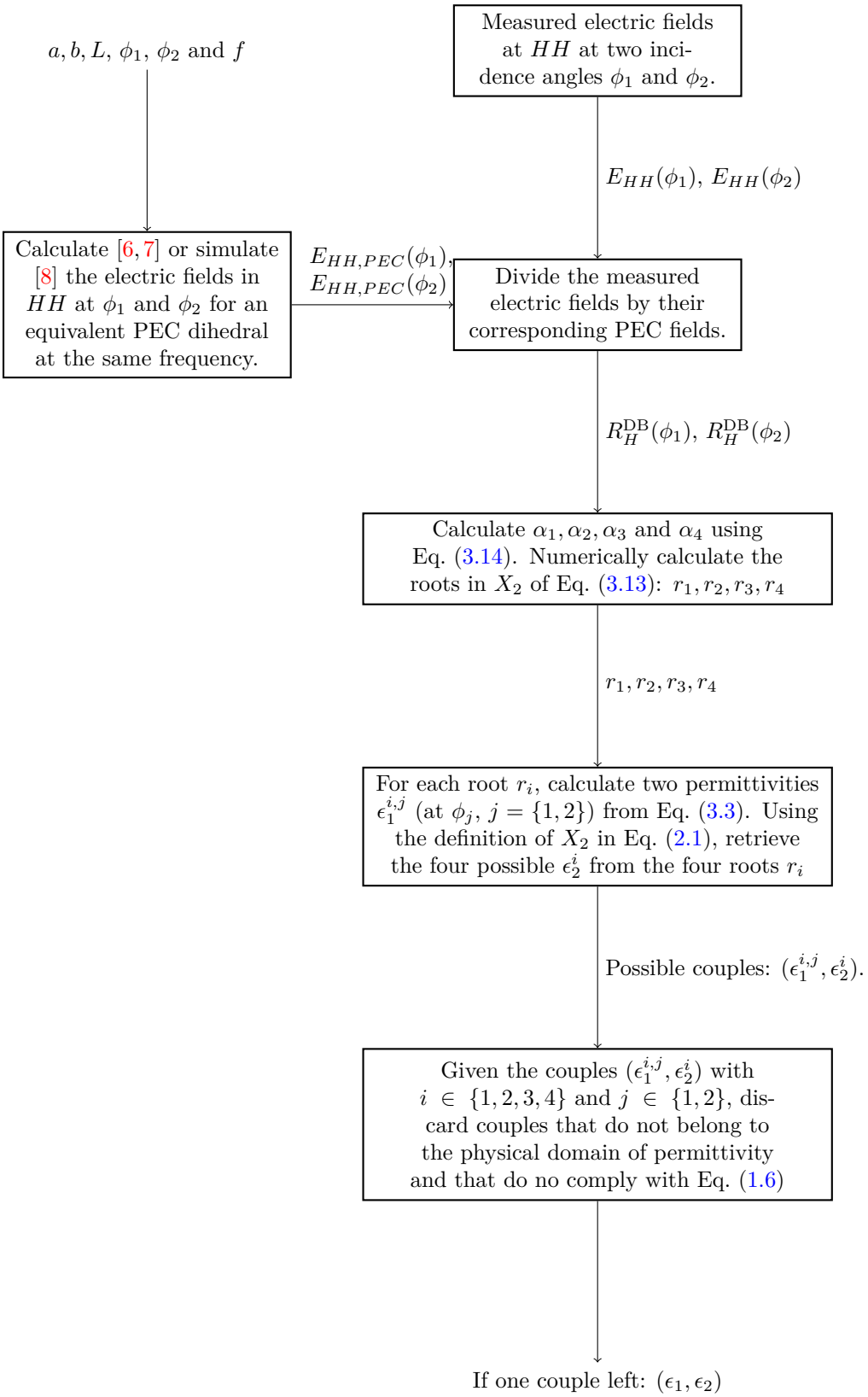

Figure 3.15 – Process of the method.

Chapter 4

Ratio method

The two previous methods both require double bounce reflection coefficients that can be difficult to obtain from measurements. To solve this problem, we normalise the fields by the ones from an equivalent PEC structure. This step implies that we have to know the structure dimensions which might not be the case in practice. To remove this normalisation step, we develop in this chapter a last method using the ratio between VV and HH fields [1].

4.1 Theory

As we may have a null or a minimal field at VV due to Brewster or Pseudo-Brewster angles, we will consider the ratio ρ^{DB} as : $\rho^{\mathrm{DB}} = \frac{R_V^{\mathrm{DB}}}{R_H^{\mathrm{DB}}}$. The assumption that $\frac{E_{VV}(\phi)}{E_{HH}(\phi)} \approx \rho^{\mathrm{DB}}$ relies on the fact that the double bounce component for a PEC dihedral differs from sign between HH and VV (see Eq. (2.11) and Eq. (2.12)).

So considering:

$$\rho^{\mathrm{DB}} = \frac{R_V^{\mathrm{DB}}}{R_H^{\mathrm{DB}}}, \tag{4.1}$$

we can substitute Eq. (2.3) and Eq. (2.5) expressions in Eq. (4.1) leading to:

$$\rho^{\mathrm{DB}} = \frac{((X_1^2+\sin^2\phi)\cos\phi - X_1)((X_2^2+\cos^2\phi)\sin\phi - X_2)}{((X_1^2+\sin^2\phi)\cos\phi + X_1)((X_2^2+\cos^2\phi)\sin\phi + X_2)} \frac{(\cos\phi + X_1)(\sin\phi + X_2)}{(\cos\phi - X_1)(\sin\phi - X_2)}. \tag{4.2}$$

By multiplying ρ^{DB} in Eq. (4.2) by the polynomial denominator of its right member we can have a polynomial equation:

$$\begin{aligned}\rho^{\mathrm{DB}}&\Big(\Big(X_1^2+\sin^2\phi\Big)\cos\phi + X_1\Big)\Big(\Big(X_2^2+\cos^2\phi\Big)\sin\phi + X_2\Big)(\cos\phi - X_1)(\sin\phi - X_2)\\ &- \Big(\Big(X_1^2+\sin^2\phi\Big)\cos\phi - X_1\Big)\Big(\Big(X_2^2+\cos^2\phi\Big)\sin\phi - X_2\Big)(\cos\phi + X_1)(\sin\phi + X_2) = 0\end{aligned} \tag{4.3}$$

that can be factored by $(X_2^2 - \sin^2\phi)(X_1^2 - \cos^2\phi)$. So it leads us to:

$$pX_1X_2 + qX_1 + rX_2 + s = 0 \tag{4.4}$$

where

$$\begin{aligned} p &= (\rho^{\mathrm{DB}} - 1)\sin\phi\cos\phi \\ q &= (\rho^{\mathrm{DB}} + 1)\cos^3\phi \\ r &= (\rho^{\mathrm{DB}} + 1)\sin^3\phi \\ s &= (\rho^{\mathrm{DB}} - 1)\cos^2\phi\sin^2\phi \end{aligned} \tag{4.5}$$

1. We thanks here Prof. Kamal Sarabandi from the University of Michigan for suggesting this approach.

Eq. (4.4), alone, provides an infinity of (ϵ_1, ϵ_2) solutions.

This equation is similar to Eq. (3.2) such that we will apply the same process of resolution. We consider two measurements $(\rho_1^{\mathrm{DB}}, \rho_2^{\mathrm{DB}})$ made at (ϕ_1, ϕ_2). As we have:

$$\epsilon_1 = X_1^2 + \sin^2\phi = \left(\frac{rX_2 + s}{pX_2 + q}\right)^2 + \sin^2\phi \tag{4.6}$$

looking alike to Eq. (3.3), we obtain a similar equation as Eq. (3.6) with the coefficients defined in Eqs. (4.7).

$$
\begin{aligned}
a &= \sin^2\phi_1 \sin^2\phi_2 \Big(\sin^2\phi_1 \cos^2\phi_2 (\rho_2^{\mathrm{DB}} - 1)^2 \big((\rho_1^{\mathrm{DB}} + 1)^2 - 4\rho_1^{\mathrm{DB}} \cos^2\phi_1\big) - \sin^2\phi_2 \cos^2\phi_1 (\rho_1^{\mathrm{DB}} - 1)^2 \big((\rho_2^{\mathrm{DB}} + 1)^2 - 4\rho_2^{\mathrm{DB}} \cos^2\phi_2\big) \Big) \\
b &= 2 \sin\phi_2 \sin^2\phi_1 \cos^2\phi_2 (\rho_2^{\mathrm{DB}} - 1)(\rho_2^{\mathrm{DB}} + 1) \Big(\sin^2\phi_1 \cos^2\phi_2 \big(-4\rho_1^{\mathrm{DB}} \cos^2\phi_1 + (\rho_1^{\mathrm{DB}} + 1)^2\big) - (\rho_1^{\mathrm{DB}} - 1)^2 \cos^2\phi_1 \sin^2\phi_2 \Big) \\
c &= 2 \sin\phi_1 \cos^2\phi_1 \sin^2\phi_2 (\rho_1^{\mathrm{DB}} - 1)(\rho_1^{\mathrm{DB}} + 1) \Big(\cos^2\phi_1 \sin^2\phi_2 \big(4\rho_2^{\mathrm{DB}} \cos^2\phi_2 - (\rho_2^{\mathrm{DB}} + 1)^2\big) + \sin^2\phi_1 \cos^2\phi_2 (\rho_2^{\mathrm{DB}} - 1)^2 \Big) \\
d &= 4 \sin\phi_1 \cos^2\phi_1 \sin\phi_2 \cos^2\phi_2 (\rho_1^{\mathrm{DB}} - 1)(\rho_1^{\mathrm{DB}} + 1)(\rho_2^{\mathrm{DB}} - 1)(\rho_2^{\mathrm{DB}} + 1)(\cos^2\phi_2 - \cos^2\phi_1) \\
e &= 2(\rho_1^{\mathrm{DB}} - 1)(\rho_1^{\mathrm{DB}} + 1) \cos^2\phi_1 \sin\phi_1 \cos^4\phi_2 \Big(\sin^2\phi_1 \cos^2\phi_2 (\rho_2^{\mathrm{DB}} + 1)^2 - \cos^2\phi_1 \sin^2\phi_2 \big(4\rho_2^{\mathrm{DB}} \cos^2\phi_2 + (\rho_2^{\mathrm{DB}} - 1)^2\big) \Big) \\
f &= 2(\rho_2^{\mathrm{DB}} - 1)(\rho_2^{\mathrm{DB}} + 1) \cos^4\phi_1 \cos^2\phi_2 \sin\phi_2 \Big(\sin^2\phi_1 \cos^2\phi_2 \big(4\rho_1^{\mathrm{DB}} \cos^2\phi_1 + (\rho_1^{\mathrm{DB}} - 1)^2\big) - (\rho_1^{\mathrm{DB}} + 1)^2 \sin^2\phi_2 \cos^2\phi_1 \big) \Big) \\
g &= \sin^2\phi_1 \cos^4\phi_2 \Big(\sin^2\phi_1 \cos^2\phi_2 (\rho_2^{\mathrm{DB}} + 1)^2 \big((\rho_1^{\mathrm{DB}} + 1)^2 - 4\rho_1^{\mathrm{DB}} \cos^2\phi_1\big) - \sin^2\phi_2 \cos^2\phi_1 (\rho_1^{\mathrm{DB}} - 1)^2 \big((\rho_2^{\mathrm{DB}} - 1)^2 + 4\cos^2\phi_2 \rho_2^{\mathrm{DB}}\big) \Big) \\
h &= \cos^4\phi_1 \sin^2\phi_2 \Big(\cos^2\phi_2 \sin^2\phi_1 (\rho_2^{\mathrm{DB}} - 1)^2 \big(4\rho_1^{\mathrm{DB}} \cos^2\phi_1 + (\rho_1^{\mathrm{DB}} - 1)^2\big) + \cos^2\phi_1 \sin^2\phi_2 (\rho_1^{\mathrm{DB}} + 1)^2 \big(4\rho_2^{\mathrm{DB}} \cos^2\phi_2 - (\rho_2^{\mathrm{DB}} + 1)^2\big) \Big) \\
k &= \cos^4\phi_1 \cos^4\phi_2 \Big(\sin^2\phi_1 \cos^2\phi_2 (\rho_2^{\mathrm{DB}} + 1)^2 \big(4\rho_1^{\mathrm{DB}} \cos^2\phi_1 + (\rho_1^{\mathrm{DB}} - 1)^2\big) - \sin^2\phi_2 \cos^2\phi_1 (\rho_1^{\mathrm{DB}} + 1)^2 \big(4\rho_2^{\mathrm{DB}} \cos^2\phi_2 + (\rho_2^{\mathrm{DB}} - 1)^2\big) \Big)
\end{aligned}
\tag{4.7}
$$

Likewise in 3.1 we obtain an eight degree equation (Eq. (3.11)) in $\xi_2 = \sqrt{\epsilon_2 - \cos^2\phi_2}$ with an identical definition of $(A, B, C, D, E, F, G, H, I)$ regarding to $(a, b, c, d, e, f, g, h, k)$ as defined in Eqs. (3.12). Unlike in 3.1, we are unable to factorize further this eight degree equation.

From this eight degree equation, at least one of the eight roots should lead to ϵ_2. To do so, we numerically compute the eight candidates for ϵ_2. Then we use Eq. (4.4) at ϕ_1 and also at ϕ_2 to get the associated candidates in ϵ_1. By doing so, we collect 16 candidates of (ϵ_1, ϵ_2). We filter out the couples that are not in the physical domain. We also keep couples that verify Eq. (4.1) at ϕ_1 and ϕ_2. This process summurized in Fig. 4.1 allows us to have for most of the cases a unique couple solution.

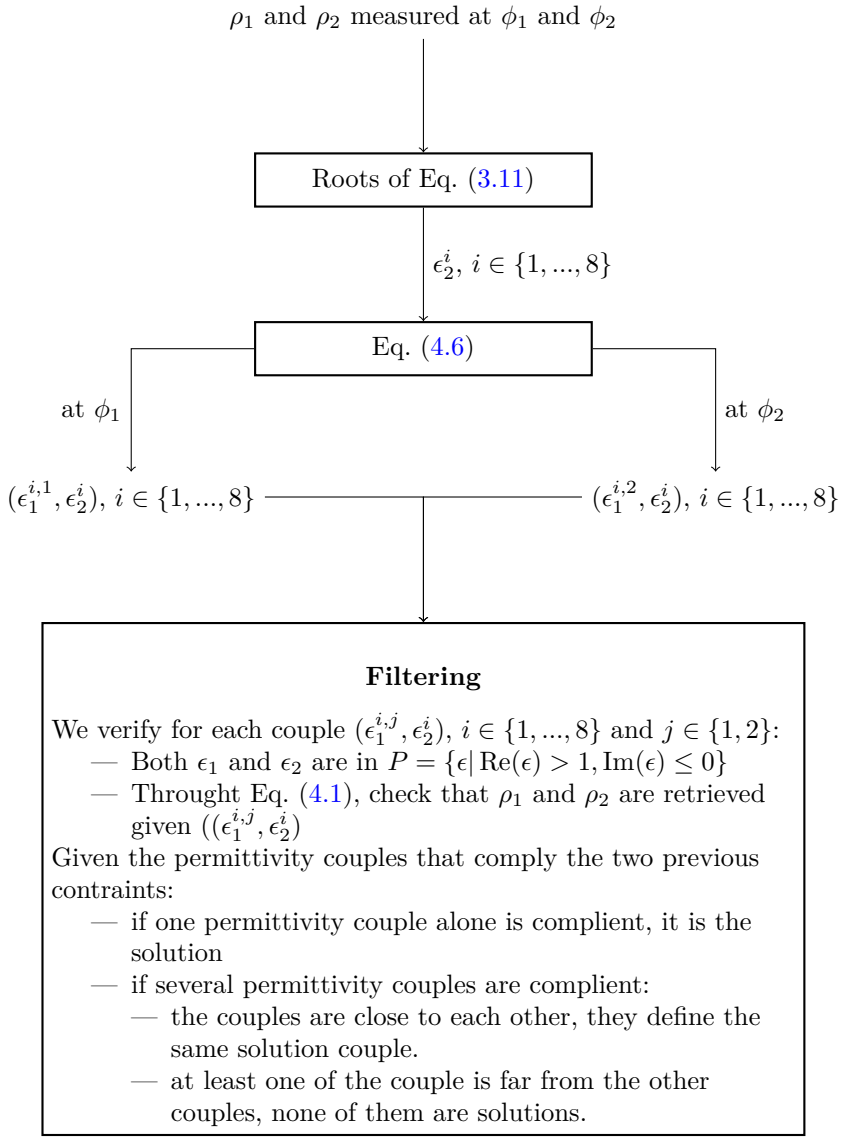

Figure 4.1 – Filtering process of the method.

4.2 Domain of validity: limits and range of possibilities

As in section 3.2 we use the data from section 2.3 to evaluate the method regarding to the object and the measuring device parameters.

4.2.1 Object parameters

First the object parameters will be dealt with. Studies on the geometry and the permittivity of the dihedral are carried out in this subsection.

Electrical dimension

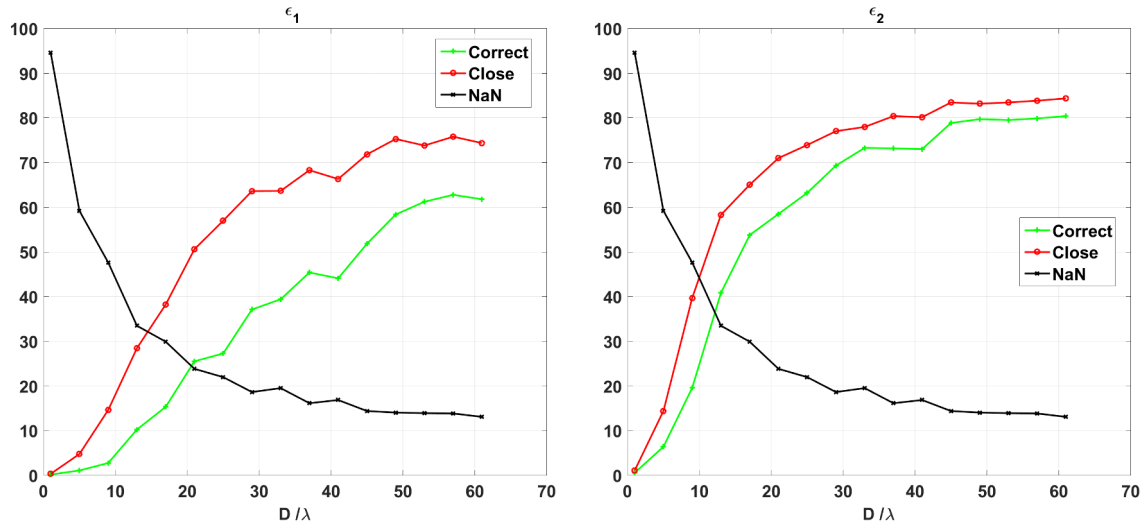

(a) For $\epsilon_1 = 10 - 3i$.

(b) For $\epsilon_2 = 2.4 - 4.5i$.

Figure 4.2 – Percentages of correct, close and absence of results with respect of the electrical dimension, for ϵ_1 (left) and ϵ_2 (right).

As in 2.3.1 and in 3.2.1, we analyse here the influence of the electrical dimension on the method. We use the same way to qualify it than the approach exposed in 3.2. The same dataset is used. As we are using a ratio between the double bounce coefficients in VV and HH and given the likelihood of the PEC backscattering signal between the polarization, there is now no need to normalize with a equivalent PEC signal. We directly compute the ratio VV over HH from the field data and invert it.

In fact we observe the exact same trends as the ones in 3.2.1. Again, the curve of correct results for ϵ_1 goes from few percent to 61% whereas for ϵ_2 it is from 6% to 80%. However the occurrence of no solution has increased compared to the previous method: it decreases from 60% of the data at $\frac{D}{\lambda} = 5$ to around 14% at $\frac{D}{\lambda} = 61$. It is explainable by the observation of the low and high incidence angles area where the method is having difficulties to find an acceptable permittivity pair as described in the following paragraph.

In Fig. 4.3, we draw the permittivities results in terms of real (Re) and imaginary (Im) parts for ϵ_1 and ϵ_2 at 0.3 and 1 GHz (corresponding respectively to a $\frac{D}{\lambda}$ equal to 18 and 60). The representation is made along the incidence angle (ϕ_1, ϕ_2). Note that colorbars of Fig. 4.3 are thresholded. The green colour corresponds to the interval containing the theoretical value.
From first sight, we can notice the axis of symmetry $\phi_1 = \phi_2$. As for the precedent method in 3.2.1, we observe the same influence of the frequency evolution: at 1 GHz we obtain more results

and homogeneous areas of correct results than at 0.3 GHz. Likewise there is a strip of 'no results' at $80 \times [0, 90]^\circ$. However, one difference with the one polarization method is the absence of results at low combinations angles ($[10, 30] \times [10, 30]^\circ$ at 1 GHz) and also for the high ones ($[70, 80] \times [70, 80]^\circ$ at 1 GHz). The phenomenon gets worse as the frequency decreases. So to have a good estimation of both permittivities, the best choice for (ϕ_1, ϕ_2) is to take it in, either $]50, 75[\times]15, 45[^\circ$ or its symmetric.

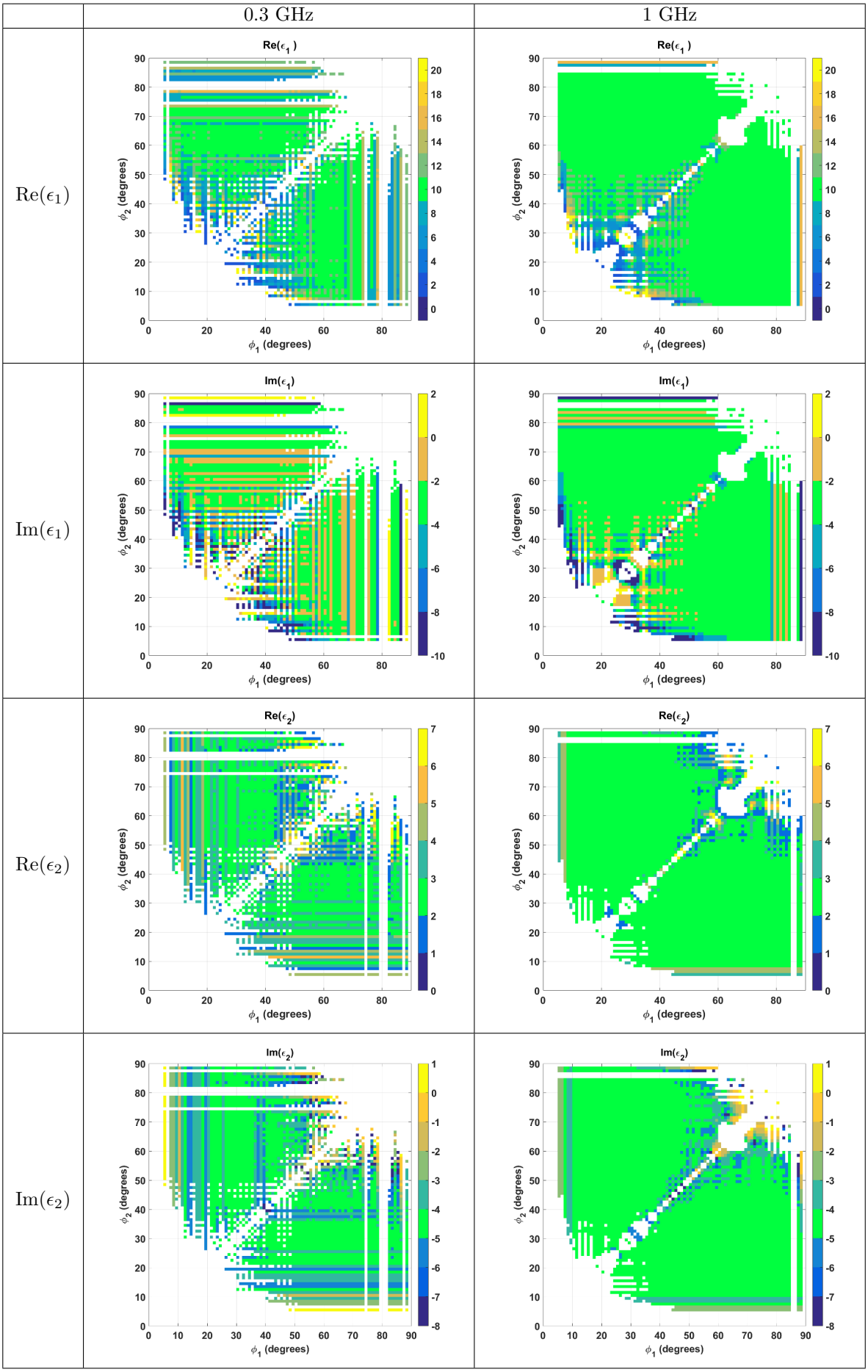

Figure 4.3 – Real and imaginary parts for ϵ_1 and ϵ_2 at 0.3 and 1 GHz.

Dihedral angle

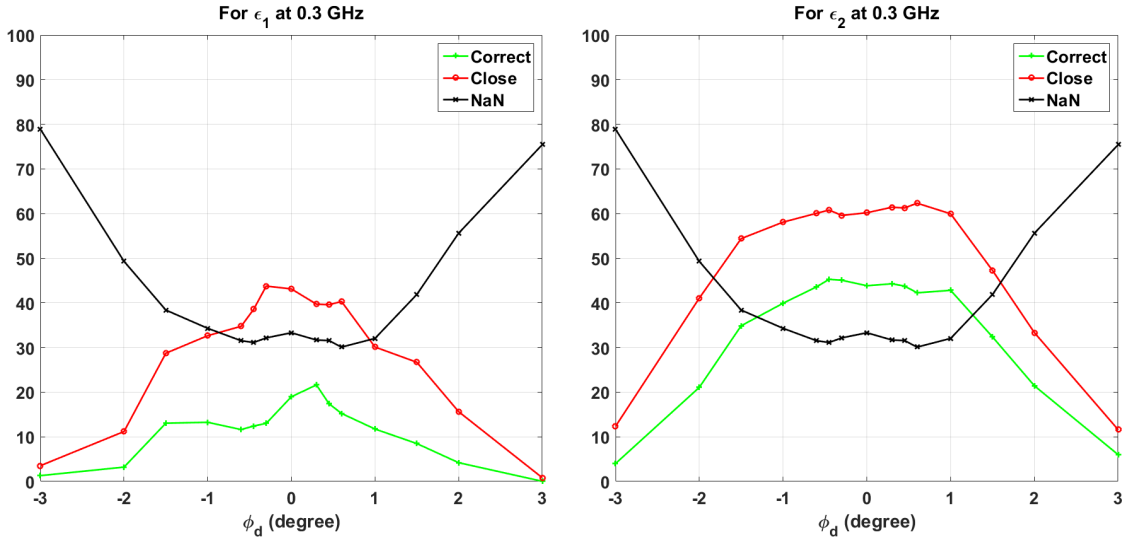

Figure 4.4 – Percentages for ϵ_1 and ϵ_2 of correct, close and absence of results at 0.3 GHz.

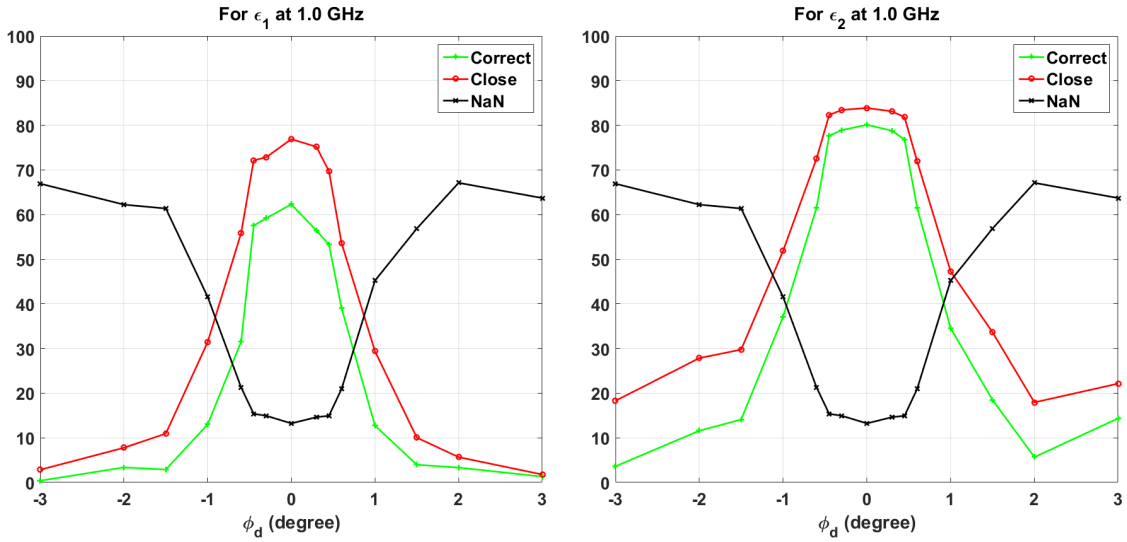

Figure 4.5 – Percentages for ϵ_1 and ϵ_2 of correct, close and absence of results at 1 GHz.

In Fig. 4.4 and Fig. 4.5, we plot the percentages of correct, close and absence of results for ϵ_1 and ϵ_2 at 0.3 and 1 GHz over the ϕ_d angle. From the first sight, we see strong similarities in shape with Fig. 3.4 and Fig. 3.5. Again at 0.3 GHz, we have at best 20 % of correct results for ϵ_1 and 45% for ϵ_2 and a minimum of 30% of no results. At 1 GHz, we find again curves with bell shape where we can expect 60% of correct results for the first permittivity and 80 % for the second. However, those good results are contained in $\phi_d \in [-1, 1]$ degrees. Outside the $[-1.5, 1.5]$ angle domain, the percentage of correct results for either ϵ_1 or ϵ_2 drops below 20%.
Again these simulations show the sensitivity of this method as the previous ones to the dihedral angle : if we have more than 1.5 degrees of difference to a perfect right angle, the ability to estimate a correct permittivity is reduced.

Mix of permittivities

We analyse our method regarding to the composition of permittivity using the sets of simulations exposed in 2.3.1.

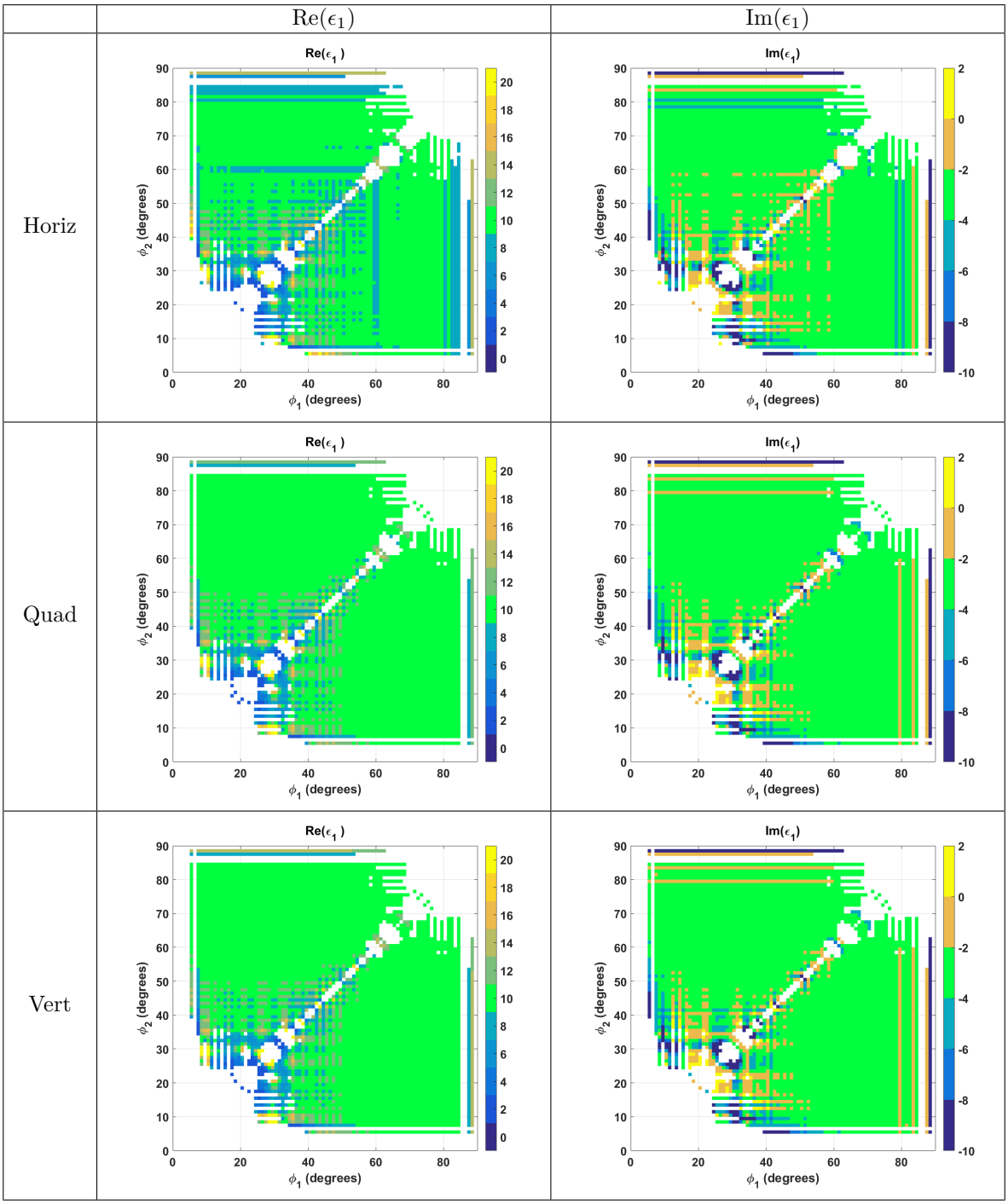

Figure 4.6 – Real and imaginary parts for ϵ_1 at 1 GHz for the different structures from the first set of simulations.

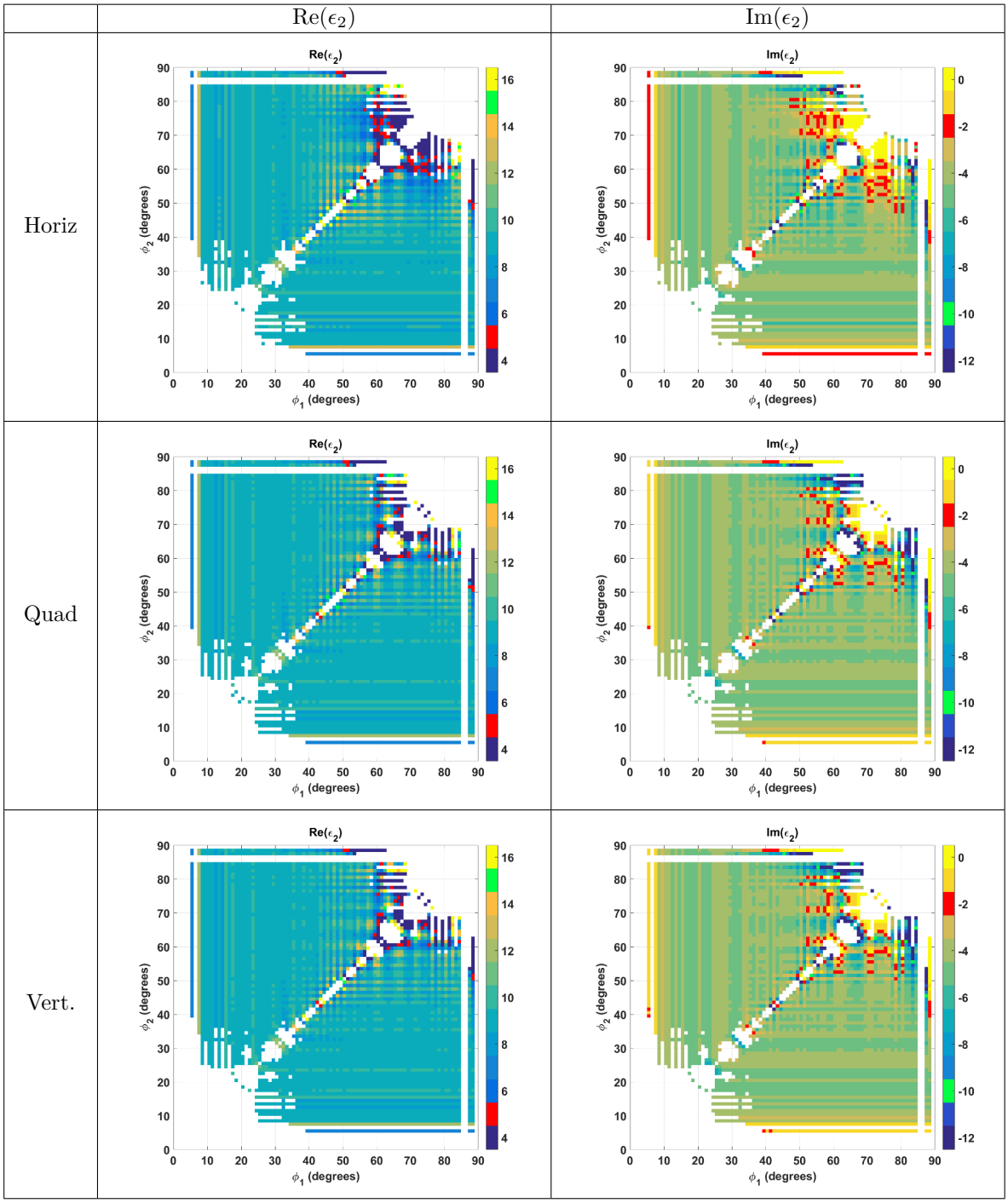

Figure 4.7 – Real and imaginary parts for the second permittivity at 1 GHz for the different structures from the first set of simulations.

First set of simulations: In Fig. 4.6 and Fig. 4.7 we observe very close results between the different simulation models. From the result on the first permittivity, we perfectly retrieve ϵ_1 value as we would from a dihedral composed of two homogeneous plates. Results are slightly less steady for the "horiz" structure or when we look at the domain $[35, 50] \times [10, 45]$ and its symmetric. For the second permittivity, we found a homogeneous permittivity around $9 - 5i$ which is roughly the

same as the effective permittivity calculated in Table. 2.1 for a volumetric fraction of 0.5. For few high incidence angles we estimate ϵ_2.

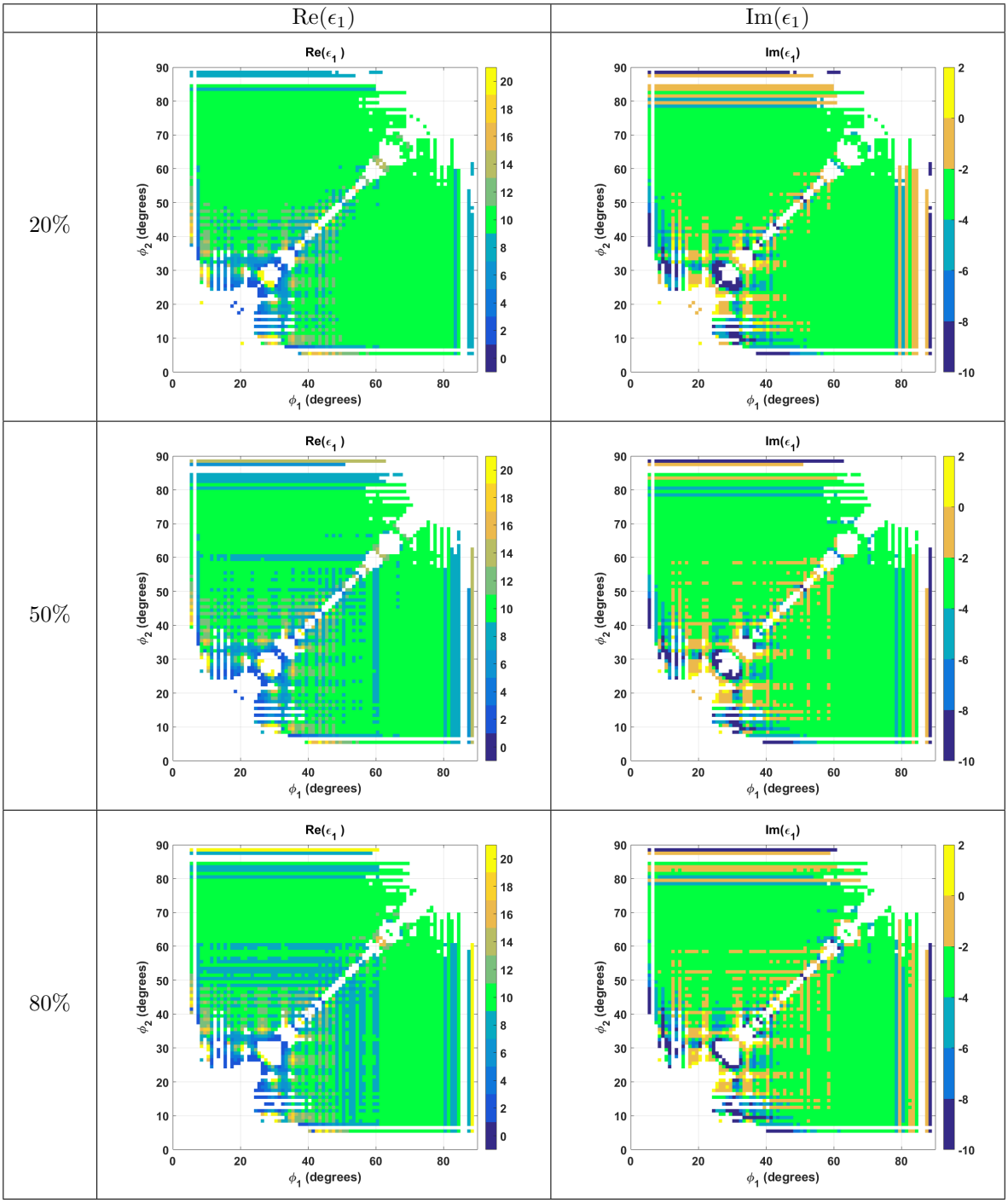

Figure 4.8 – Real and imaginary parts for ϵ_1 at 1 GHz for the different structures from the second set of simulations.

Second set of simulations: From the second set of simulations, we display the results we obtain for ϵ_1 and the second permittivity in Fig. 4.8 and Fig. 4.9. Again, in general, we retrieve ϵ_1 for

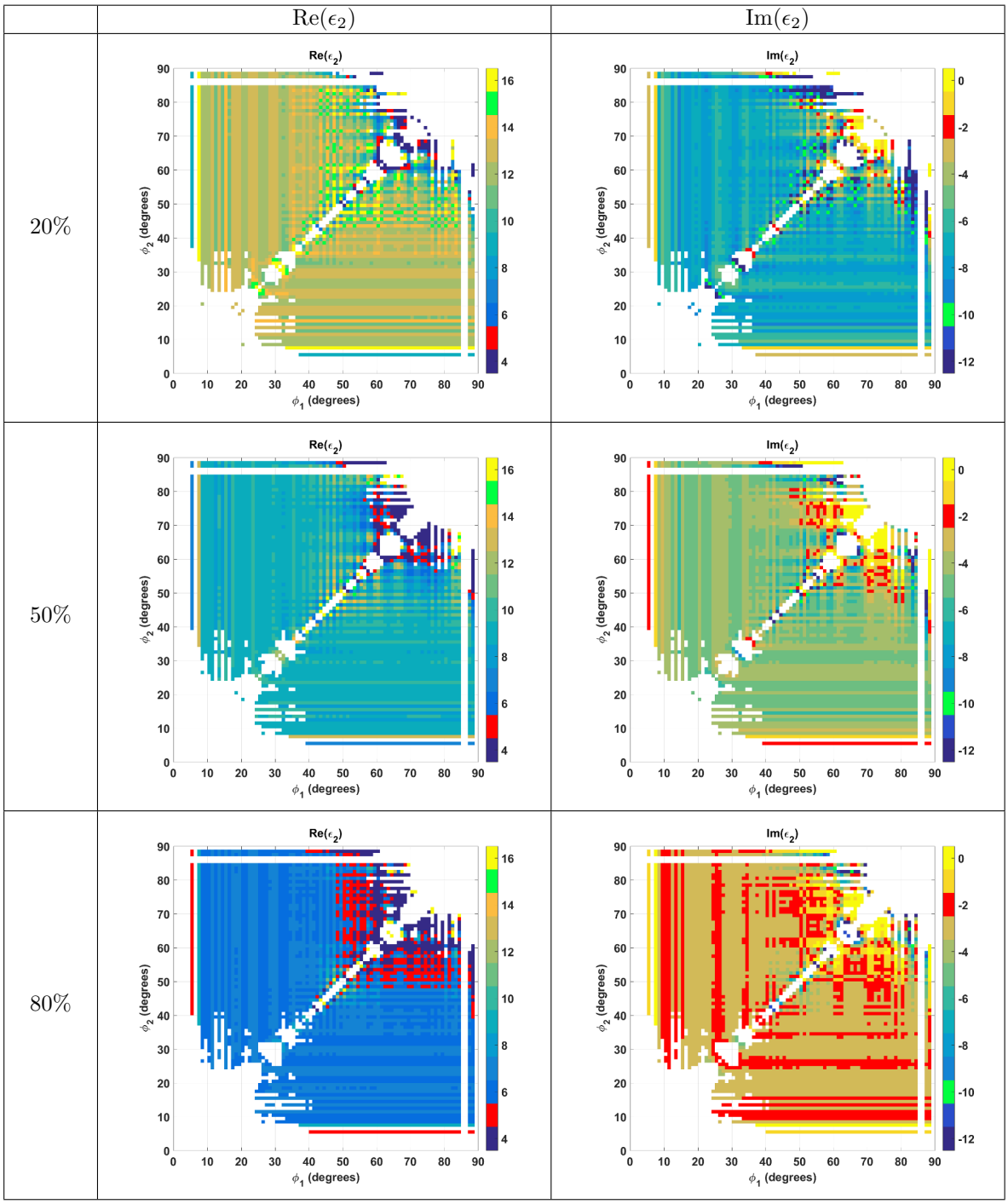

Figure 4.9 – Real and imaginary parts for the second permittivity at 1 GHz for the different structures from the second set of simulations.

most of the angle combinations even if for $[35, 60] \times [10, 45]$ it is less steady as a regular dihedral. With the second permittivity, we observe its evolution with the volumetric fraction growing from a value around $12 - 7i$ at 20% to a value near $6 - 3i$ at 80%. It looks like it follows the same rule as the ideal method exposed in 2.3.1 so that we estimate an efficient permittivity.
The results provided by these sets of simulations on this method are more similar to the ones from

the ideal method. The behaviour of the results is looking alike. ϵ_1 is always retrieve almost as if it was from a dihedral of two homogeneous surfaces. The second permittivity is following the mixing law observed in 2.3.1.

4.2.2 Parameters of measurement device

Here, we look at the impact of the position and orientation of the measuring device.

Incidence angle influence

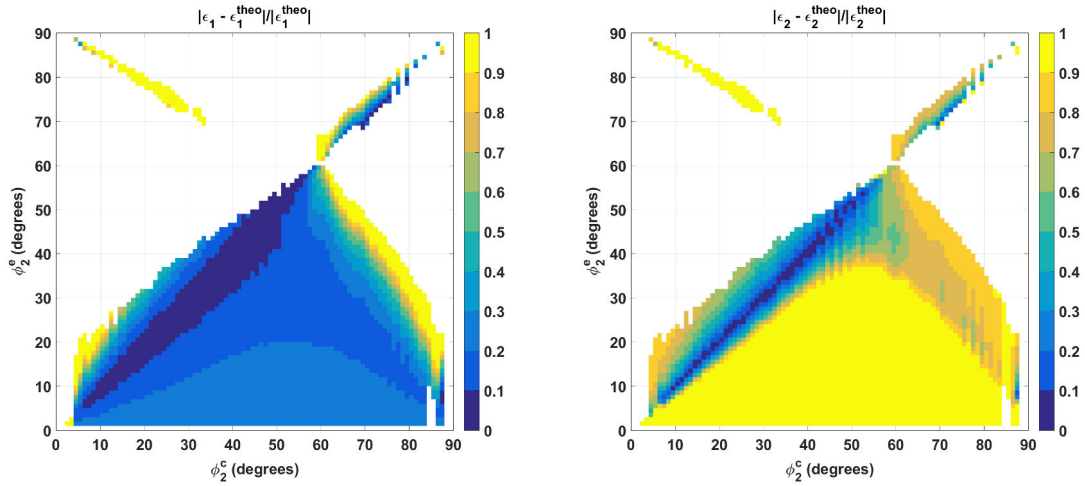

Figure 4.10 – Relative error for ϵ_1 and ϵ_2 given ϕ_2 error at 1 GHz and $\phi_1 = 60$ degrees.

In Fig. 4.10 we display the relative error on ϵ_1 and ϵ_2 at 1 GHz at $\phi_1 = 60$ degrees and given an error on ϕ_2 as in 3.2.2. We observe that ϵ_2 is quite sensitive to an error in ϕ_2 as if we step outside the $\phi_2^c = \phi_2^e$ line the error is increasing quickly. Only few degrees are allowed if we want the result to be under 10% of relative error. For ϵ_1, large area of acceptable angle errors is shown as long as we have ϕ_2^c less than 55 degrees as for ϕ_2^e. However these figures may partially reflect the behaviour of the method as we deal with two permittivities with a noticeable difference in modulus between them.
So we look at an example of error in terms of real and imaginary part at 1 GHz and at $(\phi_1, \phi_2) = (60, 50)$ degrees. In Fig. 4.11 and Fig. 4.12, we plot the results of ϵ_1 and ϵ_2 with all the combined $(\Delta\phi_1, \Delta\phi_2) \in [-10, 10] \times [-10, 10]^\circ$. We observe that ϵ_1 as the imaginary part of ϵ_2 are correctly retrieved for $(\Delta\phi_1, \Delta\phi_2) = ([-10, 3], 0)^\circ$. The error in the real part of ϵ_1 mainly varies with the error $\Delta\phi_2$ is is quite constant with $\Delta\phi_1$. In ϵ_2, the domain of correct real part is different from the domain in imaginary part. They intersect in a small domain $(\Delta\phi_1, \Delta\phi_2) = [-1, 1] \times [-1, 1]$. However the error in ϵ_2 seems to evolve in real part with $\Delta\phi_1$ and in imaginary part with $\Delta\phi_2$.

Non-null azimuth angle

In Fig. 4.13 we plot the magnitude of the resulting ratio from the backscattered fields simulated as explained in 2.3.2 for an azimuth angle in $[-10, 10]$ degrees. From it, we see that we retrieve the ratio of the double bounce coefficients for all the azimuth angles. This is supported by the previous analysis in 2.3.2 and 3.2.2 where we have been able to find back the double bounce coefficients by normalizing the electric fields by the fields from a PEC equivalent simulation.
In Fig. 4.14 we display the percentage of correct, close and absence of results for ϵ_1 and ϵ_2 at 1 GHz evolving with the azimuth angles. From these figures, we observe that the curve and so the estimation of the permittivities are quite constant over the azimuth range. It underlines the

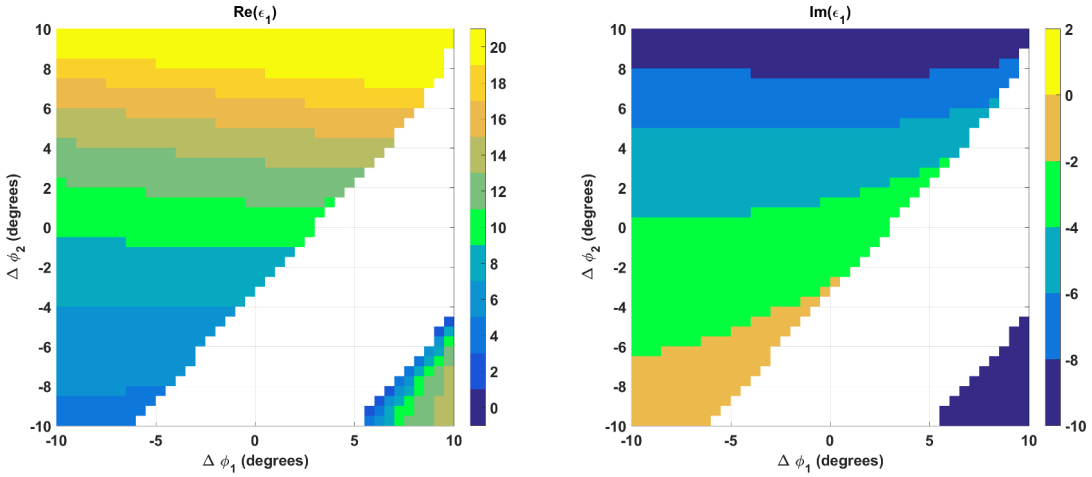

Figure 4.11 – ϵ_1 given ϕ_1 and ϕ_2 errors at 1 GHz and $\phi_1 = 60$ and $\phi_2 = 50$ degrees.

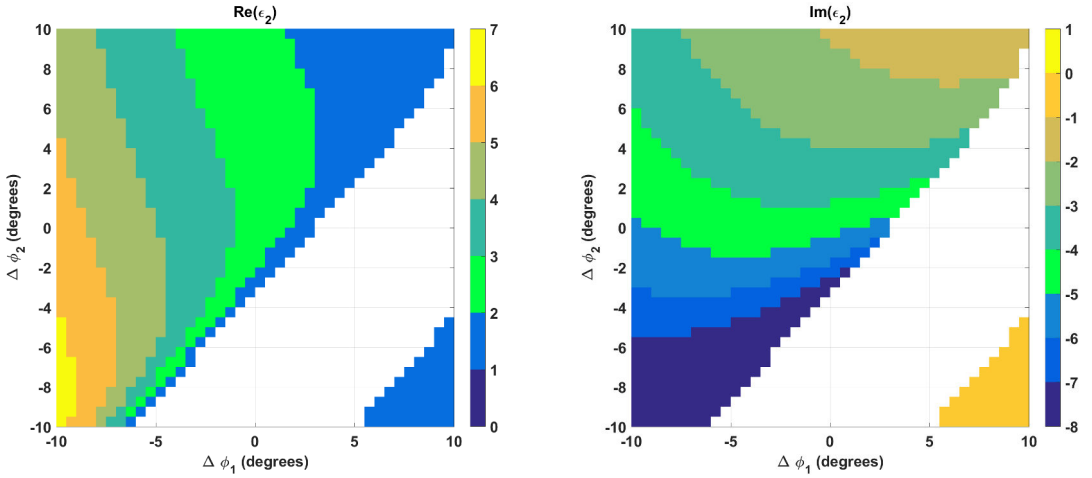

Figure 4.12 – ϵ_2 given ϕ_1 and ϕ_2 errors at 1 GHz and $\phi_1 = 60$ and $\phi_2 = 50$ degrees.

robustness of the method to a variation of the azimuth angle. Indeed for ϵ_1 we are still able to have more than 40% of correct results at an azimuth angle of ± 10 degrees. For ϵ_2 this percentage is not going below 70%. We notice that if the curves are quite constant, still we slightly get better results for an azimuth angle within the $[-2, 2]$ degrees. One can also notice that we get worse results than the previous method. This is due to the fact that this method finds more often no solution. Hence curves are more or less translated of 15 points between this method and the previous one.

Roll angle

We now take the simulated data from 2.3.2 to analyse the effect of the rotation angle on the method. In Fig. 4.15 are displayed the percentages of correct, close and absence of results for ϵ_1 and for ϵ_2 at 1 GHz. From these figures, we see bell curves for the correct and the close cases but also we notice that they are asymmetric. There is more no result cases for high positive rotation angles than for the negative ones and its is specially visible for ϵ_2 that we have more correct or close results for negative rotation angles. It may be seen for ϵ_1 if we look closely for instance at ± 4 degrees for the close curve or at ± 2 degrees for the correct results. ϵ_2 often correctly retrieved within the $[-3, 3]$ degrees range whereas ϵ_1 is restricted to $[-1, 1]$ degree. The percentage of no results is mainly below 20% except above ± 6 degrees.

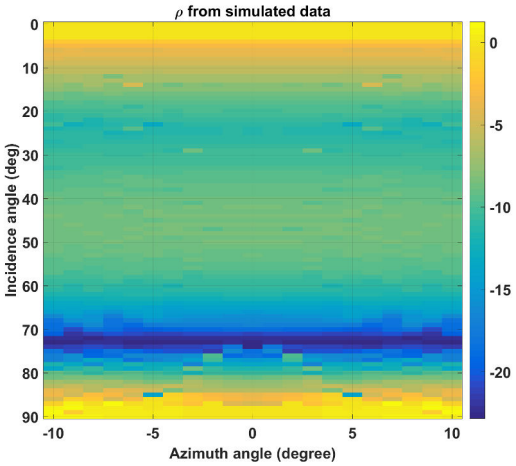

Figure 4.13 – Magnitude in dB of the ratio computed from backscattered fields simulated for several azimuth angles at 1 GHz.

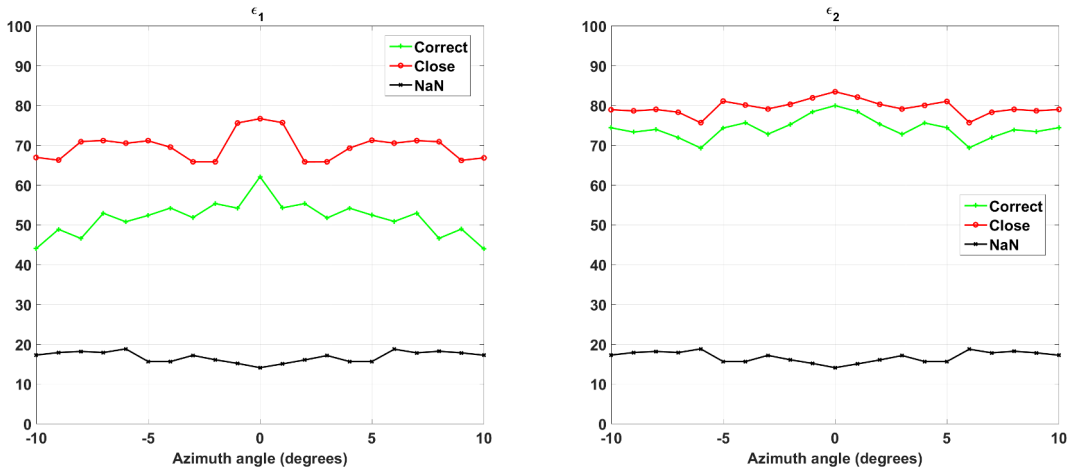

Figure 4.14 – Proportion of correct, close and no results for ϵ_1 and ϵ_2 at 1 GHz for several azimuth angles.

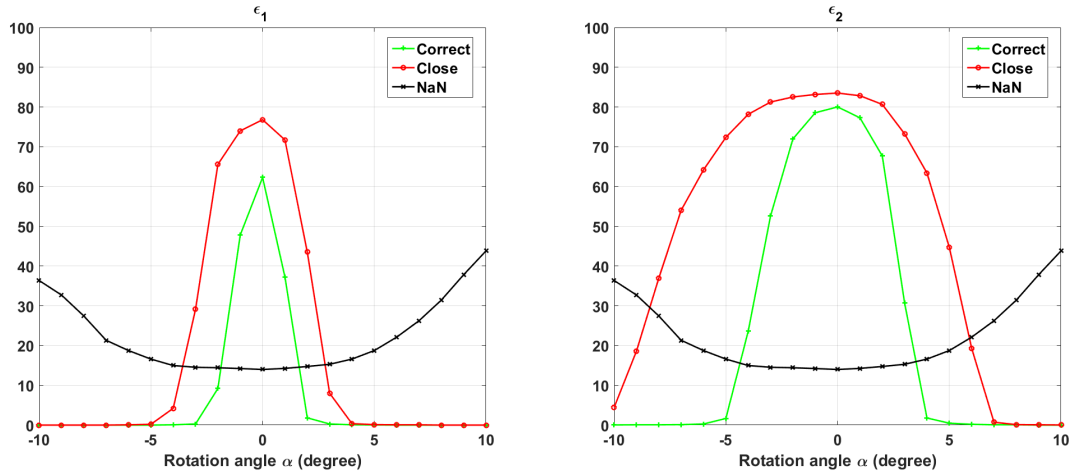

Figure 4.15 – Proportion of correct, close and no results for ϵ_1 and ϵ_2 at 1 GHz for several rotation angles.

4.3 Summary of the method

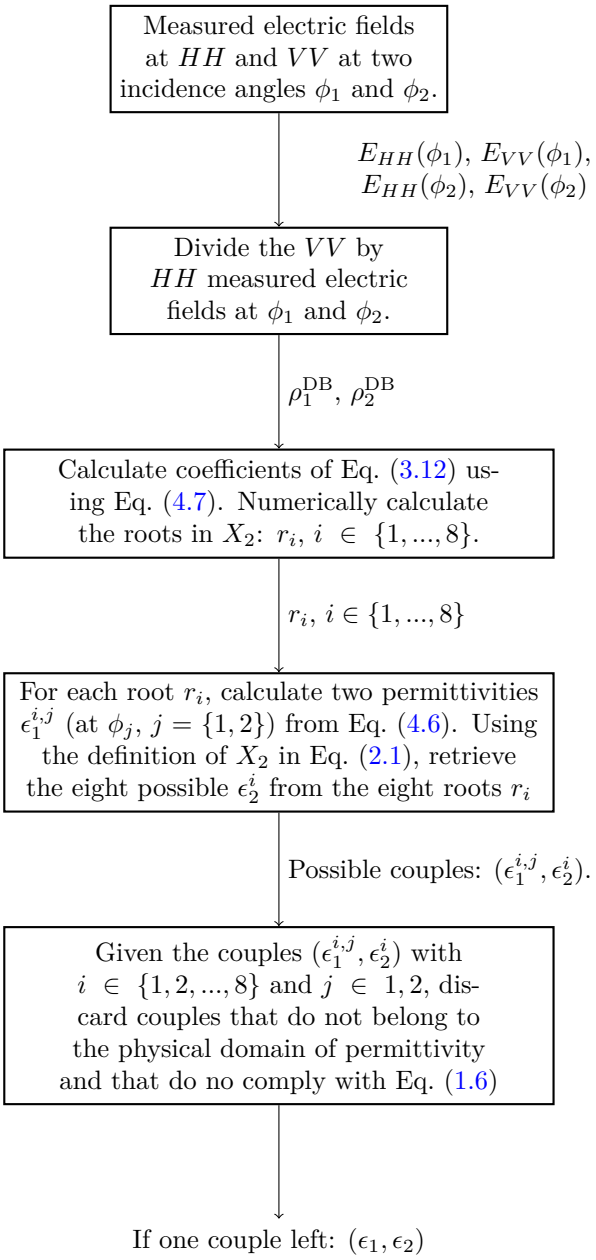

Figure 4.16 – Process of the method.

As before we summarise the method with the chart in 4.16. From the first sight, this method might look expensive regarding its requirements: in addition of VV and HH fields, we need two incidence angles. However this is the price to remove the normalisation step from the process and to directly deal with a relative quantity. All along this chapter, we obtain results without it. It allows to retrieve the permittivities without knowing the dimensions of the dihedral and in the extreme case, without knowing the frequency as long as the measurements are made at the same one. As for the previous method, we advise to use crossed incidence angle domains, $(\phi_1, \phi_2) \in [15, 45] \times [45, 75]$ and its symmetrical, to obtain the closest results to the theoretical values according to the parameters study.

As observed, the proposed method is as sensitive as the previous one with the dihedral angle. Moreover with a composition of permittivities, it is ruled by the same mixing law as the ideal method except it is now angle independent. The retrieval is invariant with azimuth angle and it is flexible with the auxiliary angle.

4.4 Summary and discussion about our three methods

The theoretical part of this dissertation has been dedicated to three main methods we have developed to retrieve the complex permittivities of a dihedral structure under radar measurements. Nonetheless, we can also mention side methods that may reveal to be useful in some cases. The first one retrieves the permittivity of a dihedral made of one material by the mean of HH double bounce coefficient. It can be found in [11]. By using the equations that bind the permittivities and the measurement Eq. 3.3 or Eq. (4.6) we can use a 'mapping' approach consisting in providing a set of ϵ_2 to generate its associated ϵ_1. The same process can be done with the swapped permittivities as it only needs to reformulate the equations.
This remark raises a thought on the choice made during the theoretical development of the last two methods when we choose to write the invariance of ϵ_1 and then to solve in ϵ_2. We can wonder what would happen if at this stage we swap the role of the permittivities: *i.e.* we write the invariance of ϵ_2 and then to solve in ϵ_1. Actually, nothing changes as it is illustrated using the data from the numerical illustration subsection in the Annex C.
Another theoretical remark concerns the axis of symmetry $\phi_1 = \phi_2$, clearly observable on simulated data but that is not obvious from the equations. Indeed, if Eq. (3.6) still possesses this symmetry, we analytically lost it when we transform it into Eq. (3.11). However observations on the method using the ratio between VV and HH suggest that if by swapping ϕ_1 and ϕ_2 the roots of Eq. (3.11) are not the same (to the roots from the 'unswapped' version), we find back the same values of ϵ_2 after applying Eq. (2.1). This insight suggests that the symmetry is kind of hidden in Eq. (3.11) but it is revealed with Eq. (2.1) when we undo the transformation to get Eq. (3.11).

One may wonder why we did not try to combine the two last developed methods and make one using the ratio of HH polarization at two incidence angles. From first sight this approach is attracting due to the fact that it gathers the advantages of the two methods: one polarization without Brewster angles, ratio without a normalization by a PEC equivalent field that could in addition imply the invariance of the results with changes in azimuth. However, the normalisation step does not disappear completely. If the incidence angles are not in the same sub-domain ($[0, 45]$ or $[45, 90]$ degrees) we still need the knowledge of $\frac{a}{b}$ (see Eq. (2.12) for the PEC case). Moreover the complexity of the equations put the approach used to develop the methods in its last possibilities [2].

In table 4.1 we briefly summarize the analysis performed over the three methods and their requirements. The dimensions of the dihedral in this table are not mentioned as a parameter. This is due to the fact they contribute in two ways. First, they are essential to normalize the backscattered electric field by an equivalent PEC signature. The second is that the dimensions and the frequency (thus the electrical dimensions) are inherently bound to the double bounce reflection. This last remark makes difficult to put the dimensions as a specific parameter as it is more a general one. In fact the electrical dimension does not allow to differentiate the methods as they all require to be equal at least to 15 (the best would be to start at 20) for each side of the plates to obtain a proper estimation of the permittivities.

For the ideal method the main advantage is the need of only one incidence angle. Moreover, its analytical expression makes it easy in use (no filtering process). On the other hand, it requires two polarized fields and a normalisation step before being applied. With the method that uses one

2. At some point, we ended with a multi-variable polynomial form (due to the different permittivities and angles) that can not be factored or transformed in a one variable polynomial form easily.

	Ideal method	One polarization	Ratio
Polarizations required	HH and VV	**HH**	HH and VV
Number of incidence angles	**one**	two	two
PEC nomalization	yes	yes	**no**
Handle dihedral angle	no	slightly	slightly
Permittivity composition	mixing law	dependent on incidence angles	mixing law
Sensitivity to incidence angle	high	high	high
Azimuth angle	with an equivalent PEC normalization: yes	with an equivalent PEC normalization: **yes**	**ok**
Rotation angle	partially, depends on the incidence domain	**ok**	slightly

Table 4.1 – Summary of the three methods

polarisation, we reduce the number of required fields but we need two incidence angles and we still have this normalisation step. By using the ratio we get a handy method where the normalisation step is removed. However it requires now two angles and two polarisations.

Chapter 5

Experimental validation

In this chapter, we will focus on the validation of the different methods using measurements from controlled environment: the Geeps anechoic chamber. To do so, we will make a dielectric dihedral from two plates, one made of PVC and one of nylon. A quasi-monostatic system is built using two identical antennas. Estimated permittivities of the two materials are compared with permittivities obtained from measurements performed with a near field probe.
In the last section, we look at the application of the last exposed method to a concrete wall corner. Measurements for few incidence angles are taken in an underground parking lot of CentraleSupélec to assess the feasibility of the ratio method *in-situ*.

5.1 Design of the measurement

The anechoic chamber in Geeps laboratory is a rectangular room of dimensions 9 by 6 meters and 6 meters height. The maximum distance between the object and the monostatic device is 4.3 meters. To make the measurement two identical antennas are used (Double Ridged Broadband Horn BBHA 9120 C from Schwarzbeck, datasheet in [51]) with a built-in frequency of operation from 2 to 19 GHz. The greatest dimension of the aperture of these antenna is 0.12 meter. It implies a minimal distance of 1.8 meter to be in far-field condition [1] relatively to the antenna in the [2,19] GHz bandwidth. This can be easily achieved with the maximum distance of 4.3 meters allowed in the anechoic chamber.

Now regarding the dimensions of the object, two issues are raised. The first is the far-field distance related to the object and the second is the electrical dimension of each plate in order to have meaningful double bounce to perform the inversion. For a dihedral made of squared plates of 0.25 meters the far-field distance goes from 2.5 to 23.7 meters within the frequency bandwidth of the antennas. As the wavelength goes from 0.15 to 0.016 meters with the frequency, the electrical dimension of each plate would go from 1.7 to 15.8. We see here that a trade-off should be made: at the lower part of the frequency bandwidth, the farfield distance is reasonable given the dimension of the anechoic chamber, in the higher part of the frequency bandwidth we have the best electrical dimension. A discussion and an illustration about the far-field distance of a dihedral is presented in Appendix D.1.

However as the gain of the antenna is the best in the [5,18] GHz (steady and high, see datasheet) we will choose this bandwidth and invert from the collected field. Moreover such wide bandwidth also have a purpose into discriminating time phenomenons from each other as we will see it later in this chapter. The corresponding electrical dimension by plate and theoretical far-field distance are given in Table. 5.1. We make a dihedral from a plate of nylon (ϵ_1) and a plate of PVC (ϵ_2). A near field probe (Agilent 85070D Dielectric Probe Kit) from Geeps laboratory is used to measure

1. $\frac{2D^2}{\lambda}$, where D is the aperture of the antenna, or if we consider an object D is its maximal dimension.

permittivities and provide us a point of comparison. It extracts the permittivity from 0.5 to 6 GHz of a flat solid material or a fluid by measuring the reflection coefficient of an open-ended probe after calibration with air. Limitations of the near-field probe allow us to perform the measurements in the [0.5, 6] GHz bandwidth and not the [5, 18] GHz. In Fig. 5.1 we display the result of the measurement in [0.5, 6] GHz of the relative permittivity of the air. As it can be seen, most of the measurement points are concentrated near 1 with a very small imaginary part (between 0 and -0.03). Thus we perform the measurement of the PVC and nylon plates on three different points denoted p_1, p_2 and p_3. Results are displayed in Fig. 5.2 for the nylon material and in Fig. 5.3 for the PVC. For PVC material, the real part of the permittivity is contained in the [3,3.5] interval and for the nylon material it is in the [2.5,3] interval. For both materials, their real parts are quite steady along the frequency and their imaginary parts are quite small and oscillate with the frequency around zero for frequencies greater than 2 GHz. With these measurements we have at least an idea of the values of permittivities we have to retrieve even if the measurements are not made in the same bandwidth [2]. Moreover, as it seems that we deal with real value permittivities (or very close to real value) the wide bandwidth gives an opportunity to distinguish the reflection on the illuminated sides of the plates from the secondary reflections coming from the transmission of the wave along the width and its reflection on the shadowed side of the plate. Such bandwidth (13 GHz) allows us to have a fine distance resolution of 0.011 meters regarding the physical 6 cm depth of each plate. As each plate is made with different permittivities the shortest electrical distance between the interface air/material and the interface material/air (so from one side of the plate to the opposite one) is around 10 cm for both plates as the wave travels at $\frac{c_0}{\sqrt{Re(\epsilon)}}$ speed inside it. So this bandwidth might also help us to distinguish in distance the double bounce reflection from the multiple reflections happening within the dihedral.

f (GHz)	5	6	8	10	12	14	16	18
λ (cm)	6	5	3.7	3	2.5	2.1	1.9	1.7
$\frac{D}{\lambda}$	4.2	5	6.7	8.3	10	11.7	13.3	15
$\frac{2D_d^2}{\lambda}$ (m)	6.2	7.5	10	12.5	15	17.5	20	22.5

Table 5.1 – Evolution of the electrical dimension and of the theoretical farfield distance with the frequency bandwidth considered and for a dihedral of $D = 0.25$ m side size implying a diagonal size of $D_d = 0.43$ m.

2. It is not the same bandwidth but it is an adjoining one.

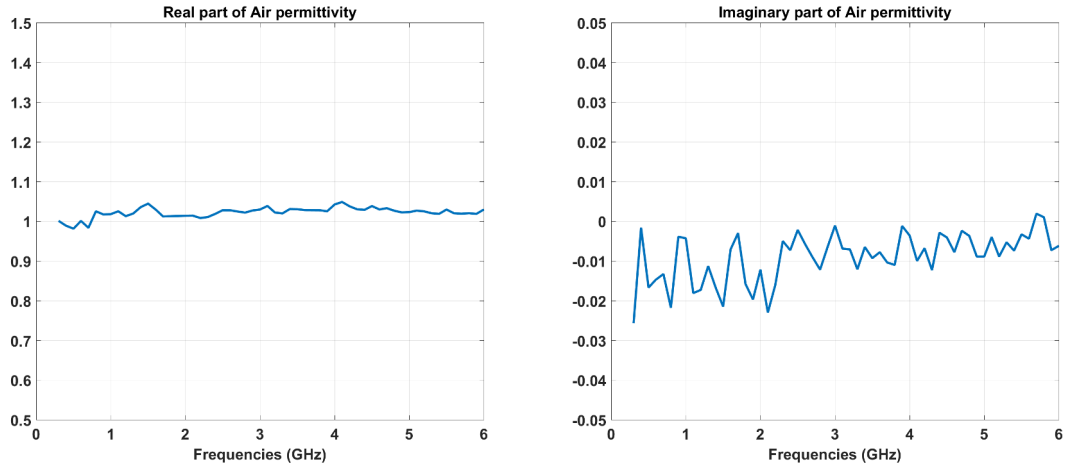

Figure 5.1 – Measured air permittivity in real and imaginary parts with the frequency from the near field probe.

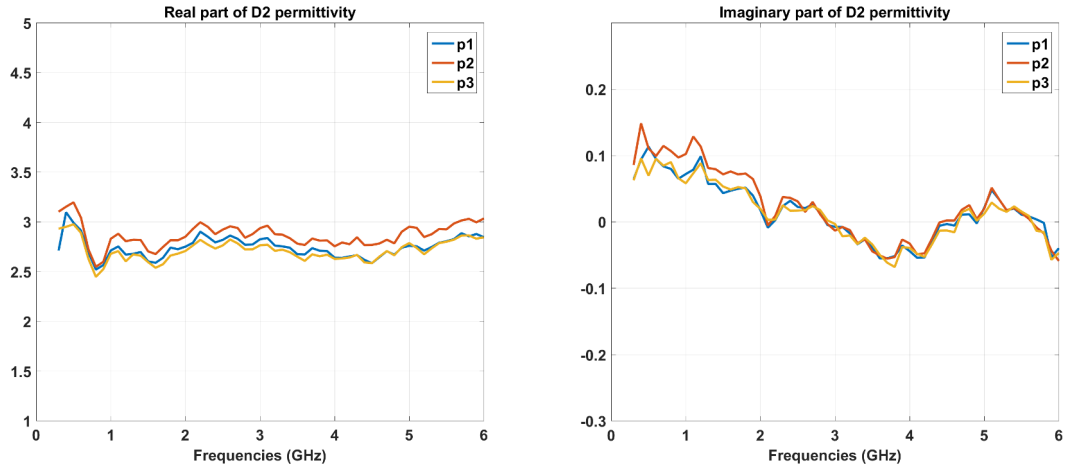

Figure 5.2 – Measured nylon permittivity (ϵ_1) in real and imaginary parts with the frequency from the near field probe.

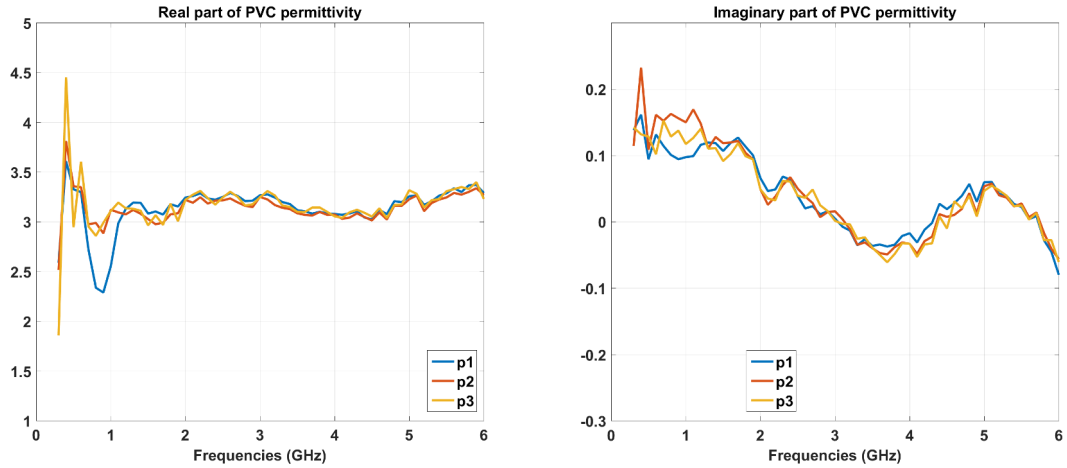

Figure 5.3 – Measured PVC permittivity (ϵ_2) in real and imaginary parts with the frequency from the near field probe.

5.2 Measurement results

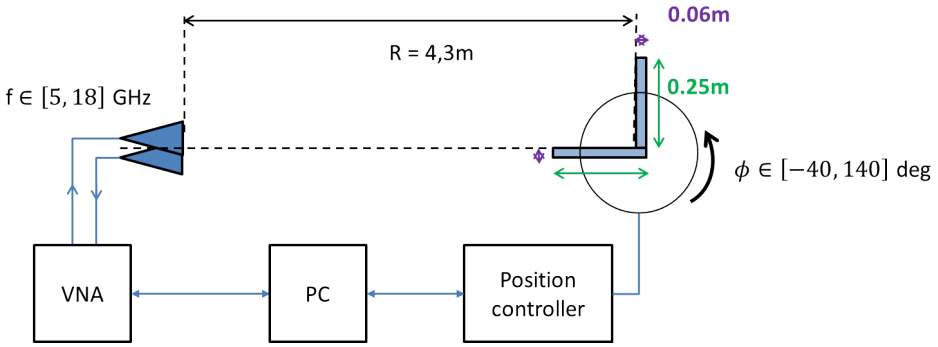

Figure 5.4 – Scheme of the measurement setup.

The rotation of the dihedral is made around 180 degrees with a 1 degree step such that the azimuth rotation of the target in the anechoic chamber correspond to a change of the incidence angle of the dihedral in our model (see scheme Fig. 5.4). The dihedral is placed on the rotating platform such that its central edge is aligned with the platform centre of rotation. Marks of the position of the dihedral on the platform are left to easily reproduce the measurement (or as we will see it later to easily apply the same measurement to a metallic dihedral). As previously mentioned, we use a quasi-monostatic system made of two identical antennas over the [5,18] GHz bandwidth. A discussion about the positioning of the antennas in order to obtain fields as close as possible to the far-field condition is presented in Appendix D.2. We collect VV and HH backscattered fields over 1301 frequency points. The antennas (in HH polarization in the picture), the target platform and the dihedral are displayed in Fig. 5.5. The plate made in PVC (ϵ_2) is in grey and the nylon one (ϵ_1) is black. Its dimensions are $(a, b, L, c) = (0.22, 0.25, 0.25, 0.06)$m. A scheme representing a top view of the measurement set-up is displayed in Fig. 5.4 where the two blue triangles represent the two antennas, the blue rectangles the two plates composing the dihedral and the circle represents the platform. The platform is commanded through the position controller by the computer. The latter synchronises the measurement stage with the VNA (Vectorial Network Analyser) [3] with the position controller.

In Fig. 5.6 is plotted the amplitude in dB of the S_{21} parameter for the two polarizations in the frequency domain. As the coarse measurement from the antennas could be considered as the measure of the total field, another measurement without the target (the dihedral) is performed. This latter measurement is subtracted from the dihedral measurement such that we keep the scattered field. At the same time, it allows to remove the electromagnetic environment of the anechoic chamber and to attenuate the coupling effect of the quasimonostatic system. In both polarization we see two dash lines at 0 and 90 degrees of incidence angles that get thinner as the frequency increases. It corresponds to the reflection of the plates when they are in front of the antennas corrupted by interferences (no straight lines but dash ones). Between 0 and 90 degrees noticeable differences between HH and VV can be seen: for HH we have signals mixed with repeatable patterns of gaps describing arcs of circles in the continuity of the gaps of the dash lines. This is not observable for VV. To understand this better we look at the signals in the time domain after performing an inverse Fourier Transform. First we operate such that we obtain a real signal in the time domain [4].

3. A VNA is a measuring device for electrical network. It is modelled as a two-port device characterised by its S-parameters (S_{11}, S_{21},S_{12}, S_{22}). In our case, as we measure what is received at one port compared to the first we are interested in S_{21} measurement.

4. *i.e.* s is a real signal in the time domain if $F(s)(f) = F(s)(-f)^*$, where $F(s)$ is the Fourier transform applied to s signal, f is the frequency variable and * is the conjugate operator.

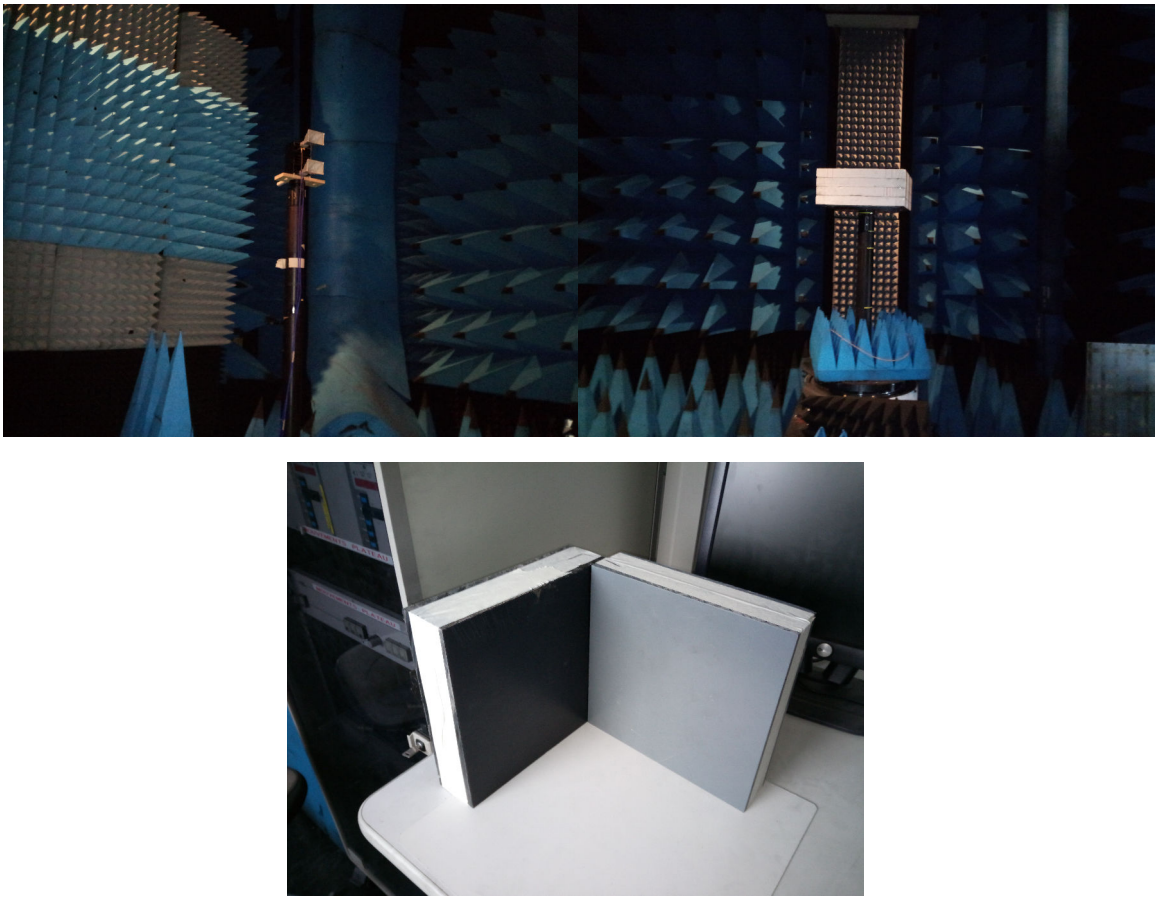

Figure 5.5 – Measurement setup: the antennas, the platform and the dihedral.

Fig. 5.7 shows the temporal evolution of the measurement (globally in the left image, at 45 degrees on the left) for HH polarization. The x axis of these figures are in distance as we can link time t and distance d with: $d = \frac{c_0 t}{2}$. Due to the aliasing, we observe the target on the left side of the picture in the negative distance domain. Given the temporal domain, we get a distance domain of $[-7.5, 7.5]$ m. However provided the length of the cables between the VNA and the antennas (both greater than 2 m) and their intrinsic impedance, we can observe the mutual coupling of the antennas at 5.4 m as displayed on the cut made at 45 degrees. Hence the signal is wrapped and the object is found at -5.1 m. Relative distance is respected : $7.5 - 5.4 - (-7.5 - (-5.1)) = 4.5$m, especially given the distance between the two antennas (around 0.17 m). A zoom on the object location is displayed in Fig. 5.8. From these images we see the displacement in range of the edges of the dihedral, the first and main reflection of the dihedral and a secondary reflection after transmission. In Fig. 5.9, we plot a scheme of the temporal signature. The dark blue and mauve lines represent the movement of the edges of the dihedral as they are aligned at 0 and 90 degrees to the specular reflections of each plates (one at 0 the other at 90 degrees) displayed here with the green dots. If we calculate the distance between those dots and the edges at 0 and 90 degrees we retrieve a and b values (around d_1 in the scheme). We can see in Fig. 5.8 that the second edge is a bit far away from the main reflection due to the fact that b is greater than a. As seen in [9], the double bounce signature should be located at the same distance from the emitter-receiver device than the central edge of the dihedral. This distance is also the one between the measurement device and the plates signature at 0 and 90 degrees *i.e.* at 4.3 meters. In Fig. 5.8, we also see in VV image the two Brewster angles near 30 and 60 degrees. The second reflection (cyan in the scheme) happens

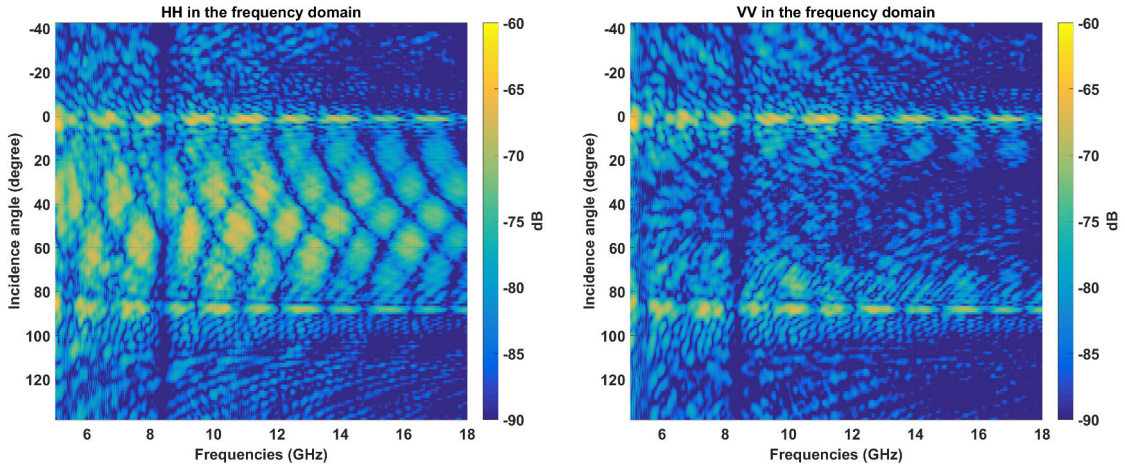

Figure 5.6 – Amplitude of the measured S_{21} in HH and VV polarizations in the frequency domain along the rotation (incidence) angle.

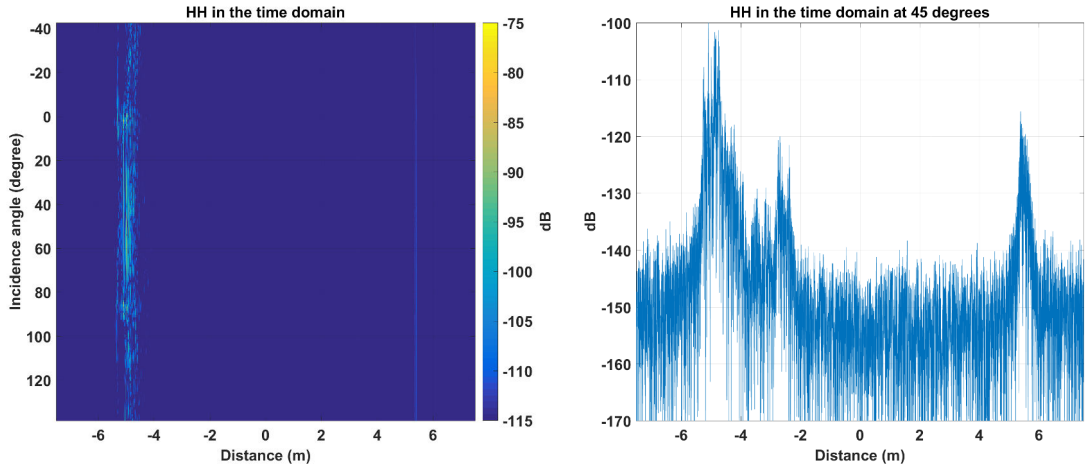

Figure 5.7 – Amplitude of the measured S_{21} in HH polarizations in the time domain along the rotation (incidence) angle (on the left) and at 45 degrees (on the right).

0.10 meters after the first reflection. This is due to the propagation delay in transmission within the material. If we take the real part of the permittivity measured with the probe, we retrieve the depth of the plate: $\frac{0.10}{\sqrt{3}} \approx 0.06$ m. As our method only relies on the double bounce we should discard the edge movements and the second reflection by selecting only the temporal event linked to the main reflection (green in the scheme) located at 4.3 meters from the antennas.

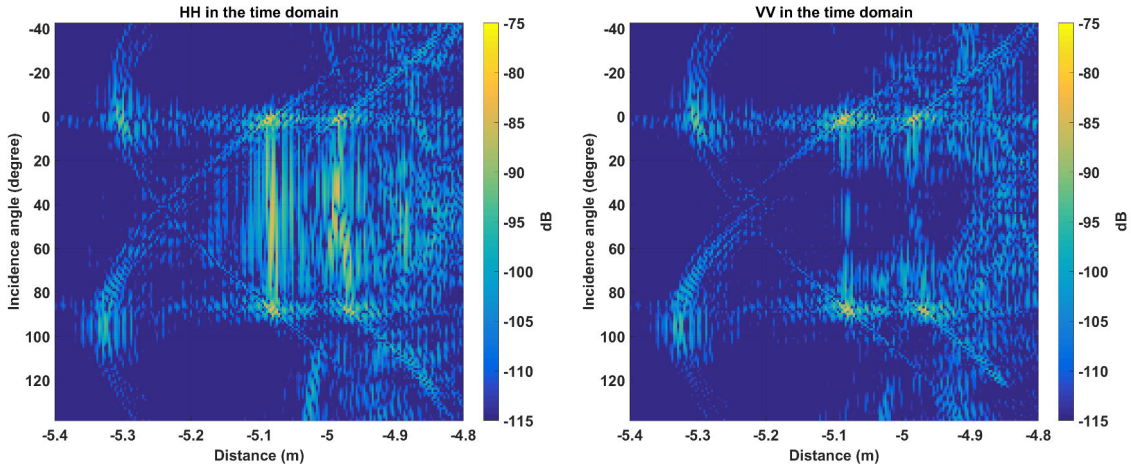

Figure 5.8 – Amplitude of the measured S_{21} in HH and VV polarizations in the time domain along the rotation (incidence) angle near 4.3 meters distance.

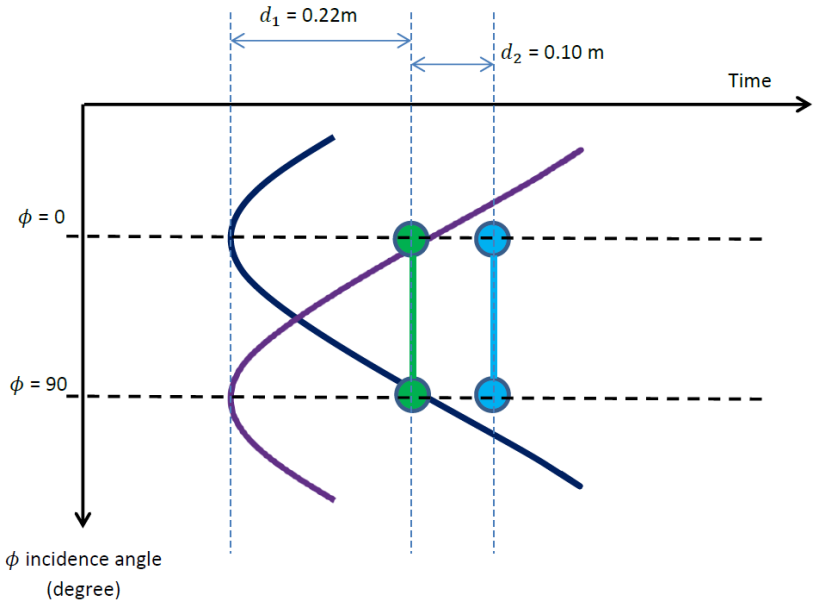

Figure 5.9 – Scheme of the measured S_{21} in the time domain along the rotation (incidence) angle.

5.3 Inverting the measurement

Given the previous analysis of the temporal signals, we gate them to select at best the double bounce component around 4.3 meters and for an incidence angle from -7 to 98 degrees as displayed in Fig. 5.10. To efficiently perform this operation we need several points between the reflection of interest occurring at -5.1 meters and the second one 10 cm behind. Here the bandwidth of 13 GHz is useful as it give us around 9 points. To increase this number of points we use a zero padding operation on the inverse Fourier transform used to put the signal in the temporal domain. By doing so, we end with a signal of 5120 points (1301 originally) such that we obtain nearly 40 points between the two phenomenon.

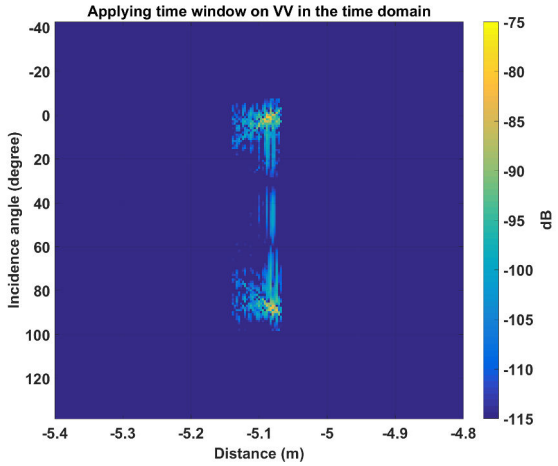

Figure 5.10 – Amplitude of the S_{21} in VV in the time domain along the rotation (incidence) angle after time gating.

Once time gating operation is done, we take the signal back to the frequency domain and obtain fields in HH and VV. Their amplitude are displayed in Fig. 5.11. From them we can see that there is no more interferences represented as dash or arc patterns [5] in Fig. 5.6. We now have for HH a rather smooth evolution with the frequency. For both polarization we can see the signature of the fully illuminated plate at 0 and 90 degrees. In HH, one could observe between 7 and 14 GHz, a built double bounce that takes over the sidelobes of the plate radiation patterns located at 0 and 90 degrees. In VV, we can clearly see the two Brewster gaps near 30 and 60 degrees. Again between 7 and 14 GHz, these gaps looks to be constant in terms of incidence angle locations. This is coherent with our model in which Brewster angles are invariant with the frequency. After 14 GHz, the gaps are slightly moving toward each other and the HH field is degrading. This might be due to the far-field condition that is not sufficiently respected. Before 7 GHz, the HH signal presents a dominant scattering of the plates at 0 and 90 degrees [6] . Now, using this two filtered signals we can compute the ratio between VV and HH polarization.

5.3.1 Inverting using the ratio

By computing the ratio from the signals in the frequency domain after filtering, we can perform the same kind of representation as in the previous chapter by building a representation with the

5. By playing with the time gating window (*i.e.* by selecting only the phenomenon of interest), one could see that these patterns are mainly built though the combination of the two reflections. They are completely built with the three reflections (one at -5.1 m, the second at -5 m and the weak third reflection at -4.9 m).

6. This phenomenon can be seen when using the theoretical P.O. solution as in Appendix D.1, Fig. D.1 for a PEC dihedral of $0.3 \times 0.3 \times 0.3$ meters dimension at 5 GHz

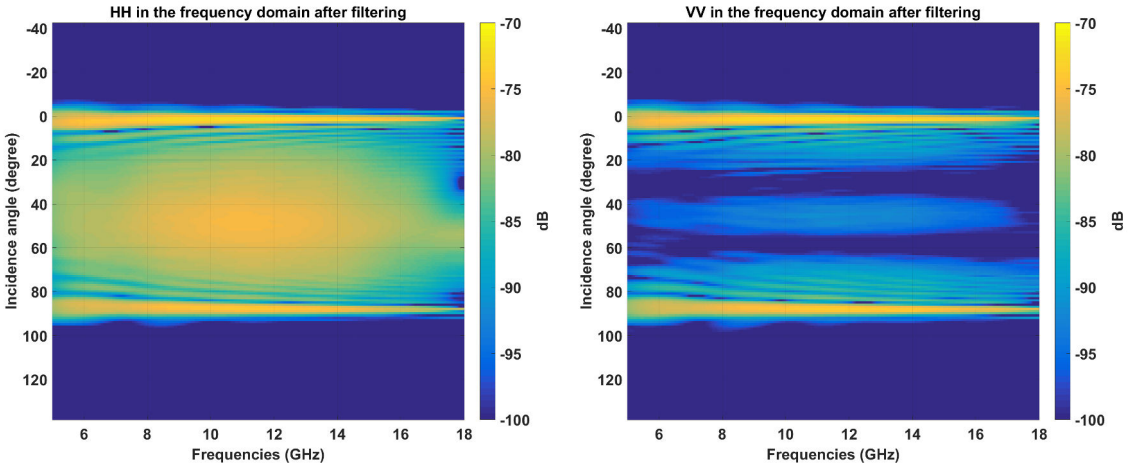

Figure 5.11 – Amplitude of the measured S_{21} in HH and VV polarizations in the frequency domain along the rotation (incidence) angle after time gating.

two measurements made at (ϕ_1, ϕ_2). In Fig. 5.12 and in Fig. 5.13 we display the calculated ϵ_1 and ϵ_2 in terms of real and imaginary parts for four frequencies: 6, 10 and 13 GHz. For recall, using the near-field probe, we measure in the [0.5, 6] GHz bandwidth, ϵ_1 (nylon) around $2.7 - 0i$ and ϵ_2 (PVC) around $3.2 - 0i$.

In Fig. 5.12, we observe the frequency evolution of the ϵ_1 (nylon) results in real and imaginary parts. The real part is getting smoother as the frequency increases. At 6 GHz,the results oscillate with ϕ_1 or ϕ_2 in $[50, 80]$ degrees range between 2 and 4. These oscillations can be retrieved in the imaginary part of ϵ_1 between 0 and -1.5. They disappear as the frequency increases and at 10 or 13 GHz, most of the results for the real part is between 2.5 and 3 over $[50, 75] \times [10, 45]$ (and its symmetrical) angular domain. In imaginary part, we get a similar behaviour except that at 10 - 13 GHz, we got an evolution by steps centred to the lower angular domain $[10, 40] \times [10, 40]$ where the imaginary part is the lowest. It increases from -1 to 0.5 (tolerance for zero) for angles from 50 to 75 degrees. One can also notice in simulation, we lack the solutions at low angular domain $[10, 40] \times [10, 40]$ degrees and at high angular domain $[50, 80] \times [50, 80]$ degrees. As before, these gaps are slowly being filled from the intermediate angles ($[15, 30]$ degrees) with erroneous values (too high) as the frequency increases.

In the case of ϵ_2 (PVC), we get smooth results at 6 GHz over the $[17, 32] \times [40, 80]$ domain. The real part is contained in $[2.5, 3]$ and the imaginary part in $[-0.5, 0]$. For angles below 17 ° results are no more meaningful as they variates too quickly from an angle to another (from 5 or more to 2 or less). For angles between 32 and 40 degrees, we still get a real part in $[2.5, 3.5]$ and an imaginary part that borders the zero value. Above, in the $[40, 80] \times [40, 80]$ angular domain, we have either, low or no solutions in the $[50, 80] \times [50, 80]$ domain, or in the intermediate area $[40, 50]$ we see repeatable peaks or drops (depending if we look at the real or imaginary parts). At 10 GHz, we get an oscillating behaviour in real as in imaginary parts. It seems to vary between 2.5 and 3.5 (resp. -1 and 0) for the real (resp. imaginary) part. For both, the more we get close to low angles, the more we will get a high imaginary part and the real part stays around 2.5 - 3. At 13 GHz, the domain $[20, 40] \times [35, 80]$ degrees is more steady. The oscillating behaviour is less present. The real part is in the $[2.5, 3]$ interval exception made for few angles where it is in the $[3, 3.5]$ interval. The imaginary part is evolving by steps from the higher incidence angle domain $[45, 90] \times [45, 90]$ where it is the lowest and it increases as soon as one angle decreases.

These results are in good agreement with the analysis made on the filtered signals: at 6 GHz,

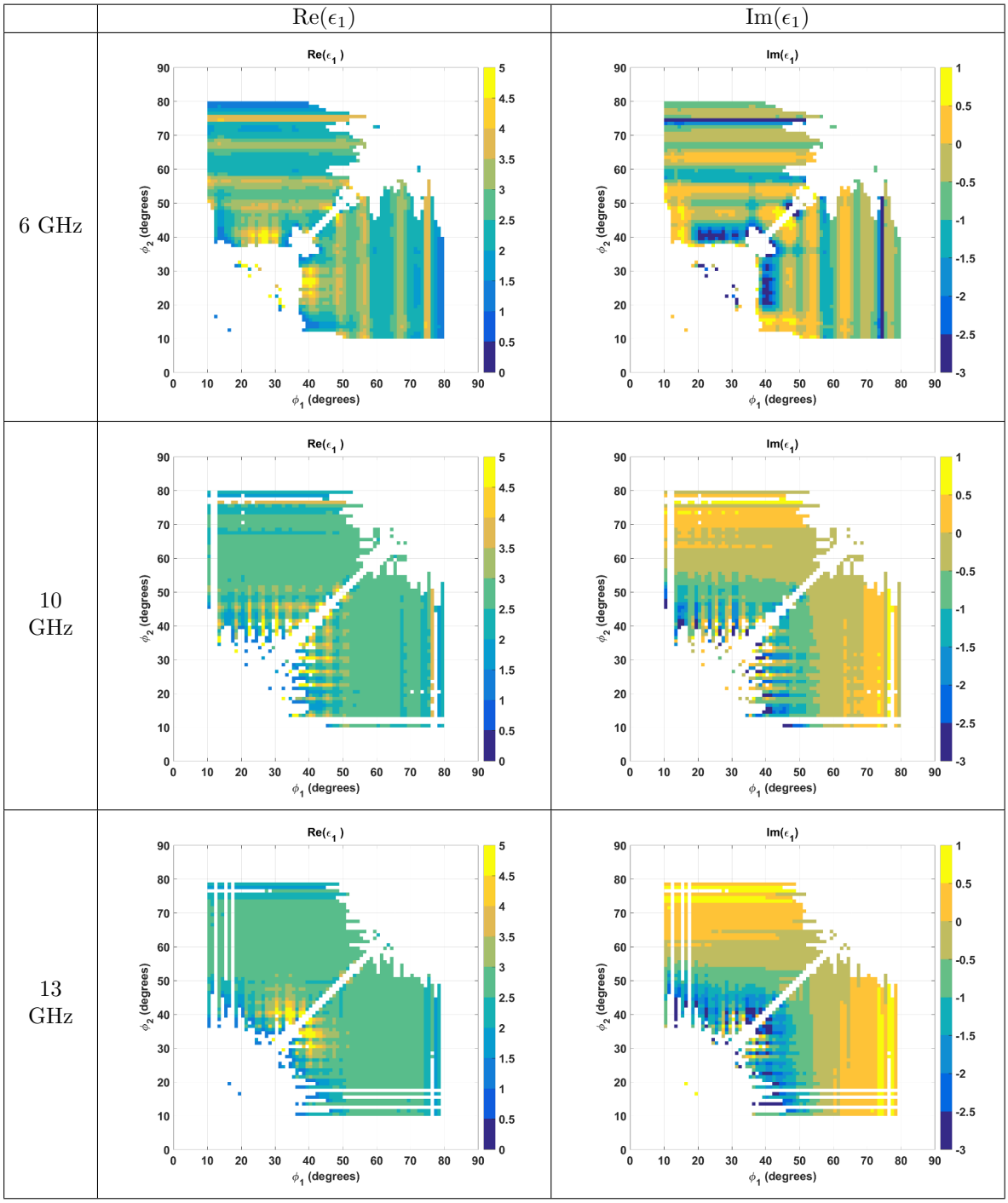

Figure 5.12 – Real and imaginary parts for ϵ_1 (nylon) at 6, 10 and 13 GHz (expected value around $2.7 - 0i$).

the results are not so nice as the electrical dimension is too low and as we mainly have the bac-scattering signals of the plates. However between 8 and 14 GHz, we obtain nice results as we are quite close to the farfield condition and we have a sufficient electrical dimension to invert the permittivities.

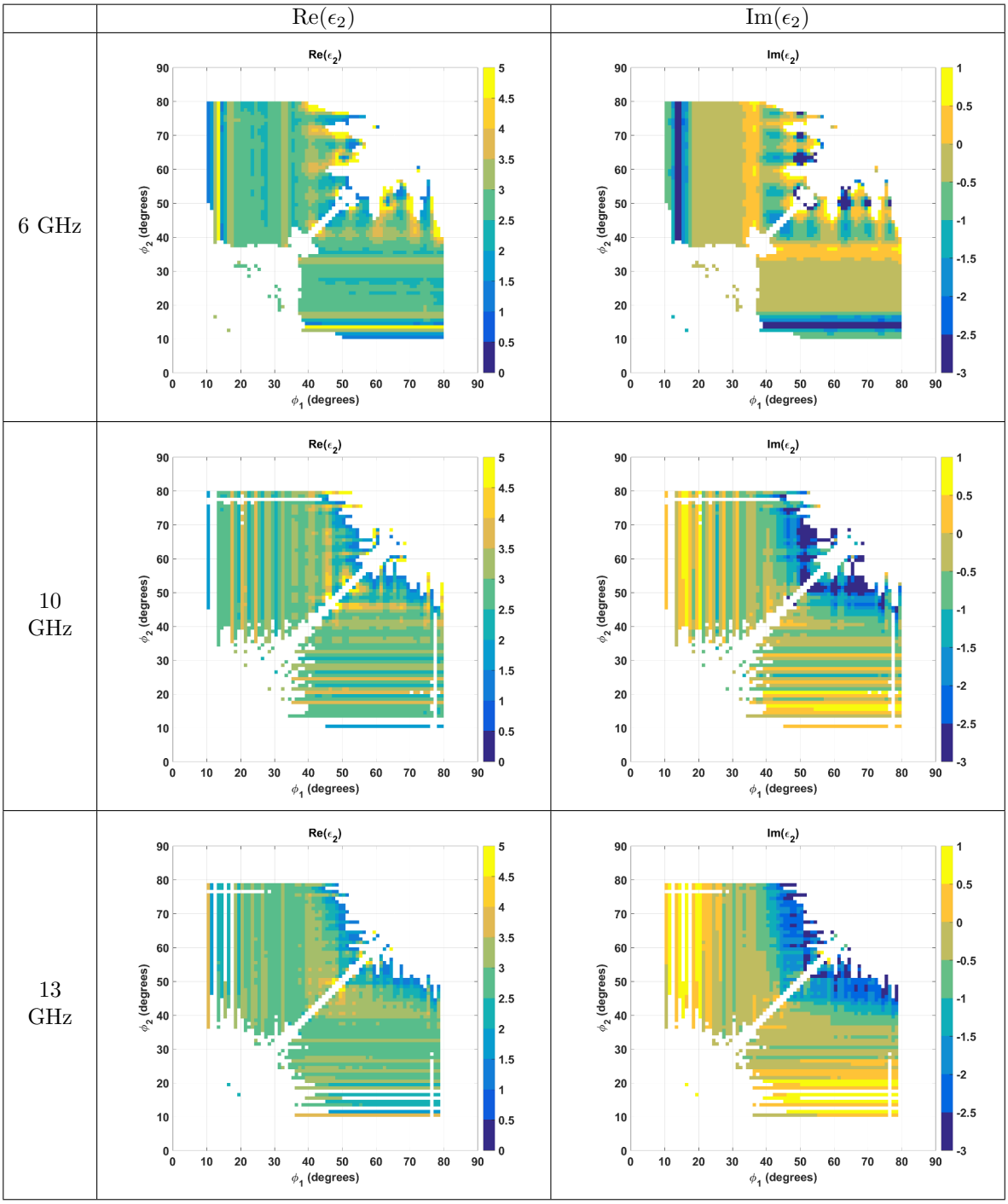

Figure 5.13 – Real and imaginary parts for ϵ_2 at 6, 10 and 13 GHz (expected value around $3.2 - 0i$).

This behaviour with the frequency range can be seen in Fig. 5.14. We select three angle combinations (ϕ_1, ϕ_2) at $(20, 60)^\circ$, $(30, 60)^\circ$ and $(40, 60)^\circ$ and plot the estimated ϵ_1 and ϵ_2 in their real and negative imaginary parts. In this Figure, we observe a transition part of the results from 5 GHz to 8 GHz (sometimes 9 GHz) where for instance ϵ_1 is evolving from $2 - i$ to $2.7 - 0.5i$ for any angle combinations. Then a quite steady interval from 9 to 15 GHz, is observed where solutions

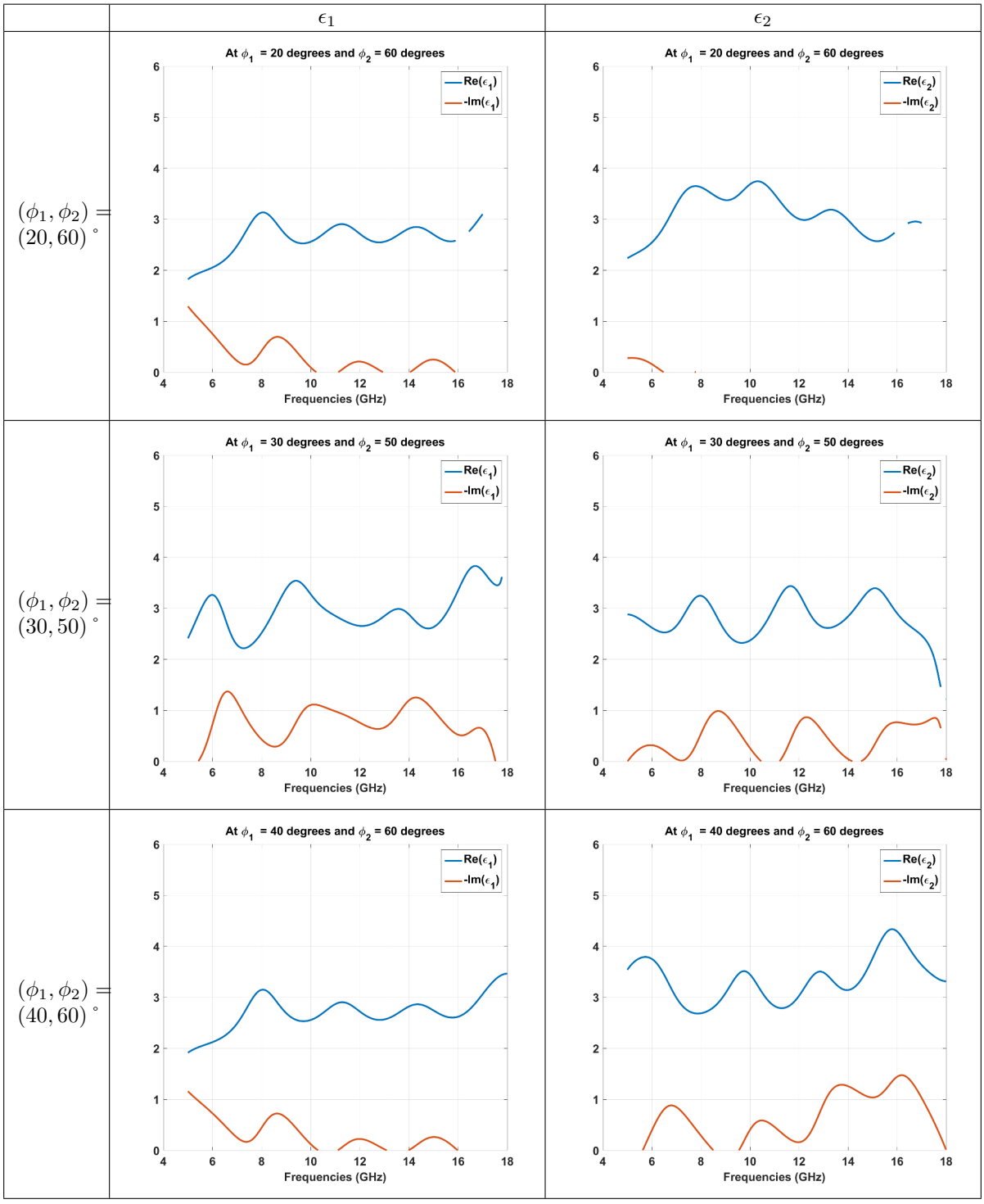

Figure 5.14 – Real and imaginary parts for ϵ_1 and ϵ_2 with the frequency at three angle combinations.

are oscillating. For ϵ_1 it is around the $2.7 - 0.5i$ and for ϵ_2 around the $3 - 0.5i$. In this frequency range the results are really close the measurements performed with the near field probe. Beyond 15 GHz, the solutions are diverging very quickly after 16 GHz.

5.3.2 Inverting using the first two methods

Unlike the method using the polarimetric ratio where only the selection of the double bounce component was required, for the first two methods we need an absolute value for R_H^{DB} and R_H^{DB}. Therefore to get these quantities we need to compensate in amplitude and phase for the propagation of the wave, the characteristics of the antennas, the loss in cables, and the scattering part due to the geometry of the dihedral.

Retrieving the double bounce coefficients.

For the compensation in amplitude, we apply the following equation derived from the radar power budget equation [52]:

$$10\log_{10}(|S_{pp}|) = 20\log_{10}(|S_{21,pp}|) + 10\log_{10}(\frac{(4\pi)^3R^4}{\lambda^2}) - 2G_{antenna,dBi} - L_{cables} \tag{5.1}$$

where S_{pp} is the scattering element in polarization pp, $S_{21,pp}$ is the measurement of S_{21} in the frequency domain after time gating at the polarization pp, R is the distance between the antennas and the object (4.3 meters), λ is the wavelength, $G_{antenna,dBi}$ is the isotropic gain of the antenna and L_{cables} is the amplitude in dB of the loss due to the propagation in the cables between the antennas and the VNA. $G_{antenna,dBi}$ is given by the datasheet of the antenna. L_{cables} is measured over the same frequency parameters as the measurement of the dihedral. The gain and the loss amplitude are plotted in Fig. 5.15. In addition of this compensation we need to take away the scattering part from the object itself as we did it when dealing with simulation data by normalising the backscattered electric field by the one of a PEC equivalent structure: $E_{pp,PEC}$. As we have the dimension of the dihedral, we can compute the amplitude of the electric field in HH and VV using [7].
Once this has been subtracted, the only step remaining is to compensate the measurement using the calibration of the anechoic chamber. To do so we make the measurement of a canonical object, here a metallic sphere of diameter $d_{sphere} = 0.25$m over 901 frequency points between 9 and 18 GHz. According to [10], to be able to use the theoretical RCS of the sphere (pictured in Fig. 5.16), we need to have a sufficiently large $k\frac{d_{sphere}}{2}$ quantity. At 9 GHz, it is superior to 20, which is large enough to use: $RCS_{PEC}^{sphere} = \pi\frac{d_{sphere}}{2}^2$ from [10]. Likewise we filter in the time domain based on the distance between the quasi-monostatic device and the object to get $S_{21,pp}^{sphere}$. We apply Eq. (5.1) to obtain the RCS of the sphere $10\log_{10}(|S_{pp}^{sphere}|)$. Hence we can compute the difference between the RCS measured and the theoretical RCS of the sphere.
To sum up and after simplifications, to retrieve the amplitude of the double bounce coefficient in pp polarization, we apply Eq. (5.2) [7]:

$$20\log_{10}(|R_{pp}^{\mathrm{DB}}|) = 20\log_{10}(|S_{21,pp}|) - 20\log_{10}(|E_{pp,PEC}|) - (20\log_{10}(|S_{21,pp}^{sphere}|) - 10\log_{10}(\pi\frac{d_{sphere}}{2}^2)) \tag{5.2}$$

In Fig. 5.17 we plot the result of such operations at 10 GHz. To provide a comparison we compute R_H^{DB} and R_V^{DB} using Eq. 1.6 with $\epsilon_1 = 2.75 - 0.5i$ and $\epsilon_2 = 3 - 0.6i$ (which is close to the results found at 10 GHz when we use the ratio in the previous subsection). We can observe that the amplitude curves in dB are quite close in HH and VV. The trend are retrieved with the incidence angle and even if there is some gaps especially with HH curve we have a good agreement.

For the phase compensation it becomes more complicated as the dihedral rotates during the measurement. Even by trying to position the central edge of the dihedral at the rotation centre of the platform, we still see in phase a drift due to the movement. Therefore the most straightforward

7. Only valid if the measurement of the dihedral and the measurement of the sphere of calibration are performed in the same conditions: identical antennas, distance, cables and frequency parameters.

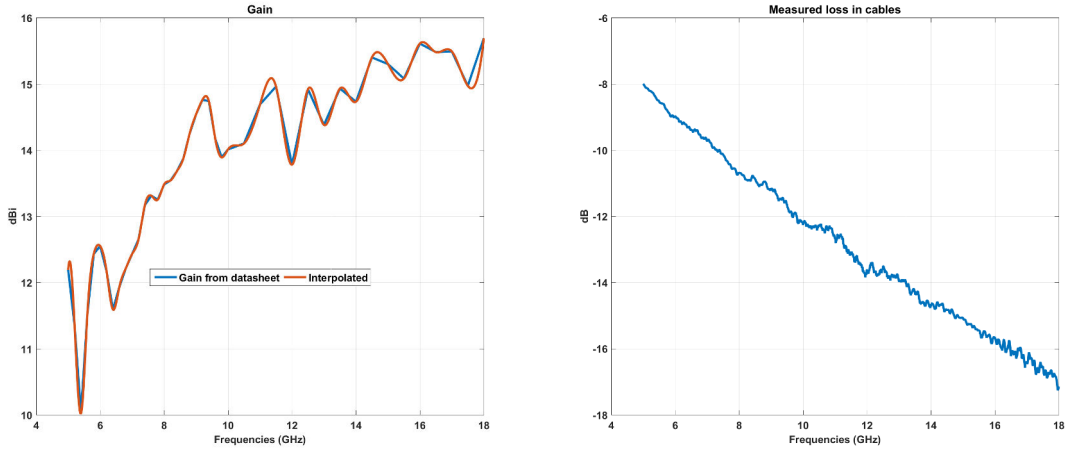

Figure 5.15 – Gain of the antenna from datasheet and its interpolation and the measured loss in the cables.

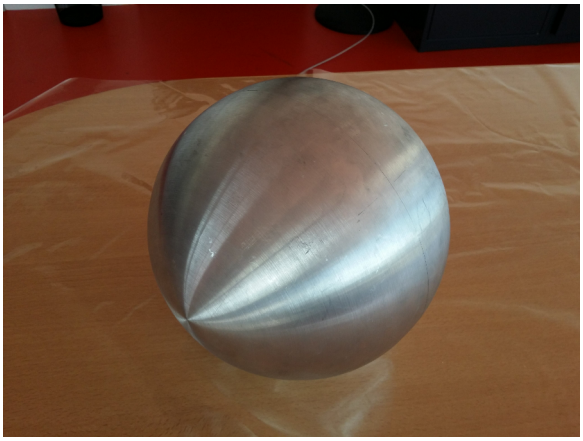

Figure 5.16 – Picture of the metallic sphere.

solution is to make the same measurement (with the same parameters and setup) to a metallic dihedral and to use its double bounce phase denoted $\angle S_{pp,PEC}$ to calibrate the phase from the dielectric case $\angle S_{pp}$. It should remove the phase drift due to the movement as we place it at the marks left for the measurement reproducibility. Eq. (5.3) describes the operation to get $\angle R_{pp}^{\mathrm{DB}}$. We use the metallic dihedral depicted in Fig. 5.18. It is made of thin square plates of dimensions 0.3 m by 0.3 m.

$$\angle R_{pp}^{\mathrm{DB}} = \angle S_{21,pp} - \angle S_{21,pp,PEC} \tag{5.3}$$

In Fig. 5.19 we plot the result of such operations at 10 GHz. Again, to provide a comparison we compute R_H^{DB} and R_V^{DB} phase using Eq. 1.6 with $\epsilon_1 = 2.75 - 0.5i$ and $\epsilon_2 = 3 - 0.6i$. Here we see that VV has roughly the same trend with the theoretical one: we observe the phase shift of around 180 degrees between low and high incidence angles and the 40-50 degrees angles. However we observe a constant offset of the phase (around 20 degrees at minimum) over the whole incidence angle interval. For HH phase, it is more critical as in addition to have 15 degree offset, we don't even retrieve the trend of a theoretical phase of R_H^{DB}. All these drawbacks could be originated to several reasons [8]. The main one is that the metallic dihedral is not identical to the dielectric

8. Regardless the fact that we deal with steel plates and not the ideal PEC material.

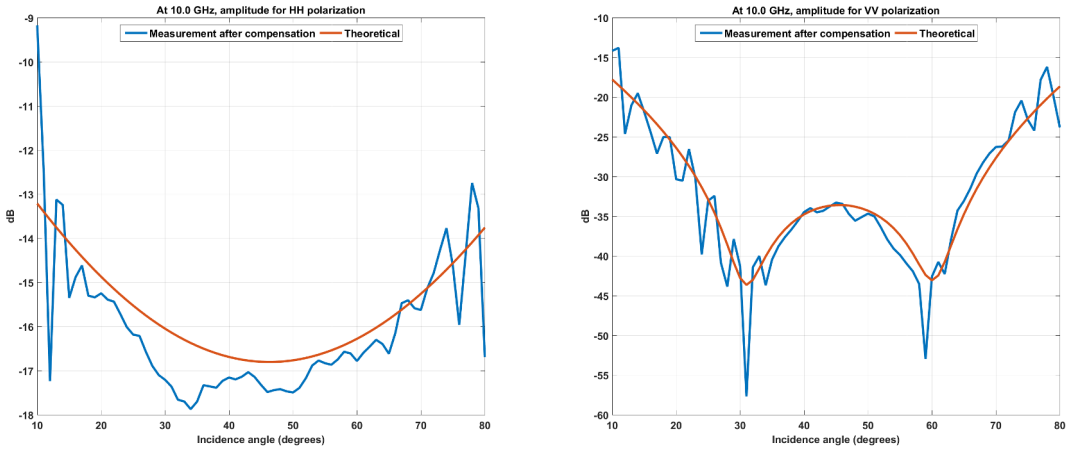

Figure 5.17 – Amplitudes in HH and VV at 10 GHz after compensation and calibration with the metallic sphere compared to amplitudes of a theoretical R_H^{DB} and R_V^{DB} computed from Eq. (1.6) using $\epsilon_1 = 2.75 - 0.5i$ and $\epsilon_2 = 3 - 0.6i$.

one in dimensions ($0.3 \times 0.3 \times 0.3$ m for the first, $0.22 \times 0.25 \times 0.25$ m for the latter) making the phase centre higher for this dihedral than the dielectric one. Moreover the metallic dihedral has a dihedral angle of few degrees off the square angle and as we have seen it in the last three chapters it is a crucial parameter. One last drawback is the fact that the metallic plates are not perfectly planar.

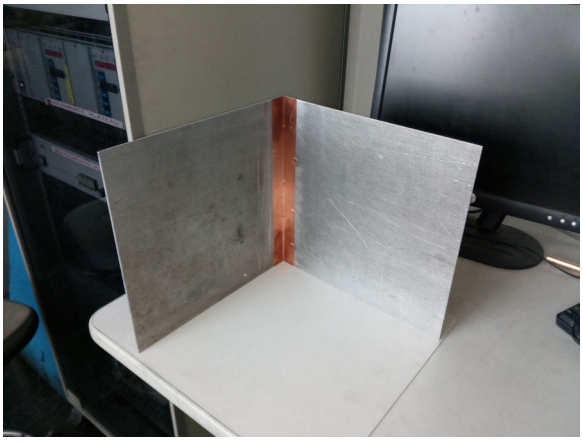

Figure 5.18 – Picture of the metallic dihedral.

Now that we have an approximated R_V^{DB} and R_H^{DB} from the measurement we can apply the methods developed in Chapter 2 and Chapter 3.

Inverting permittivities using the first method.

In Fig. 5.20 we plot the results at 10 GHz in real part and minus the imaginary part of ϵ_1 (on the left) and ϵ_2 (on the right). In the $[15, 42]$ degrees interval, ϵ_1 is estimated at a value oscillating around $2 - 1i$. For ϵ_2, we can observe an oscillating behaviour in the same angular range around the value of $3 - 0i$ then $2.5 - 0.8i$ as we get closer to the 45 degrees. In both plots, we see the

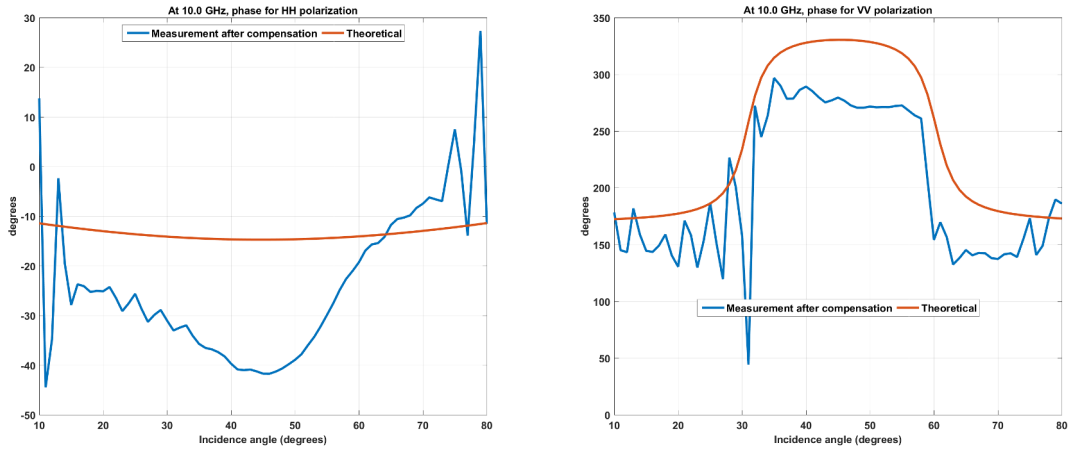

Figure 5.19 – Phases in HH and VV at 10 GHz after compensation and calibration with the metallic sphere compared to phases of a theoretical R_H^{DB} and R_V^{DB} computed from Eq. (1.6) using $\epsilon_1 = 2.75 - 0.5i$ and $\epsilon_2 = 3 - 0.6i$.

discontinuity at 45 degrees inherent to the ideal method and described in Chapter 2. In the $[50, 75]$ degrees range, we first see in the case of ϵ_1 an evolution from $2 - 1i$ to $2.5 - 0i$. ϵ_2 estimation is more stable in this domain: from 50 degrees to 70 degrees it stays at $2.5 - 1i$.
In Fig. 5.21, the results are plotted at 11 GHz. The curves are very similar to the ones at 10 GHz. Only the oscillation behaviour is more quiet confirming the estimated value at the previous frequency.

Inverting permittivities using the second method.

We apply the method from Chapter 3 using the extracted R_H^{DB}. Fig. 5.22 (resp. Fig. 5.23) shows the results of the inversion for ϵ_1 (resp. ϵ_2) in real and imaginary part at 10 GHz. From first sight, we can see two areas where no solutions are found: one is centred at $(57, 57)$ degrees and the other one smaller is centred at $(37, 37)$ degrees. ϵ_1 estimated for a real part in $[2.5, 3.5]$ and $[-1, 0]$ in imaginary part for angles in $[15, 30] \times [35, 55]$ degrees. For ϵ_2, the area where its real part is in $[2.5, 3.5]$ and its imaginary part is in $[-1, 0.5]$ is $[55, 75] \times [15, 40]$ degrees. This difference of areas of estimation and the fact that we don't retrieve well the permittivities outside these areas might be due to the error in phase of R_H^{DB} and the fact that for this method we only rely on the horizontal contribution of the double bounce.
Fig. 5.24 and Fig. 5.25 present the results but now at 11 GHz.

From these results, we can state that the results obtained from the first method are coherent with the measured permittivities performed with the near-field probe. For the second method, as we use the data from one polarization we obtain good estimate of permittivities in some areas of incidence.

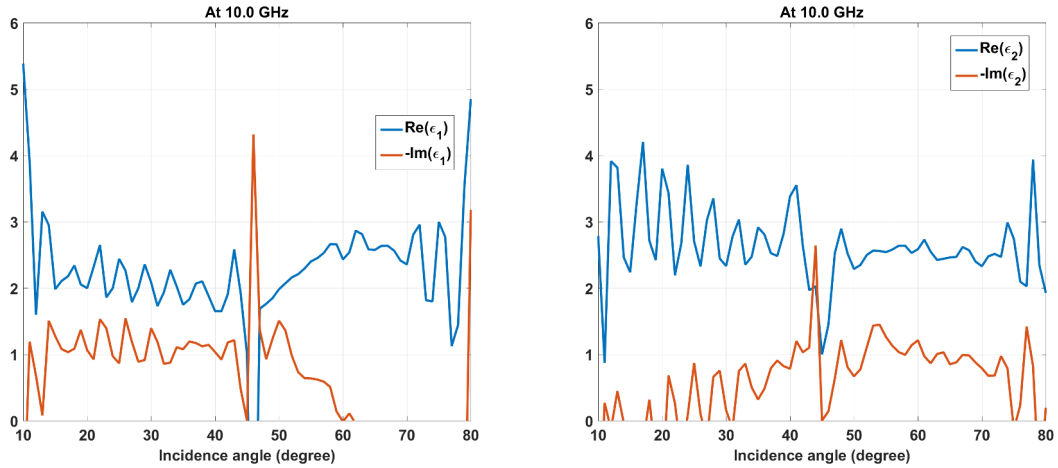

Figure 5.20 – Real and imaginary parts of ϵ_1 and ϵ_2 at 10 GHz.

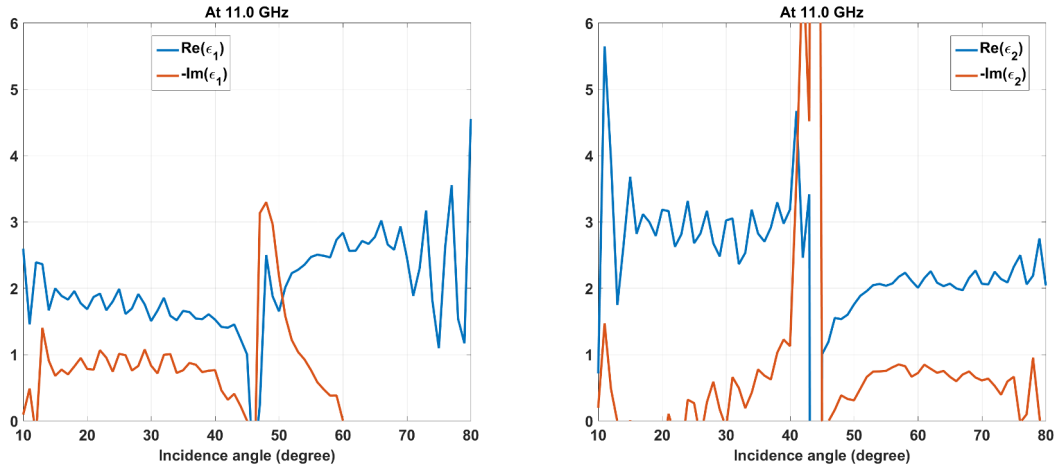

Figure 5.21 – Real and imaginary parts of ϵ_1 and ϵ_2 at 11 GHz.

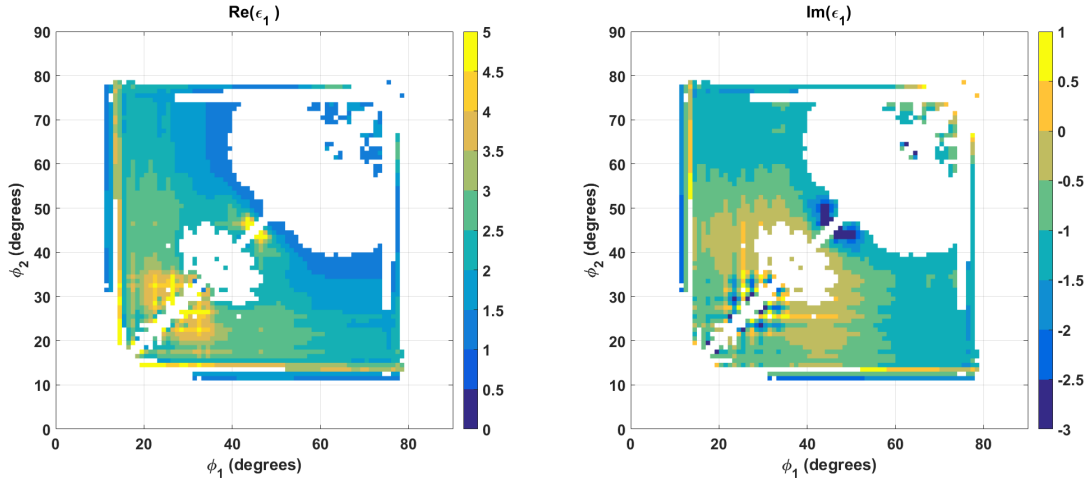

Figure 5.22 – Real and imaginary parts of ϵ_1 at 10 GHz (expected value around $2.7 - 0i$).

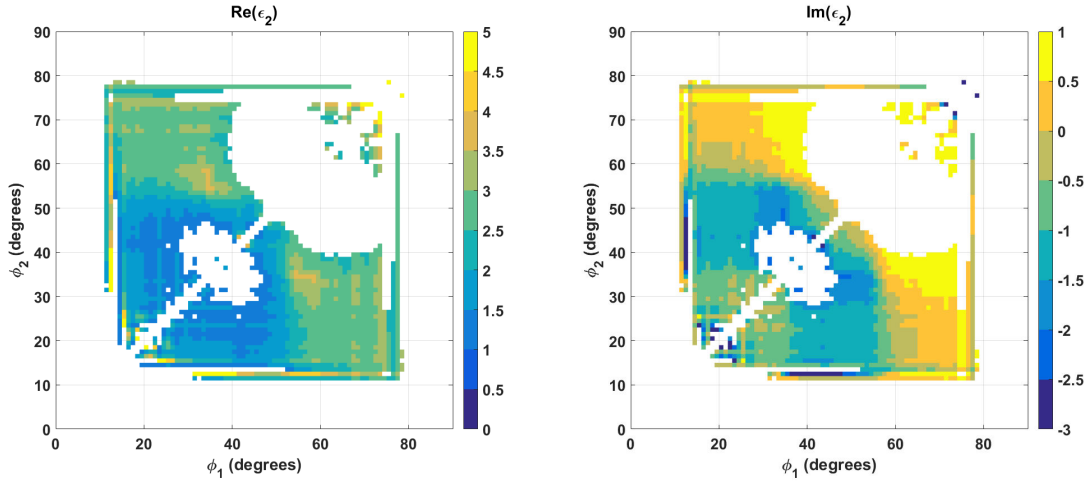

Figure 5.23 – Real and imaginary parts of ϵ_2 at 10 GHz (expected value around $3.2 - 0i$).

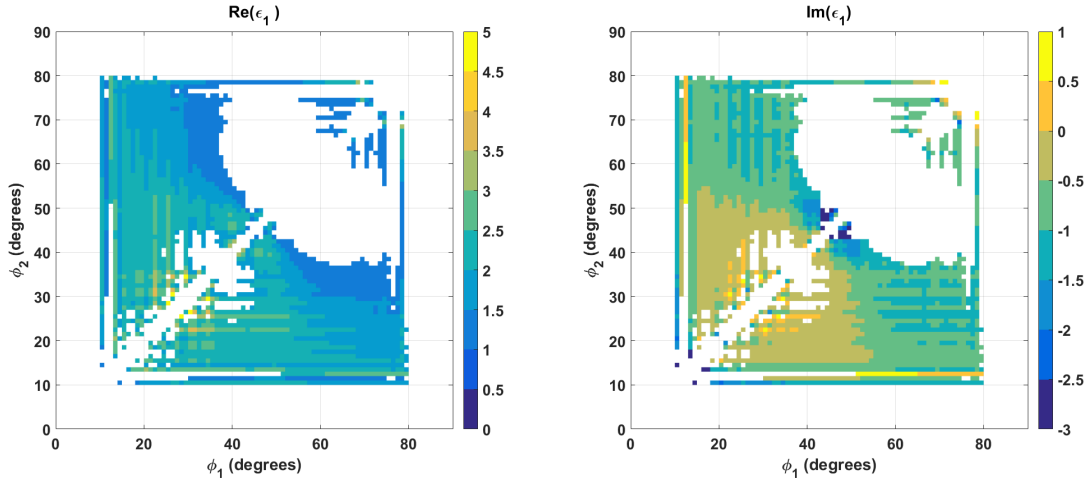

Figure 5.24 – Real and imaginary parts of ϵ_1 at 11 GHz (expected value around $2.7 - 0i$).

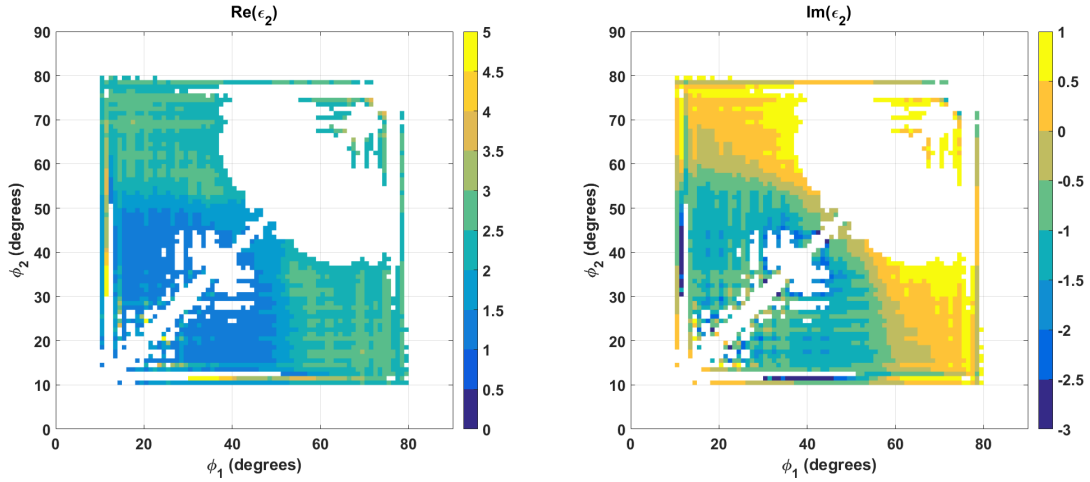

Figure 5.25 – Real and imaginary parts of ϵ_2 at 11 GHz (expected value around $3.2 - 0i$).

5.4 Measurement *in-situ*

Figure 5.26 – Wall and measurement setup.

To assess the ratio method in practice, we choose a concrete corner in the underground parking lot of Eiffel building in CentraleSupélec. In Fig. 5.26 the left image shows the concrete corner used for the measurement. The right one depicts the measurement setup that is made of the two identical antennas used previously in the anechoic chamber and two identical cables to connect the antennas to a portable VNA (Keysight N9918A). We place the trolley with the measurement setup at 4.3 meters away from the corner central edge. This distance was chosen given the height of the device on the trolley (1.1 m) and the aperture angle of the antennas (around 27 degrees) in order to keep the ground outside the illuminated area[9]. To align the antennas with the central edge of the corner, we place a laser device below the two antennas. It draws a vertical red line to guarantee that the antennas are in alignment with the central edge. In addition the laser is helpful to measure the incidence angle as the red line is also drawn on the floor. It only requires to place a printed protractor on the floor at the corner and to read it. The measurement of the mutual coupling is taken outside in the open-air. The frequency parameters are identical to the previous measurements: $[5, 18]$ GHz and 1301 points.

Therefore due to this measurement conditions, many uncertainties arise: the incidence angle is not precisely taken (from a printed protractor), likewise the distance is measured using a rangefinder but as we move the trolley to take several incidence angles the distance is also changing. To overcome this issue we tried to keep the trolley within an interval of 10 cm around the 4.3 meters first measured. We obviously are not in the far-field condition from the wall even if we only consider the greatest dimension of the illuminated area on the wall. To finish, the trolley is moving on a non-planar surface due to the rain evacuation exit. As we were to close to this exit and the trolley was tilting too much, we didn't take the measurement at 60 degrees.

In Table. 5.2 we present the temporal signals in amplitude from the measurements near the location of the wall (cables are at most 1 meter length). It is noticeable when looking at HH signal we can see the strongest peak that doesn't move in distance (around 5.6 meters) with the incidence angle. As it is at the same distance from the antennas than the wall we can infer that it is the peak corresponding to the double bounce. In addition this peak does not appear in VV polarisation, that might come from the double bounce effect. Another peak appears in distance at 5.35 meters at 20 degrees, near 5 meter at 30 degrees and at 5.35 meters at 70 degrees for both polarisation. This peak seems to move away from the double bounce signature as the incidence angle come closer

9. Considering a trigonometric approach, we have: $\frac{h}{\tan(\theta_{-3dB}/2)} \approx 4.5$m if $\theta_{-3dB} = 27$ degrees and $h = 1.1$ meter.

to 45 degrees. Hence this peak might be linked to the backscattering of one part of the wall (the closest to the measurement device) illuminated by the side of the radiation pattern of the antennas.

	HH	VV
$\phi = 20°$	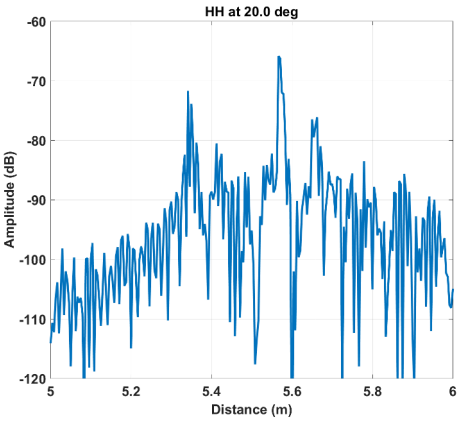	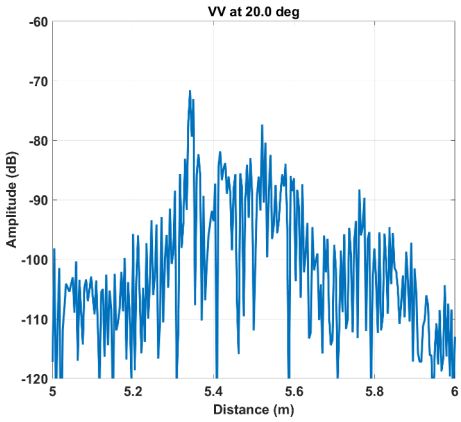
$\phi = 30°$	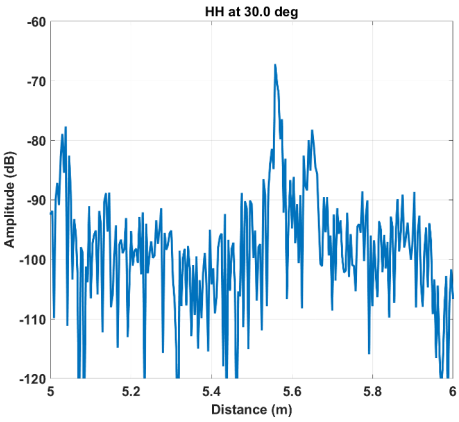	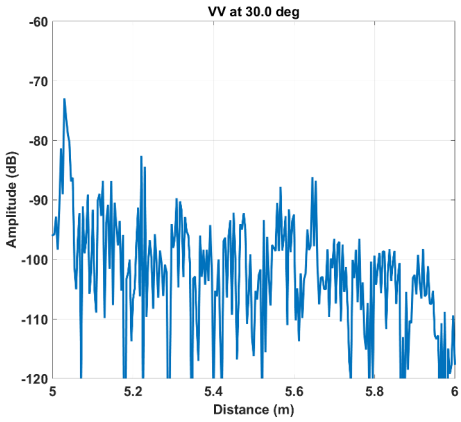
$\phi = 40°$	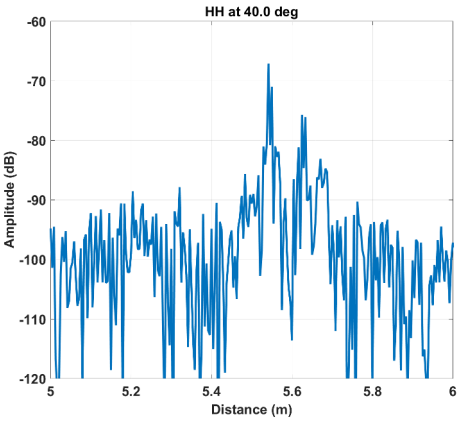	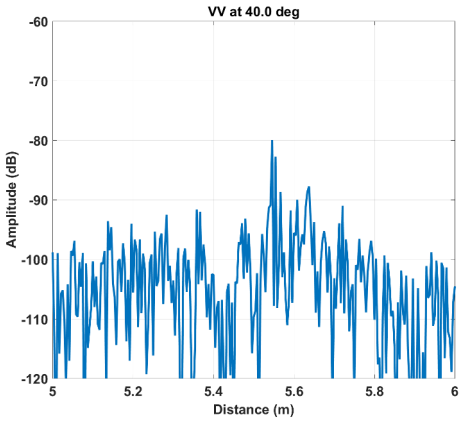

$\phi = 50°$	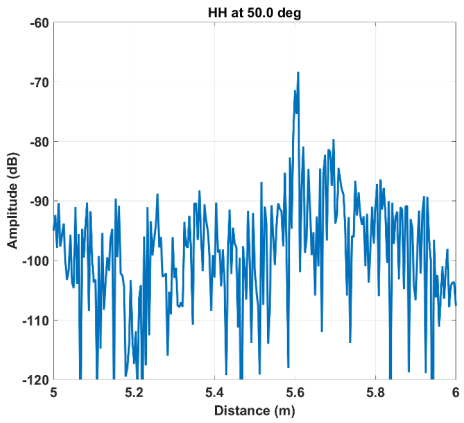	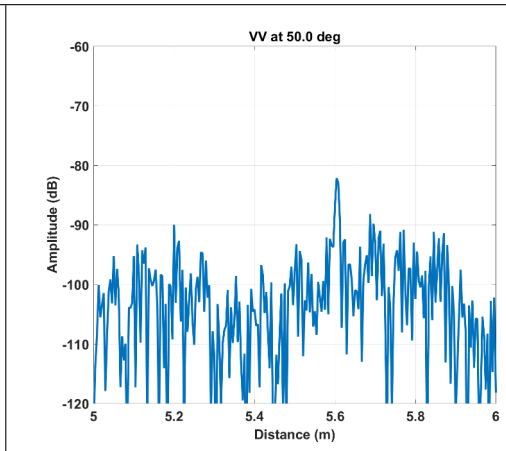
$\phi = 70°$	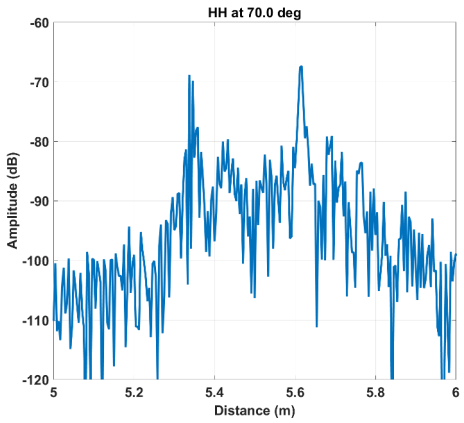	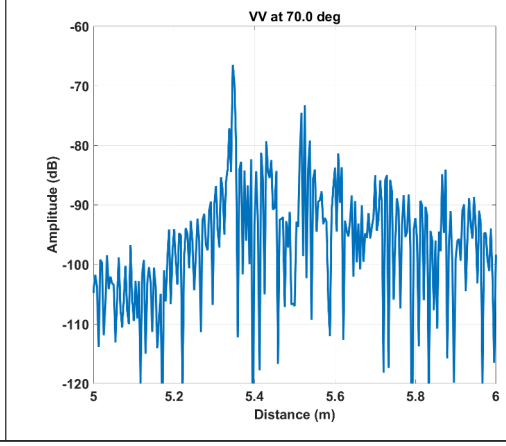

Table 5.2 – Amplitude in dB of the temporal signals in HH and VV polarizations close to the location of the wall.

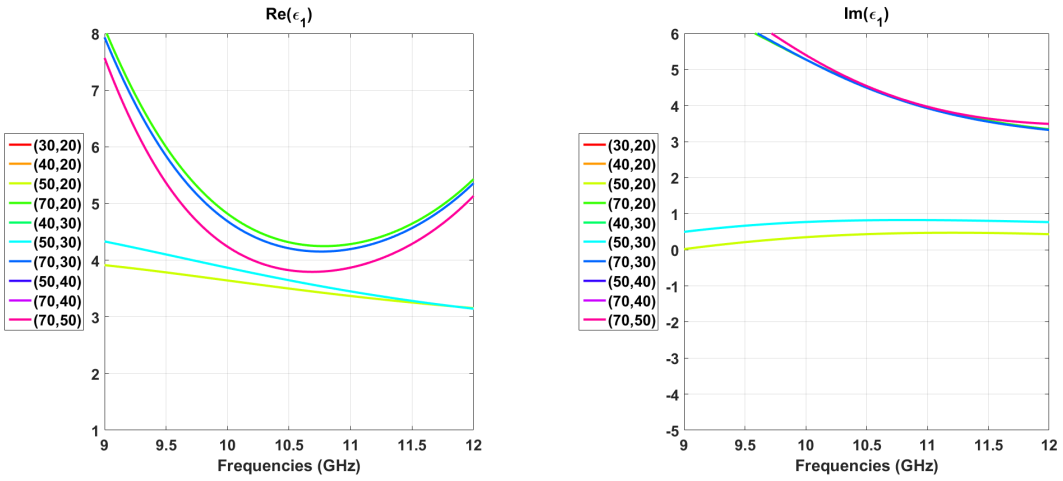

Figure 5.27 – Estimated ϵ_1 between 9 and 12 GHz before the filtering step.

HH can be easily time gated by selecting the peak as the double bounce signature is strong. For VV as it is quite difficult for some angles to distinguish the signal, we apply at the same location

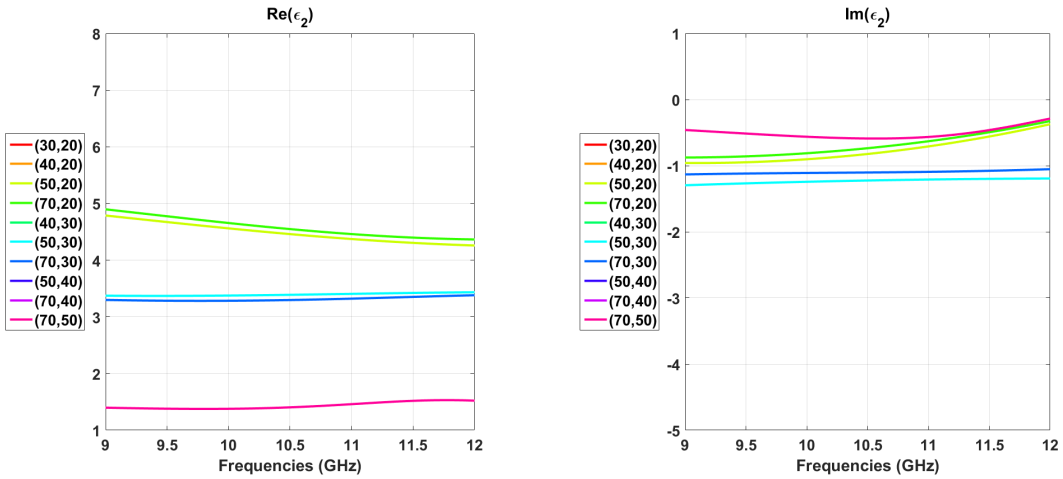

Figure 5.28 – Estimated ϵ_2 between 9 and 12 GHz before the filtering step.

the same time gating window. As a result we can now bring the windowed signal to the frequency domain and apply the ratio method developed in Chapter 4.

In Fig. 5.27 and Fig. 5.28, we plot the results of the estimated permittivities for the 9-12 GHz. These results comes from the application of the method exposed in Chapter 4 except that we remove the filter on the imaginary part of the permittivity to look at all the solutions. The colour of the curves corresponds to an angle combination as specified in the legend. From first sight, most of the combinations of angles where one angle is above and the other one is below 45 degrees are given results which corresponds to what have been observed in 4.2.1. We observe that for both permittivity the real part is evolving between 3 and 5. Most of the curves are decreasing with the frequency. The curve (purple-pink) from the $(70, 50)$ degrees is not truth-worthy as the real part of ϵ_2 is near 1.5 and the imaginary part of ϵ_1 is non-physical. In terms of imaginary part most of them are between -1.5 and 0 for ϵ_2. However for ϵ_1, we have two curves near 0, $(50, 30)$ and $(50, 20)$ degrees, the other curves are non-physical but follow the same trend, decreasing from 6 and above, to 3.5.
In Fig. 5.29 and Fig. 5.30, we present the results after adding back the filtering part on the imaginary part. It leaves us with two curves, the ones at $(50, 30)$ and $(50, 20)$ degrees. In ϵ_1, they are evolving around the same value of permittivity: 4 at 9 GHz to $3 + 0.5i$ at 12 GHz. For ϵ_2, we have a more disparate value in real part as one curve is going from nearly 5 to 4.3 and the other one is staying close to 3.5. The imaginary part of ϵ_2 is showing the same trends: one curve is evolving from -1 to -0.2 when the other one is staying at -1.2.
These values of permittivities correspond to the mortar material value around $4 - 0.5i$ found by the authors in [35] in the 8-12 GHz frequency bandwidth. These values are also compliant with air-dried or oven-dried mortar from [53]. It also matches a concrete material as characterised in [54] at low moisture content (below 4%) at 12 GHz, and it is also close to the value determined in [55].

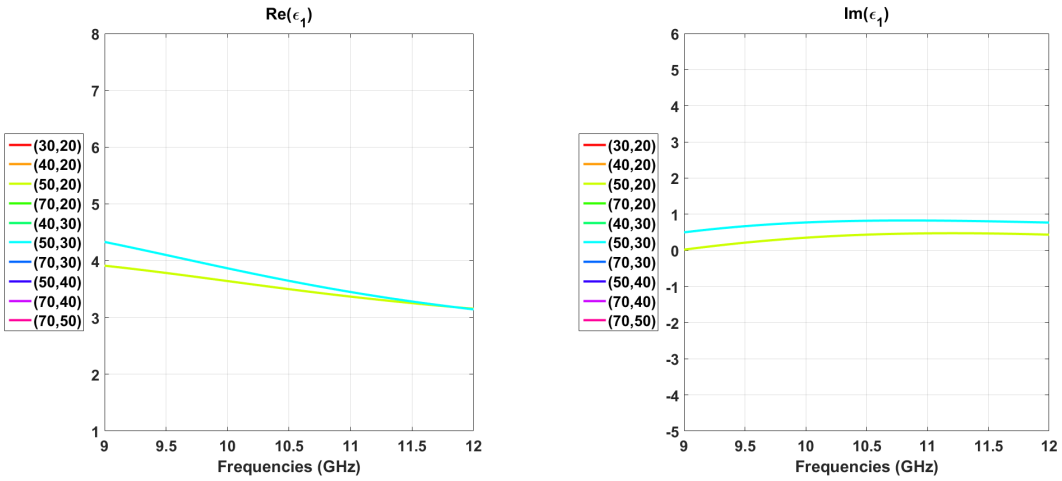

Figure 5.29 – Estimated ϵ_1 between 9 and 12 GHz.

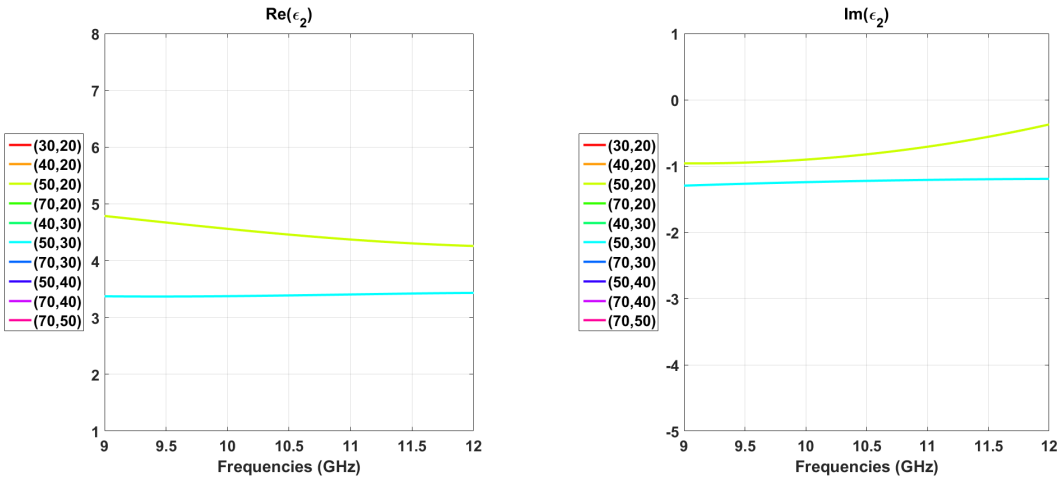

Figure 5.30 – Estimated ϵ_2 between 9 and 12 GHz.

5.5 Summary

In this chapter, we put in place an experimental validation using the controlled environment of Geeps anechoic chamber. A trade-off has been made in order to maintain a distance close to the far-field distance and to have a sufficient electrical dimension. Hence by looking in the temporal domain the signature of the dihedral rotating, we observe the movement of the edges, the backscattered fields of each plate at their own broadside, the double bounce signature and at least one reflection due to the propagation of the wave inside the plate material. After isolating the double bounce contribution, we are able to apply the method from Chapter 4. It provides quite homogeneous results over the chosen frequencies with an ϵ_1 close to $2.5 - 0.5i$ and an ϵ_2 near to $3 - 0.5i$ for high frequencies. These are good results close to the measured permittivities with the near-field probe. To assess the two first methods, as they require the absolute quantities R_V^{DB} and R_H^{DB}, we divide the compensation stage in two: one deals with the amplitude and the other one with the phase. For the amplitude we use the radar equation, the PEC scattering of an equivalent structure and the measurement of a calibration target for the anechoic chamber, to retrieve the amplitude of the double bounce coefficient. For the phase, we make the measurement for a PEC dihedral and subtract its phase to the measurement of the dielectric one. For the ideal method, this type of process is sufficient to get to good estimate of the permittivities especially in the range $[15, 40]$ degrees where they are measured close to $2.2 - 1i$ and $3 - 0.5i$ for respectively ϵ_1 and ϵ_2. However the method using one polarization from Chapter 3 provides results that are more questionable as we roughly estimate the good permittivities in separate angle areas. This might come from the error in phase worsen by the use of one polarisation alone.
We successfully apply the method from Chapter 4 to real case of a dielectric corner made of concrete in a parking lot of CentraleSupélec. Measurements were taken in HH and VV for 5 angles: 20, 30, 40, 50 and 70 degrees. We obtain for the 9-12 GHz, a real part coherent with a concrete permittivity around 3 - 5, and an imaginary part close to 0 implying a dry material.

Conclusion

During this PhD thesis, we have demonstrated analytically and validated with measurements that it is possible to retrieve the permittivity from far-field polarimetric radar data of dihedral structures. These results are important as permittivity is a key factor for the analysis of radar data. Actually, in general, we do not have access to this information, when acquiring airborne or space borne data. In addition dihedral structures are commonly present in radar images, more specifically in urban areas. The solutions we have proposed allow to determine together the permittivities of the ground (or any other horizontal surface) and of the wall (or any other vertical surfaces) constituting the dihedral.

To do this, we have developed and tested three methods to invert the permittivities in this configuration. The first method corresponds to the ideal situation: we have access to the co-polarised responses of a dihedral structure and the measurements need to be perfectly calibrated. The second method is dedicated to single polarized systems. We have shown for this case, that only HH can be used and the calibration requirements remain the same. Finally, we have lowered the constraints on the calibration with the third method as we use the ratio of the two copolarized components.

All these methods rely on the analytical formulation of a double bounce using Fresnel reflection coefficients. Indeed, any double bounce mechanisms can be modeled, at the first order, as the combination of two successive specular scattering mechanisms. We called it the double bounce equation.

As a result, we have developed and tested three methods to invert the two permittivities from the double bounce equation. An ideal method, completely analytical, was first developed from the double bounce equation. The main advantage of this method is the fact the two permittivities can be written as a direct function of the two copolarised double bounce coefficients. Among the drawbacks, two are particular annoying: the first is the 45 degrees issue. As there is an indetermination at this angle, this strongly impacts the retrieval for neighboring angles, so that the $[40, 50]^\circ$ domain has to be preferably avoided. However this divergence can also be used as an indicator of the double bounce. The second is the requirement of fully calibrated data as it needs the two complex double bounce coefficients as input.
The second method developed is based only on the horizontal polarisation. The choice of the polarization was made due to the behaviour of the double bounce coefficients in the angle range of interest. Indeed, the vertical component might lead to issue when we measure because of the double bounce. The presence of two Pseudo-Brewster angles and their corresponding magnitude drops influence the magnitude over a large range of incidence angle. To avoid this double bounce effect, we use the horizontal polarization alone. The price to this advantage is the requirement of at least two incidence angles to obtain eight possible permittivity couples that are mathematically compliant. Therefore, we filter out the non-physical solutions to keep one solution couple. As for the first method, the full calibration of the data is required as we work with the double bounce coefficient. In addition to this constraint, two angles are now required to obtain the two permittivities.
The last method is using the copolarised ratio between VV and HH polarisation of the double bounce coefficients. Within the incidence angle range where the double bounce contribution is dominant, this ratio can be approached by the ratio of the copolarised fields. Again, the advantage

of using a relative measurement is balanced by the need of two measurements at different incidence angles and the requirement of filtering the non-physical solutions. However by using the ratio we avoid the calibration step.

These three methods have been studied one by one using numerical simulations from FEKO to determine the influence of the parameters of the object or the device on the inversion results. In the first group, we have analysed the electrical dimension, the dihedral angle and the composition. For the device parameters, we have looked at its positioning in terms of incidence angle, azimuth angle and roll angle. Every method is sensitive to the electrical dimension as it is the base of the double bounce. In addition, the methods are in general highly sensitive to the dihedral angle and the incidence angle. For these two parameters, few degrees off to the reference value may lead to consequent error. On the other hand, the change in azimuth angle is handled for all methods. For the methods that need calibration, the PEC normalisation needs to be adapted to this azimuth change. For the method using the ratio, no adaptation is needed. In the case of the roll angle, every method might still work under within its own limitations. When one plate of the dihedral is composed of two different materials, the ratio and the first method of inversion rule as a mixing law of permittivities. On the other hand, the one polarisation method might detect both permittivities depending on the incidence angle combination.

The three methods have been assessed in the controlled environment of the anechoic chamber of Geeps. We used a dihedral made of PVC and nylon whose permittivities have been measured with a near field probe, a quasi-monostatic system made of two identical antennas and cables between 5 and 18 GHz. We placed the dihedral on a rotating platform at 4.3 meters of the antennas such that the rotation angle can be assimilated to the incidence angle we considered in our theoretical study. Once the measurements collected and calibrated, an analyse has been done in the time domain. As the dihedral is rotating around its central edge, one could see in the range domain the movement of the edges, the double bounce that is located at the same distance than the central edge and also two or three additional reflections due to the quasi-real permittivities of the materials involved. We discarded the other phenomenon and selected the double bounce component by time gating the time signals. Once, in frequency domain, the ratio could be computed and the last inversion method was applied. From it, we have been able to assess the compliance of the results between the near field probe and our method for few frequencies between 6 and 13 GHz. As the first two methods need a calibration, we have used the radar equation and the measurement of a canonical object (a metallic sphere) to compensate the amplitude. For the phase, we have measured a metallic dihedral to compensate the phase dihedral scattering and the rotation movement of the platform. We have been able to validate the ideal method but for the one polarisation method issues appeared as the phase of HH field was not correctly estimated.
Finally, measurements *in-situ* have been performed in an underground parking lot of CentraleSupélec. With five measurements collected at different incidence angles for both polarisations, the inversion of permittivities of a concrete corner wall has been performed using the ratio method. Eventually, we managed to retrieve consistent value for the relative permittivities. These values were relevant with respect to values we can find in literature at these frequencies.

As the ratio method is quite handy for measurements, it might worth to further study its behaviour and apply it to more cases. First, we could think at the application of such method to SAR images. Being able to determine the effective permittivities of a dihedral arrangement made by a building or tree would be significant. In order to put in place such applications from the ratio method, we can first think of taking two SAR images from two different incidences angles. Or one could also try to make a deep analyse of the SAR formation, without using the rectilinear trajectory assumption such that when applying a time-frequency method to create sub-aperture images of a building we obtain different sub-images at different incidence angles. This approach is sustained by the fact that for an identical incidence angle (so a rectilinear trajectory parallel to the building) the double bounce ratio stays unchanged. Hence either we work with two datasets taken at two incidence angles or one dataset with a sufficient change in the incidence angle such that we

could hope to apply the method.

Appendix A

Dihedral PEC formulations

In this appendix, the analytical formulations of the electric fields a PEC dihedral are given for several configurations based on Physical Optics (P.O.) approximation. They come from [6] and [7].

A.1 In bistatic configuration

In bistatic configuration, the electric fields have been calculated in [7]. All the notations, equations and schemes are from this article.
In Fig. A.1 are represented the reference frame, the dimensions of the dihedral and the angles. ϕ_r and θ_r are the spherical angles for the scattering vector $\hat{s}$. Likewise, angles ϕ_t and θ_t define the spherical angles for the incident vector $\hat{i}$. a, b and L are the dimensions of the dihedral.

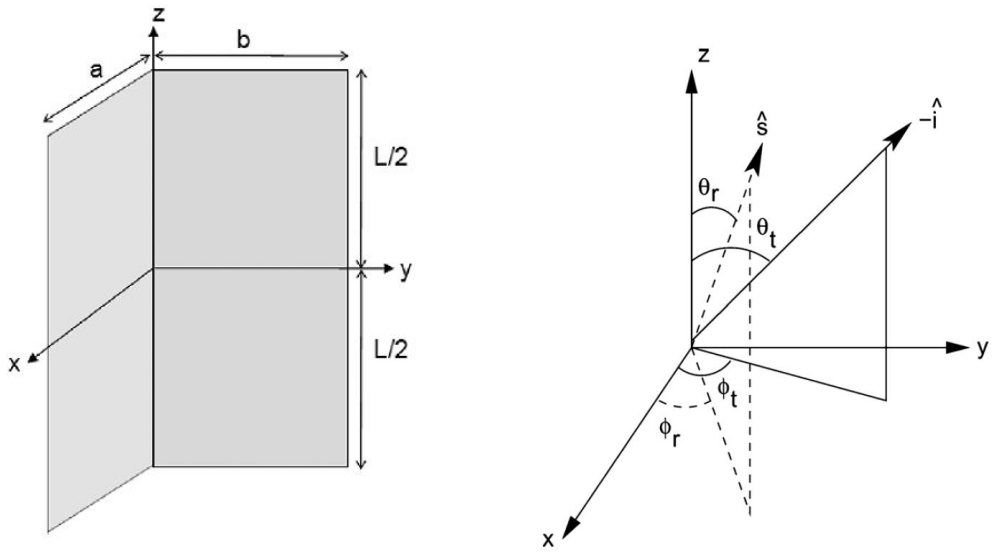

Figure A.1 – Reference frame, coordinates and dimensions of the dihedral taken from Figs. 2 and 3 in [7].

The electric fields are given by:

$$\vec{E}_{VV} = \frac{jkL}{\sqrt{\pi}} E_\theta \hat{\theta}_r \sin\theta_r \operatorname{sinc}\left[k\frac{L}{2}(\cos\theta_t + \cos\theta_r)\right] \Big(a\sin\phi_t \operatorname{sinc}\left[k\frac{a}{2}(\cos\phi_t\sin\theta_t + \cos\phi_r\sin\theta_r)\right] e^{jk\frac{a}{2}(\cos\phi_t\sin\theta_t+\cos\phi_r\sin\theta_r)} + b\cos\phi_t \operatorname{sinc}\left[k\frac{b}{2}(\sin\phi_t\sin\theta_t + \sin\phi_r\sin\theta_r)\right] e^{jk\frac{b}{2}(\sin\phi_t\sin\theta_t+\sin\phi_r\sin\theta_r)}\Big) - \frac{jk}{\sqrt{\pi}} E_\theta \hat{\theta}_r \sin\theta_r (I_{xz}\sin\phi_t + I_{yz}\cos\phi_t) \tag{A.1}$$

$$\vec{E}_{HV} = \vec{0} \tag{A.2}$$

$$\vec{E}_{VH} = \frac{-jkL}{\sqrt{\pi}} E_\phi \hat{\theta}_r \operatorname{sinc}\left[k\frac{L}{2}(\cos\theta_t + \cos\theta_r)\right] \Big(a(\sin\theta_t\cos\phi_r\cos\theta_r - \cos\phi_t\cos\theta_t\sin\theta_r)\operatorname{sinc}\left[k\frac{a}{2}(\cos\phi_t\sin\theta_t + \cos\phi_r\sin\theta_r)\right] e^{jk\frac{a}{2}(\cos\phi_t\sin\theta_t+\cos\phi_r\sin\theta_r)} + b(\sin\phi_t\cos\theta_t\sin\theta_r - \sin\theta_t\sin\phi_r\cos\theta_r)\operatorname{sinc}\left[k\frac{b}{2}(\sin\phi_t\sin\theta_t + \sin\phi_r\sin\theta_r)\right] e^{jk\frac{b}{2}(\sin\phi_t\sin\theta_t+\sin\phi_r\sin\theta_r)}\Big) - \frac{jk}{\sqrt{\pi}} E_\phi \hat{\theta}_r \big(\sin\theta_t\cos\theta_r(I_{xz}\cos\phi_r - I_{yz}\sin\phi_r) + \cos\theta_t\sin\theta_r(I_{xz}\cos\phi_t - I_{yz}\sin\phi_t)\big) \tag{A.3}$$

$$\vec{E}_{HH} = \frac{jkL}{\sqrt{\pi}} E_\phi \hat{\phi}_r \sin\theta_t \operatorname{sinc}\left[k\frac{L}{2}(\cos\theta_t + \cos\theta_r)\right] \Big(a\sin\phi_r \operatorname{sinc}\left[k\frac{a}{2}(\cos\phi_t\sin\theta_t + \cos\phi_r\sin\theta_r)\right] e^{jk\frac{a}{2}(\cos\phi_t\sin\theta_t+\cos\phi_r\sin\theta_r)} + b\cos\phi_r \operatorname{sinc}\left[k\frac{b}{2}(\sin\phi_t\sin\theta_t + \sin\phi_r\sin\theta_r)\right] e^{jk\frac{b}{2}(\sin\phi_t\sin\theta_t+\sin\phi_r\sin\theta_r)}\Big) + \frac{jk}{\sqrt{\pi}} E_\phi \hat{\phi}_r \sin\theta_t (I_{xz}\sin\phi_r + I_{yz}\cos\phi_r) \tag{A.4}$$

In those equations k is the wave number, $\hat{\phi}_r$ and $\hat{\theta}_r$ are the two last unitary vectors of the spherical scattered reference frame, E_ϕ and E_θ are the amplitudes of the incident field. I_{xz} and I_{yz} are integral terms linked to the dimensions of xz or yz plates. These two integrals have their integration limits depending on six illumination cases illustrated in Fig. 4 in [7].
I_{xz} and I_{yz} can written as:

$$I_{xz}^{(1,2,3)} = \frac{e^{jk\frac{L}{2}\psi_z}}{jk\psi_z} X \operatorname{sinc}\left[k\frac{X}{2}\left(\psi_x + \frac{\cot\theta_t}{\cos\phi_t}\psi_z\right)\right] e^{-jk\frac{X}{2}(\psi_x + \frac{\cot\theta_t}{\cos\phi_t}\psi_z)} - \frac{e^{-jk\frac{L}{2}\psi_z}}{jk\psi_z} X \operatorname{sinc}\left[k\frac{X}{2}\psi_x\right] e^{-jk\frac{X}{2}\psi_x}$$
$$I_{yz}^{(1,2,3)} = \frac{e^{jk\frac{L}{2}\psi_z}}{jk\psi_z} Y \operatorname{sinc}\left[k\frac{Y}{2}\left(\psi_y + \frac{\cot\theta_t}{\sin\phi_t}\psi_z\right)\right] e^{-jk\frac{Y}{2}(\psi_y + \frac{\cot\theta_t}{\sin\phi_t}\psi_z)} - \frac{e^{-jk\frac{L}{2}\psi_z}}{jk\psi_z} Y \operatorname{sinc}\left[k\frac{Y}{2}\psi_y\right] e^{-jk\frac{Y}{2}\psi_y} \tag{A.5}$$

for the first three cases, and

$$
\begin{aligned}
I_{xz}^{(4,5,6)} &= \frac{e^{jk\frac{L}{2}\psi_z}}{jk\psi_z} X \operatorname{sinc}\left[k\frac{X}{2}\psi_x\right] e^{-jk\frac{X}{2}\psi_x} - \frac{e^{-jk\frac{L}{2}\psi_z}}{jk\psi_z} X \operatorname{sinc}\left[k\frac{X}{2}\left(\psi_x + \frac{\cot\theta_t}{\cos\phi_t}\psi_z\right)\right] e^{-jk\frac{X}{2}(\psi_x + \frac{\cot\theta_t}{\cos\phi_t}\psi_z)} \\
I_{yz}^{(4,5,6)} &= \frac{e^{jk\frac{L}{2}\psi_z}}{jk\psi_z} Y \operatorname{sinc}\left[k\frac{Y}{2}\psi_y\right] e^{-jk\frac{Y}{2}\psi_y} - \frac{e^{-jk\frac{L}{2}\psi_z}}{jk\psi_z} Y \operatorname{sinc}\left[k\frac{Y}{2}\left(\psi_y + \frac{\cot\theta_t}{\sin\phi_t}\psi_z\right)\right] e^{-jk\frac{Y}{2}(\psi_y + \frac{\cot\theta_t}{\sin\phi_t}\psi_z)}
\end{aligned}
\tag{A.6}
$$

for the last three ones. The upper indices on I_{xz} and I_{yz} indicate the case number of illumination. Depending of the illumination case, the integral limits X and Y are different. The six conditions and their corresponding X and Y are given in table A.1. Hence given the transmitter device location (ϕ_t, θ_t), we can find X and Y, compute corresponding I_{xz} and I_{yz} and then the different $\vec{E}$. The (ψ_x, ψ_y, ψ_z) quantities are defined by:

$$
\begin{aligned}
\psi_x &= \cos\phi_t \sin\theta_t - \cos\phi_r \sin\theta_r \\
\psi_y &= \sin\phi_t \sin\theta_t - \sin\phi_r \sin\theta_r \\
\psi_z &= \cos\theta_t + \cos\theta_r
\end{aligned}
\tag{A.7}
$$

	X	Y
Case 1: $\cot\phi_t \leq \frac{a}{b}$ and $\cot\theta_t \leq \frac{L}{b}\sin\phi_t$ and $\cot\phi_t \geq 0$ and $\cot\theta_t \geq 0$	$b\cot\phi_t$	b
Case 2: $\cot\phi_t \geq \frac{a}{b}$ and $\cot\theta_t \leq \frac{L}{a}\cos\phi_t$ and $\cot\theta_t \geq 0$	a	$a\tan\phi_t$
Case 3: $\cot\theta_t \geq \frac{L}{b}\sin\phi_t$ and $\cot\theta_t \geq \frac{L}{a}\cos\phi_t$	$L\cos\phi_t\tan\theta_t$	$L\sin\phi_t\tan\theta_t$
Case 4: $\cot\phi_t \geq 0$ and $\cot\phi_t \leq \frac{a}{b}$ and $-\frac{L}{b}\sin\phi_t \leq \cot\theta_t$ and $\cot\theta_t \leq 0$	$b\cot\phi_t$	b
Case 5: $\cot\phi_t \geq \frac{a}{b}$ and $\frac{-L}{a}\cos\phi_t \leq \cot\theta_t$ and $\cot\theta_t \leq 0$	a	$a\tan\phi_t$
Case 6: $-\frac{L}{b}\sin\phi_t \geq \cot\theta_t$ and $\cot\theta_t \leq -\frac{L}{a}\cot\phi_t$	$-L\cos\phi_t\tan\theta_t$	$-L\sin\phi_t\tan\theta_t$

Table A.1 – Cases of illumination and their corresponding X and Y.

One can notice that Eqs. (A.5) and Eqs. (A.6) are presenting a singularity at $\psi_z = 0$. In this case, [7] suggests to use the following limits:

$$
\begin{aligned}
\lim_{\psi_z\to 0} I_{xz} &= \left(LX \mp \frac{X^2\cot\theta_t}{2\cos\phi_t}\right)\operatorname{sinc}\left[k\frac{X}{2}\psi_x\right] e^{-jk\frac{X}{2}\psi_x} \pm \frac{X\cot\theta_t}{jk\psi_x\cos\phi_t}\left(\cos\left(k\frac{X}{2}\psi_x\right) - \operatorname{sinc}\left[k\frac{X}{2}\psi_x\right]\right) e^{-jk\frac{X}{2}\psi_x} \\
\lim_{\psi_z\to 0} I_{yz} &= \left(LY \mp \frac{Y^2\cot\theta_t}{2\sin\phi_t}\right)\operatorname{sinc}\left[k\frac{Y}{2}\psi_y\right] e^{-jk\frac{Y}{2}\psi_y} \pm \frac{Y\cot\theta_t}{jk\psi_y\sin\phi_t}\left(\cos\left(k\frac{Y}{2}\psi_y\right) - \operatorname{sinc}\left[k\frac{Y}{2}\psi_y\right]\right) e^{-jk\frac{Y}{2}\psi_y}
\end{aligned}
\tag{A.8}
$$

The upper sign in these equations is for the first three cases of illumination, the lower sign for the last three cases. Again, in these equations, singularities appear if $\psi_x = 0$ in the first equation, or if $\psi_y = 0$ in the second. Solutions are therefore given by:

$$
\begin{aligned}
\lim_{\psi_x\to 0}\left(\lim_{\psi_z\to 0} I_{xz}\right) &= LX \mp \frac{X^2\cot\theta_t}{2\cos\phi_t} \\
\lim_{\psi_y\to 0}\left(\lim_{\psi_z\to 0} I_{yz}\right) &= LY \mp \frac{Y^2\cot\theta_t}{2\sin\phi_t}
\end{aligned}
\tag{A.9}
$$

With I_{xz} and I_{yz}, the fields $\vec{E}_{HH}$, $\vec{E}_{VH}$, $\vec{E}_{HV}$ and $\vec{E}_{VV}$ can be calculated.

A.2 In monostatic configuration

In this section, we present two formulations of the backscattered fields in monostatic configuration. First, we look at the formulation from [6] in a monostatic configuration as the one pictured

in Fig. 1.10 for a PEC dihedral with no specific dihedral angle. Then we will express using [7] the fields in the monostatic configuration we are interested.

A.2.1 For any dihedral angle

As said, we present here the main results of [6]. As in the previous section, all the notations and results are from [6]. The geometry is exposed in Fig. A.2.

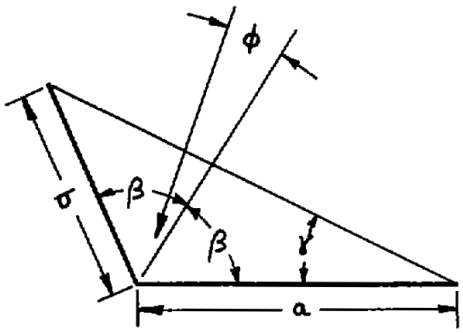

Figure A.2 – Coordinates and dimensions of the dihedral taken from Fig. 1 in [6].

Knott divided the scattering of the dihedral in four contributions: two linked of the backscattering of each plate and two from the double bounce from one plate to the other one. The scattering coefficient from each plate is given independently from the polarisation by:

$$\begin{aligned} S_a &= -ika\frac{l}{\lambda}\sin(\beta+\phi)e^{-ika\cos(\beta+\phi)}\,\mathrm{sinc}(ka\cos(\beta+\phi)) \\ S_b &= -ikb\frac{l}{\lambda}\sin(\beta-\phi)e^{-ikb\cos(\beta-\phi)}\,\mathrm{sinc}(kb\cos(\beta-\phi)) \end{aligned} \tag{A.10}$$

For the double bounce contributions, the scattering coefficients are expressed as:

$$\begin{aligned} S_{ab} &= -ikb'\frac{l}{\lambda}\sin(3\beta+\phi)e^{-ikb'\cos(2\beta)\cos(\beta+\phi)}\,\mathrm{sinc}(kb'\cos(2\beta)\cos(\beta+\phi)) \\ S_{ba} &= -ika'\frac{l}{\lambda}\sin(3\beta-\phi)e^{-ika'\cos(2\beta)\cos(\beta-\phi)}\,\mathrm{sinc}(ka'\cos(2\beta)\cos(\beta-\phi)) \end{aligned} \tag{A.11}$$

The double bounce contribution is dependent on the polarisation and it is here written for HH. The contribution for VV is obtained by substituting $\sin(3\beta\pm\phi)$ in the previous equations by $-\sin(\beta\mp\phi)$. Eqs. (A.11) are expressed as function of a' and b' that are the illuminated face width. The two quantities are defined by:

$$a' = \left\{ \begin{array}{ll} 0, & \phi \le -\alpha \\ a, & -\alpha \le \phi \le \gamma-\alpha \\ b\frac{\sin(\beta-\phi)}{\sin(3\beta-\phi)}, & \phi \ge \gamma-\alpha \end{array} \right\} \tag{A.12}$$

$$b' = \left\{ \begin{array}{ll} a\frac{\sin(\beta+\phi)}{\sin(3\beta+\phi)}, & \phi \le \gamma-\beta \\ b, & \gamma-\beta \le \phi \le \alpha \\ 0, & \phi \ge \alpha \end{array} \right\} \tag{A.13}$$

, where γ is defined as $\tan\gamma = \frac{b\sin(2\beta)}{a-b\cos(2\beta)}$.

The total contribution is the summation of S_a, S_b, S_{ab} and S_{ba}.

A.2.2 For right angle dihedrals

The following results are based on [7]. In the situation displayed in Fig. 1.10, it implies: $\theta_t = \theta_r = 90$ degrees and $\phi_t = \phi_r$. We denote $\phi_t = \phi$ to simplify. Therefore we are in the particular case described in A.1 where $\psi_z = 0$ and in addition, ψ_x and ψ_y are null.

Thus we directly have $\vec{E}_{VH} = 0$, and the limiting equations from Eqs. (A.9) are becoming:

$$\begin{aligned} I_{xz} &= LX \\ I_{yz} &= LY \end{aligned} \tag{A.14}$$

The cases 3 and 6 can not be satisfied due to the definition domain of ϕ ($[0, 90]$ degrees) and the fact that $\theta_t = 90$ degrees. Cases 5 and 2 are now equivalent to $\cot\phi \geq \frac{a}{b}$. Likewise cases 4 and 1 are also equivalent to $\cot\phi \leq \frac{a}{b}$. It reduces the six illumination cases to two regarding the value of $\cot(\phi)$ to $\frac{a}{b}$.

As a result, the backscattered electric fields can be expressed as:

$$\begin{aligned} \vec{E}_{VV} = \frac{jkL}{\sqrt{\pi}} E_\theta \hat{\theta}_r \operatorname{sinc}\left[\frac{kL}{2}\right] & \\ \left(a\sin\phi \operatorname{sinc}\left[ka\cos\phi\right] e^{jka\cos\phi} + b\cos\phi \operatorname{sinc}\left[kb\sin\phi\right] e^{jkb\sin\phi}\right) & \\ - \frac{jkL}{\sqrt{\pi}} E_\theta \hat{\theta}_r (X\sin\phi + Y\cos\phi) & \end{aligned} \tag{A.15}$$

$$\begin{aligned} \vec{E}_{HH} = \frac{jkL}{\sqrt{\pi}} E_\phi \hat{\phi}_r \operatorname{sinc}\left[\frac{kL}{2}\right] & \\ \left(a\sin\phi \operatorname{sinc}\left[ka\cos\phi\right] e^{jka\cos\phi} + b\cos\phi \operatorname{sinc}\left[kb\sin\phi\right] e^{jkb\sin\phi}\right) & \\ + \frac{jkL}{\sqrt{\pi}} E_\phi \hat{\phi}_r (X\sin\phi + Y\cos\phi) & \end{aligned} \tag{A.16}$$

, where $X = a$ and $Y = a\tan\phi$ if $\cot\phi \geq \frac{a}{b}$ or, $X = b\cot\phi$ and $Y = b$ if $\cot\phi \leq \frac{a}{b}$.

Appendix B

Chapter 2 proofs

In this appendix, we presented some proofs of the Chapter 2. The first section is dedicated to the proceedings of the solution identification and the last section is an insight of the mathematical issue encountered at the incidence angle of 45 ° .

B.1 Solutions identification

As exposed in section 2.1, we factorised the second degree equation Eq. (2.7) and obtained non-trivial solutions [1] to our problem. As we solve in X_2, we might think that one of two roots of the second degree equation is bound to it and therefore to ϵ_2. But which root, X_2^+ or X_2^- ? To answer this question, we substitute in the algebraic expression of the roots (Eq. (2.8)) the double bounce formula expressed with the permittivities (Eq. (1.6)). As the calculations are quite long and tedious but not complicated, we will present here the main steps and intermediate results.

For recall, Eq. (2.8) is written:

$$X_2^{\pm} = \frac{1}{2\sin\phi}\left(Q \pm \sqrt{Q^2+R}\right)$$

with:

$$Q = \frac{K\Lambda(\cos^2\phi - \sin^2\phi)}{\Lambda - \Gamma\cos^2\phi}$$
$$R = 4\sin^2\phi\cos^2\phi\left(1 + \frac{\cos^2\phi - \sin^2\phi}{\Lambda - \Gamma\cos^2\phi}\Gamma\right)$$

So first, let's define $Y_1 = \sqrt{\epsilon_1 - \sin\phi^2}$ and $Y_2 = \sqrt{\epsilon_2 - \cos\phi^2}$ to simplify the calculation. So we have:

$$R_H^{\mathrm{DB}} = \frac{(\cos\phi - Y_1)(\sin\phi - Y_2)}{(\cos\phi + Y_1)(\sin\phi + Y_2)} \text{ and } R_V^{\mathrm{DB}} = \frac{\left[(Y_1^2 + \sin\phi^2)\cos\phi - Y_1\right]\left[(Y_2^2 + \cos\phi^2)\sin\phi - Y_2\right]}{\left[(Y_1^2 + \sin\phi^2)\cos\phi + Y_1\right]\left[(Y_2^2 + \cos\phi^2)\sin\phi + Y_2\right]}$$

We can now substitute these quantities (R_H^{DB} and R_V^{DB}) in the intermediate quantities (K, Λ and Γ) to express them as function of Y_1 and Y_2.

When stated earlier that the calculus are not complicated, it means that they follow the same scheme as it is about substituting expressions in another one. After substitution, the first step is to have the same denominator in the quantity to calculate, then factorise what can be factorise in the numerator, expand the rest, play with the identity $\cos^2\phi + \sin^2\phi = 1$ and try to factorize as much

1. The trivial ones are removed when we went from the four to the second degree equation.

as possible in order to simplify numerator and denominator, then move on to the next quantity to express.

Let's start with K quantity:

$$K = \frac{R_H^{\mathrm{DB}} + 1}{R_H^{\mathrm{DB}} - 1} = \frac{(\cos\phi - Y_1)(\sin\phi - Y_2) + (\cos\phi + Y_1)(\sin\phi + Y_2)}{(\cos\phi - Y_1)(\sin\phi - Y_2) - (\cos\phi + Y_1)(\sin\phi + Y_2)} = \frac{\cos\phi\sin\phi + Y_1Y_2}{-(Y_2\cos\phi + Y_1\sin\phi)}$$

$$\boxed{K = \frac{\cos\phi\sin\phi + Y_1Y_2}{-(Y_2\cos\phi + Y_1\sin\phi)}}$$

Then: $R_V^{\mathrm{DB}} - 1 = \dfrac{\Big[(Y_1^2 + \sin\phi^2)\cos\phi - Y_1\Big]\Big[(Y_2^2 + \cos\phi^2)\sin\phi - Y_2\Big]}{\Big[(Y_1^2 + \sin\phi^2)\cos\phi + Y_1\Big]\Big[(Y_2^2 + \cos\phi^2)\sin\phi + Y_2\Big]} - 1$

$$\iff R_V^{\mathrm{DB}} - 1 = \frac{\nu}{\Big[(Y_1^2 + \sin\phi^2)\cos\phi + Y_1\Big]\Big[(Y_2^2 + \cos\phi^2)\sin\phi + Y_2\Big]}$$

where $\nu = \Big[(Y_1^2 + \sin\phi^2)\cos\phi - Y_1\Big]\Big[(Y_2^2 + \cos\phi^2)\sin\phi - Y_2\Big] - \Big[(Y_1^2 + \sin\phi^2)\cos\phi + Y_1\Big]\Big[(Y_2^2 + \cos\phi^2)\sin\phi + Y_2\Big]$.

It leads after expansion of ν to:

$$\boxed{R_V^{\mathrm{DB}} - 1 = \frac{-2\big(Y_2Y_1^2\cos\phi + \sin\phi^2\cos\phi Y_2 + Y_1Y_2^2\sin\phi + \cos\phi^2\sin\phi Y_1\big)}{(Y_1^2\cos\phi + \sin\phi^2\cos\phi + Y_1)(Y_2^2\sin\phi + \cos\phi^2\sin\phi + Y_2)}}$$

Likewise, we obtain:

$$\boxed{R_V^{\mathrm{DB}} + 1 = \frac{2\Big(Y_1^2Y_2^2\cos\phi\sin\phi + \cos\phi^3\sin\phi Y_1^2\sin\phi^3\cos\phi Y_2^2 + \sin\phi^3\cos\phi^3 + Y_1Y_2\Big)}{(Y_1^2\cos\phi + \sin\phi^2\cos\phi + Y_1)(Y_2^2\sin\phi + \cos\phi^2\sin\phi + Y_2)}}$$

We can now calculate $\Lambda = R_V^{\mathrm{DB}} - 1 - K(R_V^{\mathrm{DB}} + 1)$. To do that, we set $D_R = (Y_1^2\cos\phi + \sin\phi^2\cos\phi + Y_1)(Y_2^2\sin\phi + \cos\phi^2\sin\phi + Y_2)$ which is the denominator of $R_V^{\mathrm{DB}} + 1$ and $R_V^{\mathrm{DB}} - 1$. And we calculate $D_R(Y_2\cos\phi + Y_1\sin\phi)\Lambda$. After expansion of the terms, we can factorise them back to obtain:

$$\boxed{\Lambda = \frac{2\cos\phi\sin\phi(Y_1Y_2 + \cos\phi\sin\phi)(Y_1^2 - \cos\phi^2)(Y_2^2 - \sin\phi^2)}{(Y_1^2\cos\phi + \sin\phi^2\cos\phi + Y_1)(Y_2^2\sin\phi + \cos\phi^2\sin\phi + Y_2)(Y_2\cos\phi + Y_1\sin\phi)}}$$

In the case of $\Gamma = (R_V^{\mathrm{DB}} - 1)(1 - K^2)$, we first write it as:

$$\Gamma = \frac{-2\big(Y_2Y_1^2\cos\phi + \sin\phi^2\cos\phi Y_2 + Y_1Y_2^2\sin\phi + \cos\phi^2\sin\phi Y_1\big)}{(Y_1^2\cos\phi + \sin\phi^2\cos\phi + Y_1)(Y_2^2\sin\phi + \cos\phi^2\sin\phi + Y_2)} \times \underbrace{\left[\frac{(Y_2\cos\phi + Y_1\sin\phi)^2 - (\cos\phi\sin\phi + Y_1Y_2)^2}{(Y_2\cos\phi + Y_1\sin\phi)^2}\right]}_{\kappa}$$

By isolating κ and developing its numerator, we are able to simplify it to :

$$\kappa = \frac{-(Y_1^2 - \cos\phi^2)(Y_2^2 - \sin\phi^2)}{(Y_2\cos\phi + Y_1\sin\phi)^2}$$

In addition, by also noticing that $(Y_1Y_2+\cos\phi\sin\phi)(Y_1\cos\phi+Y_2\sin\phi) = \cos\phi Y_1^2Y_2+\sin\phi Y_1Y_2^2+\sin\phi\cos\phi^2Y_1+\cos\phi\sin\phi^2Y_2$ we obtain:

$$\boxed{\Gamma = \frac{2(Y_1Y_2+\cos\phi\sin\phi)(Y_1\cos\phi+Y_2\sin\phi)(Y_1^2-\cos\phi^2)(Y_2^2-\sin\phi^2)}{(Y_1^2\cos\phi+\sin\phi^2\cos\phi+Y_1)(Y_2^2\sin\phi+\cos\phi^2\sin\phi+Y_2)(Y_2\cos\phi+Y_1\sin\phi)^2}}$$

Now that all the "first" intermediate quantities are expressed as function of Y_1 and Y_2, we will do the same using the previous results to $\Lambda-\cos\phi^2\Gamma$ in order to, at the end, be able to express Q and R from Eq. (2.8) as function of Y_1 and Y_2.

First, for $\Lambda-\cos\phi^2\Gamma$, we get the following result by having the same denominator and factorizing the numerator:

$$\boxed{\Lambda-\cos\phi^2\Gamma = \frac{2\cos\phi(\sin\phi^2-\cos\phi^2)Y_1(Y_1Y_2+\cos\phi\sin\phi)(Y_1^2-\cos\phi^2)(Y_2^2-\sin\phi^2)}{(Y_1^2\cos\phi+\sin\phi^2\cos\phi+Y_1)(Y_2^2\sin\phi+\cos\phi^2\sin\phi+Y_2)(Y_2\cos\phi+Y_1\sin\phi)^2}}.$$

So finally we obtain: $\boxed{Q = \frac{K\Lambda(\cos\phi^2-\sin\phi^2)}{\Lambda-\cos\phi^2\Gamma} = \frac{\sin\phi(Y_1Y_2+\cos\phi\sin\phi)}{Y_1}}$

R can be easily expressed as : $R = 4\sin^2\phi\cos^2\phi\left(1+\frac{\cos^2\phi-\sin^2\phi}{\Lambda-\Gamma\cos^2\phi}\Gamma\right)$.

Hence, we get $\boxed{R = \frac{-4\cos\phi\sin\phi^3Y_2}{Y_1}}$.

Now considering the sum Q^2+R we can simplify it to : $Q^2+R = \frac{\sin\phi^2}{Y_1^2}(Y_1Y_2-\cos\phi\sin\phi)^2$.

Therefore, Eq. (2.8) can be rewritten as:

$$\begin{aligned}
X_2^{\pm} &= \frac{1}{2\sin\phi}\left(Q\pm\sqrt{Q^2+R}\right)\\
&= \frac{1}{2\sin\phi}\left[\frac{\sin\phi(Y_1Y_2+\cos\phi\sin\phi)}{Y_1}\pm\frac{\sin\phi(Y_1Y_2-\cos\phi\sin\phi)}{Y_1}\right]\\
&= \frac{1}{2Y_1\sin\phi}\left[\sin\phi(Y_1Y_2+\cos\phi\sin\phi)\pm\sin\phi(Y_1Y_2-\cos\phi\sin\phi)\right]
\end{aligned}$$

.

As a consequence, we have:

$\boxed{X_2^+ = Y_2}$

$\boxed{X_2^- = \frac{\cos\phi\sin\phi}{Y_1}}$

such that, X_2^+ leads to ϵ_2 and X_2^- to ϵ_1.

B.2 Issue at 45 degrees of incidence angle

We present here the inquiry carried to determine the origin of the issue at 45 ° of incidence angle.

1) First step From [2], we know that at $\phi=\frac{\pi}{4}$, we get $(R_H^{\mathrm{DB}})^2 = R_V^{\mathrm{DB}}$. We can now wonder how this relation is bound to the discontinuity of the solutions. It is the goal of this section.

Let's first express R_V^{DB} and R_H^{DB} at $\phi = \frac{\pi}{4}$:

$$R_V^{\mathrm{DB}} = \frac{\frac{\sqrt{2}}{2}\epsilon_1 - \sqrt{\epsilon_1 - \frac{1}{2}}}{\frac{\sqrt{2}}{2}\epsilon_1 + \sqrt{\epsilon_1 - \frac{1}{2}}} \times \frac{\frac{\sqrt{2}}{2}\epsilon_2 - \sqrt{\epsilon_2 - \frac{1}{2}}}{\frac{\sqrt{2}}{2}\epsilon_2 + \sqrt{\epsilon_2 - \frac{1}{2}}}$$
$$\iff R_V^{\mathrm{DB}} = \frac{\epsilon_1 - \sqrt{2\epsilon_1 - 1}}{\epsilon_1 + \sqrt{2\epsilon_1 - 1}} \times \frac{\epsilon_2 - \sqrt{2\epsilon_2 - 1}}{\epsilon_2 + \sqrt{2\epsilon_2 - 1}}$$

Let's define $T_1 = \sqrt{2\epsilon_1}$ and $T_2 = \sqrt{2\epsilon_2}$.

Therefore we have: $R_H^{\mathrm{DB}} = \frac{(1-T_1)(1-T_2)}{(1+T_1)(1+T_2)}$ and $R_V^{\mathrm{DB}} = \frac{\frac{T_1^2+1}{2} - T_1}{\frac{T_1^2+1}{2} + T_1} \times \frac{\frac{T_2^2+1}{2} - T_2}{\frac{T_2^2+1}{2} + T_2}$

$$\iff R_V^{\mathrm{DB}} = \frac{(T_1^2 - 2T_1 + 1)(T_2^2 - 2T_2 + 1)}{(T_1^2 + 2T_1 + 1)(T_2^2 + 2T_2 + 1)} = \frac{(1-T_1)^2(1-T_2)^2}{(1+T_1)^2(1+T_2)^2} = (R_H^{\mathrm{DB}})^2$$

Finally we obtain:

$$\boxed{R_V^{\mathrm{DB}} = \frac{(1-T_1)^2(1-T_2)^2}{(1+T_1)^2(1+T_2)^2} = (R_H^{\mathrm{DB}})^2} \tag{B.1}$$

We now show that $\frac{1}{2}\Gamma - \Lambda = 0$ (*i.e.* at $\phi = \frac{\pi}{4}$, $\Lambda - \cos\phi^2\Gamma = 0$).

$$K = \frac{1 + R_H^{\mathrm{DB}}}{R_H^{\mathrm{DB}} - 1} = \frac{(1-T_1)(1-T_2) + (1+T_1)(1+T_2)}{(1-T_1)(1-T_2) - (1+T_1)(1+T_2)} = \frac{1 + T_1T_2}{-T_1 - T_2}$$

So given that:

$$\begin{aligned} R_V^{\mathrm{DB}} &= (R_H^{\mathrm{DB}})^2 \\ \Lambda &= ((R_H^{\mathrm{DB}})^2 - 1) - K((R_H^{\mathrm{DB}})^2 + 1) = (R_H^{\mathrm{DB}})^2(1-K) - 1 - K \\ \Gamma &= ((R_H^{\mathrm{DB}})^2 - 1)(1 - K^2), \end{aligned}$$

we get, $\frac{1}{2}\Gamma - \Lambda = (R_H^{\mathrm{DB}})^2\left[\frac{1}{2} - \frac{1}{2}K^2 - 1 + K\right] - \left[\frac{1}{2} - \frac{1}{2}K^2 - 1 - K\right]$

$$\iff \frac{1}{2}\Gamma - \Lambda = (R_H^{\mathrm{DB}})^2\left[-\frac{1}{2} + K - \frac{1}{2}K^2\right] - \left[-\frac{1}{2} - K - \frac{1}{2}K^2\right] = \frac{-(R_H^{\mathrm{DB}})^2}{2}\left[1-K\right]^2 + \frac{1}{2}\left[1+K\right]^2$$

And as we have, $K - 1 = \frac{(1+T_1)(1+T_2)}{-T_1 - T_2}$ and $K + 1 = \frac{(1-T_1)(1-T_2)}{-T_1 - T_2}$ we obtain:

$$\frac{1}{2}\Gamma - \Lambda = \frac{1}{2(T_1+T_2)^2}\underbrace{\left[-(R_H^{\mathrm{DB}})^2(1+T_1)^2(1+T_2)^2 + (1-T_1)^2(1-T_2)^2\right]}_{=0 \text{ from Eq. (B.1)}}$$

Hence, we have: $\frac{1}{2}\Gamma - \Lambda = 0$

2) The indetermination: By definition of Λ and Γ, we can write:

$$\begin{aligned} \Lambda - \cos\phi^2\Gamma &= R_V^{\mathrm{DB}} - 1 - K(R_V^{\mathrm{DB}} + 1) - \cos\phi^2(R_V^{\mathrm{DB}} - 1)(1 - K^2) \\ &= R_V^{\mathrm{DB}} \underbrace{(\cos\phi^2 K^2 + \sin\phi^2 - K)}_{\chi_1} - \underbrace{(\cos\phi^2(K^2 - K) + \sin\phi^2(1+K))}_{\chi_2} \end{aligned}$$

.

We can expressed χ_1 as:

$$\chi_1 = \cos\phi^2\left[\left(\frac{R_H^{\mathrm{DB}}+1}{R_H^{\mathrm{DB}}-1}\right)^2 - \left(\frac{R_H^{\mathrm{DB}}+1}{R_H^{\mathrm{DB}}-1}\right)\right] + \sin\phi^2\left[1-\left(\frac{R_H^{\mathrm{DB}}+1}{R_H^{\mathrm{DB}}-1}\right)\right]$$

$$\iff \chi_1 = \frac{1}{(R_H^{\mathrm{DB}}-1)^2}\Big[\cos\phi^2\big((R_H^{\mathrm{DB}})^2+2R_H^{\mathrm{DB}}+1-(R_H^{\mathrm{DB}})^2+1\big)+\sin\phi^2\big((R_H^{\mathrm{DB}})^2-2R_H^{\mathrm{DB}}+1-(R_H^{\mathrm{DB}})^2+1\big)\Big]$$

$$\iff \chi_1 = \frac{2}{(R_H^{\mathrm{DB}}-1)^2}\Big[R_H^{\mathrm{DB}}(\cos\phi^2-\sin\phi^2)+1\Big]$$

For χ_2, we have:

$$\chi_2 = \cos\phi^2\left[\left(\frac{R_H^{\mathrm{DB}}+1}{R_H^{\mathrm{DB}}-1}\right)^2 + \left(\frac{R_H^{\mathrm{DB}}+1}{R_H^{\mathrm{DB}}-1}\right)\right] + \sin\phi^2\left[1+\left(\frac{R_H^{\mathrm{DB}}+1}{R_H^{\mathrm{DB}}-1}\right)\right]$$

$$\iff \chi_2 = \frac{1}{(R_H^{\mathrm{DB}}-1)^2}\Big[\cos\phi^2\Big[2(R_H^{\mathrm{DB}})^2+2R_H^{\mathrm{DB}}\Big]+\sin\phi^2\Big[2(R_H^{\mathrm{DB}})^2-2R_H^{\mathrm{DB}}\Big]\Big]$$

$$\iff \chi_2 = \frac{2R_H^{\mathrm{DB}}}{(R_H^{\mathrm{DB}}-1)^2}\Big[R_H^{\mathrm{DB}}+\cos\phi^2-\sin\phi^2\Big]$$

Hence,

$$\begin{aligned}\Lambda-\cos\phi^2\Gamma &= R_V^{\mathrm{DB}}\chi_1-\chi_2\\ &= \frac{2}{(R_H^{\mathrm{DB}}-1)^2}\Big[R_V^{\mathrm{DB}}R_H^{\mathrm{DB}}(\cos\phi^2-\sin\phi^2)+R_V^{\mathrm{DB}}-(R_H^{\mathrm{DB}})^2-R_H^{\mathrm{DB}}(\cos\phi^2-\sin\phi^2)\Big]\end{aligned}$$

It can be written as: $\Lambda-\cos\phi^2\Gamma = \dfrac{2}{(R_H^{\mathrm{DB}}-1)^2}\Big[(\cos\phi^2-\sin\phi^2)\Big[R_V^{\mathrm{DB}}-1\Big]R_H^{\mathrm{DB}}+R_V^{\mathrm{DB}}-(R_H^{\mathrm{DB}})^2\Big]$.

This last equation shows why $\Lambda-\cos\phi^2\Gamma=0$ at $\phi=\frac{\pi}{4}$: $(\cos\phi^2-\sin\phi^2)$ and $R_V^{\mathrm{DB}}-(R_H^{\mathrm{DB}})^2$ are null at this angle given the results from the first paragraph.

Therefore, $\dfrac{\Lambda-\cos\phi^2\Gamma}{\cos\phi^2-\sin\phi^2} = \dfrac{2}{(R_H^{\mathrm{DB}}-1)^2}\Big[(R_V^{\mathrm{DB}}-1)R_H^{\mathrm{DB}}+\dfrac{R_V^{\mathrm{DB}}-(R_H^{\mathrm{DB}})^2}{\cos\phi^2-\sin\phi^2}\Big]$. As a consequence, the ratio $\dfrac{R_V^{\mathrm{DB}}-(R_H^{\mathrm{DB}})^2}{\cos\phi^2-\sin\phi^2}$ is undetermined at $\phi=\frac{\pi}{4}$, making $\dfrac{\Lambda-\cos\phi^2\Gamma}{\cos\phi^2-\sin\phi^2}$ quantity also undetermined. This $\dfrac{\Lambda-\cos\phi^2\Gamma}{\cos\phi^2-\sin\phi^2}$ is explicitly found in Q and R expressions in Eq. (2.8), making them and the roots $X_2^{\pm}$ also undetermined at this angle.

Appendix C

Differences between the two kinds of solvers

In this appendix, we illustrate the invariance of the results to the choice of variable used to solve the problem. In Chapters 3 and in 4, after stating the need of two measurements, we wrote the invariance of the permittivity to them. This step (Eq. (3.3) and Eq. (4.6)) was done in both cases for ϵ_1 which allows us to solve in ϵ_2 (ξ_1 and ξ_2). The question is then if the results of the inversion change if we write the ϵ_2 invariance and solve in ϵ_1.
As said, we illustrate in the next two paragraphs this matter by building two solvers: the first one is the one developed in the Chapters 3 and 4, the second is the results from swapping the role of the permittivity when the invariance is written. The first paragraph is dedicated to the method from Chapter 3 and the second to the one from Chapter 4. To do that, we use the same simulated data from the section 2.3.1: the backscattered fields are calculated at 0.3 and 1 GHz for a dihedral structure of dimensions $(a, b, c, L) = (18, 18, 1, 18)$m and where permittivities are set to $\epsilon_1 = 10 - 3i$ and $\epsilon_2 = 2.4 - 4.5i$.

For the method developed in Chapter 3 In Fig. C.1, we plot the maximum difference along the frequency axis between the permittivity estimated by the two solvers. It is expressed as $\log_{10}(max(|\epsilon_i^{s1} - \epsilon_i^{s2}|))$ where i denotes which permittivity is concerned, and $s1$ and $s2$ are notations for the first and the second solver. Note that we omit the cases where one solver provides results but not the other one. These cases are removed from the calculation. At one frequency, if both solvers give a result in ϵ_1 or ϵ_2, we calculate the previous quantity. From the figures, we clearly see that there is no difference between the permittivities up to 10^{-7}.

For the method developed in Chapter 4 Likewise in Fig; C.2, we plot the same quantity as for the previous method, and again, we have little difference between the results of the two solvers. However, we can notice that patterns are appearing and that for very high incidence angles, very low ones and the borders we see the difference increasing up to 10^{-3} at most.

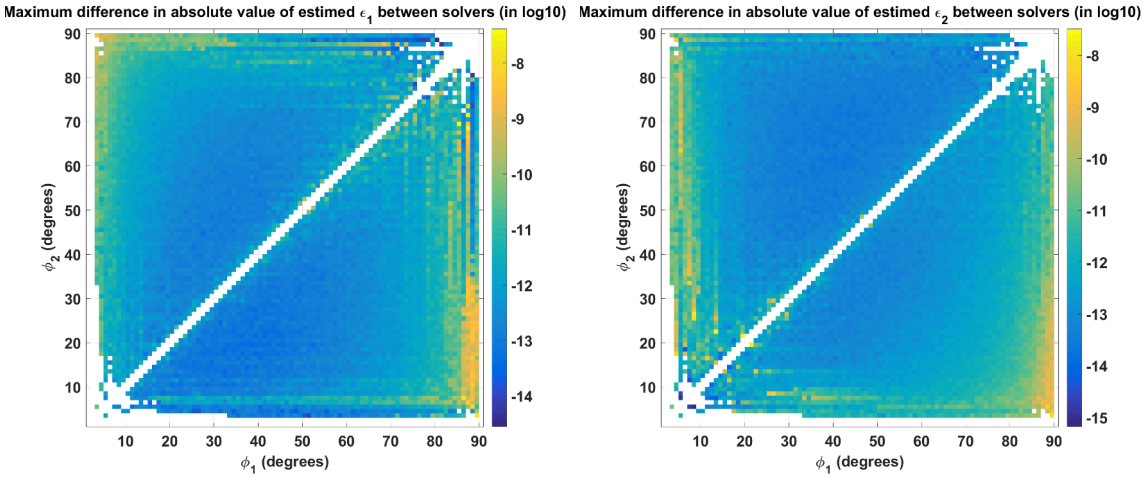

Figure C.1 – Maximum differences in $\log_{10}$ along the frequency axis between the solvers for each permittivity.

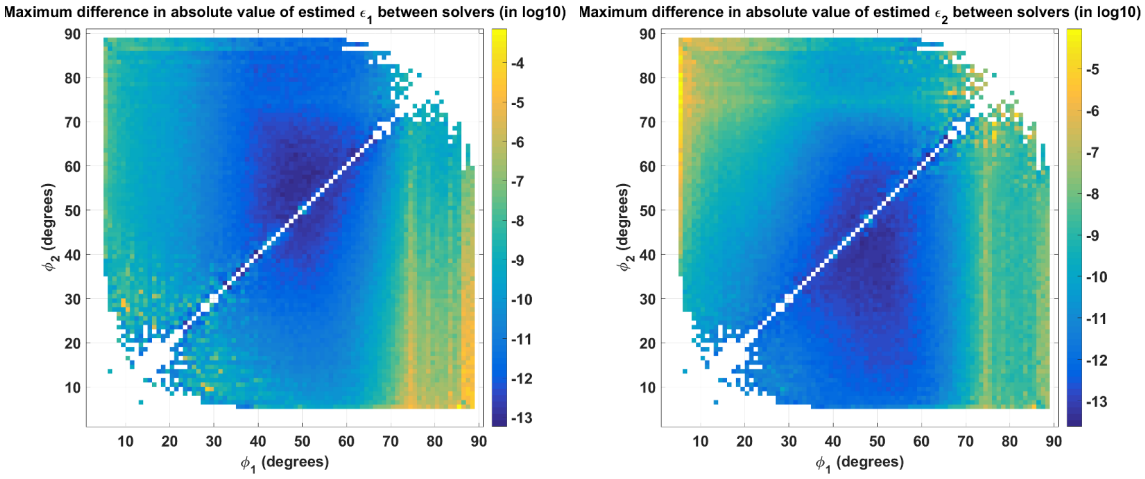

Figure C.2 – Maximum differences in $\log_{10}$ along the frequency axis between the solvers for each permittivity.

Appendix D

Appendix to section 5.1

In this appendix, we expose some further explainations related to the section 5.1 especially to the farfield condition of the dihedral and the quasi-monostatic arrangement of the antennas. The first topic is illustrated with a PEC dihedral of dimension $0.3 \times 0.3 \times 0.3$ m simulated with the Method of Moment from FEKO at different distances. In the second section, we analyse the different configurations available to build a quasi-mostatic system that provides the closest signature to a monostatic one.

D.1 Farfield of a PEC dihedral

As we are going to study the farfield condition of the dihedral in the situation of the measurement that is being designed in section 5.1, we use the Method of Moments from FEKO to simulate a $0.3 \times 0.3 \times 0.3$ m structure. To simplify the simulation, we consider a PEC dihedral, such that we can compare the results from the results from APO solution provided by [7] (also in appendix A). A plane wave is used as the incident wave as the farfield distance of the antennas is 1.8 meter at maximum in the antenna bandwidth. For recall, the distance between antennas and the dihedral is set at 4.3 meter. As we want to determine if at this distance the dihedral is at a farfield condition, we use the nearfield card in FEKO to calculate the scattered field for all the polarisation vectors in addition of the propagation vector. Therefore, we can observe the evolution in amplitude and phase of the simulated fields from 0.5 m to 30 m with a step of 0.5 m. We begin at 0.5 m such that we are able to observe the field evolution from near to far field, even it is unrealistic given the antenna chart and the setup put in place.

We plot in Fig. D.1 and Fig. D.2 the field components at respectively 5 and 18 GHz, from a 0 to 10 meters distance and at 45 degrees of incidence angle. We threshold the y axis at -80 dB even if some curves are located below (and thus considered being null). The fields are named in relation with the spherical frame of FEKO (r,ϕ,θ). Hence ϕ (here and only here) denotes the H polarisation at the emission as at the reception. Likewise, θ denotes the V polarisation. r denotes the scattered direction. One condition we may look first is the presence of null fields in the scattered direction of propagation r. In order to obtain a scattered plane wave, field's components in the r direction should be null and as we can see in the Figures: $E_{\phi,r}$ is null everywhere (below -80 dB at 5 as at 18 GHz) as for $E_{\theta,r}$ (also below -80 dB).
From these figures we can also check that as the APO solution we have $\vec{E}_{HV} = \vec{0}$ and $\vec{E}_{VH} = \vec{0}$ (see section A.2.2). These facts are verified as $E_{\phi,\theta}$ and $E_{\theta,\phi}$ are also located below the -80 dB boundary. Only the $E_{\phi,\phi}$ and $E_{\theta,\theta}$ (corresponding to E_{HH} and E_{VV} in our usual notation) are not null (from 6 dB to -20 at 5 GHz and from 6 dB to -10 dB at 18 GHz). We can also notice that they decrease with the distance as an inverse function of it except for the first meters (enhanced later in this section).

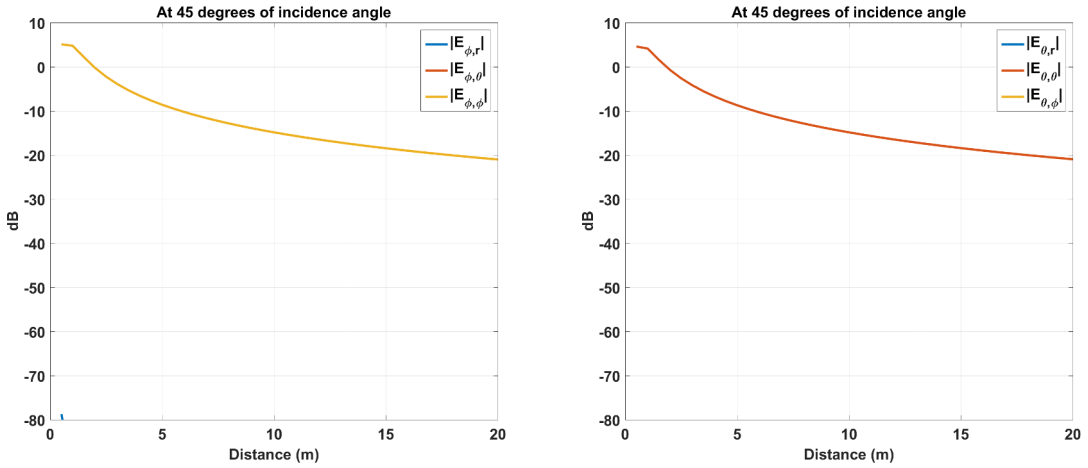

Figure D.1 – Amplitudes in dB of fields evolving with the distance at 5 GHz at 45 degrees of incidence.

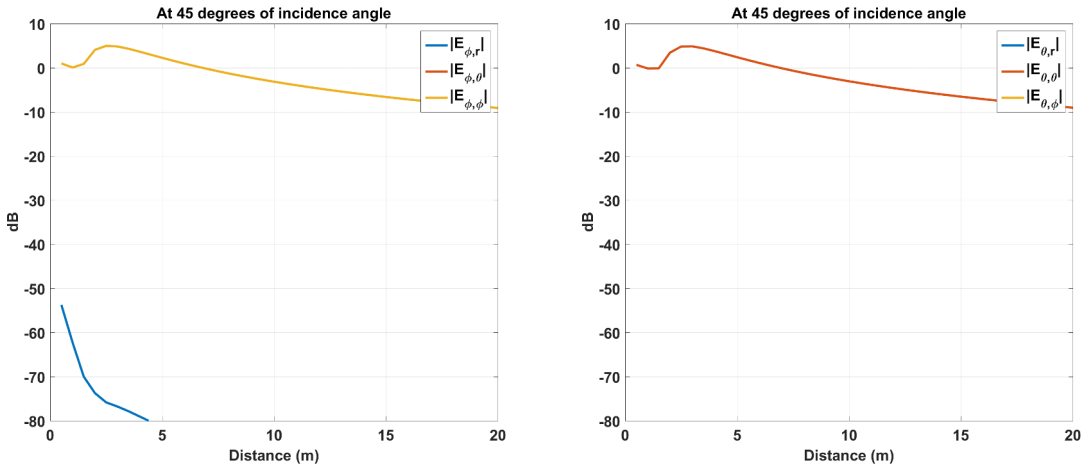

Figure D.2 – Amplitudes in dB of fields evolving with the distance at 18 GHz at 45 degrees of incidence.

This similarity with the APO solution is more visible on cuts plotted in Fig. D.3 at 5 GHz and in Fig. D.4 at 18 GHz in HH and VV polarisations around 4.3 meter (4, 4.5 and 5 meters) for the 0-90 degrees incidence angle. Note that to be able to compare in amplitude between the APO and the MoM solutions we multiply by the distance the MoM solution and divide by $2\sqrt{\pi}$ the APO solution. From these Figures, we observe few differences in dB between the APO and the MoM solutions (maximum 2 dB at 45 degrees at 18GHz, or locally at 5 GHz). However in trend, the curve behaved differently. At 18 GHz, the two solutions are looking alike whereas at 5 GHz, the lobes are shifted in incidence angle. For instance the main backscattering lobes at 0 and 90 degrees for the APO solutions are at 3 and 87 degrees.

Another way to assess the farfield condition is the field stabilisation with the distance. In this aim, we plot in Fig. D.5 and in Fig. D.6 at respectively 5 and 18 GHz, the field variations in amplitude and phase with the distance for three incidence angles (45, 30 and 15 degrees, representative of the double bounce area) in both HH and VV polarisations. To do so, we compute the first order numerical derivative of the field amplitude in dB (after compensating the distance as in Fig. D.3

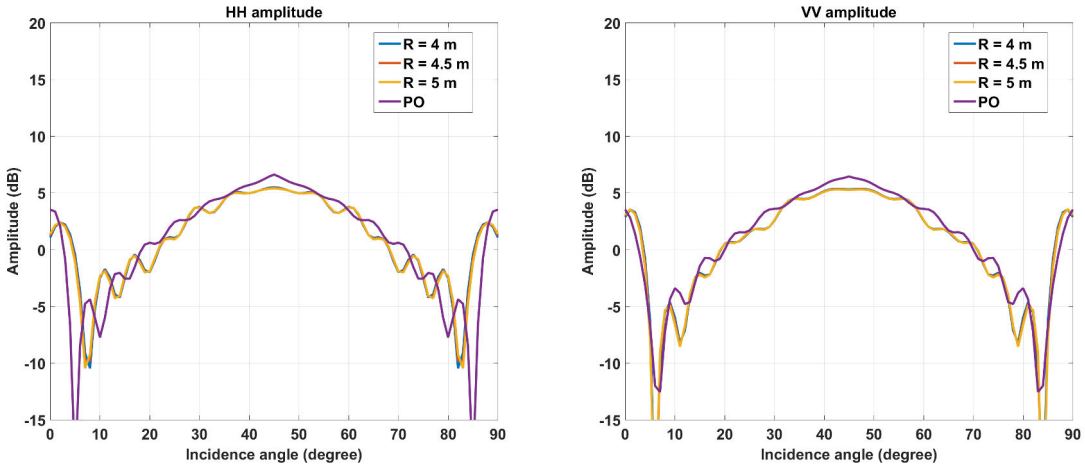

Figure D.3 – HH and VV amplitudes at 5 GHz for few distances around 4.3 meters and the APO solution.

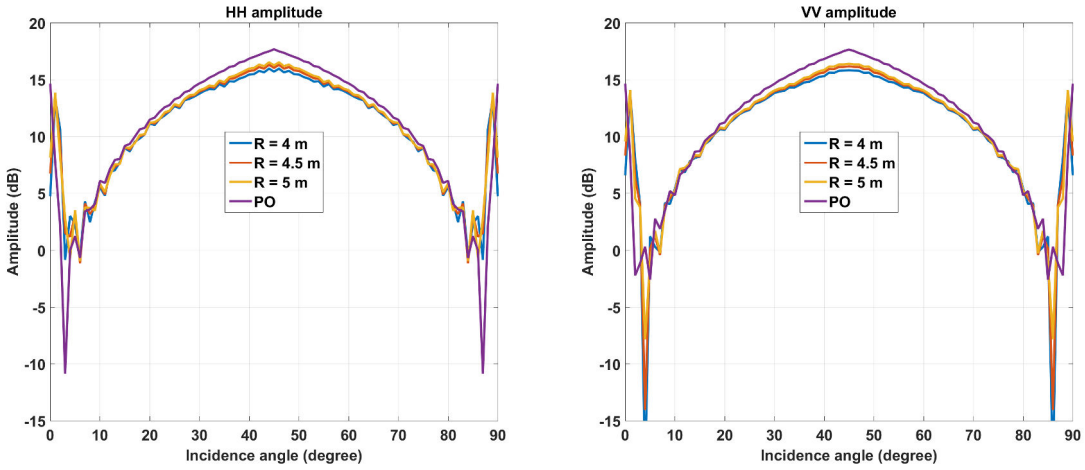

Figure D.4 – HH and VV amplitudes at 18 GHz for few distances around 4.3 meters and the APO solution.

and Fig. D.4) and of the field phase in degrees. As expected, for large distance, the derivative of the amplitude tends toward zero and the derivative of the phase toward a constant value (as we didn't compensate its propagation term in distance). It means that the propagation part of the field with the distance could be written as $\frac{e^{jkR}}{R}$ where R is the distance and k the wavenumber.
From the first figure we notice that we have less than half a dB difference starting at 2 meters and this for both polarizations and any incidence angles. Furthermore, the 45 and 30 degrees curves are the closest to 0. We can also observe that if the amplitude in HH and VV are very similar in Fig. D.3 and Fig. D.4, they do not evolve the same way with the distance even if in farfield the APO solutions is making them equal (in amplitude). What have been said at 5 GHz also holds at 18 GHz, except that now, the derivative is below 0.5 dB at 4 meters and it is now the central incidence angles that are the most slow to tend toward 0.
In terms of phase, at 5 GHz, both polarisations are near their farfield limits at 4 meters (within the degree) whereas for 18 GHz, the convergence is slower as at 6 meters only the 15 degrees curve is within the degree and only at 8 meters all the curves respect this condition.

As a conclusion, we look at several characteristics of the farfield condition: the wave plane structure of the scattered field (and thus its null component with the scattered direction of propagation), the similarity in amplitude with the APO solution in HH and VV polarisation and the compliance to a propagation in free space by looking at the numerical derivative with the distance. We have seen that the wave plane structure is always respected regardless frequencies or polarisations. We saw that at 5 GHz the farfield condition might be respected at 4.3 meters in terms of amplitude and phase as the MoM and APO solutions are looking alike and their variations in distance are quite constant. However at 18 GHz, the farfield condition is not respected (especially in terms of phase variations) as the phase stabilises after a distance of 8 meters even if in amplitude the APO and MoM solutions are very similar.

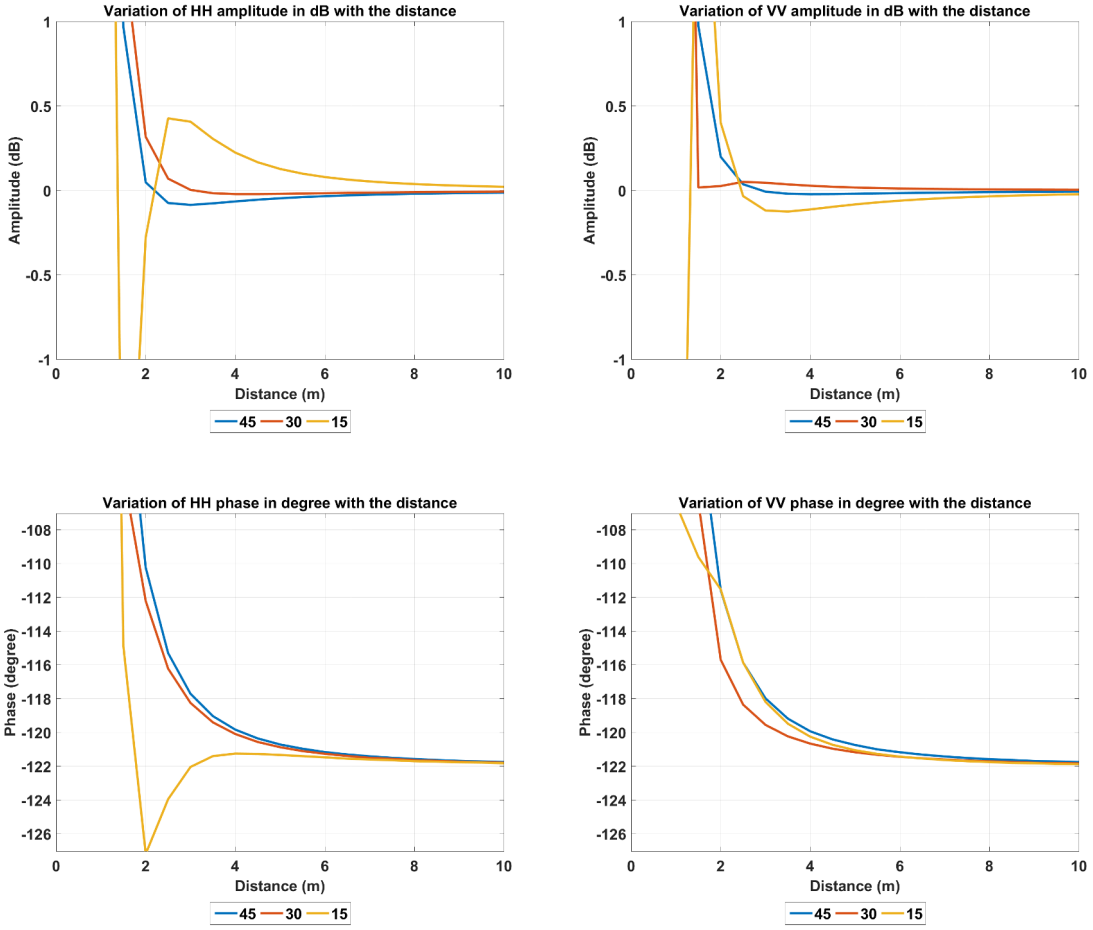

Figure D.5 – HH and VV amplitude and phase variations at 5 GHz for incidence angles at 45, 30 and 15 degrees.

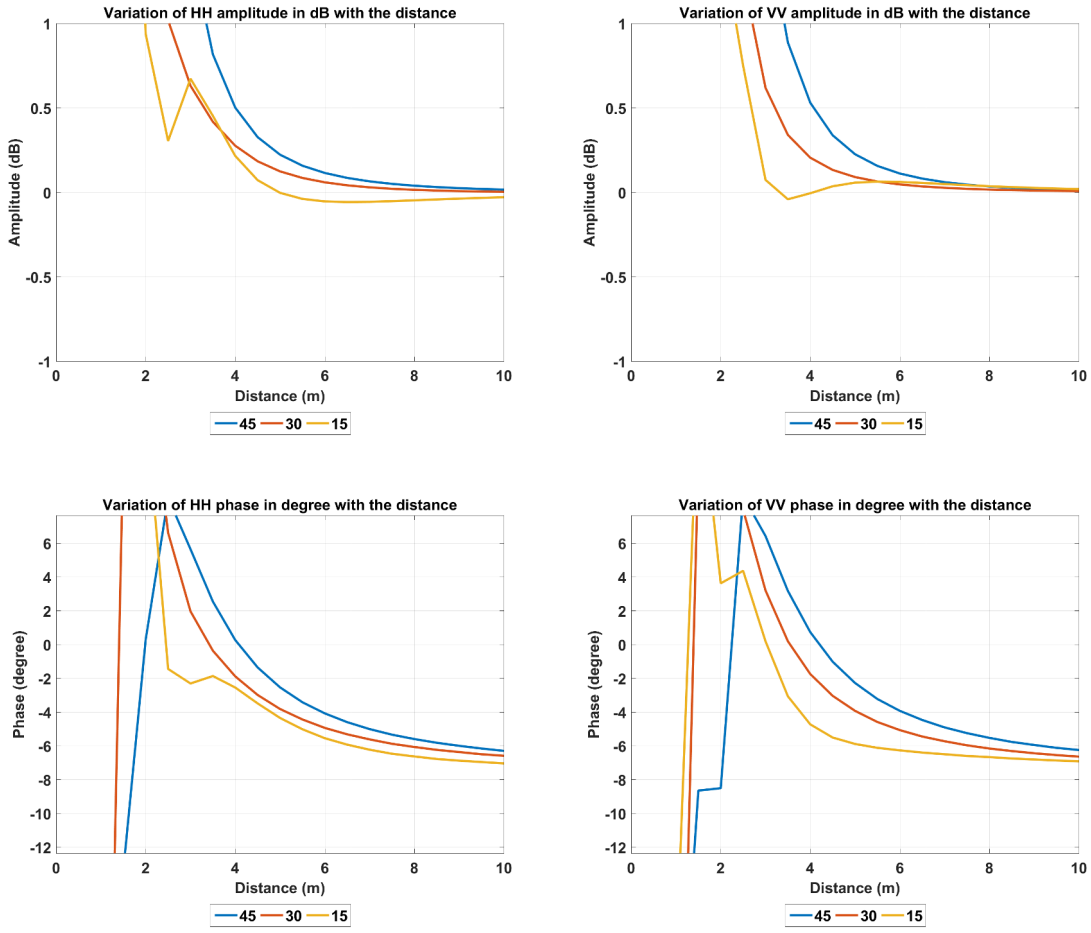

Figure D.6 – HH and VV amplitude and phase variations at 18 GHz for incidence angles at 45, 30 and 15 degrees.

D.2 Quasi-monostatic question

This study was made to determine which quasi-monostatic antenna configuration is providing us the closest results to an ideal monostatic one. For recall, the distance between the dihedral central edge and the two antennas is 4.3 meters, and the distance between the two antennas (from aperture centre to aperture centre) is roughly 20 cm. We could considered the two quasi-monostatic configurations displayed in Fig. D.7 anf Fig. D.8 (the gap between the two antennas is the scheme exaggerated to correctly see the difference between the two figures).
Configuration (CQM1) displayed in Fig. D.7 is such that the two antennas (greenish cones) are contained in (Oxz) plane. In Fig. D.8 the two antennas are contained in the plane formed by the y axis and the bisector ray between the two antennas rays at the incidence angle of ϕ degrees (CQM2).

We use FEKO Method of Moment (MoM) to compute at 4.3 meters these configurations for a PEC dihedral whose dimensions are $(a, b, L) = (0.3, 0.3, 0.3)$m . We compare the simulated fields with the calculated fields using the P.O. solution from [7] (also expressed in Appendix A.2.2) for a perfect monostatic case such that we will be able to assess which configuration is the closest to the monostatic one. Fields results are given in Fig. D.9 for CQM1 and in Fig. D.10 for CQM2 in amplitude and phase along with the monostatic APO solution from A.2.2. This is done for few frequency points: 9, 12,15 and 18 GHz. To be able to compare the two fields (the simulated MoM and the APO solution), we compensate the MoM solution by the propagation distance.

From Fig. D.9, we observe that the more the frequency is increasing, the more the amplitude and the phase of the signals in both polarisations are altered. In amplitude we observe a hollow that is increasing from 12 to 15 Ghz and then is divided in two at 18 GHz. A drop of at least 10 dB between the theroretical APO and the simulation can be noticed. In phase a increasing bump from 12 to 18 GHz, located near 45 degrees making a 90 degrees shift between the 9 and the 18 GHz phase at this incidence angle instead of being constant over the incidence angle range.
In Fig. D.10, the amplitude of the MoM simulation are now quite close to the theoretical APO solution for every frequency. The maximum difference is being seen at 18 GHz where a few dB are missing (2 dB). Likewise in phase, we see few changes: a hollow is forming from 12 to 18 GHz, but it is not as important as the one from CQM1.

From this short study, we can conclude that the use of the configuratio CQM2 is the best option for a quasimonostatic system to get as close as possible to a the monostatic signature. In addition, in the case we studied, it is adviseable to stay between 9 and 12 GHz and order to have a relatively stable phase with the incidence angle.

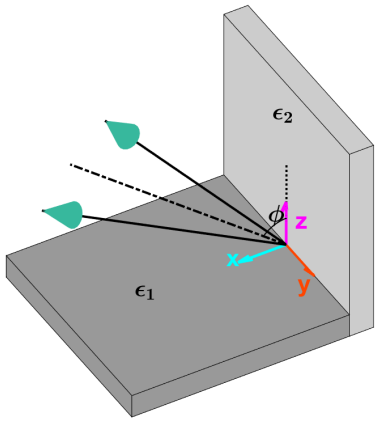

Figure D.7 – First quasi-monostatic configuration (CQM1).

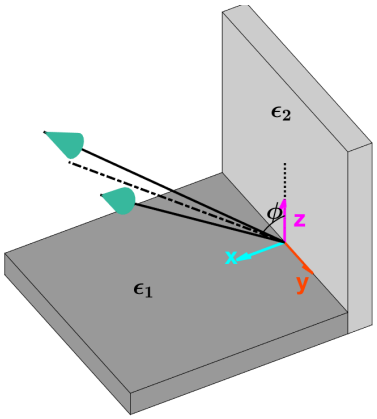

Figure D.8 – Second quasi-monostatic configuration (CQM2).

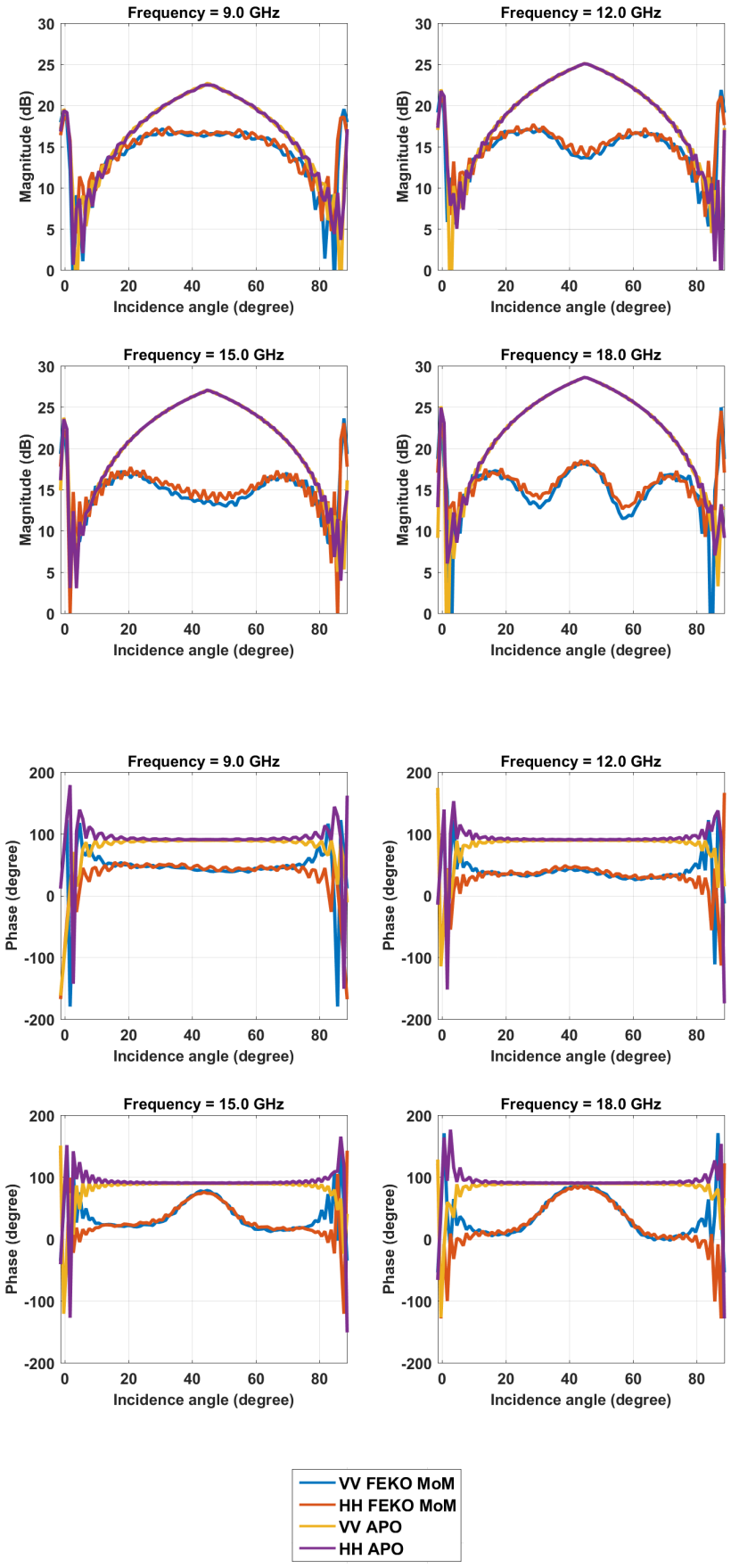

Figure D.9 – Amplitudes and phases of the backscattered fields for CQM1 at few frequencies, compared to APO solution.

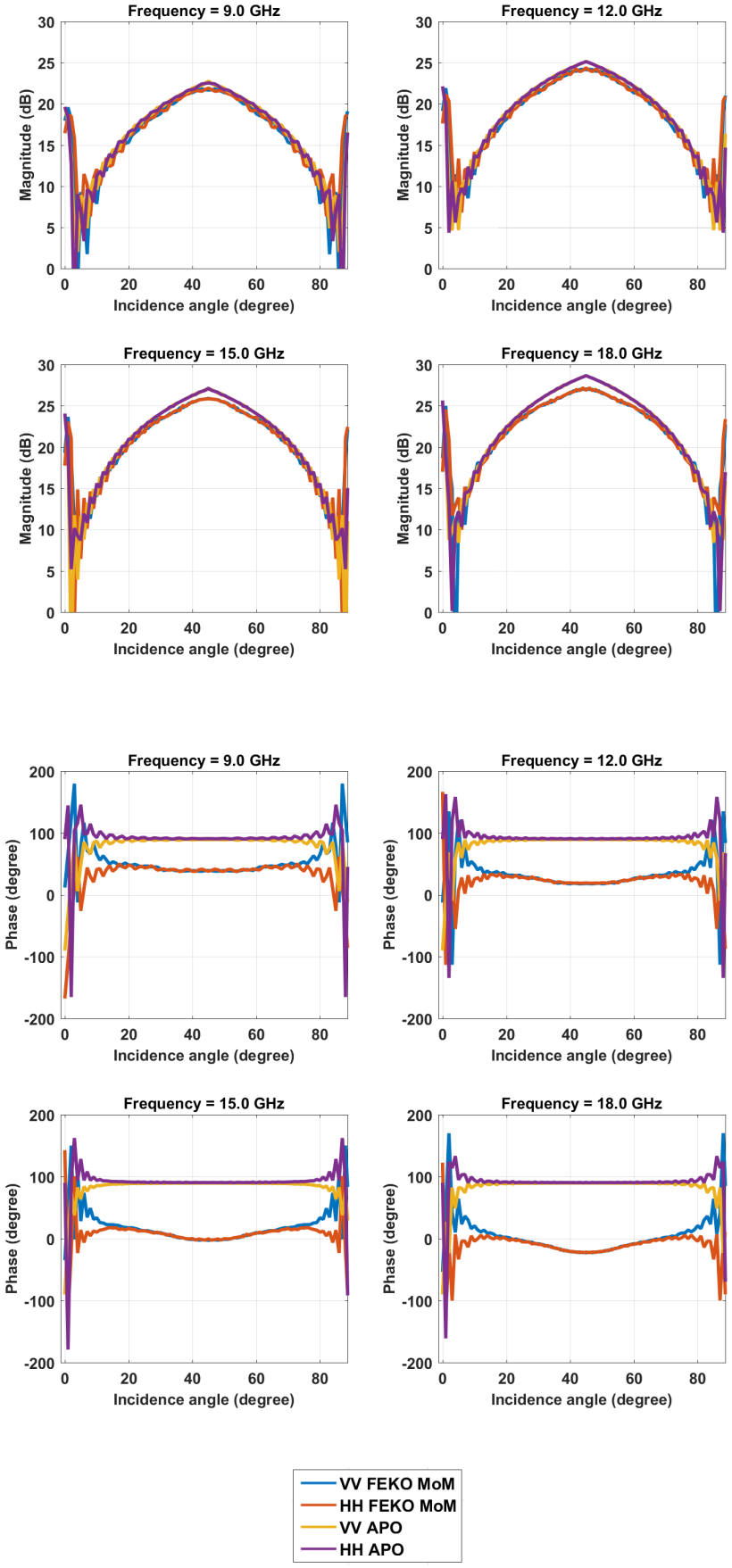

Figure D.10 – Amplitudes and phases of the backscattered fields for CQM2 at few frequencies, compared to APO solution.

Appendix E

Publications

Journals:

1. O. Couderc, L. Thirion-Lefevre, and R. Guinvarc'h, "Analytical Solution for Permittivities of a Dihedral Configuration," *IEEE Antennas and Wireless Propagation Letters*, vol. 17, pp. 485–488, March 2018

Conference proceedings:

1. O. Couderc, L. Thirion-Lefevre, and R. Guinvarc'h, "Is it possible to retrieve the complex permittivities using double bounce?," in *2016 IEEE International Symposium on Antennas and Propagation (APSURSI)*, pp. 1993–1994, June 2016
2. F. Doyelle, O. Couderc, L. Thirion-Lefevre, and R. Guinvarc'h, "Inversion of the Permittivities for a Double Bounce Mechanism," in *PIERS 2017*, Nov. 2017
3. O. Couderc, L. Thirion-Lefevre, and R. Guinvarc'h, "Moisture Retrieval Using Monostatic Radar Double Bounce," in *2018 IEEE International Geoscience and Remote Sensing Symposium (IGARSS)*, 2018

Bibliography

[1] R. Azzam and E. E. Ugbo, "Contours of constant pseudo-Brewster angle in the complex ϵ plane and an analytical method for the determination of optical constants," *Appl. Opt.*, vol. 28, pp. 5222–5228, Dec 1989.

[2] Y. K. Shestopaloff, "Polarization invariants and retrieval of surface parameters using polarization measurements in remote sensing applications," *Appl. Opt.*, vol. 50, pp. 6606–6616, Dec 2011.

[3] H. Fujiwara, *Spectroscopic ellipsometry: principles and applications*. John Wiley & Sons, 2007.

[4] E. Ceraldi, G. Franceschetti, A. Iodice, D. Riccio, and G. Ruello, "On the use of the specular direction copolarised ratio for the retrieval of soil dielectric constant," in *2003 IEEE International Geoscience and Remote Sensing Symposium (IGARSS)*, vol. 7, pp. 4144–4146 vol.7, July 2003.

[5] E. Ceraldi, G. Franceschetti, A. Iodice, and D. Riccio, "Estimating the soil dielectric constant via scattering measurements along the specular direction," *IEEE Transactions on Geoscience and Remote Sensing*, vol. 43, pp. 295–305, Feb 2005.

[6] E. Knott, "RCS reduction of dihedral corners," *IEEE Transactions on Antennas and Propagation*, vol. 25, pp. 406–409, May 1977.

[7] J. A. Jackson, "Analytic Physical Optics Solution for Bistatic, 3D Scattering From a Dihedral Corner Reflector," *IEEE Transactions on Antennas and Propagation*, vol. 60, pp. 1486–1495, March 2012.

[8] FEKO, "EM Software & Systems-S.A," 2012.

[9] A. Mokadem, *Analysis of scattering by urban areas in the frame of NLOS target detection in SAR images.* PhD Thesis, Supélec, Feb. 2014.

[10] M. I. Skolnik, "Radar Cross Section," in *Radar Handbook*, ch. 11, McGraw-Hill, 2006.

[11] O. Couderc, L. Thirion-Lefevre, and R. Guinvarc'h, "Analytical Solution for Permittivities of a Dihedral Configuration," *IEEE Antennas and Wireless Propagation Letters*, vol. 17, pp. 485–488, March 2018.

[12] L. Thirion-Lefevre and R. Guinvarc'h, "The double Brewster angle effect," *Comptes Rendus Physique*, vol. 19, no. 1, pp. 43 – 53, 2018.

[13] J.-S. Lee and E. Pottier, "Introduction to the Polarimetric Target Decomposition Concept," in *Polarimetric Radar Imaging: From Basics to applications*, ch. 6, pp. 179–227, CRC Press, 2009.

[14] T. Griesser and C. Balanis, "Backscatter analysis of dihedral corner reflectors using physical optics and the physical theory of diffraction," *IEEE Transactions on Antennas and Propagation*, vol. 35, no. 10, pp. 1137–1147, 1987.

[15] P. Corona, G. Ferrara, and C. Gennarelli, "Backscattering by loaded and unloaded dihedral corners," *IEEE Transactions on Antennas and Propagation*, vol. 35, no. 10, pp. 1148–1153, 1987.

[16] G. Franceschetti, A. Iodice, and D. Riccio, "A canonical problem in electromagnetic backscattering from buildings," *IEEE Transactions on Geoscience and Remote Sensing*, vol. 40, pp. 1787–1801, Aug 2002.

[17] A. L. Antunes Neves, *Application au domaine biomédical des moyens de caractérisation électromagnétique de matériaux dans le spectre des micro-ondes.* PhD Thesis, Université d'Aix-Marseille, Octobre 2017.

[18] M. Adous, *Electromagnetic characterization of concrete in the frequency range 50 MHz - 13 GHz.* PhD Thesis, Université de Nantes, Oct. 2006.

[19] M. Jamil, M. Hassan, H. Al-Mattarneh, and M. F. M. Zain, "Concrete dielectric properties investigation using microwave nondestructive techniques," *Materials and structures*, vol. 46, no. 1-2, pp. 77–87, 2013.

[20] A. Saintenoy, *Radar de sol : imagerie du sous-sol et quantification de paramètres physiques.* Habilitation à diriger des recherches, Université Paris Sud, Novembre 2014.

[21] K. Takahashi, H. Preetz, and J. Igel, "Soil properties and performance of landmine detection by metal detector and ground-penetrating radar soil characterisation and its verification by a field test," *Journal of Applied Geophysics*, vol. 73, no. 4, pp. 368–377, 2011.

[22] T. Chung, C. Carter, T. Masliwec, and D. Manning, "Impulse radar evaluation of asphalt-covered bridge decks," *IEEE Transactions on Aerospace and Electronic Systems*, vol. 28, no. 1, pp. 125–137, 1992.

[23] T. Chung, C. Carter, T. Masliwec, and D. Manning, "Impulse radar evaluation of concrete, asphalt and waterproofing membrane," *IEEE Transactions on Aerospace and Electronic systems*, vol. 30, no. 2, pp. 404–415, 1994.

[24] R. Azzam, "Explicit equations for the second Brewster angle of an interface between a transparent and an absorbing medium," *JOSA*, vol. 73, no. 9, pp. 1211–1212, 1983.

[25] R. Azzam, "Maximum minimum reflectance of parallel-polarized light at interfaces between transparent and absorbing media," *JOSA*, vol. 73, no. 7, pp. 959–962, 1983.

[26] J. A. Stratton, "Boundary-Value Problems," in *Electromagnetic Theory*, ch. 9, pp. 482–599, John Wiley & Sons, Inc., 1941.

[27] F. Sagnard, F. Bentabet, and C. Vignat, "Theoretical study of method based on ellipsometry for measurement of complex permittivity of materials," *Electronics Letters*, vol. 36, no. 22, pp. 1843–1845, 2000.

[28] K. Tsuzukiyama, T. Sakai, T. Yamazaki, and O. Hashimoto, "Ellipsometry for measurement of complex dielectric permittivity in millimeter-wave region," in *Microwave Conference, 2003 33rd European*, pp. 487–490, IEEE, 2003.

[29] F. Sagnard, F. Bentabet, and C. Vignat, "In situ measurements of the complex permittivity of materials using reflection ellipsometry in the microwave band: theory (part I)," *IEEE Transactions on Instrumentation and Measurement*, vol. 54, pp. 1266–1273, June 2005.

[30] Y. Oh, K. Sarabandi, and F. T. Ulaby, "An empirical model and an inversion technique for radar scattering from bare soil surfaces," *IEEE Transactions on Geoscience and Remote Sensing*, vol. 30, no. 2, pp. 370–381, 1992.

[31] P. Paillou, Y. Lasne, E. Heggy, J.-M. Malézieux, and G. Ruffie, "A study of P-band SAR applicability and performance for Mars exploration: Imaging subsurface geology and detecting shallow moisture," *Journal of Geophysical Research. Planets*, vol. 111, p. E06S11, 2006.

[32] P. Paillou, J. Lunine, G. Ruffié, P. Encrenaz, S. Wall, R. Lorenz, and M. Janssen, "Microwave dielectric constant of Titan-relevant materials," *Geophysical Research Letters*, vol. 35, no. 18, 2008.

[33] J. Mouginot, A. Pommerol, W. Kofman, P. Beck, B. Schmitt, A. Herique, C. Grima, A. Safaeinili, and J. Plaut, "The 3–5 MHz global reflectivity map of Mars by MARSIS/Mars Express: Implications for the current inventory of subsurface H2O," *Icarus*, vol. 210, no. 2, pp. 612–625, 2010.

[34] H. Shirai and M. Ishikawa, "Complex permittivity estimation from free space RCS measurement," in *Communications and Electronics (ICCE), 2010 Third International Conference on*, pp. 290–293, IEEE, 2010.

[35] K. Arunachalam, V. Melapudi, L. Udpa, and S. Udpa, "Microwave NDT of cement-based materials using far-field reflection coefficients," *NDT & E International*, vol. 39, no. 7, pp. 585–593, 2006.

[36] F. T. Ulaby and C. Elachi, "Scattering matrix representation for simple targets," in *Radar polarimetry for geoscience applications*, ch. 3, pp. 17–52, Artech House, Inc., 1990.

[37] A. Freeman and S. L. Durden, "A three-component scattering model for polarimetric SAR data," *IEEE Transactions on Geoscience and Remote Sensing*, vol. 36, pp. 963–973, May 1998.

[38] Y. Yamaguchi, T. Moriyama, M. Ishido, and H. Yamada, "Four-component scattering model for polarimetric SAR image decomposition," *IEEE Transactions on Geoscience and Remote Sensing*, vol. 43, pp. 1699–1706, Aug 2005.

[39] A. Freeman, "Fitting a Two-Component Scattering Model to Polarimetric SAR Data From Forests," *IEEE Trans. Geoscience and Remote Sensing*, vol. 45, no. 8, pp. 2583–2592, 2007.

[40] R. Guinvarc'h and L. Thirion-Lefevre, "Propagation in urban areas. Orientation, permittivity and entropy," in *2015 IEEE International Geoscience and Remote Sensing Symposium (IGARSS)*, pp. 1594–1597, IEEE, 2015.

[41] L. Thirion-Lefevre and R. Guinvarc'h, "The Brewster effect on polarimetric information," in *2015 IEEE International Geoscience and Remote Sensing Symposium (IGARSS)*, pp. 227–230, July 2015.

[42] T. Watanabe, H. Yamada, H. Kobayashi, Y. Yamaguchi, and M. Arii, "Indoor experiment on vegetation permittivity measurement using Brewster's angle," in *2011 3rd International Asia-Pacific Conference on Synthetic Aperture Radar (APSAR)*, pp. 1–4, Sept 2011.

[43] T. Watanabe, H. Yamada, M. Arii, S. E. Park, and Y. Yamaguchi, "Model experiment of permittivity retrieval method for forested area by using Brewster's angle," in *2012 IEEE International Geoscience and Remote Sensing Symposium*, pp. 1477–1480, July 2012.

[44] S. Cloude, "Depolarisation in surface and volume scattering," in *Polarisation: Applications in Remote Sensing*, ch. 3, pp. 115–177, Oxford University Press, 2009.

[45] M. Arii, J. J. van Zyl, and Y. Kim, "Retriveval of soil moisture under vegetation using Polarimetric Scattering Cubes," in *Geoscience and Remote Sensing Symposium (IGARSS), 2010 IEEE International*, pp. 1323–1326, IEEE, 2010.

[46] N. Lahlou, L. Ferro-Famil, and S. Allain-Bailhache, "Retrieving soil moisture below a vegetation layer using polarimetric tomographic SAR data," in *Geoscience and Remote Sensing Symposium (IGARSS), 2014 IEEE International*, pp. 3239–3242, IEEE, 2014.

[47] J. E. Hipp, "Soil electromagnetic parameters as functions of frequency, soil density, and soil moisture," *Proceedings of the IEEE*, vol. 62, no. 1, pp. 98–103, 1974.

[48] M. T. Hallikainen, F. T. Ulaby, M. C. Dobson, M. A. El-Rayes, and L.-K. Wu, "Microwave dielectric behavior of wet soil-part 1: Empirical models and experimental observations," *IEEE Transactions on Geoscience and Remote Sensing*, no. 1, pp. 25–34, 1985.

[49] M. C. Dobson, F. T. Ulaby, M. T. Hallikainen, and M. A. El-Rayes, "Microwave dielectric behavior of wet soil-Part II: Dielectric mixing models," *IEEE Transactions on Geoscience and Remote Sensing*, no. 1, pp. 35–46, 1985.

[50] N. R. Peplinski, F. T. Ulaby, and M. C. Dobson, "Dielectric properties of soils in the 0.3-1.3-GHz range," *IEEE Transactions on Geoscience and Remote Sensing*, vol. 33, pp. 803–807, May 1995.

[51] "Double-Ridged Horn Antennas." http://www.schwarzbeck.de/en/antennas/broadband-horn-antennas/double-ridged-horn-antenna.html#BBHA9120C. Accessed: 2018-09-10.

[52] S. Kingsley and S. Quegan, "Fundamentals," in *Understanding radar systems*, ch. 1, SciTech Publishing, 1999.

[53] H. C. Rhim and O. Buyukozturk, "Electromagnetic properties of concrete at microwave frequency range," *Materials Journal*, vol. 95, no. 3, pp. 262–271, 1998.

[54] H. M. A. Al-Mattarneh, D. K. Ghodgaonkar, and W. M. B. W. A. Majid, "Microwave Sensing of Moisture Content in Concrete Using Open-Ended Rectangular Waveguide," *Subsurface Sensing Technologies and Applications*, vol. 2, pp. 377–390, Oct 2001.

[55] M.-K. Olkkonen, V. Mikhnev, and E. Huuskonen-Snicker, "Complex permittivity of concrete in the frequency range 0.8 to 12 GHz," in *Antennas and Propagation (EuCAP), 2013 7th European Conference on*, pp. 3319–3321, IEEE, 2013.

[56] O. Couderc, L. Thirion-Lefevre, and R. Guinvarc'h, "Is it possible to retrieve the complex permittivities using double bounce?," in *2016 IEEE International Symposium on Antennas and Propagation (APSURSI)*, pp. 1993–1994, June 2016.

[57] F. Doyelle, O. Couderc, L. Thirion-Lefevre, and R. Guinvarc'h, "Inversion of the Permittivities for a Double Bounce Mechanism," in *PIERS 2017*, Nov. 2017.

[58] O. Couderc, L. Thirion-Lefevre, and R. Guinvarc'h, "Moisture Retrieval Using Monostatic Radar Double Bounce," in *2018 IEEE International Geoscience and Remote Sensing Symposium (IGARSS)*, 2018.

université PARIS-SACLAY
ÉCOLE DOCTORALE
Physique et ingénierie : électrons, photons, sciences du vivant (EOBE)

Titre : Inversion de permittivités d'une structure dièdrique au moyen de la polarimétrie radar.

Mots clés : inversion, permittivité, double rebond, monostatique

Résumé : Dans la situation d'un radar monostatique la configuration diédrique présente l'avantage de renvoyer un signal fort grâce au mécanisme de double rebond. De plus, il s'agit d'une configuration omniprésente par exemple en zone urbaine, avec des structures rue-bâtiment, ou en forêt, avec des structures de type sol-arbre. Les signaux rétrodiffusés sont donc liés à ces structures, plus précisément aux matériaux les composant, via leurs permittivités diélectriques. Retrouver ces permittivités depuis la mesure des champs rétrodiffusés permettrait l'identification des matériaux de la structure diédrique. Ceci mène à des applications telles que la détection de défauts dans la structure, l'estimation de la teneur en eau des sols ou du béton, ou *in fine* à des thématiques de classification, pour des objets dans des images radar par exemple, ou de détection de changement.

En modélisant le mécanisme de double rebond lié à la structure de dièdre par deux réflexions successives via les coefficients de Fresnel, trois méthodes d'inversion des permittivités ont été mises en place au cours de la thèse. La première, analytique, utilise à un angle d'incidence donné la mesure des champs copolarisés. Les deux autres méthodes, alliant une partie analytique et une partie numérique, nécessitent la mesure, du ratio polarimétrique pour l'une, du champ horizontal pour l'autre, effectuée à deux angles d'incidence différents. Ces méthodes ont été validées numériquement à l'aide de la méthode d'Optique Géométrique fournie par le logiciel FEKO. Des mesures en chambre anéchoique ont été effectuées afin de valider ces méthodes. De même une mesure *in-situ* a été effectuée sur un dièdre en béton formé par un angle entre deux murs.

Title : Permittivities retrieval of a dihedral structure using radar polarimetry.

Keywords : inversion, permittivity, double bounce, monostatic

Abstract : For a monostatic radar, the dihedral arrangement exhibits a strong response compare to bare surface. This phenomenon can be seen in radar images of urban areas or forestry as building and streets and trunks and ground are forming such structures. This signature can be modelled with the double bounce equation as a cascade of Fresnel reflection coefficients. These coefficients depend on the permittivities of the structures. Finding these permittivities from the backscattered fields may allowed to identify the materials involved in the dihedral. Thereforethis can be applied for default detection, moisture retrieval and classification topics for instance.

By modelling the double bounce scattering with Fresnel coefficients, three methods have been developed to retrieve these permittivities. The first one uses a single incidence angle and the measurements of copolarised fields. The last two methods need the measurement of the copolarised fields ratio or of the horizontal electric field alone at two different incidence angles. All these methods have been validated, first numerically using FEKO RL-GO method, then experimentally, with measurements in anechoic chamber. At last, *in-situ* measurements have been performed on a wall corner made of concrete to assess the method on a real case.

Université Paris-Saclay
Espace Technologique / Immeuble Discovery
Route de l'Orme aux Merisiers RD 128 / 91190 Saint-Aubin, France